Statistical Properties of the X-ray Radiation at Large Scale Facilities

Dissertation

zur Erlangung des Doktorgrades
an der Fakultät für Mathematik, Informatik und Naturwissenschaften
Fachbereich Physik
der Universität Hamburg

vorgelegt von

RUSLAN KHUBBUTDINOV

Hamburg
2022

Gutachter/in der Dissertation:	Prof. Dr. Ivan A. Vartaniants
	Prof. Dr. Christian G. Schroer
	Prof. Dr. Alexey P. Menushenkov
Gutachter/in der Disputation:	Prof. Dr. Ivan A. Vartaniants
	Prof. Dr. Christian G. Schroer
	Prof. Dr. Alexey P. Menushenkov
	Prof. Dr. Edgar Weckert
	Prof. Dr. Daniela Pfannkuche
Vorsitzender des Prüfungskommission:	Prof. Dr. Daniela Pfannkuche
Datum der Disputation:	13 Dezember 2021
Vorsitzender Fach-Promotionsausschusses PHYSIK:	Prof. Dr. Wolfgang Parak
Leiter des Fachbereichs PHYSIK:	Prof. Dr. Günter Sigl
Dekan der Fakultät MIN:	Prof. Dr.-Ing. Norbert Ritter

Zusammenfassung

Neue wissenschaftliche Erkenntnisse und die Schaffung neuartiger Materialien liegen in den Produktionstechnologien, der Industrieentwicklung, dem Digitalisierungsgrad, den Hightech-Anwendungen und damit dem Lebensstandard und dem Wohlstand. Die Entwicklung dieser hochmodernen Materialien hängt entscheidend von den verfügbaren Instrumenten und Technologien zu ihrer systematischen Untersuchung und Analyse ab. Eines dieser Instrumente, das den Fortschritt vorantreibt, ist ein Röntgenmikroskop in Großforschungsanlagen, eine hochmoderne Maschine, welche „die Komplexität der Natur entschlüsselt". Die Synchrotron-Speicherringe (SSR) der 4. Generation, die auch als beugungsbegrenzte Speicherringe (DLSR) oder Röntgen-Freie-Elektronen-Laser (XFEL) bekannt sind, sind die besten Beispiele für solch fortschrittliche Mikroskope. Das Untersuchungsprinzip solcher Röntgenmikroskope in Großforschungsanlagen basiert auf der Anwendung fortschrittlicher Forschungsmethoden und bildgebender Verfahren. Die Hauptmerkmale der angewandten Methoden und Techniken basieren auf der räumlichen und zeitlichen Auflösung des Röntgenstrahls und der Verwendung einer hochkohärenten hellen Röntgenphotonenquelle.

Eine der anspruchsvollsten Aufgaben für die DLSR- und XFEL-Photonendiagnostik ist die genaue Bestimmung der statistischen Parameter der Photonenquelle. Ein hervorragender Ansatz und die Analysemethode, die Informationen über die Photonenquelle liefert, liegt im Rahmen der statistischen Optik. Die Strahlungsquelle an DLSR-Anlagen unterscheidet sich deutlich von der ihres Vorgängers, und die Strahlungsquelle am XFEL besitzt eine einzigartige zeitliche Struktur und statistische Eigenschaften. Daher besteht ein erheblicher Bedarf an der Entwicklung geeigneter und wirksamer Methoden, die die Strahlungseigenschaften solcher hochmodernen Einrichtungen korrekt beschreiben.

Die vorliegende Arbeit konzentriert sich auf die umfassende Analyse statistischer Eigenschaften moderner Röntgenquellen an Großforschungsanlagen, wie dem Hochenergiespeicherring PETRA IV der 4. Generation, European XFEL (EuXFEL) und XFEL am Pohang-Beschleunigerlabor (PAL-XFEL). Besondere Aufmerksamkeit wird den Effekten geschenkt, die die Kohärenzeigenschaften und die Quelleneigenschaften in diesen Einrichtungen beeinträchtigen können. Die vorliegende Arbeit gliedert sich in zwei Teile, wobei im ersten Teil eine umfassende Analyse der Kohärenzeigenschaften der DLSR-Strahlung vorgestellt wird. Aufmerksamkeit wird den optischen Effekten auf den durch die Strahllinie transportierten Photonenstrahl, den Effekten der Elektronenstrahl-Energieverteilung auf die Kohärenz und Helligkeit einer DLSR-Photonenquelle und den Resonanzenergie-Verstimmungseffekten geschenkt. Als adäquater Ansatz zur Charakterisierung von Photonenstrahleigenschaften an DLSR-Anlagen wird eine Methode im Rahmen der statistischen Optik vorgeschlagen. Die Analyse wird durch semianalytische Simulationen basierend auf dem vorgeschlagenen Modell und spezialisierter Software unterstützt.

Der zweite Teil der Arbeit widmet sich der Photonenquellendiagnostik und der genauen Bestimmung der statistischen Parameter von Hochenergie-XFEL-Anlagen. In diesem Teil werden die Ergebnisse von Experimenten diskutiert, die am EuXFEL und PAL-XFEL durchgeführt wurden. Die Photonenstrahlcharakterisierung wird im Rahmen der statistischen Optik beschrieben, wobei besonderes Augenmerk auf die Monochromatorauflösung und das Zusammenspiel zwischen Auflösung und Größe der Austrittsspalte des Monochromators gelegt wurde. Die verwendete Methode wurde auf drei verschiedene Betriebsmodi des EuXFEL angewendet und mit einfachen analytischen Simulationen überprüft. Auch der Einfluss des Energy-Chirp-Effekts auf die Analyseergebnisse wurde berücksichtigt. Darüber hinaus wird die Photonenquellendiagnostik für die PAL-XFEL-Anlage vorgestellt. Diese Anlage kann sowohl im Modus der selbstverstärkten Spontanemission mit einem breitbandigen Strahl und einem gefilterten monochromatischen Strahl als auch im Modus des Self-Seeding mit hochintensiver Strahlung betrieben werden.

Abstract

The development of cutting-edge materials crucially depends on the available instruments and technologies for its systematic study and analysis. One of the instruments that drive the progress is an X-ray microscope, a state-of-the-art machine that is "decoding the complexity of nature". The 4^{th} generation synchrotron storage rings (SSR), which are also known as Diffraction-limited storage rings (DLSR), and X-Ray Free-Electron Lasers (XFEL) are the best examples of such advanced microscopes. The investigation principle by such X-ray microscopes is based on applying advanced research methods and imaging techniques. The key requirements are the space and time resolution, high flux, and coherence of the probing X-ray beam that are provided by the 4^{th} generation X-ray sources and XFELs.

One of the most challenging tasks for the DLSRs and XFELs is photon diagnostics, namely, the precise determination of the photon source statistical parameters. The photon statistics of the 4^{th} generation sources are notably different from that of their predecessors. Therefore, there is a significant demand for developing adequate and effective methods that correctly describe radiation properties from such ultimate facilities. An excellent approach and the analysis method, providing the information about the photon source, lies within the framework of statistical optics.

The present thesis is focused on the extensive analysis of statistical properties of modern X-ray sources at large-scale facilities, such as the 4^{th} generation high-energy storage ring PETRA IV, European XFEL (EuXFEL), and XFEL at Pohang Accelerator Laboratory (PAL-XFEL). Special attention is paid to the effects that may decrease coherence characteristics and impact source properties at these facilities. The present thesis is divided into two parts, where a comprehensive analysis of the coherence properties of the DLSR radiation is presented in the first part. Attention is paid to the optics effects on the photon beam transported through the beamline, electron beam energy spread effects on coherence and brightness of a DLSR photon source, and resonant energy detuning effects. A method in the framework of statistical optics is proposed as an adequate approach for the characterization of photon beam properties at DLSR facilities. The analysis is backed up with semi-analytical simulations based on the proposed model.

The second part of the thesis is devoted to photon source diagnostics and precise determination of the statistical parameters at the high-energy XFEL facilities. Results of experiments performed at EuXFEL and PAL-XFEL are discussed in this part of the thesis. The method within the framework of statistical optics for the EuXFEL photon beam characterization is described, where special attention was paid to the monochromator resolution and interplay between the resolution and the size of the exit slits of the monochromator. The method was applied to three different regimes of the XFEL operation and was checked with simple analytical simulations. The influence of the energy chirp effect on the analysis results was considered as well. Further, the photon source diagnostics is presented for the PAL-XFEL facility, operating in the Self-Amplified Spontaneous Emission (SASE) regime with the wide bandwidth beam and filtered monochromatic beam, as well as in the regime of Self-Seeding (SS) with highly intense radiation.

Hiermit erkläre ich an Eides statt, dass ich die vorliegende Dissertationsschrift selbst verfasst und keine anderen als die angegebenen Quellen und Hilfsmittel benutzt habe.

I hereby declare, on oath, that I have written the present dissertation by my own and have not used other than the acknowledged resources and aids.

Hamburg, den 01.12.2022
Ruslan Khubbutdinov

Contents

Chapter 1

Introduction

Optical Coherence and Quantum Optics

Coherence is the most fundamental aspect of light and quantum theory. In the field of quantum optics, M. Born, L. Mandel, E. Wolf, and R. J. Glauber during the 20^{th} century, developed most of the coherence quantum theories of light. The concept of coherence is very closely related to wave-particle duality. According to quantum physics, which was developed at the beginning of the 20^{th} century, electromagnetic radiation appears in the form of quanta, packets with fixed energies, which can be described as both waves and as particles, photons [1, 2]. Considering the wave picture, coherence is described best as a property of light that causes interference effects, firstly observed with conventional thermal sources. In the '30s, M. Born, who made significant contributions to quantum mechanics, solid-state physics, and optics, gave a more detailed look at the theory of electromagnetic light, diffraction, and interference [3] within the frame of classical optics. The field of quantum optics has largely developed since the first lasers appeared at the beginning of the '60s. At that time, E. Wolf, who made significant advances in optics, including diffraction, coherence, spectroscopy, and scattering, together with M. Born, published the famous book "Principles of Optics" where the basic principles of electromagnet radiation, diffraction, and interference effects were described [4]. However, no fundamental in-depth theory of light based on quantum theory existed before R. Glauber [5] and E. C. G. Sudarshan [6] established the foundation for quantum optics in 1963 so that the theory on the relationship of the visibility (waves) and distinguishability (particles) was developed. In particular, R. Glauber by introducing coherent photon states developed a quantum mechanical treatment of the correlation functions. This dramatically changed the scope of scientific research. Since then, coherent light has given rise to more quantum physical phenomena than regular light. In 1965, in Reviews of Modern Physics, L. Mandel and E. Wolf published "Coherence properties of optical fields", bridging classical, semiclassical and quantum optical theories of coherence and statistical optics [7], followed by the brilliant book "Optical Coherence and Quantum Optics" published in 1995 [8]. So much effort devoted to the study of coherence and correlations was not in vain. Coherence, both classical and quantum, can explain many physical phenomena. Therefore, exploiting coherence and interference methods nowadays allows us to discover and percieve, ultimately helping us deepen our understanding of nature.

Interferometry

Countless experiments have been performed to understand the properties of light and coherence, pioneered by T. Young, A. Michelson and E. Morley, C. Davisson and L. Germer, R. Hanbury Brown, and R. Q. Twiss. Young's double-slit interferometry experiment was part of classical physics long before the development of quantum mechanics and the concept of wave-particle duality. At the beginning of the 19^{th} century, this experiment demonstrated the wave behavior of light [9], while at the beginning of the 20^{th} century, the same type of experiment, conducted by C. Davisson and L. Germer demonstrated that particles may show the wave behavior [10] as well. Michelson and Morley's interferometry disproved the existence of the aether [11], leading to the special theory of relativity and the revolution in physics at the beginning of the 20^{th} century. Hanbury Brown and Twiss (HBT) intensity interferometers [12, 13] were originally used in astronomy, although they are also heavily used in the field of quantum optics. In general, the HBT interference effect can be attributed to the wave-particle duality of the beam under investigation. The results of a given experiment depend on whether the beam is composed of fermions or bosons. Even nowadays, this type of interferometry experiment lift the veil of secrecy, shrouding the physics of light and matter, space and time.

Applications of coherence methods and correlation techniques

Coherence and correlations techniques play a prominent role in many-body physics, statistical physics, and information technology. Correlation itself is a measure of how two or more systems or processes are related. Correlation techniques and methods have been extensively used in physics, and quantum physics [14] over the past several years. For instance, a fundamental challenge nowadays for quantum computation and simulation is to construct a large-scale network of highly connected coherent qubits. A recent experiment on a 53-qubit processor completed the task, whereas a supercomputer would take 10,000 years [15].

In astrophysics, correlation methods and interferometry are used to extract precise information about astronomical objects and large-scale cosmic events. For instance, the interferometer at Laser Interferometer Gravitational-Wave Observatory (LIGO) made the first direct observation of gravitational waves [16] in 2015. The experiment confirmed a vital prediction of general relativity, validating the theory's prediction of space-time distortion in the context of large-scale cosmic events. Another example can be made of the Event Horizon Telescope, which consists of several interferometry stations around Earth, where interferometry techniques were used in order to get the first-ever created image of the shadow of the black hole [17].

In modern condensed matter physics, the coherence properties of light are the key to the successful investigation of materials on the atomic scales [18]. Rapidly evolving imaging methods, which are staying in the core of structural analysis, are based on the utilization of coherent properties of the incoming bright x-ray beams. In this case, a fundamental understanding of the structure of modern materials is essentially based on X-ray measurements at large-scale facilities, such as SSRs or XFELs. Therefore, a better understanding of source properties is needed.

Coherent sources

With the development of new technologies [19], the construction of next-generation x-ray storage rings has become possible. Source brilliance and coherence of the future storage rings are the critical parameters for successful synchrotron radiation experiments. High values of these properties will allow focusing of the synchrotron beams efficiently to the nanometer range [20, 21]. It will enable an effective application of coherence-based techniques such as Coherent Diffraction Imaging (CDI), potentially reaching sub-nanometer resolution [21]. It will also extend X-ray photon correlation techniques into the regime of nanoseconds and allow for low dose correlation experiments [22].

To exploit coherence properly, a better understanding of the coherence properties of DLSR sources is necessary. These ultimate storage rings are expected to have a high degree of coherence, which means that traditional methods of X-ray tracing will not be sufficient to predict the parameters of X-ray beams at the experimental stations. Therefore, presently it is a big demand for developing adequate and effective methods that may correctly describe properties of radiation from the ultimate storage rings close to the diffraction limit. Clearly, such description should be based on the application of the first- and higher-order correlation functions [20, 23].

In parallel to the development of new DLSRs, the appearance of XFELs with their laser-like X-rays and unprecedented short and intense pulses open new possibilities for X-ray imaging and material investigation. For instance, XFELs proved extremely useful in Single Particle Imaging (SPI) experiments [24–26] and biomolecular imaging [27] in order to determine its three-dimensional (3D) structure with the ultimate resolution. Performance of the pump-probe experiments is another excellent application of the ultrashort XFEL pulses. In this kind of experiment, a sample is first pumped by the conventional infrared laser, and after some time delay, the dynamics is measured by the probe pulse. Results obtained during these experiments allow us to reveal ultrafast phase transition [28, 29], study dynamics of plasma–matter interactions [30] and ionization process, and laser–induced molecular dynamics [31, 32]. With the advent of such XFEL sources, it has become clear that essential information about the sample may be deduced only from multiple measurements accomplished by many realizations (pulses) of the radiation field from these sources. Therefore, these pulsed sources, in principle, cannot be treated as stationary ones; hence, such properties as spatial and temporal coherence have to be revised as well.

Thesis outline

The present thesis is focused on the extensive analysis of statistical properties of modern X-ray sources such as 4^{th} generation high-energy storage ring PETRA IV and European X-ray free-electron laser (EuXFEL) as well as Pohang Accelerator Laboratory X-ray free-electron laser (PAL-XFEL). Special attention is paid to the effects that may lead to a degradation of coherence characteristics at these sources.

The first part of the thesis is dedicated to the demonstration of the applicability of the general partially coherent radiation treatment approach developed in optics. This theory was applied to describe the properties of partially coherent X-ray beams at synchrotrons of the third generation and ultra-low emittance, high-brightness synchrotron light sources of the fourth generation as PETRA IV. A short introduction of the X-ray sources, brief theory of light and statistical optics, and compressed theory of the synchrotron radiation are given in the first chapters. The first part ends with a chapter where a comprehensive analysis of the coherence properties of the DLSR radiation is presented. Attention is paid to the optics effects on the photon beam transported through the beamline, electron beam energy spread effects on coherence and brightness of a DLSR photon source, and resonant energy detuning effects. A method in the framework of statistical optics is proposed as an adequate approach for the characterization of photon beam properties at DLSR facilities. The analysis is backed up with semi-analytical simulations based on the proposed model and simulations carried out by the specialized software.

The second part of the thesis is devoted to photon beam diagnostics and the precise determination of the statistical parameters at the high-energy XFEL facilities. Results of experiments performed at EuXFEL and PAL-XFEL are discussed in this part of the thesis. The method within the framework of statistical optics for the EuXFEL photon beam characterization is described, where special attention was paid to the monochromator resolution and interplay between the resolution and the size of the exit slits of the monochromator. The relationship between the beam statistics determined in the interferometry experiments and the statistical properties of the X-ray beam incoming to the monochromator is demonstrated. This method was applied to the three different regimes of the XFEL operation and was checked with simple analytical simulations. The influence of the energy chirp effect on the analysis results was considered as well. The second part ends with a chapter where photon beam diagnostics is presented for the PAL-XFEL facility, operating in a Self-Amplified Spontaneous Emission regime with the wide bandwidth beam and filtered monochromatic beam, as well as in the regime of Self-Seeding with highly intense radiation.

Chapter 2

X-rays and Synchrotron sources

2.1 X-rays

X-ray is high-energy electromagnetic radiation, naturally occurring from various sources, such as radioactive elements, astrophysical objects, and can be produced artificially (see Fig. 2.1) by a human made source. X-rays were discovered in 1895 by German physics professor Wilhelm Röntgen while experimenting with Crookes tubes and Lenard tubes (modified Crookes tube, [33]). He wrote a report, "On a new kind of rays.", which was the first paper written on X-rays [34]. Röntgen referred to the radiation as "X" to indicate that it was an unknown type of radiation. Later the article was published in Nature [35], describing the behavior and properties of X-rays in the different media. Since then, X-rays have found use in a wide range of scientific and medical applications.

Before their discovery, X-rays were just a type of unidentified radiation emanating from experimental discharge tubes. They were noticed by scientists investigating cathode rays produced by such tubes, which are energetic electron beams that were first observed in 1869. Many of the early Crookes tubes (see for example Fig. 2.1 (b)) were radiating X-rays. Crookes tubes created free electrons by ionization of the residual air in the tube by a high voltage in the range from a few kilovolts to 100 kV. This voltage accelerated electrons coming from the cathode to the anode. X-rays were created when electrons struck the anode or the glass wall of the tube. The spectrum of radiation emitted by an X-ray tube is a characteristic curve with several peaks (see Fig. 2.1 (c)). Two separate processes result in such a curve: the bremsstrahlung and the characteristic radiation. During the first process, the deceleration of an electron by an atomic nucleus results in electromagnetic radiation, described by a continuous spectrum. The characteristic radiation is caused by the atoms in the anode, ionized due to the electron-atom collisions. In this case, core holes formed as a result of the ejection of bound electrons from the inner shells due to the photoelectric effect, filled by the electrons from the outer shells, so that the energy of the emitted photon is the energy difference between the higher and lower states. The latter leads to the characteristic spikes in the spectrum of the emitted radiation.

In general, these electromagnetic waves can be observed in the wavelength range from 0.01 nm to 10 nm. Therefore, this kind of radiation becomes useful for structure determination on

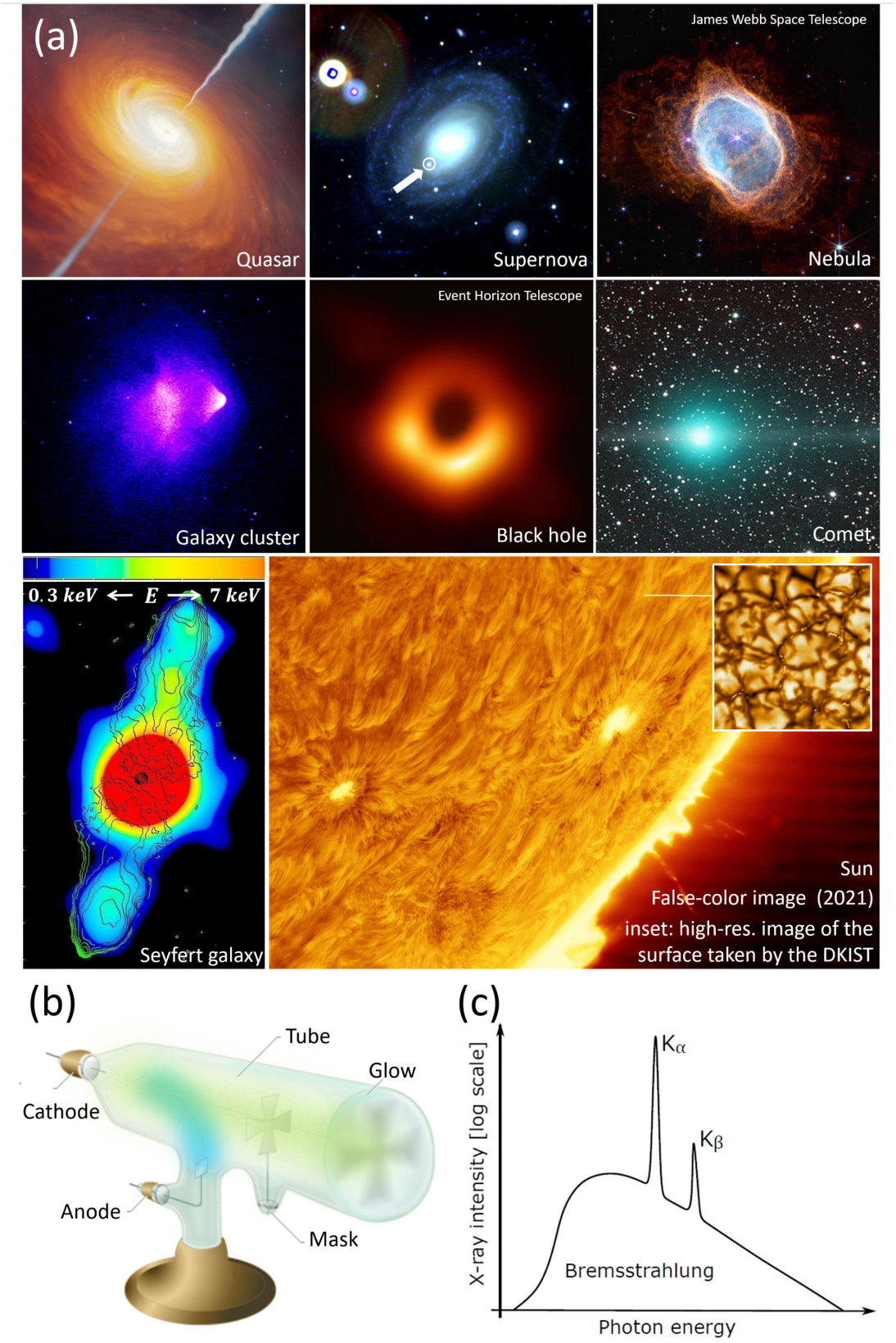

Figure 2.1: (a) The most bright astrophysical X-ray photon sources. (b) A picture of a Crookes tube (c) The spectrum from an X-ray tube.

atomic length scales, as well as relatively thick objects, since the X-rays possess high penetration depth. The latter also implies that a scattered signal from a relatively small sample can be weak as well. In this case, a highly intense X-ray source is required in order to obtain a high signal-to-noise ratio. The intensity of X-ray radiation is usually characterized by the spectral photon flux F, which shows the number of emitted photons per unit time and 0.1% of the radiation bandwidth (BW)

$$F \approx \frac{photons/sec}{0.1\%bandwidth}, \tag{2.1}$$

and by spectral brightness B, which shows amount of spectral photon flux per unit solid angle Ω [$mrad^2$] and per unit projected area S [mm^2]

$$\mathcal{B} \approx \frac{F}{\Omega S}. \tag{2.2}$$

The spectral brightness of the X-ray sources varies in the wide range from 10^5 to 10^{35} $photons/\ s/mm^2/\ mrad^2/\ 0.1\%BW$ (see Fig. 2.2 for examples). The brightness of the modern X-ray tubes is in the range 10^7 - 10^{12} $photons/\ s/mm^2/\ mrad^2/\ 0.1\%BW$, which is comparably small. However, X-ray tube-based instruments made their quick way into numerous applications in medicine, materials science, chemistry, and biology. For instance, the first experiment studying diffraction on crystals was performed with the X-ray tube by William Henry and William Lawrence Bragg [36], who became one of the founders of X-ray crystallography field. The discovery of the synchrotron radiation and modernization of storage rings raised the brightness bar to the level 10^{23} $photons/s/mm^2/mrad^2/0.1\%BW$, which only XFELs can overcome, setting a limit to the enormous value of 10^{35} $photons/\ s/mm^2/\ mrad^2/\ 0.1\%BW$.

2.2 Synchrotron sources

2.2.1 First generation storage ring facilities

The storage rings are currently the main sources of bright X-ray radiation. In addition to its high brightness, X-rays from the synchrotron are also highly stable in energy, intensity, size, and position of the beam. The energy of photons varies within a wide spectrum, from the IR range to hard X-rays. Often, beams from the storage rings are linearly polarized in the plane of the ring, although elliptically polarized beams can also be created by adding special devices [38].

For the first time, synchrotron radiation was observed in the '40s as a parasitic one in the particle accelerators designed for experiments in high-energy physics. The observation was made in a wide variety of different research laboratories: General Electric Research Laboratory, USA; Lebedev Institute, Russia; Cornell Electron Synchrotron, USA. In such experiments, bending magnets (Fig. 2.4) hold the particles in the accelerating ring and set their trajectory. The synchrotron radiation properties depend on multiple factors, the energy of the particle E_γ

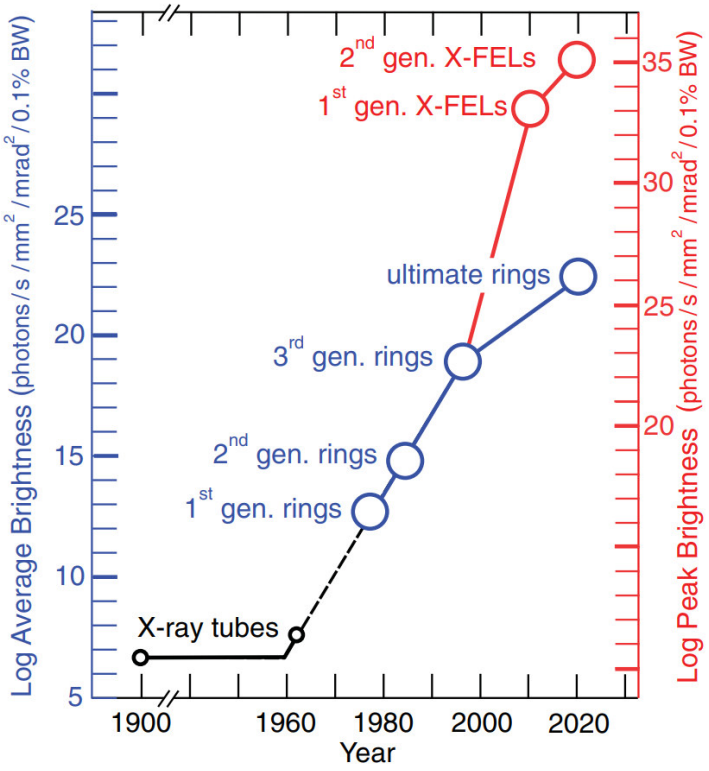

Figure 2.2: (a) Evolution and peak brightness of X-ray sources. This Figure was adapted from [37]

in the storage ring is one of them.

$$E_\gamma = \gamma mc^2, \tag{2.3}$$

where mc^2 is the rest mass energy of the particle and γ is the Lorentz factor

$$\gamma = \frac{1}{\sqrt{1-\left(\frac{\nu}{c}\right)^2}} = \frac{1}{\sqrt{1-\beta_\nu^2}}, \tag{2.4}$$

with ν being the speed of particles, c is the speed of light in vacuum and $\beta_\nu = \nu/c$. First accelerators that emerged in the '30s maintained comparably low energy of the beam up to 1 GeV. In the next 30 years, the upper limit of the particle beam energy raised to the bar of 100 GeV. Modern particle colliders, such as the Large Hadron Collider (LHC) capable of maintaining electron beam energy up to huge energies of 6.5 TeV and collision energy of 13.6 TeV. However, synchrotron accelerators are dedicated to studying the condensed matter, biology, and chemistry, operating in standard regimes with the electron beam energy up to 8 GeV. In this case typical Lorentz factor, found at synchrotron accelerators, lie in the range $2 \cdot 10^3 < \gamma < 16 \cdot 10^3$, and the electron beam is considered to be ultrarelativistic. Synchrotron radiation is generated when relativistic particles are accelerated or subjected to periodic acceleration in a magnetic field. At the synchrotron accelerators, due to centripetal acceleration, particles lose energy and emit electromagnetic waves (Fig. 2.3 (b)) [39]. If the particle is moving at relativistic speeds, then the radiation is emitted as a narrow cone tangent to the path of the particle (Fig. 2.3 (c))

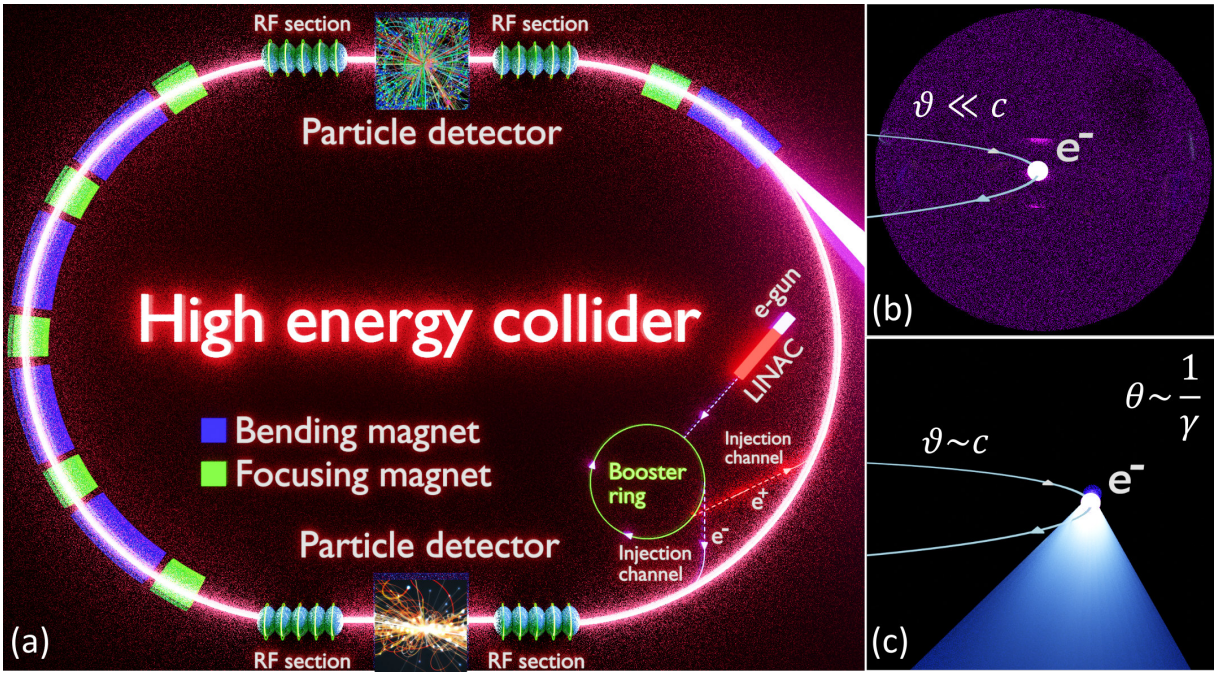

Figure 2.3: (a) Schematic view of the high energy collider (b) Isotropic electromagnetic radiation emitted due to acceleration of a charged particle traveling at small velocities compared to the speed of light. (c) Relativistically moving charged particles emit radiation in a narrow cone tangent to the path of the particle.

$$\theta \approx \frac{1}{\gamma}. \tag{2.5}$$

Such synchrotron radiation, produced at a particle accelerator already may be exploited in the experiments [40, 41]. While the number of synchrotrons was growing, the next major advance was the development of first-generation facilities. In particular, the development concerned the electron storage ring, which is the basis for all of today's synchrotron sources.

2.2.2 Second generation storage rings. Dedicated synchrotron radiation sources

Second generation facilities, which are dedicated synchrotron radiation sources, built already containing several main components [42], which maintain the viability of the particles and provide a stable X-ray radiation beam (see Fig. 2.4 (a)): an electron gun, a booster ring, the storage ring, radiofrequency section, bending magnets and beamlines.

The electron gun is the source of electrons, usually generated by thermionic emission from a hot filament. The electron gun is working in the continuous regime since a regular supply of electrons is required. The electrons are accelerated using a linear accelerator (linac) to about 100 MeV. Electrons have the ability to be lost in the machine due to collisions with gas particles (remaining after obtaining a vacuum) in the storage ring. After the electron current is obtained, it is directed from the linac to a booster ring for further acceleration (Fig. 2.4 (a)). The acceleration may be continued to the desired energy of the electrons in the main storage. Injection from the booster ring is happening periodically into the storage ring so that the specified storage

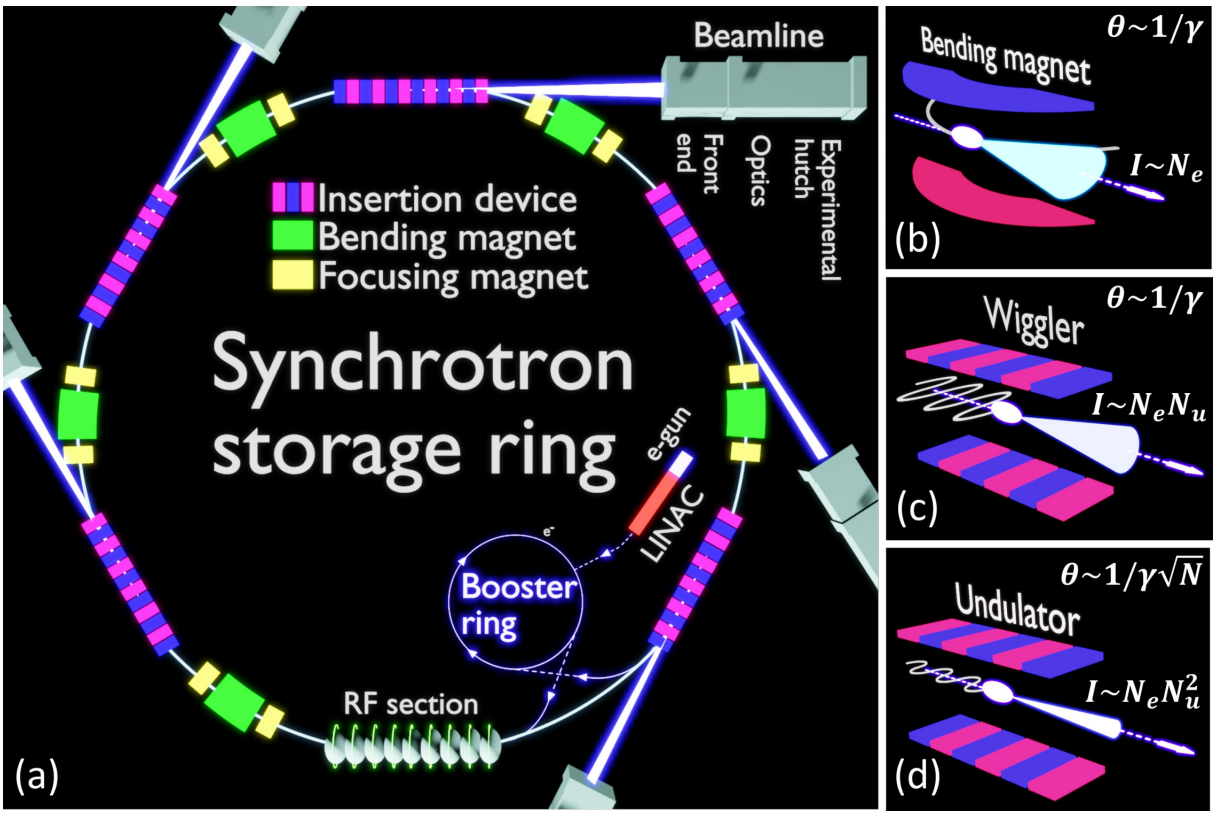

Figure 2.4: a) Schematic view of the storage ring with the main components : Accelerator, Radio frequency (RF) system, Bending magnet (BM), Insertion device (ID) and Beamline (reproduced from [43]). Schematic representation of the various magnetic devices commonly used to produce synchrotron radiation: b) bending magnet, c) wiggler, d) undulator.

ring current is maintained.

To form a bright photon beam, a large number of emitting particles are needed. Most synchrotron sources are storage rings in which particles repeatedly circulate and generate X-rays each time they pass through sections with magnetic devices (see Fig. 2.4 (b-d)). Several different experimental stations are located along the synchrotron ring and use the same electron bunches. The distance between the electronic bunches is set by radio frequency (RF) accelerators. In addition, RF accelerators recover the electron energy spent on synchrotron radiation. The frequency of field oscillations in RF accelerators can be from several MHz up to 1 GHz, which means that the time difference between successive X-ray pulses can be up to 1 ns.

Stable trajectory and a closed path of the electrons are provided by the use of an array of magnets [42] of the ring. Three types of magnets are commonly used: bending magnets (cause the electrons to change their path and eventually maintain a circular orbit), quadrupole magnets (focus the electron beam and compensate for Coulomb repulsion between the electrons), sextupole magnets (correcting for chromatic aberrations that arise from the focusing by the quadrupoles). Bending magnets were commonly used at second-generation facilities, which cause a curved trajectory of the electron beam and a broad radiation cone around the bend Fig. 2.4 (b). However, dipole bending magnets alone (Fig. 2.4 (a,b)) cannot maintain a closed orbit of the electrons if the latter deviates from the ideal reference orbit. Since then, focusing pair

of vertical and horizontal quadrupole magnets has brought them back towards the ideal orbit. The arrangement of different types of magnets is called the magnetic lattice.

The beamline is finishing the list of main elements of the synchrotron facility. Beam defining apertures placed in the beginning of the beamline to set the angular acceptance of the synchrotron radiation. By that, radiation filters out the low-energy tail of the synchrotron radiation spectrum, which is strongly absorbed by matter and can damage optical components. Then the beam is monochromatized (if necessary) and focused in the optics hutch before it becomes available at the experimental hutch to researchers. Second-generation facilities maintained electron bunch energy in the range of 0.7 to 5 GeV. Examples include the following dedicated synchrotron facilities: Tantalus, University of Wisconsin-Madison, USA; National Synchrotron Light Source at the Brookhaven National Laboratory, USA; Aladdin at the University of Wisconsin Synchrotron Radiation Center, USA; Photon Factory at the KEK laboratory, Japan; BESSY II at the Helmholtz-Zentrum Berlin, Germany; Stanford Synchrotron Radiation Laboratory at SLAC, USA; and HASYLAB (Hamburger Synchrotronstrahlungslabor) at DESY, Germany. Development of the dedicated synchrotron sources allowed to increase brightness up to 10^{15} $photons/s/mm^2/mrad^2/0.1\%BW$ (see Fig. 2.2).

2.2.3 Third generation storage ring facilities

The next step in the modernization up to 3^{rd} generation synchrotron facilities was made towards increasing the source coherence and brightness. Examples of the third generation storage rings include the following facilities: ESRF, Grenoble, France; APS, Chicago, USA; SPring-8, Japan and PETRA III, Hamburg, Germany. Coherent characteristics and brightness of the photon beam were sufficiently improved by adding special devices such as wigglers and undulators. If a magnetic structure is periodically set and the magnetic field is strong, then the wiggler radiation is produced Fig. 2.4 (c). At this type of radiation source, the particle experiences a harmonic oscillation as it moves through the structure with high oscillation amplitude and, as a consequence, a broader spectrum. Although one may obtain more power from such a source, the brightness will be lower due to the broader radiation cone. If the magnetic field is relatively weak, then the undulator radiation is produced Fig. 2.4 (d). At this type of radiation source, the particle experiences a harmonic oscillation with a small undulation amplitude due to a lower magnetic field. In this case, the radiation cone will be much narrower. Introducing such a structure in the electron storage ring, one may obtain synchrotron radiation with small angular divergence and higher intensity.

Third generation synchrotrons typically reliant upon undulators and their brightness reaches up to 10^{21} $photons/s/mm^2/mrad^2/0.1\%BW$ (see Fig. 2.2). Coherence properties of the X-ray radiation are also improved. However, only 1 % of the beam is sufficiently coherent to be used in coherence-based applications. Consequently, the sources with a higher degree of coherence are strongly required in order to get the full benefit from the X-ray beam without the use of strong spatial filtering of the radiation [44].

Figure 2.5: Examples of the 4^{th} generation synchrotron sources with the specified parameters.

2.2.4 Fourth generation facilities. Diffraction - limited storage rings

Nowadays, fourth-generation facilities are constructed (see examples in Fig. 2.5), having many straight sections specially optimized to produce high brightness undulator radiation. Due to a new conceptual approach, that is, the design of a multi-bend achromat lattice of the synchrotron storage ring, the brightness of the next generation X-ray storage rings can be increased by two to three orders of magnitude [45], [46] (for the comparison of X-ray sources see in Fig. 2.2).

Another distinctive feature of these 4^{th} generation facilities is a very small size of the main source of X-rays (i.e., electron bunch), and as a consequence, highly coherent X-ray radiation (up to 90% [47]) Corresponding characteristics describing dimensional parameters of the source are electron beam emittance $\varepsilon_{e,x}$ in horizontal and in $\varepsilon_{e,y}$ vertical directions accordingly. Typical values of electron beam emittance found at storage rings of the 4^{th} generation do not exceed 350 pm rad in both spatial directions. The first storage ring constructed using multi-bend

Table 2.1: The present and planned fourth generation sources target parameters [47–51].

Source	MAX IV	SIRIUS	ESRF-EBS	APS-U	PETRA IV
Energy, GeV	3	3	6	6	6
ε_x (pm · rad)	200-330	250	120-30	42-32	20-30
ε_y (pm · rad)	2-8	2	5-30	4-32	4-10
Current, mA	500	350	200	200	200
Brightness, ph/(s·mm^2·mrad^2·0.1%)	$4 \cdot 10^{21}$	10^{21}	10^{22}	$2 \cdot 10^{22}$	10^{23}

achromat technology was 3 GeV synchrotron source MAX IV (Lund, Sweden) (see Fig. 2.5), which recently reached its planned specifications of horizontal emittance of about 200 - 330 pm rad (depending on insertion device gap settings) [48]. Additional parameters are given in the Table 2.1. Brazilian SIRIUS 3 GeV project is in the commissioning stage with horizontal emittance planned in the range of 150 – 250 pm rad [52]. The high-energy ESRF 6 GeV storage ring has finished the upgrade to the EBS ESRF facility, which is reached the horizontal emittance of 133 pm rad, and other facilities worldwide (APS-U, SPring-8, ALS, Soleil, Diamond, and etc.) are in construction or planning stage. At DESY in Hamburg, an upgrade of the high-energy 6 GeV storage ring PETRA III to PETRA IV facility (Fig. 2.6 (a)) is also planned, and the world's lowest emittance of about 4 pm rad for hard x-rays is targeted at this storage ring [51]. In addition, a very high brilliance of the source will be maintained at this facility (see Fig. 2.6 (b)).

Next-generation synchrotron sources, in particular PETRA IV facility, have the potential to make a significant contribution to today's main challenges in the investigation of multifunctional hybrid materials, electronic transport phenomena, and electrochemical processes in charge storage materials under working conditions, as well as materials under extreme conditions of pressure and temperature with highest resolution and sensitivity [53]. Another advantage of this synchrotron facility is well defined time structure of the pulse with a short duration. Such pulsed synchrotron radiation sources are ideal facilities for performing time-resolved experiments, as it was shown during the last years using pump-probe X-ray spectroscopy and diffraction, X-ray photon correlation spectroscopy, nuclear resonance scattering, and time-of-flight spectroscopy of electrons and ions. Although time-resolved studies emerge more at free-electron lasers, like FLASH or European XFEL utilizing femtosecond pulse width, time-resolved experiments will be coveted at the future storage-ring-based synchrotron radiation sources as well.

As the X-ray source will be highly coherent up to 10 keV, the full beam can, in principle, be captured and focused, limited in performance only due to optics quality. Experiments at higher X-ray energies or with high energy resolution will also experience these brightness gains. To fully exploit the potential of 4^{th} generation sources, optics need to be adapted in size, improved in terms of aberrations, and be able to handle higher X-ray intensities. X-ray microscopy techniques are those that will profit the most from the record emittance and spectral brightness of 4^{th} generation synchrotron sources. Diffraction-limited focusing of the full undulator beam will have a significant impact on all X-ray analytical techniques, as they can then all be efficiently

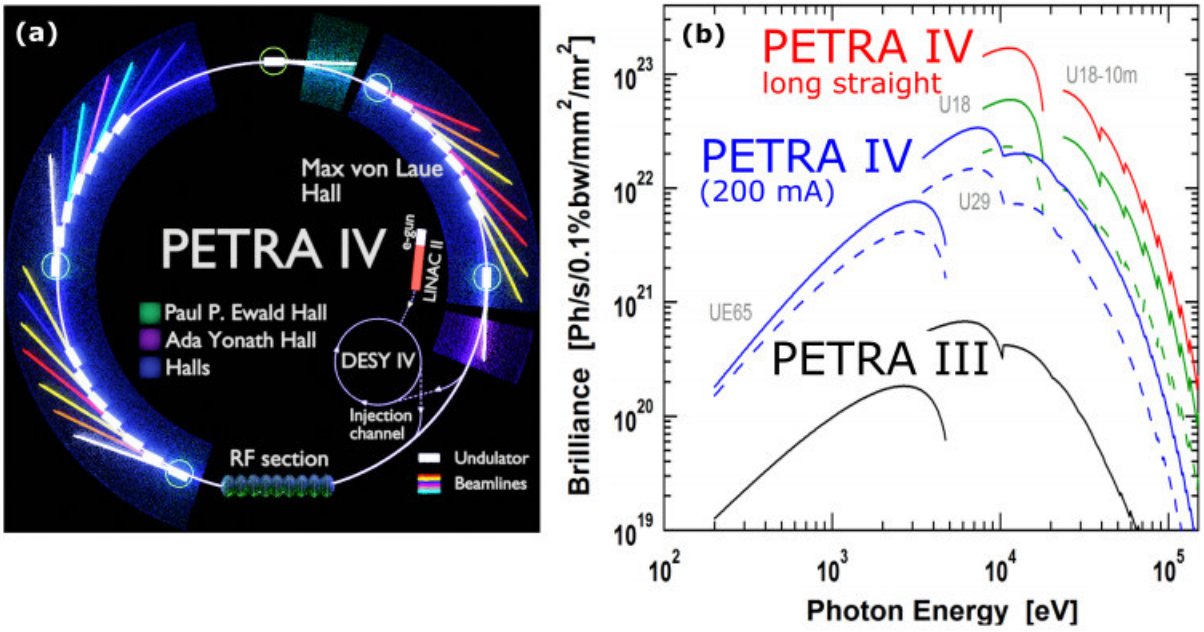

Figure 2.6: (a) Schematic view of the 4^{th} generation synchrotron radiation source (reproduced from [54]) (b) Comparison between the brightness of PETRA IV storage ring (blue, green, and red curves) and PETRA III (black curves) storage ring. This figure was adapted from reference [51]

used as contrast mechanisms in scanning microscopy. In this way, the "X-ray microscope" will give quantitative access on the nanometer scale to the local structure and properties of the materials under investigation.

Chapter 3

Theory of light and statistical optics

In this chapter, a brief electromagnetic theory is reviewed, as well as the propagation of light in free space and through optical elements. Moreover, the correlation theory of scalar wavefields, the concept of radiometry, and the notion of radiance are considered. Such notions as time and space coherence within the framework of statistical optics are discussed as well. It is also shown how the coherence properties of the source will determine the nature of the field. It is convenient and simpler mathematically to employ the space-frequency rather than space-time description while addressing these problems. Corresponding results in the space-time and space-frequency domains are related via the basic Fourier transform relations.

3.1 Theory of light and wave propagation

The starting point for the description of the evolution of electromagnetic waves in vacuum and matter is set by Maxwell's equations, which are the basis of classical electrodynamic theory:

$$\bigtriangledown \times \mathbf{B}(\mathbf{r},t) = \mu_0 \epsilon(\mathbf{r}) \frac{\partial}{\partial t} \mathbf{E}(\mathbf{r},t) \tag{3.1}$$

$$\bigtriangledown \times \mathbf{E}(\mathbf{r},t) = -\frac{\partial}{\partial t} \mathbf{B}(\mathbf{r},t) \tag{3.2}$$

$$\bigtriangledown \cdot \mathbf{B}(\mathbf{r},t) = 0 \tag{3.3}$$

$$\bigtriangledown \cdot \epsilon(\mathbf{r}) \mathbf{E}(\mathbf{r},t) = 0 \tag{3.4}$$

The Eqs. (3.1)-(3.4) are written under the assumption of a static and linear medium without charge and current densities. The electric field $\mathbf{E}(\mathbf{r},t)$ depends on the three dimensional spatial coordinate $\mathbf{r} = (x,y,z)$ and time t. The magnetic induction $\mathbf{B}(\mathbf{r},t)$ can be expressed through the magnetic field as

$$\mathbf{B}(\mathbf{r},t) = \mu_0 \mathbf{H}(\mathbf{r},t), \tag{3.5}$$

where for non-magnetic static media, magnetic permeability equal to the magnetic field constant $\mu = \mu_0$.

In the case when the electric permittivity $\epsilon(\mathbf{r}) = \epsilon_0 \epsilon_r(\mathbf{r})$ varying only slowly on length scales comparable to the wavelength of the field Eqs. (3.1)-(3.4) can be combined to form a pair of vector wave equations, describing the propagation of electromagnetic waves by applying the curl vector operator $\bigtriangledown \times$ to $\bigtriangledown \times \mathbf{E}$ and using the vector identity $\bigtriangledown \times \bigtriangledown = \bigtriangledown(\bigtriangledown \cdot A) - \bigtriangledown^2$

$$\left[\epsilon(\mathbf{r}) \mu_0 \frac{\partial^2}{\partial^2 t} - \bigtriangledown^2\right] \mathbf{E}(\mathbf{r},t) = 0, \tag{3.6}$$

$$\left[\epsilon(\mathbf{r}) \mu_0 \frac{\partial^2}{\partial^2 t} - \bigtriangledown^2\right] \mathbf{H}(\mathbf{r},t) = 0. \tag{3.7}$$

Decoupled Eqs. (3.6) and (3.7) imply that the electric field does not depend on the components of the mangetic field, which allows the transition to a scalar theory.

The Fourier decomposition into a continuous sum of monochromatic components of the scalar electric wave field $E(\mathbf{r},t)$ may be written as

$$E(\mathbf{r},t) = \frac{1}{\sqrt{2\pi}} \int_0^\infty E(\mathbf{r},\omega) e^{-i\omega t} d\omega. \tag{3.8}$$

The so-called Helmholtz equation for an inhomogeneous media can be derived by inserting the spectral wave field decomposition of Eq. (3.8) into Eq. (3.6):

$$[\bigtriangledown^2 + k^2 n^2(\mathbf{r},\omega)] E(\mathbf{r},\omega) = 0, \tag{3.9}$$

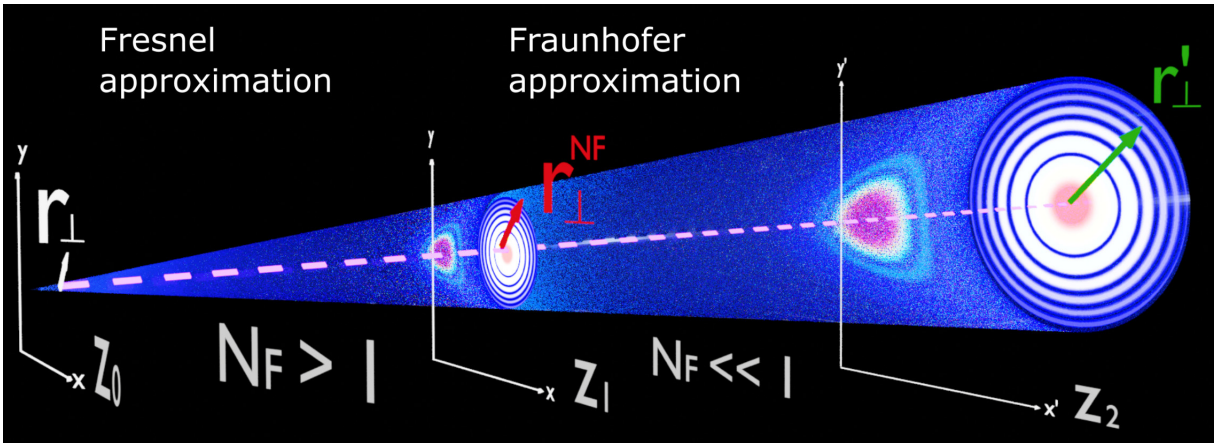

Figure 3.1: Scheme of the free space propagation. The source plane located at $z = 0$ with the vector $r_\perp$ = (x,y). The plane located at z_1 represents the area of the near-field propagation. In the paraxial far-field plane at z_2 the vector in transverse coordinates $r'_\perp$ = (x',y'). The Fresnel number N_F is the number that determines the applicability of the near- and far-field approximations.

where $k = 2\pi/\lambda$ is the wave number, $n(\mathbf{r},\omega) = \sqrt{\epsilon(\mathbf{r},\omega)/\epsilon_0}$ is the refractive index. The quantity $\epsilon(\mathbf{r},\omega)$ cointains all non-magnetic and spatially dependent properties of the matter. It is convenient to use the solutions of the Helmholtz equation when considering the propagation of monochromatic wave fields either through free space or through a medium characterized by a refractive index.

3.1.1 Free space propagation

The absence of any matter and sources of electromagnetic waves prompts the definition of free space, where the electric permittivity is constant $\epsilon(\mathbf{r},\omega) = \epsilon_0$. In vacuum the index of refraction is $n(\mathbf{r},\omega) = 1$ and in this case the Helmholtz Equation (3.9) reduces to

$$[\bigtriangledown^2 + k^2]E(\mathbf{r},\omega) = 0. \tag{3.10}$$

Following [55, 56], for a description of free space forward propagation along an optical axis z, it is necessary to derive an equation connecting the wave field at a plane $z = z_1$ to an incident wavefield at a plane z_0. It can be done with the help of angular spectrum decomposition of plane waves (PW), so that the required equation is

$$E_{PW}(r,\omega) = exp[ikr] = exp[i(k_x x + k_y y)] \cdot exp[ik_z z], \tag{3.11}$$

being a solution to the Helmholtz Eq. (3.10). In Eq. (3.11) the wave vector $k_z = \pm\sqrt{k^2 - k_x^2 - k_y^2}$ describing evanescent waves traveling in opposite directions, and the propagation of a plane wave along z is represented by the multiplicative factor $exp[ik_z z]$. For the initial wave $E(x,y,z = 0;\omega)$ same propagation factor can be used if the wave can be represented as the infinite sum of plane waves. The latter is achieved by a two-dimensional Fourier integral with respect to k_x

and k_y

$$E(x,y,z=0,\omega) = \frac{1}{(2\pi)^2}\int\int \tilde{E}(k_x,k_y,z=0,\omega)exp[i(k_x x + k_y y)]dk_x dk_y. \tag{3.12}$$

Here $\tilde{E}(k_x,k_y,z=0;\omega)$ denotes the Fourier transform of the initial wave $E(x,y,z,\omega)$. Since the plane wave propagation factor is known, it can be used to propagate each plane wave component by multiplication with the factor

$$E_{PW} = exp[ik_z z] \tag{3.13}$$

into a plane at $z_1 > 0$. The Eq. (3.13) is called the plane wave propagator. The final equation of propagation can thus be described by the method of angular spectrum decomposition of plane waves [56, 57]

$$E(x,y,z_1,\omega) = \frac{1}{(2\pi)^2}\int\int \tilde{E}(k_x,k_y,z=0)exp[iz_1\sqrt{k^2-k_x^2-k_y^2}]exp[i(k_x x + k_y y)]dk_x dk_y. \tag{3.14}$$

or

$$E(x,y,z_1,\omega) = \mathcal{F}^{-1}\Big\{exp[iz_1\sqrt{k^2-k_x^2-k_y^2}]\cdot\mathcal{F}\{E(x,y,z=0)\},\Big\} \tag{3.15}$$

where $\mathcal{F}$ and $\mathcal{F}^{-1}$ denote the Fourier and inverse Fourier transform with respect to x,y and k_x,k_y.

There are two approximations that significantly simplify Eq. (3.14). As shown in Figure 3.1 in particular, the paraxial (small-angle or Fresnel) and second the far-field (Fraunhofer) approximation within the small-angle approximation are useful for fast calculations of wave field propagation.

3.1.2 Fresnel approximation

The propagation of wave fields within Fresnel approximation may be applied if the transverse components k_x and k_y of the wave vector $\mathbf{k}$ are small compared to its magnitude $|\mathbf{k}|$. In this case, the field is called paraxial, it has amplitude values only in the vicinity $\sim D$ of the optical axis z and obeys the relation $k^2 \gg k_x^2 + k_y^2 = (2\pi/D)^2$. The latter implies that the paraxial condition is

$$D \gg \lambda. \tag{3.16}$$

The Eq. (3.16) states, that the paraxial approximation can be used, when the field under consideration has the projected area in the transverse xy-plane much larger than its wavelength. In this case the plane wave propagator in Eq. (3.13) can be rewritten with the help of a binomial expansion of $k_z = \sqrt{k^2-k_x^2-k_y^2} \approx k - (k_x^2+k_y^2)/2k + ...$, truncated after the 2^{nd} term:

$$E_{PW}^{Fresnel} = exp(ikz)exp\big[i\big(\frac{k_x^2+k_y^2}{2k}\big)z\big]. \tag{3.17}$$

The propagation equation (3.15) described by the method of spectrum decomposition of plane waves may be rewritten taking into account the Eq. (3.17)

$$E(x,y,z_1,\omega) \approx exp(ikz)\mathcal{F}^{-1}\Big\{exp\big[iz\big(\frac{k_x^2+k_y^2}{2k}\big)\big]\cdot\mathcal{F}\{E(x,y,z=0,\omega)\}\Big\}. \tag{3.18}$$

Introducing the two-dimensional convolution of two functions $f(x,y)$ and $g(x,y)$ as

$$f(x,y)\star g(x,y) = \mathcal{F}^{-1}[\{\mathcal{F}[f(x,y)]\}\cdot\{\mathcal{F}[g(x,y)]\}], \tag{3.19}$$

the Eq. (3.18) may be rewritten in slightly different but more convenient convolution form. To do so, the Eq. (3.18) first should be modified as

$$E(x,y,z_1,\omega) = \mathcal{F}^{-1}\Big\{\mathcal{F}\mathcal{F}^{-1}\{exp(ikz)exp\big[iz\big(\frac{k_x^2+k_y^2}{2k}\big)\big]\}\cdot\mathcal{F}\{E(x,y,z=0,\omega)\}\Big\}, \tag{3.20}$$

then compared to Eq. (3.19) can be rewritten into convolution form

$$E(x,y,z,\omega) = E(x,y,z=0,\omega)\star P(x,y,z), \tag{3.21}$$

where the real-space form of the Fresnel propagator $P(x,y,z)$ is given by

$$P(x,y,z) = exp(ikz)\mathcal{F}^{-1}\{exp\big[iz\big(\frac{k_x^2+k_y^2}{2k}\big)\big]\} = \tag{3.22}$$

$$= -\frac{ik\,exp(ikz)}{z}exp\big[ik\big(\frac{x^2+y^2}{2z}\big)\big].$$

The other form of Eq. (3.18) is [57]

$$E(x',y',z) \approx -\frac{ik\,exp(ikz)}{z}exp\big[ik\big(\frac{x'^2+y'^2}{2z}\big)\big]\cdot\mathcal{F}\Big\{E(x,y,z=0,\omega)exp\Big[ik\big(\frac{x^2+y^2}{2z}\big)\Big]\Big\}, \tag{3.23}$$

obtained using the spherical wave definition and the following transverse coordinates $\mathbf{r}'_\perp = (x',y')$, which are scaled with respect to the propagation distance via the reciprocal coordinates $\mathbf{k}_\perp = (k_x,k_y)$, $k_x = kx'/z$, and $k_y = ky'/z$ (see Fig. 3.1).

3.1.3 Far-field propagation within the paraxial approximation

The far zone is reached by the wave for the case of propagation distances that are very large compared to the characteristic length scale D of the unpropagated wave-field (at the source position z=z_0 and $D \sim \mathbf{r}_\perp$), i.e., $\lambda z \gg D$. In terms of dimensionless Fresnel number [56]

$$N_F = \frac{D^2}{\lambda z} \tag{3.24}$$

the far zone is reached for $N_F \ll 1$, or at distances $z \gg D^2/\lambda$. This is a sufficient condition to ignore the exponent which appears under Fourier transform in Eq. (3.23), so that dedicated far-field propagation equation is gives

$$E(x', y', z, \omega) \approx -\frac{ik\ exp(ikz)}{z} exp\left[ik\left(\frac{x'^2 + y'^2}{2z}\right)\right] \cdot \mathcal{F}\Big\{E(x, y, z = 0, \omega)\Big\}. \tag{3.25}$$

Therefore, the propagated wave field in the far zone can be obtained simply by the single Fourier transform.

3.1.4 Propagation through the optical elements

Considering the propagation of wave fields , optical elements are often involved, such as apertures (Fig. 3.2 (a, b, c), thin lenses, compound refractive lenses (CRLs) (Fig. 3.2 (d)) and transmission gratings. The transmission through a thin optical element can be performed by multiplication with a transmission function $T(\mathbf{r}, \omega)$ defined in the transverse plane so that the propagated field right after the optical element is

$$E_{out}(\mathbf{r}_\perp, z, \omega) = T(\mathbf{r}_\perp, \omega) \cdot E_{in}(\mathbf{r}_\perp, z, \omega), \tag{3.26}$$

where $E_{in}(\mathbf{r}_\perp, z, \omega)$ is the incident field. For instance the transmission function of a pinhole of the diameter D (Fig. 3.2 (a)) is

$$T(\mathbf{r}_\perp, \omega) = \begin{cases} 1, \text{for } |\mathbf{r}| < D/2 \\ 0, \text{elsewhere.} \end{cases} \tag{3.27}$$

The transmission function of the slit of a size D (Fig. 3.2 (b)) may be defined as

$$T(\mathbf{r}_\perp, \omega) = \begin{cases} 1, \text{for } |r_x| < D_x/2 \ \text{ and } \ |r_y| < D_y/2 \\ 0, \text{elsewhere.} \end{cases} \tag{3.28}$$

A thin lens with the focal distance f(ω) and an infinite aperture may be defines as

$$T(\mathbf{r}_\perp, \omega) = exp\left(\frac{-ik|\mathbf{r}_\perp|^2}{2f(\omega)}\right). \tag{3.29}$$

In this case, lenses used for the optical light can also be used for the focusing of X-rays with a small change related to the complex refractive index

$$n(\omega) = 1 - \delta(\omega) + i\beta_{abs}(\omega), \tag{3.30}$$

where $\delta(\omega)$ is the decrement of the refractive index and $\beta_{abs}(\omega)$ is the absorption coefficient. Because the real part of the refractive index $n(\omega)$ is smaller than unity for X-rays, these lenses are produced by making voids in the material. Then lenses are combined together to improve

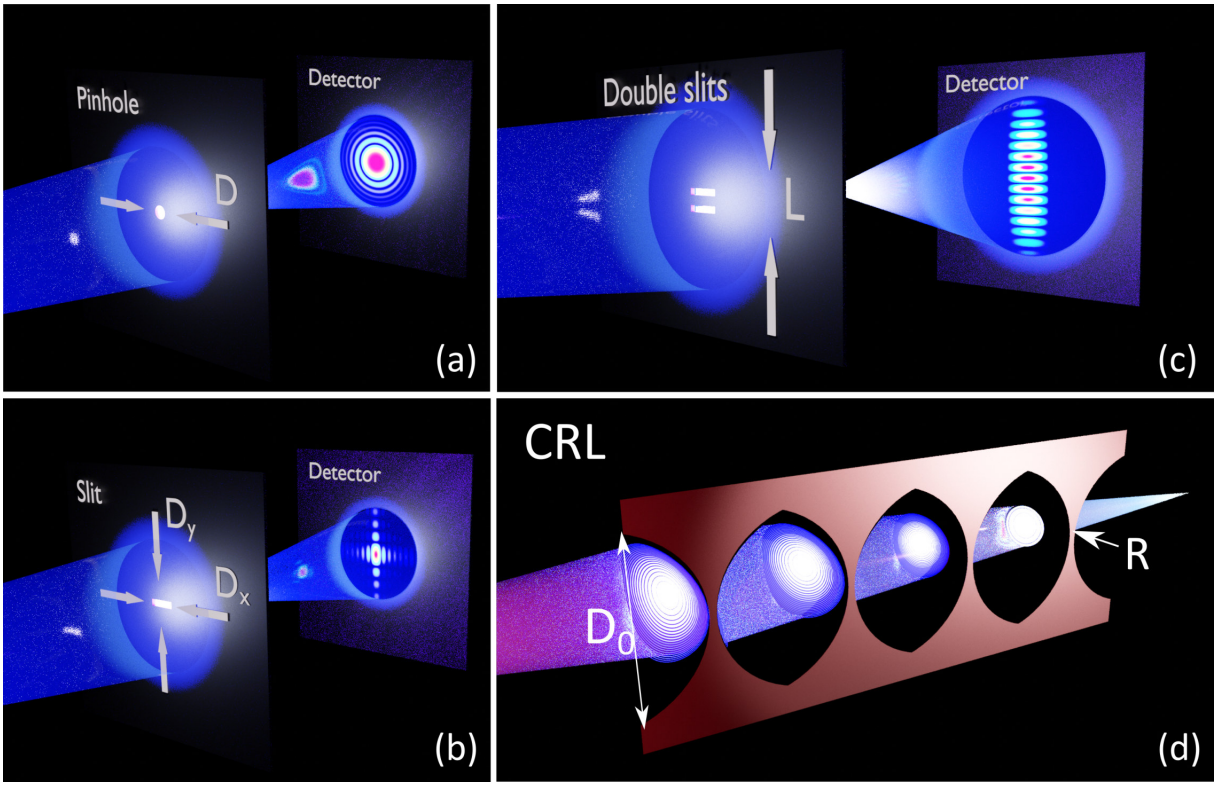

Figure 3.2: Propagation scheme of wave fields through optical elements and the far-field amplitude distribution in the case of (a) a pinhole with the diameter D (b), a slit with size D (c) double slits at a distance L. Example of the CRL with the opening aperture D_0 and the curvature radius R of the lens.

the focusing properties of the lens (Fig. 3.2 (d)). The transmission function of CRLs with the focal distance $f(\omega)$ maybe defined as [58]

$$T(\mathbf{r}_\perp, \omega) = O(\mathbf{r}_\perp, \omega) exp\left(\frac{-ik|\mathbf{r}_\perp|^2}{2f(\omega)}\right), \tag{3.31}$$

with the additional function $O(\mathbf{r}_\perp, \omega)$, which describes the opening aperture of the lens D_0

$$O(\mathbf{r}_\perp, \omega) \sim exp\left(\frac{-|\mathbf{r}_\perp|^2}{4D_0^2(\omega)}\right), \tag{3.32}$$

The focal distance and the opening aperture of the CRL stucked from N lenses can be found through the curvature radius R of the lens, decrement of the refractive index, and the absorption coefficient

$$f(\omega) = \frac{R}{2N\delta(\omega)}, \quad D_0(\omega) = \sqrt{\frac{R}{4Nk\beta_{abs}(\omega)}}. \tag{3.33}$$

If the optical element is not thin, then the complete integral should be considered, using the transmission function of the element and the propagator. In some particular cases, the description of the element may be simplified. For instance, such an optical element as the VLS grating, which gives simultaneously focusing of the wave field and the energy dispersion, may be replaced with the plane grating followed by the 'virtual' thin lens with the focal distance $f(\omega)$

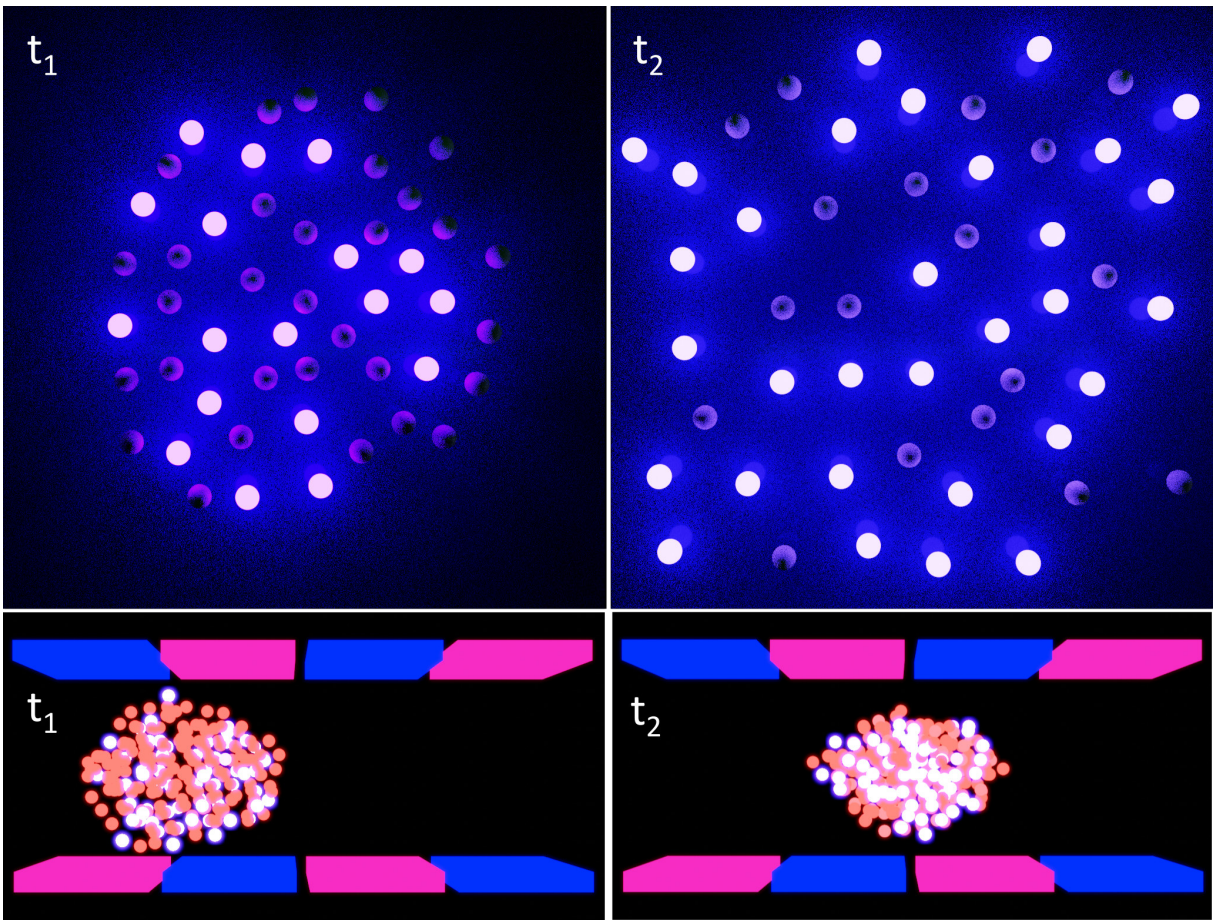

Figure 3.3: Fluctuating source of light, consisting of a number of radiators. Top panels show source fluctuations at different times t_1 and t_2 due to random realizations of radiators. The bottom panels show source fluctuations at different times due to random energy realizations.

given by the VLS grating [59]. Then the scattered field from the VLS grating may be found as

$$E_{out}(\mathbf{r},\omega) = \int T(\mathbf{r}',\omega)R_{gr}(\mathbf{r}')P(\mathbf{r}-\mathbf{r}')E_{in}(\mathbf{r}',\omega)e^{i\mathbf{k}\mathbf{r}'}d\mathbf{r}', \tag{3.34}$$

where $R_{gr}(\mathbf{r}')$ is the reflection function of the grating, transmission function of $T(\mathbf{r}',\omega)$ is given by Eq. (3.29), and the propagator in the paraxial approximation for the focal distance $f(\omega)$ defined as

$$P(\mathbf{r}-\mathbf{r}') = \frac{-ik}{2\pi f(\omega)} exp\left[ik\frac{(\mathbf{r}-\mathbf{r}')^2}{2f(\omega)}\right]. \tag{3.35}$$

3.2 Framework of statistical optics

Due to the statistical nature of light, a description of radiation properties within the classical electromagnetic theory will not be sufficient. Usually, the real system under consideration implies a heterogeneous source or several independent point sources. For instance, let us assume a system where each point source radiates for some period of time, but due to Heisenberg's uncertainty principle [60], it is not known when precisely (see Fig. 3.3).

In this case, the concept of probability plays an important role. Studying the source fluctuations, with each of the possible outcome of the measurement x_1, $x_2 \cdots x_n$, one may associate a probability ρ_i (i=1, 2 $\cdots$) or probability density $\rho(x)$ for continuous variate x. The latter shows the probability for x to be found in the interval x to $x + dx$. The corresponding normalization condition at the interval [a, b] is

$$\int_a^b \rho(x)dx = 1. \tag{3.36}$$

Associated important quantities are average $< x >$ (expectation value) and n^{th} moment $< x^n >$ of random variable x defined as

$$< x >= \int x\rho(x)dx, \tag{3.37}$$

$$\sigma_n =< x^n >= \int x^n\rho(x)dx. \tag{3.38}$$

Considering a source fluctuating in time t, random variables $x_1 \cdots x_n$ form a continuum, where $x(t)$ is called a random process [8]. If the x does not depend on t deterministically, its values can only be described statistically by a probability distribution or probability density $\rho(x, t)$. In this case, for $< x(t) >$ and $< x(t)^n >$ the probability density $\rho(x)$ in Eqs. (3.37) and (3.38) may be written as $\rho(x, t)$ [8].

Alternatively, the random process may be represented as the set of all possible realizations or samples of the function $x(t)$. The countable collection of all possible realizations is known as the 'ensemble' of $x(t)$. In the experiments the repetition of time-dependent measurements will yield different realizations (samples of function $x(t)$), which can be labeled as ${}^{(1)}x(t)$,${}^{(2)}x(t) \cdots$ (see for example Fig. 3.4(a)). Therefore, the average $< x(t) >$ is defined as [8]

$$< x >= \lim_{N\to\infty} \frac{1}{N} \sum_{r=1}^{N} {}^{(r)}x(t), \tag{3.39}$$

which is equivalent to Eq. (3.37).

In the case, when the character of the fluctuations does not change with time, the random process is called 'stationary' (see for example Fig. 3.4(b)). The latter means that the probability density is invariant under an arbitrary translation T of the origin of time [8]

$$\rho(x, t) = \rho(x, t + T), \tag{3.40}$$

and so the average $< x(t) >=< x(t + T) >$.

In the situation, when every realization of the ensemble ${}^{(r)}x(t)$ of the stationary process $x(t)$ carries the same statistical information, the different time averages $<^{(r)} x(t) >$ become equal and coincide with the ensemble average. In this case, the stationary random process $x(t)$ is called the 'ergodic' process.

For the system with heterogeneous sources or several independent point sources, due to the superposition principle, the total radiation field, being the sum of all fields from individual sources, fluctuates as a function of time. As optical fields fluctuate very rapidly, much faster than it is possible to measure, only average intensities are accessible within experiments. In

this case, expected values of wave fields can be found within the concept of ergodicity, when the ensemble average replaces the time average.

3.2.1 Joint probability and correlations

The probability function $\rho(x,t)$, introduced earlier, contains no information about possible correlations between $x(t_1)$ and $x(t_2)$ and does not describe the random process completely. Such information is provided by the joint probability density [8]

$$\mathfrak{p}[x_2(t_2); x_1(t_1)], \tag{3.41}$$

or

$$\mathfrak{p}(x_2, t_2; x_1, t_1) = \mathfrak{p}(x_2, x_1; t_2, t_1). \tag{3.42}$$

Such probability $\mathfrak{p}(x_2, x_1; t_2, t_1)$ contains all the informatoin carried by $\rho(x,t)$, and implies the following property

$$\int \mathfrak{p}(x_2, t_2; x_1, t_1) dx_2 = \rho(x_1, t_1), \tag{3.43}$$

where t_2 disappeared during the integration for reasons of compatibility [8]. The probability allows calculating two-time correlation (or autocorrelation) function of the random process $x(t)$ such as [8]

$$\Gamma(t_1, t_2) =< x(t_1)x(t_2) >= \int x_1 x_2 \mathfrak{p}(x_2, t_2; x_1, t_1) dx_1 dx_2. \tag{3.44}$$

The function $\Gamma(t_1, t_2)$ yields information on how far correlations extend in time. For the stationary process $\mathfrak{p}(x_2, t_2; x_1, t_1) = \mathfrak{p}(x_2, t_2 + T; x_1, t_1 + T)$. If time translation T is chosen as $T = t - t_1$ then according to Eq. (3.44)

$$\Gamma(t_1, t_2) =< x(t_1)x(t_2) >= \int x_1 x_2 \mathfrak{p}(x_2, t_2 + t - t_1; x_1, t) dx_1 dx_2 = \tag{3.45}$$

$$< x(t)x(t+\tau) >= \Gamma(\tau), \tag{3.46}$$

where $\tau = t_2 - t_1$ is the time difference. When $< x(t) >$ is independent of t and $\Gamma(t_1, t_2)$ depends only from τ, the process $x(t)$ is called 'stationary in the wide sense'.

In the general case, the function $\Gamma(t_1, t_2)$ may depend on spatial coordinates $\mathbf{r}$ as well, providing information on how far correlations extend in space and time.

3.2.2 Coherence

Coherence is the manifestation of the purity of a quantum state of light or matter [8, 62]. The concept of coherence has long been associated with interference since it is the most direct way of measuring it. In the framework of statistical optics, the radiation field is characterized by notions such as time and space coherence, which are temporal and spatial measures over which the fields are well correlated. If the direction of propagation of fields is well defined, it is convenient to decompose the region of coherence into orthogonal components in the direction

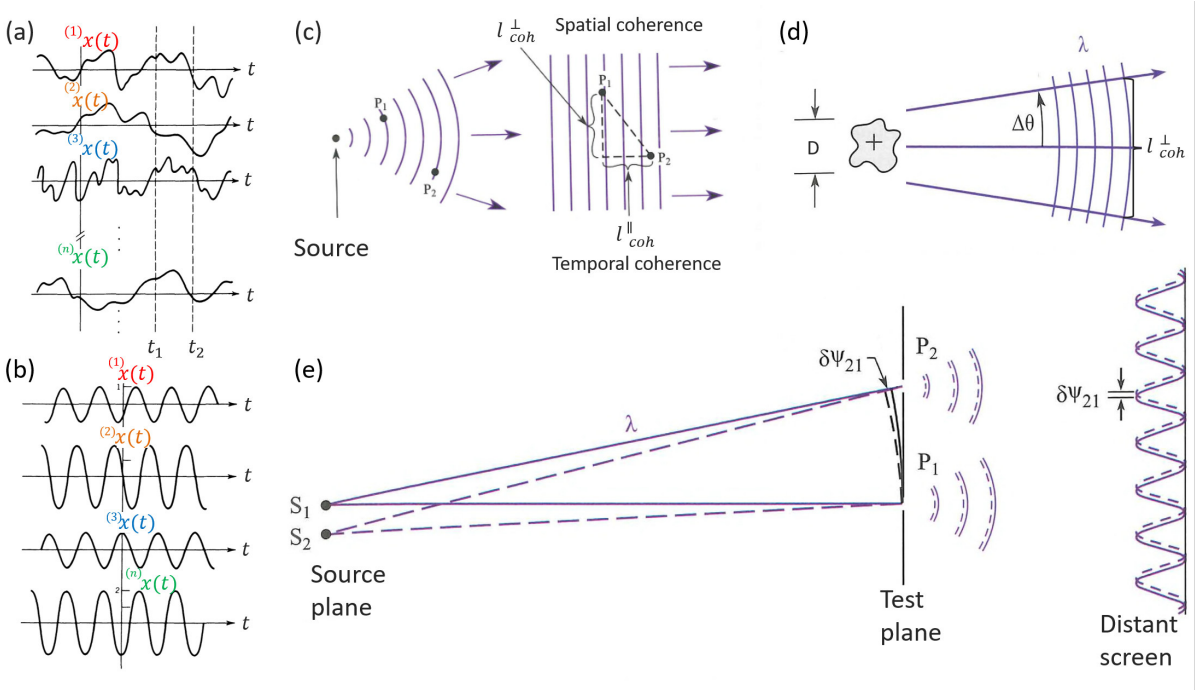

Figure 3.4: (a) An ensemble of simple functions ${}^{(1)}x(t), \cdots {}^{(n)}x(t)$ of a random process $x(t)$. (b) An ensemble of simple functions ${}^{(1)}x(t), \cdots {}^{(n)}x(t)$ of a stationary process $x(t)$, but not ergodic. (c) Representation of transverse and longitudinal (temporal) coherence of the radiation. (d) Scheme of calculation of the coherence length from the uncertainty of angle and source size. (e) Double slit diffraction pattern for the radiation from the incoherent source. Figures (a,b) were adapted from [55] and (c-e) from [61].

of propagation and transverse to it (see Fig. 3.4 (c)). Notions time and space coherence are closely related to Heisenberg's Uncertainty Principle, which define limits of quantum mechanical distributions

$$\Delta\mathcal{E} \cdot \Delta\tau \geq \hbar/2, \tag{3.47}$$

$$\Delta x \cdot \Delta p \geq \hbar/2, \tag{3.48}$$

where $\Delta\mathcal{E}$ is the rms bandwidth of photon energy required to generate a pulse of rms duration $\Delta\tau$ and $\Delta p = \hbar\Delta k$ defines uncertainty in vector momentum. The Eqs. (3.47, 3.48) divided by the Planck constant $\hbar$ give

$$\Delta\omega \cdot \Delta\tau \geq 1/2, \tag{3.49}$$

$$\Delta x \cdot \Delta k \geq 1/2, \tag{3.50}$$

relations between the quantities of pulse duration and the spectral bandwidth as well as uncertainty in position and wave vector, obeying Gaussian statistics. Therefore, resultant fields are described mathematically in terms of Fourier transforms in time and space. In this frame, according to Eq. (3.49), temporal coherence defines the degree of monochromaticity of the source. In other words, the larger range of frequencies $\Delta\omega$ a wave contains, the faster the wave decorrelates. Temporal coherence is the measure of the average correlation between the value of a wave and itself delayed by τ, at any pair of times t_1 and t_2 (or coordinates $P_1 = ct_1$ and $P_2 = ct_2$, see Fig. 3.4 (a)).

Thus, it characterizes how well a wave can interfere with itself at a different time. The delay over which the phase difference of the radiation changes by a significant amount (and hence the correlation decreases by significant amount) is defined as the coherence time τ_c.

Coherence time may be explained in the frame of Michelson type of experiment, where the radiation pulse is separated into two and forced to pass different path lengths to combine them back together again afterward. If the difference between the path lengths is less than $c\tau_c$, the interference pattern will occur at the end, after averaging over a large number of radiation pulses. The latter means that the radiation field is correlated within the time of coherence. The optical path difference at which the interference pattern disappears $l^{\parallel}_{coh}$ is defined as

$$l^{\parallel}_{coh} = \frac{\lambda^2}{2\Delta\lambda}. \tag{3.51}$$

It can be shown from Eq. (3.50) that spatial coherence is related to the finite source size and the characteristic emission angle of the radiation. In this case, the framework of interest is located in planes orthogonal to the direction of propagation. The smallest source size D resolvable with finite wavelength λ can be determined from Eq. (3.50). If the spectral bandwidth is small $\delta\lambda/\lambda$, then the uncertainty in momentum may be replaced by uncertainty in angle $\Delta\theta$, which yields

$$\Delta x \cdot \Delta\theta \geq \frac{\lambda}{4\pi}. \tag{3.52}$$

Replacing Δx by the source diameter D and uncertainty $\Delta\omega$ with half angle θ (see Fig. 3.4 (b)) the phase space volume is obtained

$$D \cdot \theta \sim \lambda/2\pi. \tag{3.53}$$

The Eq. (3.53) will be important when considering the following chapters. If theta is replaced with $\theta \sim l^{\perp}_{coh}/z$ (see Fig. 3.4) in Eq. (3.53) then relation for the spatial coherence length is obtained

$$l^{\perp}_{coh} \sim \frac{z\lambda}{D}. \tag{3.54}$$

which will be discussed in section 3.5. As longitudinal coherence in Michelson type of experiment, in the same way, the spatial coherence can be shown in the frame of Young's pinhole experiment. In this case, the radiation is directed through two slits to the screen in the far diffraction zone, and the interference pattern is observed by changing the distance L between the slits (see Fig. 3.2 (c)). If the slits are located close to each other, then a clear diffraction pattern is seen. As the distance between the slits increases to some value $L = D > l^{\perp}_{coh}$, one comes to the situation when the interference pattern is not seen anymore after averaging over the ensemble of pulses.

3.2.3 Mutual Coherence Function

The basic theory of optical coherence is the first-order coherence theory, when the amplitudes of wave fields or intensities are correlated [4, 8, 62]. The measure of the first-order coher-

ence is given by the mutual coherence function (MCF) defined as [8]

$$\Gamma(\mathbf{r_1}, \mathbf{r_2}, t_1, t_2) =< E^*(\mathbf{r_1}, t_1)E(\mathbf{r_2}, t_2) > . \tag{3.55}$$

It describes correlations between two values of the electric field $E(\mathbf{r_1}, t_1)$ and $E(\mathbf{r_2}, t_2)$ at different points $\mathbf{r_1}$ and $\mathbf{r_2}$ and times t_1 and t_2. The brackets $< \ldots >$ denote ensemble average. In the space-time domain the corresponding normalized MCF is defined as [8]

$$\gamma(\mathbf{r_1}, \mathbf{r_2}, t_1, t_2) = \frac{\Gamma(\mathbf{r_1}, \mathbf{r_2}, t_1, t_2)}{\sqrt{< I(\mathbf{r_1}, t_1) >}\sqrt{< I(\mathbf{r_2}, t_2) >}}, \tag{3.56}$$

where $\tau = t_1 - t_2$ is the time difference, and the avaerage intensity $< I(\mathbf{r}, t) >$ is obtained when two points and times coincide

$$< I(\mathbf{r}, t) >= \Gamma(\mathbf{r}, \mathbf{r}, t, t) =< |E(\mathbf{r}, t)|^2 > . \tag{3.57}$$

The function $\gamma(\mathbf{r_1}, \mathbf{r_2}, t_1, t_2)$ is known as the complex degree of coherence (SDC). The modulus of the CDC is often measured in interference experiments as the contrast of the interference fringes. A characteristic width of the CDC $|\gamma(\mathbf{r_1}, \mathbf{r_2}, t_1, t_2)|$ in the spatial domain and in the temporal domain is usually called the transverse and the temporal coherence length.

For stationary and ergodic wave-fields, the MCF is invariant under time translation and can be written as [8]

$$\Gamma(\mathbf{r_1}, \mathbf{r_2}, \tau) =< E^*(\mathbf{r_1}, t)E(\mathbf{r_2}, t + \tau) >_T, \tag{3.58}$$

where the time average

$$f(\mathbf{r}, t) = \lim_{T\to\infty} \int_{-T/2}^{T/2} f(\mathbf{r}, t)dt. \tag{3.59}$$

In the space-frequency domain the cross-spectral density function (CSD) of a stationary source is introduced by the Fourier transform of the MCF (see for example Fig. 3.5 (b))

$$W(\mathbf{r_1}, \mathbf{r_2}, \omega) = \int \Gamma(\mathbf{r_1}, \mathbf{r_2}, \tau)e^{-i\omega\tau}\, d\tau, \tag{3.60}$$

where $\tau = t_1 - t_2$ (which is valid for a stationary source). It is important to note, that CSD function is Hermitian in the sense that

$$W(\mathbf{r_2}, \mathbf{r_1}, \omega) = W^*(\mathbf{r_1}, \mathbf{r_2}, \omega).$$

The spectral density of the radiation field is obtained when two points $\mathbf{r_1}$ and $\mathbf{r_2}$ coincide $\mathbf{r} = \mathbf{r_1} = \mathbf{r_2}$

$$S(\mathbf{r}, \omega) = W(\mathbf{r_1}, \mathbf{r_2}, \omega). \tag{3.61}$$

A convenient measure of the spatial coherence is the normalized CSD (see for example Fig. 3.5 (c))

$$\mu(\mathbf{r_1}, \mathbf{r_2}, \omega) = \frac{W(\mathbf{r_1}, \mathbf{r_2}, \omega)}{\sqrt{S(\mathbf{r_1}, \omega)}\sqrt{S(\mathbf{r_2}, \omega)}}, \tag{3.62}$$

which is called the spectral degree of coherence (SDC). The values of this function are ranging from zero to one.

Another convenient measure of coherence is the degree of coherence ζ, which characterizes coherence properties of the wavefield by a single number and can be introduced as [63, 64]

$$\zeta(\omega) = \frac{\int |W(\mathbf{r_1}, \mathbf{r_2}, \omega)|^2 \, d\mathbf{r_1} d\mathbf{r_1}}{(\int S(\mathbf{r}, \omega) \, d\mathbf{r})^2}. \tag{3.63}$$

The values of the parameter $\zeta(\omega)$ lie in the range of $0 \leq \zeta(\omega) \leq 1$, where $\zeta(\omega) = 0$ and $\zeta(\omega) = 1$ correspond to incoherent and fully coherent radiation, respectively.

In order to perform coherence analysis in the spatial domain, it is assumed that temporal separation τ is small relative to the coherence time $\tau_c = 2\pi/\omega$, defined by the spectral bandwidth $\Delta\omega$ of the wave field. In this case, a source is considered narrow-band, and the radiation produced by such a source, which spectrum lies inside a narrow band $[\omega_0 - \Delta\omega, \omega_0 + \Delta\omega]$ is quasi-monochromatic.

In the quasi-monochromatic regime (i.e. $\Delta\omega \ll \omega$), it is possible to approximate the MCF in Eq. (3.55) as [8]

$$\Gamma(\mathbf{r_1}, \mathbf{r_2}, \tau) \approx J(\mathbf{r_1}, \mathbf{r_2}) e^{-i\omega_0 \tau}, \tag{3.64}$$

provided that $|\tau| \leq 1/\Delta\omega$. Here $J(\mathbf{r_1}, \mathbf{r_2})$ is the Mutual Optical Intensity (MOI) defined as

$$J(\mathbf{r_1}, \mathbf{r_2}) = \Gamma(\mathbf{r_1}, \mathbf{r_2}, 0) = < E^*(\mathbf{r_1}, t) E(\mathbf{r_2}, t) > . \tag{3.65}$$

Taking into account all of the above, one may represent CSD for quasi-monochromatic radiation as

$$W(\mathbf{r_1}, \mathbf{r_2}, \omega) = J(\mathbf{r_1}, \mathbf{r_2}) \delta(\omega - \omega_0), \tag{3.66}$$

which describes correlations between two complex values of the electric field at different points $\mathbf{r_1}$ and $\mathbf{r_1}$ at a given frequency.

Finally, for quasi-monochromatic radiation, which means that the effective bandwidth is small compared with its mean frequency (i.e $\Delta\omega/\omega_0 \ll 1$), the CSD $W(\mathbf{r_1}, \mathbf{r_2}, \omega)$ and MOI $J(\mathbf{r_1}, \mathbf{r_2})$ functions as well as spectral density $S(\mathbf{r}, \omega)$ and intensity $\mathrm{I}(\mathbf{r}) \equiv \Gamma(\mathbf{r}, \mathbf{r}, 0) = < E^*(\mathbf{r}, t) E(\mathbf{r}, t) >$ functions are equivalent.

In some particular cases it is convinient to replace positional vector of CSD function with the following vectors

$$\mathbf{r} = (\mathbf{r_1} + \mathbf{r_2})/2, \quad \Delta\mathbf{r} = (\mathbf{r_1} - \mathbf{r_2}), \tag{3.67}$$

where vector $\mathbf{r}$ indicates position at which a two-slits system is introduced to probe coherence, and $\Delta\mathbf{r}$ is the vector describing the separation between the two slits. Thus, a new CSD function $G(\mathbf{r}, \Delta\mathbf{r}, \omega)$ (see for example Fig. 3.5 (f)) defined as

$$G(\mathbf{r}, \Delta\mathbf{r}, \omega) = \left\langle E^*(\mathbf{r} + \Delta\mathbf{r}/2, \omega) E(\mathbf{r} - \Delta\mathbf{r}/2, \omega) \right\rangle, \tag{3.68}$$

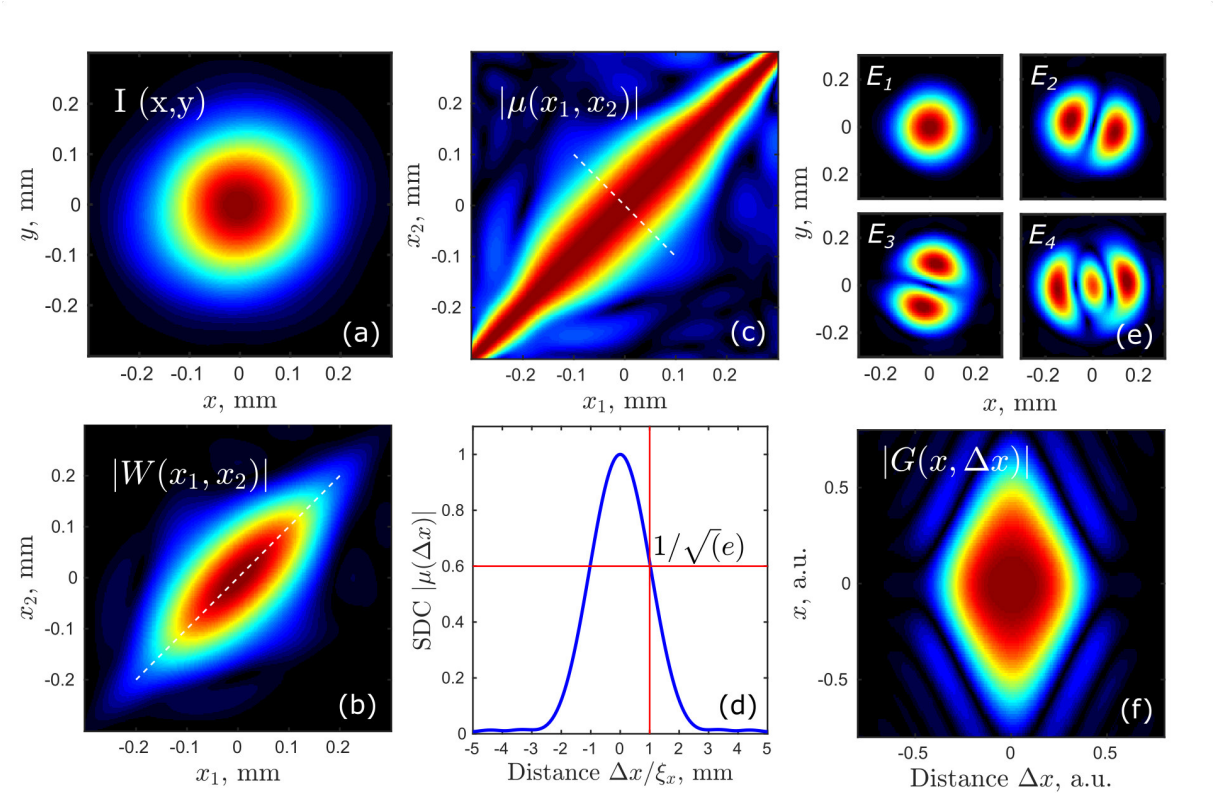

Figure 3.5: (a) Intensity distribution of the modeled radiation, with the degree of coherence $\zeta = 0.4$, (b) Absolute value of the CSD function in the horizontal direction for the modeled radiation. The intensity function in the horizontal direction x, may be found as the diagonal cut of $|W(x_1, x_2)|$ shown by the dashed line. (c) The absolute value of the normalized SDC function $|\mu(x_1, x_2)|$ and (d) the absolute value of the SDC along the anti-diagonal line shown in (c) as a function of the separation of two points $|\mu(\Delta x/\xi_x)|$, normalized to the coherence length of the modeled radiation $\xi_x = 0.1$ mm. At a separation equal to the coherence length ξ_x the SDC drops to $1/\sqrt{e} = 0.61$. (e) The first four modes $E_1 ... E_4$ of the modeled radiation, showed in (a). (f) Absolute value of the CSD function $G(x, \Delta x)$ of the modeled radiation.

and normalized SDC in this case is defined as

$$g(\mathbf{r}, \Delta\mathbf{r}, \omega) = \frac{G(\mathbf{r}, \Delta\mathbf{r}, \omega)}{\sqrt{G(\mathbf{r} + \Delta\mathbf{r}/2, \omega) G(\mathbf{r} - \Delta\mathbf{r}/2, \omega)}}. \tag{3.69}$$

The fringe visibility $V = \frac{I_{max} - I_{min}}{I_{max} + I_{min}} = \frac{2\sqrt{I_1 I_2}}{I_1 + I_2} g$ of an interference experiment may be written as

$$V = \frac{2G(\mathbf{r}, \Delta\mathbf{r}, \omega)}{G(\mathbf{r} + \Delta\mathbf{r}/2, 0, \omega) G(\mathbf{r} - \Delta\mathbf{r}/2, 0, \omega)} \tag{3.70}$$

3.3 Coherent-mode representation of the cross-spectral density function

It is well-known [8] that, under very general conditions, one can represent the CSD of a partially coherent, statistically stationary field of any state of coherence as a series

$$W(\mathbf{r_1}, \mathbf{r_2}, \omega) = \sum \beta_j(\omega) E_j^*(\mathbf{r_1}, \omega) E_j(\mathbf{r_2}, \omega), \tag{3.71}$$

here $\beta_j(\omega)$ are eigenvalues and independent coherent modes $E_j(\mathbf{r}, \omega)$ are eigen-functions of the Fredholm integral equation of the second kind

$$\int W(\mathbf{r_1}, \mathbf{r_2}, \omega) E_j(\mathbf{r_1}, \omega)\, d\mathbf{r_1} = \beta_j(\omega) E_j(\mathbf{r_2}, \omega). \tag{3.72}$$

According to Eq. (3.71) and Eq. (3.61) the spectral density can be represented as (see for example Fig. 3.5 (e))

$$S(\mathbf{r}, \omega) = \sum \beta_j(\omega) |E_j(\mathbf{r}, \omega)|^2. \tag{3.73}$$

Substitution of Eq. (3.71) and Eq. (3.73) into Eq. (3.63) gives for the global degree of coherence

$$\zeta(\omega) = \frac{\sum \beta_j^2(\omega)}{(\sum \beta_j(\omega))^2} \tag{3.74}$$

Important characteristics of this coherent mode decomposition are: the mode functions $E_j(\mathbf{r}, \omega)$ form an orthonormal set, the eigenvalues $\beta_j(\omega)$ are real and non-negative $\beta_j(\omega) \geq 0$, and $\beta_0(\omega) \geq \beta_1(\omega) \geq ....$ If there is only one single mode present then radiation is fully coherent, while for incoherent radiation the CSD contains a significant number of modes. Thus we can define the coherent fraction (CF) of radiation field $\zeta^{CF}(\omega)$ as an occupation or normalized weight of the first mode

$$\zeta^{CF}(\omega) = \frac{\beta_0(\omega)}{\sum_0^\infty \beta_j(\omega)} \tag{3.75}$$

3.4 Gaussian Schell-model

Gaussian Schell-model (GSM) is a simplified but often used model [8, 64, 65] that represents radiation from a real X-ray source based on the following approximations. The source is modelled as a plane two-dimensional source, the source is spatially uniform, i.e. the SDC depends only on the difference $\mathbf{r_2} - \mathbf{r_1}$, the SDC $\mu(\mathbf{r_2} - \mathbf{r_1})$ and spectral density $S(\mathbf{r})$ are Gaussian functions. In the frame of GSM cross-spectral density function, spectral density and SDC are defined as [8]

$$W(\mathbf{r_1}, \mathbf{r_2}) = \mu(\mathbf{r_2} - \mathbf{r_1}) \sqrt{S(\mathbf{r_1})} \sqrt{S(\mathbf{r_2})}, \tag{3.76}$$

$$S(\mathbf{r}) = S_0 exp\left(\frac{-r_x^2}{2\sigma_x^2} + \frac{-r_y^2}{2\sigma_y^2}\right), \tag{3.77}$$

$$\mu(\mathbf{r_2}-\mathbf{r_1}) = exp\left(\frac{-(r_{x2}-r_{x1})^2}{2\xi_x^2}+\frac{-(r_{y2}-r_{y1})^2}{2\xi_y^2}\right), \tag{3.78}$$

where S_0 is a normalization constant, $\sigma_{x,y}$ is the rms source size and $\xi_{x,y}$ is the transverse coherence length in the source plane in x- and y- direction, respectively (see for example Fig. 3.5 (d)). One of the important features of this model is that CSD function is separable into two transverse directions

$$W(\mathbf{r_1},\mathbf{r_2}) = W(r_{x1},r_{x2})W(r_{y1},r_{y2}). \tag{3.79}$$

The same is valid for the global degree of coherence defined in Eq. (3.63)

$$\zeta = \zeta_x\zeta_y, \tag{3.80}$$

where in each transverse direction [65]

$$\zeta_i(\omega) = \frac{\int |W(r_{i1},r_{i2})|^2\, dr_{i1}dr_{i2}}{(\int S(r_i)\, dr_i)^2} = \frac{\xi_i/\sigma_i}{\sqrt{4+(\frac{\xi_i}{\sigma_i})^2}}, \tag{3.81}$$

with $i = x, y$.

Coherent modes in the GSM are described by the Hermite-Gaussian functions [64–67]

$$\beta_i/\beta_j = \varkappa^j, \tag{3.82}$$

$$E_j(r_i) = \left(\frac{\varkappa^j}{2\pi k\sigma^2\zeta_i}\right)^{1/4}\frac{1}{\sqrt{2^j j!}}H_j\left(\frac{r_i}{\sigma\sqrt{2\zeta_i}}\right)exp\left(\frac{r_i^2}{4\sigma^2\zeta_i}\right), \tag{3.83}$$

where the coefficient $\varkappa_i = (1-\zeta_i)/(1+\zeta_i)$ is introduced, $H_j\left(r_i/\sigma\sqrt{2\zeta_i}\right)$ are the Hermite polynomials of order j, and i = x,y. The zero mode is a Gaussian function and propagation of Hermite-Gaussian modes in the far-field region gives Hermite-Gaussian modes of the same shape. In the frame of GSM, according to Eq. (3.75) coherent fraction of the radiation field for one transverse direction may be determined as

$$\zeta_i^{CF} = \left(\sum_{j=0}^{\infty}\frac{\beta_j(\omega)}{\beta_0(\omega)}\right)^{-1} = \left(\sum_{j=0}^{\infty}\kappa^j\right)^{-1} \approx \frac{2\zeta_i}{1+\zeta_i}. \tag{3.84}$$

3.5 Propagation of correlation functions

It can be shown then that propagation of a cross-correlation function is described by the Helmholtz equation as well

$$[\bigtriangledown^2 + k^2]W(\mathbf{r_1},\omega_1,\mathbf{r_2},\omega_2) = 0 \tag{3.85}$$

and the propagation of the cross-spectral correlation function is described as [8]

$$W(\mathbf{r_1},\mathbf{r_2},z_1,\omega) = \int W(\mathbf{r_1}',\mathbf{r_2}',z_0,\omega)P^*(\mathbf{r_1},\mathbf{r_1}',\omega)P(\mathbf{r_2},\mathbf{r_2}',\omega)d\mathbf{r_1}'d\mathbf{r_2}' \tag{3.86}$$

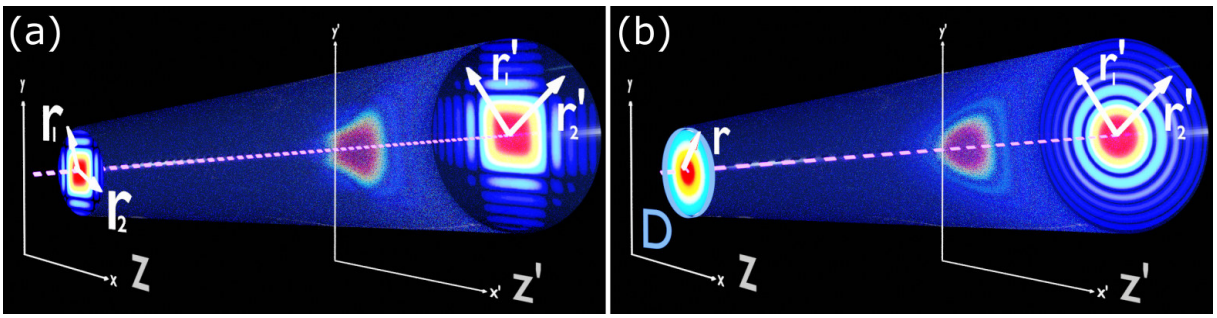

Figure 3.6: Scheme of propagation of correlation functions for (a) general case and (b) Van Cittert-Zernike theorem.

where $P(\mathbf{r}, \mathbf{r}', \omega)$ is a propagator in free space (see Fig. 3.6 (a))

$$P(\mathbf{r}, \mathbf{r}', \omega) = \frac{-ik}{2\pi} \frac{e^{ikz}}{z} exp\left(ik \frac{|\mathbf{r} - \mathbf{r}'|^2}{2z} \right) \tag{3.87}$$

The propagation of the CSD function through a thin optical element with a transmission function $T(\mathbf{r}, \omega)$ (listed in section 3.1.4) by the analogy with Eq. (3.26) can be described as [64]

$$W_{out}(\mathbf{r_1}, \mathbf{r_2}, z, \omega) = T^*(\mathbf{r_1}, \omega) T(\mathbf{r_2}, \omega) W_{in}(\mathbf{r_1}, \mathbf{r_2}, z, \omega). \tag{3.88}$$

The important Van Cittert-Zernike theorem concerning correlation functions, implies that the wavefront from an incoherent source will appear mostly coherent at large distances. For an incoherent source MOI function at the source is defined as

$$J(\mathbf{r}_1, \mathbf{r}_2) = I(\mathbf{r}_1) \delta(\mathbf{r}_2 - \mathbf{r}_1). \tag{3.89}$$

In the paraxial approximation, assuming quasimonochromaticity of radiation, the propagated mutual intensity function from the source position can be written as

$$J(\mathbf{r}_1', \mathbf{r}_2') = \left(\frac{k}{2\pi} \right)^2 \int I(\mathbf{r}) \frac{exp(ik(|\mathbf{r}_2' - \mathbf{r}| - |\mathbf{r}_1' - \mathbf{r}|))}{|\mathbf{r}_2' - \mathbf{r}||\mathbf{r}_1' - \mathbf{r}|} d\mathbf{r}, \tag{3.90}$$

or in the far zone

$$J(\mathbf{r}_1', \mathbf{r}_2') = \left(\frac{k}{2\pi} \right)^2 \frac{exp\left(\frac{ik}{z} (|\mathbf{r}_2'|^2 - |\mathbf{r}_1'|^2) \right)}{z^2} \times \tag{3.91}$$

$$\times \int I(\mathbf{r}) exp\left(-\frac{ik}{z} (\mathbf{r}_2' - \mathbf{r}_1') \right) d\mathbf{r} =$$

$$= \frac{exp(i\Psi)}{(\lambda z)^2} \int I(\mathbf{r}) exp\left(-\frac{i2\pi}{\lambda z} (\mathbf{r}_2' - \mathbf{r}_1') \right) d\mathbf{r}.$$

The normalized MOI in this case, may be written as

$$\mu(\mathbf{r_1}', \mathbf{r_2}') = \frac{exp(-i\Psi) \int I(\mathbf{r}) exp\left(-\frac{i2\pi}{\lambda z} (\mathbf{r}_2' - \mathbf{r}_1') \right) d\mathbf{r}}{\int I(\mathbf{r}) d\mathbf{r}}. \tag{3.92}$$

In Eqs. (3.90, 3.91), $\mathbf{r}$ and $\mathbf{r}'$ are the vectors located in the transverse plane at the source position and observation position accordingly (see Fig. 3.6 (b)). As a result, MOI at the observation plane, up to a factor $exp(i\Psi)$, may be found by the two-dimensional Fourier transform of the intensity distribution $I(\mathbf{r})$ over the source surface. The factor $exp(i\psi)$ can be neglected in cases:

$$z \gg \frac{|\mathbf{r}_2'|^2 - |\mathbf{r}_1'|^2}{\lambda} \rightarrow exp(i\Psi) \approx 1$$
$$\text{points } \mathbf{r}_2 \text{ and } \mathbf{r}_1 \text{ are at the same separation} \rightarrow exp(i\Psi) = 1$$

For example, according to the Van Cittert-Zernike theorem, the normalized MOI of the source with the radius D is described by the Airy function (see Fig. 3.6 (b)). In the frame of GSM, for completely incoherent sources ($\zeta = 0$), the effect of an increased spatial coherence length upon far-field propagation can be found as well [44]

$$\xi \sim \frac{\lambda z}{D}. \tag{3.93}$$

Equation (3.93) implies, that coherence length improves by propagation distance z and by a reduction of the source size D. It was also shown that coherence properties of synchrotron radiation sources are not accurately described by the Van Cittert-Zernike theorem [68], since the latter is assumed to be partially coherent. However, Eq. (3.93) is useful to obtain a rough estimate of the coherence properties of undulator-based X-ray sources described in the following chapter.

3.6 Basic concept of radiometry. Wigner distribution

In the frame of basic radiometry, the radiant intensity F_ω (with the help of Eq. (3.89)) [8]

$$F_\omega = \int_{2\pi} I(\mathbf{r}', \omega) d\Omega, \tag{3.94}$$

shows the rate at which the source radiates energy at frequency ω per unit solid angle $d\Omega$ around $\mathbf{r}'$-direction. A basic radiometry law describes the rate dF_ω at which energy at frequency ω is radiated into the element $d\Omega$ of solid angle by an element $d\sigma$ of planar source with σ size

$$d^2F_\omega = \mathcal{B}_\omega(\mathbf{r}, \mathbf{r}', \omega) cos(\theta) d\sigma d\Omega, \tag{3.95}$$

where $\mathbf{r}$ position vector of the point in the source plane at which the element $d\sigma$ is located, θ is the angle between vector $\mathbf{r}'$ and the normal to the element $d\sigma$. Here the function $\mathcal{B}_\omega(\mathbf{r}, \mathbf{r}')$ is called the spectral radiance or brightness. Therefore, Eq. (3.95) implies the total radiation rate as

$$F_\omega = \int_{2\pi} d\Omega cos(\theta) \int_\sigma d^2r \mathcal{B}_\omega(\mathbf{r}, \mathbf{r}', \omega). \tag{3.96}$$

Comparing Eq. (3.94) and (3.96) it can be found, that

$$I(\mathbf{r}',\omega) = cos(\theta)\int_{\sigma}\mathcal{B}_{\omega}(\mathbf{r},\mathbf{r}',\omega)d^2r. \tag{3.97}$$

In Eq. (3.98) the intensity $I(\mathbf{r}',\omega)$ may be calculated via back propagation in Eq. 3.90, acounting for Eq. 3.66

$$I(\mathbf{r}',\omega) = \left(\frac{k}{2\pi}\right)^2 cos^2(\theta)\int_{\sigma}W(\mathbf{r}_1,\mathbf{r}_2,\omega)exp(-ik\mathbf{r}'(\mathbf{r}_2-\mathbf{r}_1))d\mathbf{r}_1d\mathbf{r}_2. \tag{3.98}$$

Comparing Eqs. (3.97) and (3.98), in the paraxial approximation with small angle θ, it is possible to write

$$\int\mathcal{B}_{\omega}(\mathbf{r},\mathbf{r}',\omega)d\mathbf{r} = \left(\frac{k}{2\pi}\right)^2\int W(\mathbf{r}_1,\mathbf{r}_2,\omega)exp(-ik\mathbf{r}'(\mathbf{r}_2-\mathbf{r}_1))d\mathbf{r}_1d\mathbf{r}_2. \tag{3.99}$$

At this point, it is convenient to replace positional vectors according to Eq. (3.67), then the relation in Eq. (3.99) is satisfied for

$$\mathcal{B}_{\omega}(\mathbf{r},\mathbf{r}',\omega) = \left(\frac{k}{2\pi}\right)^2\int G(\mathbf{r}-\Delta\mathbf{r}/2,\mathbf{r}+\Delta\mathbf{r}/2,\omega)exp(-ik\mathbf{r}'\Delta\mathbf{r})d\Delta\mathbf{r}. \tag{3.100}$$

Thus, the final expression for the radiance or spectral brightness $\mathcal{B}_{\omega}(\mathbf{r},\mathbf{r}',\omega)$ is derived. This expression is very similar to the definition of the Wigner function, describing the phase-space distribution function

$$\mathfrak{W}(\mathbf{r},\mathbf{r}') = \left(\frac{k}{2\pi}\right)^2\int G(\mathbf{r},\Delta\mathbf{r})exp(-ik\mathbf{r}'\Delta\mathbf{r})d\Delta\mathbf{r}, \tag{3.101}$$

which is, in fact, the Fourier transform of the CSD function. Therefore Wigner-function formulation may describe the diffraction effects. If the thin object is defined in the transverse plane by the transmission function $T(\mathbf{r})$ then the Wigner function of the trnasnission function

$$\mathfrak{W}_T(\mathbf{r},\mathbf{r}') \sim \int T^*(\mathbf{r}+\Delta\mathbf{r}/2)T(\mathbf{r}-\Delta\mathbf{r}/2)exp(-ik\mathbf{r}'\Delta\mathbf{r})d\Delta\mathbf{r}, \tag{3.102}$$

can be introduced to describe the diffraction, where the filed which leaving the object as the convolution [69]

$$\mathcal{B}_{out}(\mathbf{r},\mathbf{r}',\omega) \sim \int\mathcal{B}_{in}(\mathbf{r},\mathbf{r}')\mathfrak{W}_T(\mathbf{r},\mathbf{r}'-\mathbf{r}'')d\mathbf{r}''. \tag{3.103}$$

Chapter 4

Theory of Synchrotron Radiation

A brief Synchrotron Radiation theory is reviewed in this chapter concerning power radiated by relativistic electrons subjected to the periodic acceleration, the spectrum of the radiation, electron bunch phase space, and main parameters of radiation such as photon source size, divergence, and brightness.

The concept of brightness, which is used as a quality factor of synchrotron radiation and free-electron laser (FEL) sources, is historically rooted in radiometry [4, 8], as has been shown in section 3.6. Radiometry treats radiation within the framework of geometrical optics and characterizes sources in terms of radiance, that is the maximum photon flux density in phase space, measured as a spectral photon flux per unit area per unit of the solid angle (see Eq. (3.95)). A pleasant peculiarity of the radiance is that for non-dissipative systems this quantity is invariant along the direction of propagation. Therefore, it is strictly related to the maximum spectral photon flux that can be obtained at the sample position, assuming an ideal optical system. Other macroscopic quantities of interest can be derived by the convolution with the computed phase-space distribution. Starting from the very basics, various publications are available, which deal with the generalization of the concept of radiance and Wigner distribution to the case of partially coherent sources of synchrotron radiation [70–73]. During the generalization process, it is crucial to have a working transition from pure geometrical optics (when source parameters are relatively big) to wave optics (in the case when the source dimensional parameters are close to the diffraction limit). Such transitions are provided by the substitution of the phase space of optical rays in geometrical optics with a Wigner distribution $\mathfrak{W}$. For the case of storage rings, one can approximate the transverse phase space distribution with a Gaussian distribution, obtaining such vital parameters as transverse beam size divergence. Moreover, for undulator sources, it is common to approximate the single-electron radiation at resonance with a Gaussian beam. In contrast to the real undulator field, Gaussian functions are factorizable in transverse directions, and therefore a simplified expression for the brightness is usually presented.

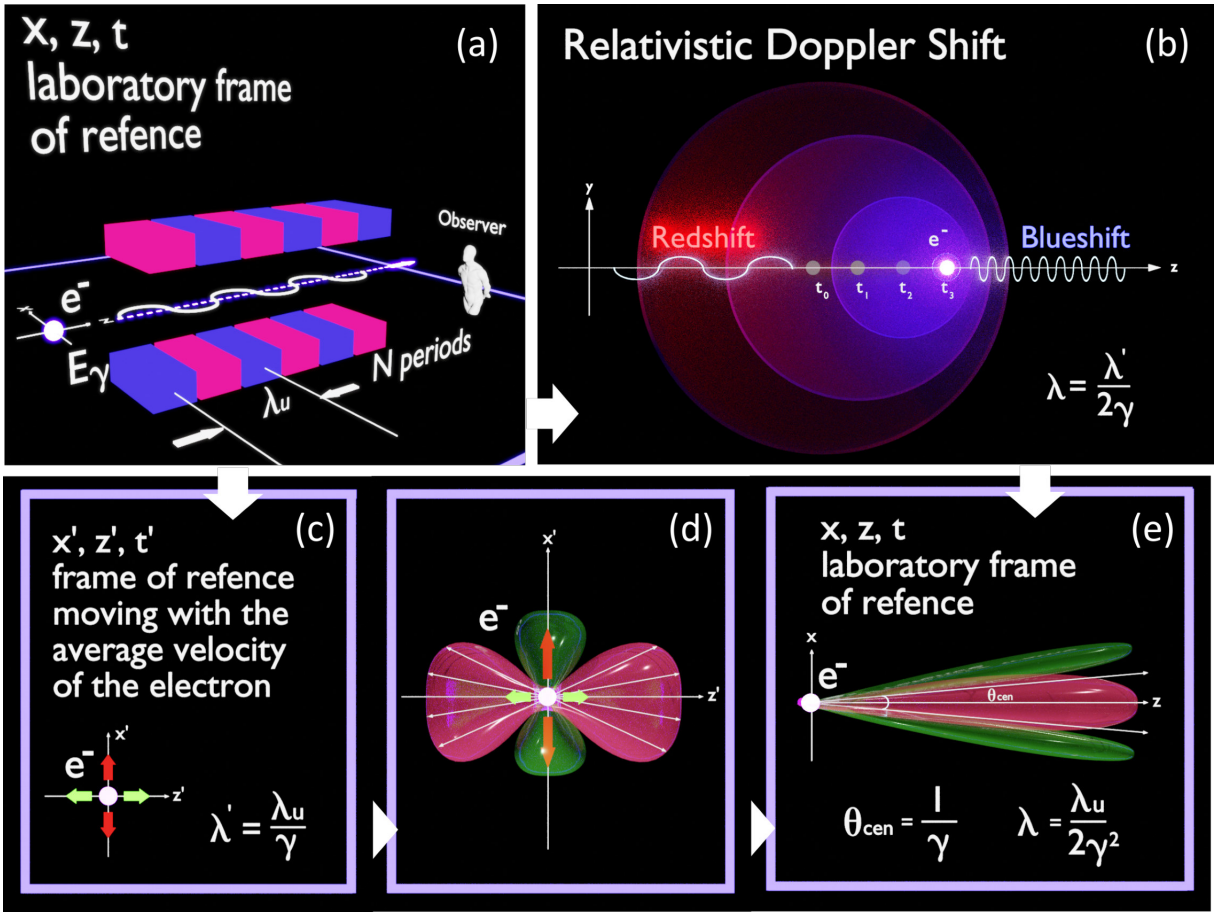

Figure 4.1: Schematic representation of the procedure for calculating the power radiated by relativistic electrons subjected to the periodic acceleration in the undulator (reproduced from [74]). (a) Initial laboratory frame of reference, (b) Relativistic Doppler shift, (c) Frame of reference moving with the average velocity of the electron, (d) Dipole radiation of the oscillating electron in the frame of reference moving with the average velocity, (e) Dipole radiation of the oscillating electron in the laboratory frame.

4.1 Synchrotron Radiation

An outline for the procedure of calculating power radiated by relativistic electrons subjected to the acceleration in the periodic magnetic structure is shown in Fig. 4.1. In Fig. 4.1 (a) schematically shown the lateral position of an electron as a function of propagation along the z-axis. The electron moves from left to right. Due to the relativistic Doppler shift effect, the frequency of light emitted by the electron and seen by an observer in the laboratory frame is defined as [75]

$$\omega = \omega' \gamma (1 - \beta_v cos(\theta')), \tag{4.1}$$

where ω' is the frequency emitted by the moving source, θ is the angle at which the source emits the radiation. For the system, shown in Fig. 4.1, the electron is moving towards the observer, then the angle $\theta' = \pi$, and the radiation frequency is

$$\omega = \omega'\gamma(1+\beta_v), \tag{4.2}$$

or the wavelength

$$\lambda = \frac{\lambda'}{\gamma(1+\beta)} \sim \frac{\lambda'}{2\gamma}. \tag{4.3}$$

Therefore, the wavelength of radiation that the observer sees will be much smaller than the source emits. In order to find the radiation wavelength of the source, it is easier to move to the reference frame moving with the average speed of the electron. In Fig. 4.1 (c) the same motion is shown in the frame of reference moving along the z-axis together with the average speed of the electron. In the particle rest frame, it sees a magnetic field from the undulator rushing towards it. If in the laboratory frame the magnet period is λ_u then because of Lorentz contraction the electron sees it as

$$\lambda' = \frac{\lambda_u}{\gamma}. \tag{4.4}$$

In the particle rest frame during one period of electron oscillations along x, two electron oscillations along z pass ('trembling', see [76]). These oscillations generate dipole radiation (see Fig. 4.1 (d)). The radiation frequency in the frame of reference moving with the electron is equal to the electron oscillation frequency which, in terms of wavelength, is represented by Eq. (4.4). The radiation diagram of an electron in the laboratory frame of reference can be obtained using the Lorentz transformations. In this case the angle at which the observer views the radiation from source will also be affected as [75]

$$sin\theta = \frac{sin\theta'}{\gamma(1-\beta_v cos\theta')}. \tag{4.5}$$

Since the point at which the electric dipole has zero amplitude in the moving frame corresponds to the angle $\theta'=\pi/2$, the same point appears in the laboratory frame, according to Eq. (4.5) at the angle $\theta \approx 1/\gamma$.

As can be seen from Fig. 4.1 (d), due to perpendicular motion of the electron, generated radiation propagating along the z-axis, while the radiation produced due to longitudinal oscillation is observed off-axis. Since particles move with relativistic velocities, in the laboratory frame, due to Lorentz transformations, the wavelength of the emitted radiation according to Eqs. (4.3) and (4.4) is reduced to the X-ray wavelength

$$\lambda = \frac{\lambda_u}{2\gamma^2}. \tag{4.6}$$

For instance, an undulator with a period of a few centimeters, in the case when the Lorentz factor is about $\gamma \sim 10^4$ will provide radiation with wavelengths of nanometers (i.e. X-ray range).

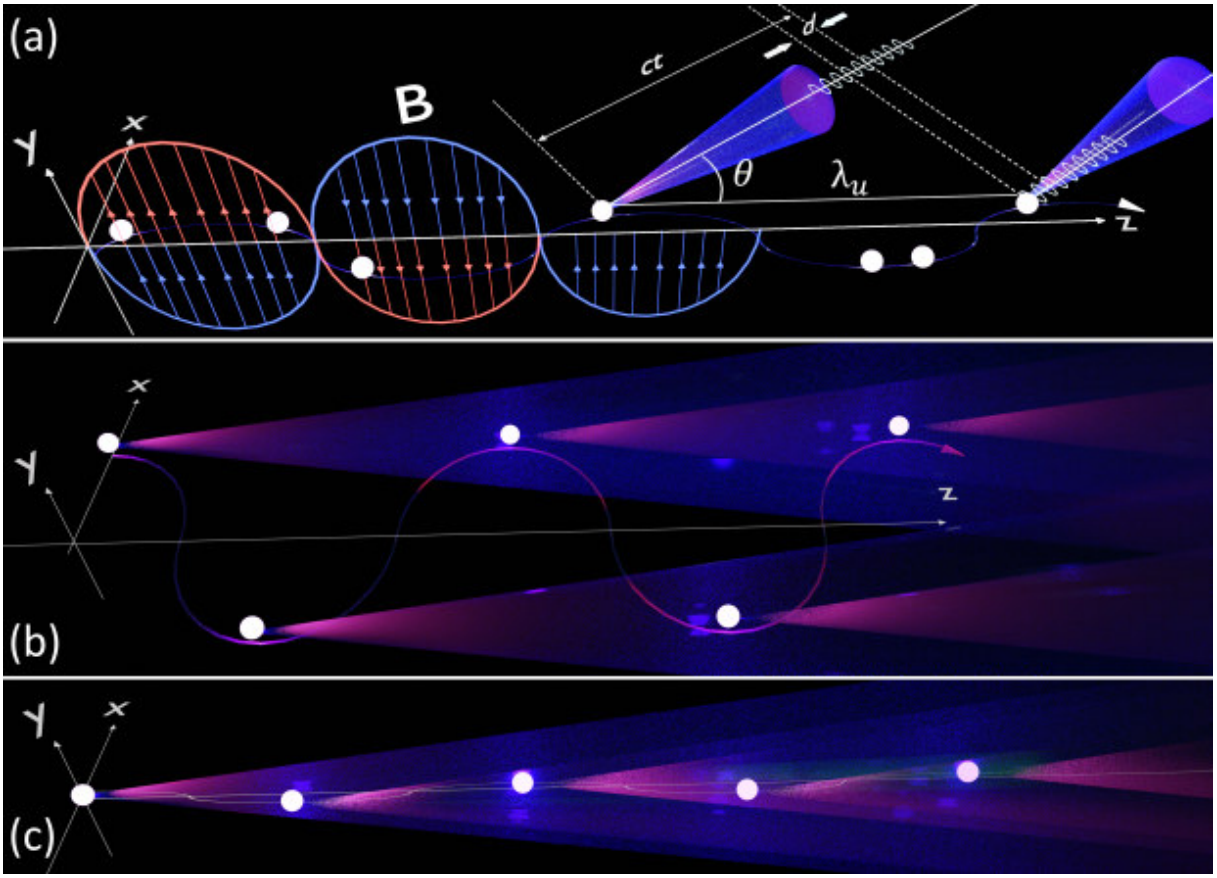

Figure 4.2: (a) Oscillating electron trajectory in the periodic magnetic structure with the magnetic field B and period λ_u. Difference between wigglers (b) and undulators (c) in the size of the excursions from a straight path of electron motion. In these figures, distances and angles were over-exaggerated.

4.2 Insertion devices and spectrum of the radiation

The lateral position of an electron as a function of propagation along the z-axis is shown in Fig. 4.2(a). The deflection of the electron is caused by a magnetic field which induces a Lorentz force on the particle.

$$\mathbf{F} = e[\mathbf{E} + \boldsymbol{\nu} \times \mathbf{B}]. \tag{4.7}$$

In the absence of external fields, the force is perpendicular to both the motion of the electron and the magnetic field vector B

$$\mathbf{F} = m\frac{d^2\mathbf{r}}{dt^2} = e[\boldsymbol{\nu} \times \mathbf{B}]. \tag{4.8}$$

It is convenient to replace the time derivative dt with the space derivative $dz = cdt$ as

$$\frac{d\mathbf{r}}{dt} = c\frac{d\mathbf{r}}{dz}, \quad \frac{d^2\mathbf{r}}{dt^2} = c^2\frac{d^2\mathbf{r}}{dz^2}. \tag{4.9}$$

Then equations of motion for the electron in the periodic magnetic field are

$$\begin{aligned} \frac{d^2x}{dz^2} &= \frac{e}{\gamma m_e c}(B_y - \frac{dy}{dz}B_z), \\ \frac{d^2y}{dz^2} &= \frac{e}{\gamma m_e c}(\frac{dx}{dz}B_z - B_x), \end{aligned} \tag{4.10}$$

where the mass m was replaced with the relativistic mass γm_e. In the case where the electron deflection occurs only in horizontal plane induced only by vertical magnetic field, as shown in Fig. 4.2, the Eq. (4.10) simplifies as

$$\begin{aligned} \frac{d^2x}{dz^2} &= \frac{eB_y}{\gamma m_e c}, \\ \frac{d^2y}{dz^2} &= 0. \end{aligned} \tag{4.11}$$

The magnetic field is assumed to be sinusoidal with the period λ_u

$$B_y = -B_0 sin(\frac{2\pi z}{\lambda_u}), \tag{4.12}$$

where B_0 is the value of the undulator magnetic field. The integration of Eq. (4.11) with the help of Eq. 4.12 gives the relative transverse velocity in the horizontal direction

$$\beta_{v,x} = \frac{dx}{dz}(z) = \frac{B_0 e}{\gamma m_e c}\frac{\lambda_u}{2\pi}cos(\frac{2\pi z}{\lambda_u}). \tag{4.13}$$

The Eq. (4.13) shows a horizontal angular deflection from z axis, therefore, the deflection parameter which shows the peak angular deflection is defined as

$$K = \frac{B_0 e}{m_e c}\frac{\lambda_u}{2\pi}. \tag{4.14}$$

Second integration of the Eq. (4.11) gives the electron motion in the periodic magnetic structure depending on its properties

$$x(z) = \frac{K}{\gamma}\frac{\lambda_u}{2\pi}sin(\frac{2\pi z}{\lambda_u}). \tag{4.15}$$

Therefore, the peak angular deflection is K/γ. As recalled, due to the relativistic motion, the radiation cone from the particle lies within the angle $\theta_{cen} \sim 1/\gamma$. The latter means that if the $K \gg 1$ the electron trajectory will not overlap with the emitted cone of SR (see Fig. 4.2 (b)), and there will be much more overlap if $K \leq 1$ (Fig. 4.2 (c)). In this way, the transition from undulatory radiation to wiggler radiation can be explained by the coefficient of undulation K as

$$\begin{cases} K \leq 1, & \text{undulator radiation.} \\ K \geq 1, & \text{wiggler radiation.} \end{cases} \tag{4.16}$$

In the undulator case, if the angular deviations of the electron are significantly less than the angular divergence of the radiation, then the radiation field of the electron interferes with the field of the same electron, formed at the next period of the magnetic field, at a given wavelength and at its harmonics n. As a consequence, this radiation has a lower angular divergence and a smaller spectral width (Fig. 2.4 (d)). The opening angle of such radiation can be approximated by the expression

$$\theta \approx \frac{1}{\gamma N^{1/2}}, \tag{4.17}$$

and the intensity increases by approximately N_u^2 times due to constructive interference. For the constructive interference between wavefronts emitted by the electron, the distance d between the first emitted wavefront and the second one (see Fig. 4.2 (a)) should contain a whole number of wavelengths over one period of the electron oscillation. Introduced relative transverse velocity in the horizontal direction $\beta_{v,x}$ is the part of the total velocity

$$\beta_v^2 = \beta_{v,x}^2 + \beta_{v,z}^2. \tag{4.18}$$

The relative longitudinal velocity then is defined as

$$\beta_{v,z}^2 = \beta_v^2 - \frac{K^2}{\gamma^2} cos^2\left(\frac{2\pi z}{\lambda_u}\right), \tag{4.19}$$

where β_v for the relativistic case is simplified as

$$\beta_v = \sqrt{1 - \left(\frac{1}{\gamma^2}\right)^2} \approx 1 - \frac{1}{2\gamma^2}, \tag{4.20}$$

Using the result, $cos2\alpha = 2cos^2 - 1$ and the approximation $(1-x)^{1/2} \sim 1 - x/2$, in Eq. (4.19) the longitudinal velocity can be rewritten as

$$\beta_{v,z} = \beta_v \left(1 - \frac{K^2}{4\beta_v^2\gamma^2} - \frac{K^2}{4\beta_v^2\gamma^2} cos\left(\frac{4\pi z}{\lambda_u}\right)\right), \tag{4.21}$$

which means that the average velocity in the forward direction is

$$\beta_{v,z} = \beta_v - \frac{K^2}{4\beta_v\gamma^2} \approx 1 - \frac{1}{2\gamma^2} - \frac{K^2}{4\beta_v\gamma^2}, \tag{4.22}$$

The time, which takes the electron to travel one period is $t = \lambda_u/v_z = \lambda_u/c\beta_{v,z}$. During this time the first wavefront will travel the distance $ct = \lambda_u/\beta_{v,z}$. Therefore, the separation between the wavefronts, which should be equal to the whole number of wavelengths, is defined as

$$n\lambda = \frac{\lambda_u}{\beta_{v,z}} - \lambda_u cos(\theta), \tag{4.23}$$

Inserting Eq. (4.22) into Eq. (4.23), considering $(1-x)^{-1} \approx 1 + x$, and $1 - cos(\theta) = 2sin^2(\theta/2)$,

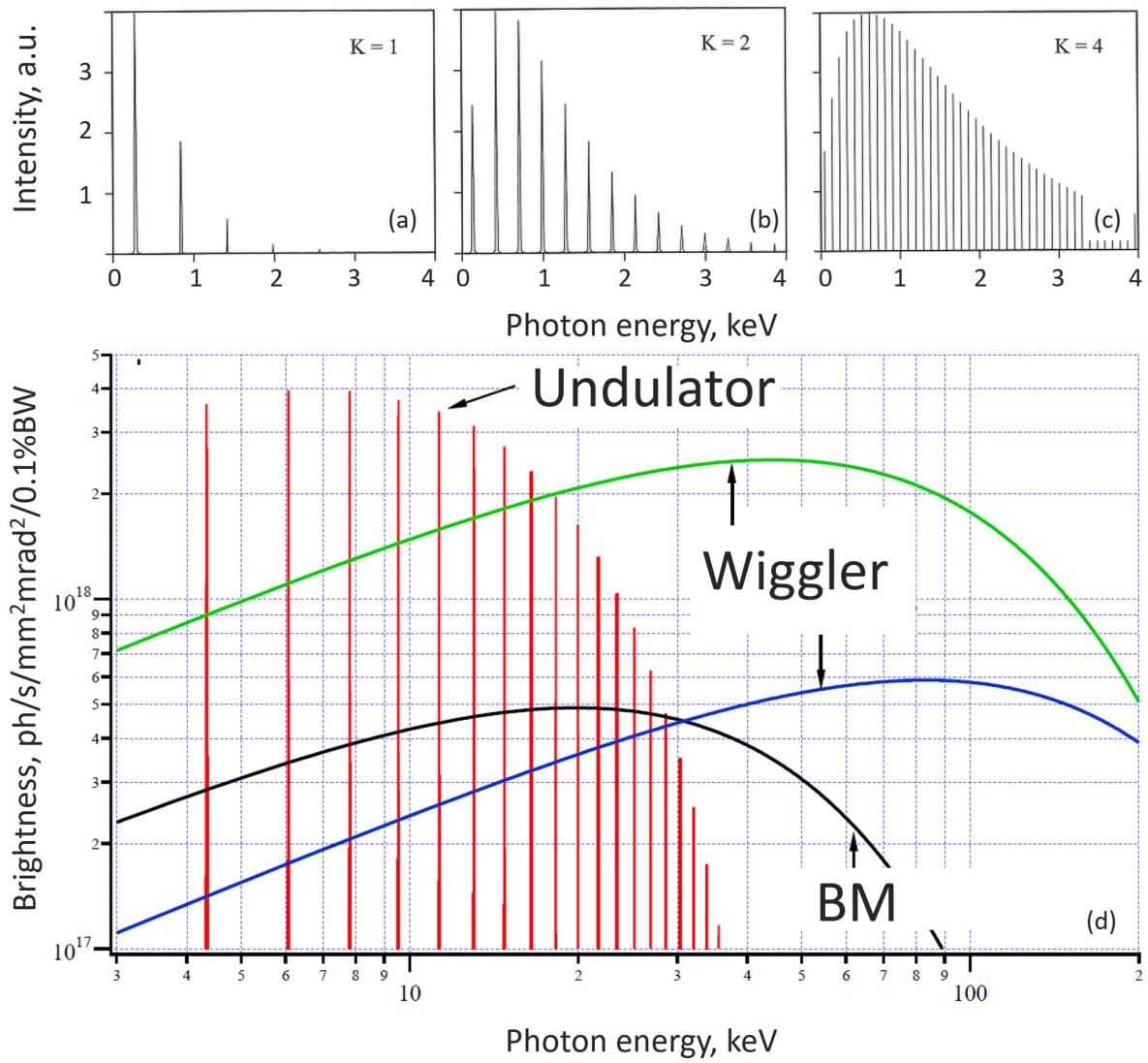

Figure 4.3: Difference between undulator spectrum for changing K parameter: (a) $K = 1$ (b) $K = 4$ and wiggler (c) $K = 4$. The figure is adapted from [77]. (d) Examples of spectral brightness form different insertion devices: Undulator, Wiggler, and Bending Magnet.

as well as the approximation for a small angles, the final common undulator equation can be obtained

$$\lambda_n = \frac{\lambda_u}{n\,2\gamma^2}\left(1 + \frac{K^2}{2} + \gamma^2\theta^2\right). \tag{4.24}$$

The Eq. (4.24) shows that the wavelength of the undulator radiation primarily depends on the period λ_u and the energy, but also K and the observation angle θ. The radiation spectrum of a linear undulator consists not only of the wavelengths described by equation (4.24), but also contains harmonics with wavelength $\lambda_n = n\lambda$, where n = 1, 2, 3, 4, ... Example of the undulator spectrum is show in Fig. 4.3.

The transformation from wiggler to undulator radiation is achieved in practice not by reducing the amplitude of electron oscillations (which is achieved by decreasing the magnetic

field strength between the magnetic pole pairs and would result in a drop in flux) but instead by reducing the magnetic pole period λ_u. The harmonic spectrum (see Fig. 4.3) transforms into a continuous spectrum at $K \gg 10$. Such a spectrum includes a range of high photon energies; therefore, wigglers are used to generate X-ray photons with energies from several tens to hundreds of keV.

According to Eq. (4.24) undulator spectrum can be tuned by changing K, which in turn is achieved by changing the gap between the two sets of magnetic poles and thereby the magnetic field strength B_0. The relative bandwidth or the spectral width of the undulator harmonics is much smaller than for other insertion devices and depends on the number of periods

$$\frac{\Delta\lambda}{\lambda} = \frac{1}{Nn}, \tag{4.25}$$

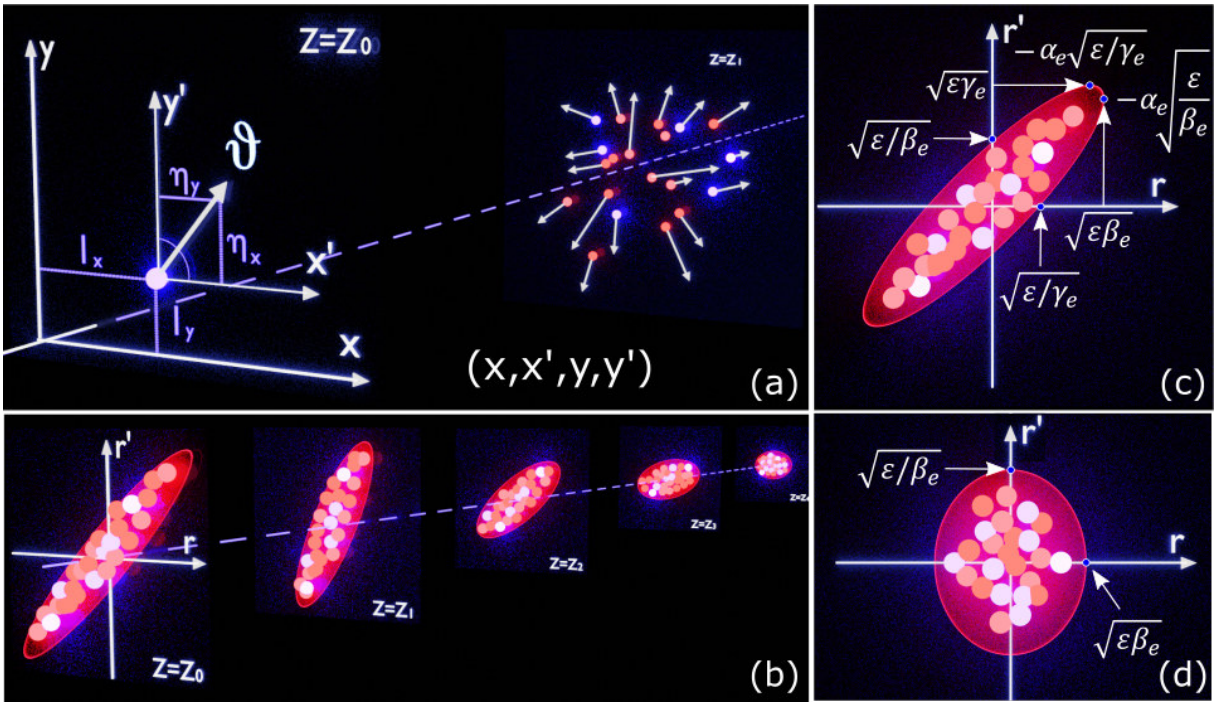

Figure 4.4: (a) Example of the electron transverse l_x, l_y and angular η_x, η_y displacements from the central orbit in the phase space representation. (b) Transformation of the electron beam emittance along the propagation direction. (c) Definition of phase space area through optical functions. (d) Emittance of the electron beam at focus position.

4.3 Emittance of the electron bunch

The properties of the X-ray radiation, including the spectral brightness and the degree of spatial coherence, are determined by the properties of a single electron along with the properties of the total electron bunch. Since the electron bunch is circulating in the storage ring, passing many insertion devices, correcting and refocusing magnets, the beam dynamics is always changing. A real electron beam consists of a huge number of particles $\sim 10^{12}$ so that the calculation of each electron trajectory becomes difficult. In this case, it is more convenient to trace the evolution of macroscopic electron beam parameters like beam size and beam divergence along a storage ring. Each particle of a beam is characterized by its transverse l_x, l_y and angular η_x, η_y displacements from the central orbit (see Fig. 4.4 (a)). These displacements are dependent on the longitudinal position z and thus vary along the storage ring. Four of these quantities together with z compose the phase space of the electron beam. By taking a Poincaré section (a snapshot at a fixed z) a distribution of points in the 4-dimensional transverse phase space area (x,x',y,y') may be obtained, where each point represents a single particle. Implying linear beam dynamics the motions in the horizontal and vertical planes may be decoupled, so that transverse areas of the phase space (x,x') and (y,y') may be considered separately and written as (r,r'). The transverse and angular displacements (r,r') usually characterized by the variances values

$$\sigma_e^2 =< r^2 >= \frac{1}{N}\sum_{i=1}^{N} r_i^2, \quad \sigma_e' =< r'^2 >= \frac{1}{N}\sum_{i=1}^{N} r_i'^2, \tag{4.26}$$

while their mean values are vanishing $< r^2 >=< r'^2 >=0$ if the beam is centered on the orbit axis. The quantity σ_e represents electron beam size and σ_e' represents electron beam divergence. According to Liouville's theorem, the phase space distribution is invariant under conservative forces. The same applies to the phase space area. This gives rise to the definition of the electron beam emittance

$$\varepsilon_e = \frac{\text{phase space area}}{\pi} = \sigma_e \sigma_e', \tag{4.27}$$

which indicates the area in the phase space covered by the beam and therefore characterizes an intrinsic property of the electron beam. The electron beam emittance stays invariant, however, electron beam size and divergence may vary while particles are moving through the magnetic lattice of the storage ring. In order to trace the beam parameters through the storage ring, the phase space area is defined by the convenient form of an ellipse (see Fig.4.4 (b,c))

$$\varepsilon_e = \gamma_e r^2 + 2\alpha_e r r' + \beta_e r'^2, \tag{4.28}$$

where γ_e,α_e,β_e are called optical functions (Twiss parameters) and represent electron beam parameters per unit emittance. Therefore, the electron beam parameters across the storage ring may be found through these optical functions, which also change through the magnet lattice. For example, a transformation of the Beta function β_e through the Double-bend-achromat (DBA) and Multi-bend-achromat magnetic lattices of the storage ring is shown in Fig. 4.5. There are special positions across the magnetic lattice: the straight sections where the insertion devices are placed, and the electron beam is focused. At this position, the machine is tuned such that the Alpha function α_e vanishes (Fig. 4.4 (d)), so the electron beam parameters may be easily found as

$$\sigma_e = \sqrt{\varepsilon_e \beta_e} \quad \sigma_e' = \sqrt{\frac{\varepsilon_e}{\beta_e}}. \tag{4.29}$$

In general an electron beam with emittance $\varepsilon_e = \varepsilon_e^x \varepsilon_e^y$ described by a Gaussian distribution function in the longitudinal and transverse directions. In the straight section at the electron beam focus $z = 0$, the electron bunch distribution function f_e may be written as

$$f_e(x, x', y, y', z = 0) = \frac{1}{(2\pi)^2 {\varepsilon_e}^x \varepsilon_e^y} exp\left\{-\frac{1}{2}\left(\frac{x^2}{\sigma_e^{x2}} + \frac{x'^2}{\sigma_e^{x'2}} + \frac{y^2}{\sigma_e^{y2}} + \frac{y'^2}{\sigma_e^{y'2}}\right)\right\} \tag{4.30}$$

4.4 Brightness of the Synchrotron Radiation source

The photon source of the electron bunch may be completely characterized by its spectral brightness $\mathcal{B}$ which is defined through the phase space distribution function of emitted photons

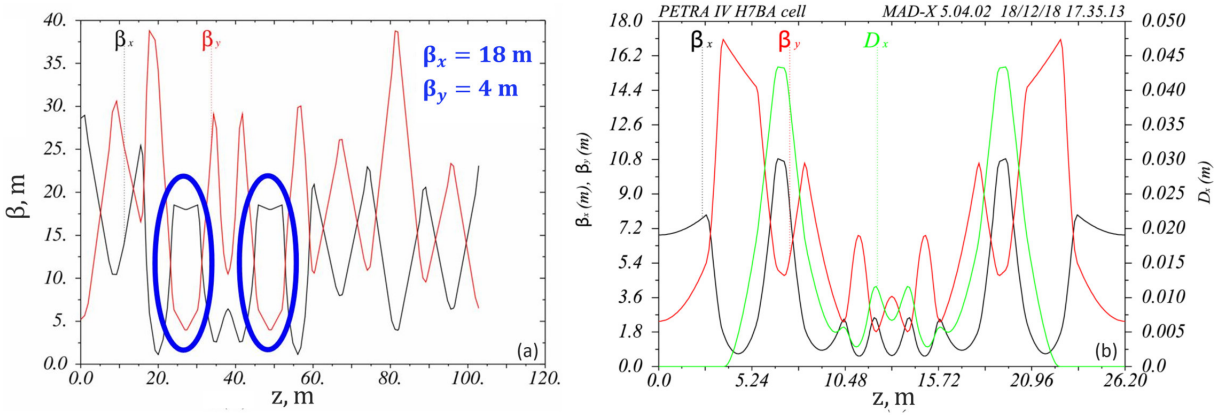

Figure 4.5: (a) Example of the Beta function in the DBA lattice. The positions of the straight sections and corresponding Beta functions are marked with blue color. (b) Example of the optical functions of the hybrid multi-bend-achromat (MBA) of PETRA IV (adapted from [54]).

by the analogy with the phase space of particles. If the diffraction effects are neglected and photons are considered as classical point particles, the phase space method is a convenient way to describe geometric optics. The distribution of the photon flux F at transverse plane z is specified by the brightness function $\mathcal{B}$, which shows the intrinsic strength of a radiation source, defined as [78]

$$\mathcal{B}(\mathbf{r}, \mathbf{r}', z) = \frac{d^4 F}{d^2\mathbf{r} d^2\mathbf{r}'}. \tag{4.31}$$

Similar to the conservation law of the phase space of the electron beam, the brightness at a given phase point z_0 on a transverse plane is the same as the brightness at the corresponding phase point z_1 on another transverse plane.

$$\mathcal{B}(\mathbf{r}, \mathbf{r}', z_0) = \mathcal{B}(\mathbf{r}, \mathbf{r}', z_1) = \mathcal{B}_0. \tag{4.32}$$

The total flux F may be found from the Eq. (4.31) as

$$F = \int \mathcal{B}_0(\mathbf{r}, \mathbf{r}') d^2\mathbf{r} d^2\mathbf{r}'. \tag{4.33}$$

The integration of Eq. (4.31) only over angles $d^2\mathbf{r}'$ or positions $d^2\mathbf{r}$ gives a spatial density of flux $d^2F/d^2\mathbf{r}$ or angular (spectral) flux $d^2F/d^2\mathbf{r}'$

$$\frac{d^2F}{d^2\mathbf{r}} = \int \mathcal{B}_0(\mathbf{r}, \mathbf{r}') d^2\mathbf{r}', \tag{4.34}$$

$$\frac{d^2F}{d^2\mathbf{r}'} = \int \mathcal{B}_0(\mathbf{r}, \mathbf{r}') d^2\mathbf{r}.$$

At this point, abstracting from the electron bunch current and focusing on the filament electron beam (i.e., parallel electrons, spread along z with $\varepsilon_e = 0$ and current $\mathcal{I}$), either spectral flux or brightness of the radiation from such a beam can be found individually. The same quantities F and $\mathcal{B}$ for the radiation from the total electron beam may be obtained thereafter

by the convolution of a filament beam with the electron bunch distribution f_e (Eq. (4.30)). The spectral flux F may be found from the radiated power from the single electron. In this case, Poynting vector $\mathbf{S}$, which describes an energy flux (the energy transfer per unit area per unit time) of an electromagnetic field, is used

$$\mathcal{S} \sim < \mathbf{E}(\mathbf{r},t) \times \mathbf{H}(\mathbf{r},t) > \sim < |\mathbf{E}(\mathbf{r},t)|^2 >, \tag{4.35}$$

where $\mathbf{E}(\mathbf{r},t)$ and $\mathbf{H}(\mathbf{r},t)$ are the electric and magnetic field vectors of single electron radiation. The energy radiated per unit surface is given by

$$\frac{d^2\mathcal{P}}{dr^2} \sim \int |\mathbf{E}(\mathbf{r},t)|^2 dt \tag{4.36}$$

The following Parseval's theorem is helpful to transfer to the spectral domain

$$\int |\mathbf{E}(\mathbf{r},t)|^2 dt = \int |\mathcal{F}\{\mathbf{E}(\mathbf{r},t)\}|^2 dt \sim \int |\mathbf{E}(\mathbf{r},\omega)|^2 d\omega, \tag{4.37}$$

where the $\mathcal{F}$ defines a Fourier transform. Such a radiation power into a small bandwidth from a filament electron beam may be written as

$$\frac{d^3\mathcal{P}}{dr^2 d\omega} \sim |\mathbf{E}(\mathbf{r},\omega)|^2 \tag{4.38}$$

The flux F, as defined in Eq. (2.1) shows a number of emitted photons N_{ph} per unit time into a small bandwidth $\Delta\omega$. Assuming that the number of emitted photons $N_{ph} = \mathcal{P}/\hbar\omega$, radiation power from a filament electron beam is an additive quantity (sum of power produced by each electron), and the number of electrons per second is $N_e = \mathcal{I}/e$, the definition of the flux F may be given using Eq. (4.38)

$$\frac{d^2F}{d^2\mathbf{r}} \sim \frac{\Delta\omega}{\omega}\frac{\mathcal{I}}{e}|\mathbf{E}(\mathbf{r},\omega)|^2 \tag{4.39}$$

In the framework of wave optics spectral brightness may be found through the definition of the Wigner function $\mathfrak{W}(\mathbf{r},\mathbf{r}',z)$ of the electric fields (see Eq. (3.100)) [79]

$$\mathcal{B}(\mathbf{r},\mathbf{r}',z) \sim \mathfrak{W}(\mathbf{r},\mathbf{r}',z) \sim \int < E^*(\mathbf{r}-\frac{1}{2}\Delta\mathbf{r})E(\mathbf{r}+\frac{1}{2}\Delta\mathbf{r}) > e^{-ik\mathbf{r}'\Delta\mathbf{r}} d\Delta\mathbf{r} \tag{4.40}$$

which is also invariant and satisfies the Eq. (4.32). In Eq. (4.40) coordinates $\mathbf{r}'$ and $\Delta\mathbf{r}'$ are introduced according to Eq. (3.67).

Both definitions of flux and brightness in Eq. (4.39) and Eq. (4.40) require the information about an amplitude of the electric field $E(\mathbf{r},\omega)$ of the radiation produced by a single electron. Due to the periodic structure of the undulator, the angular distribution of the electric field, formed by a single electron in the paraxial approximation, appears in the form of a *sinc*-function. [76, 78, 80] (see Fig. 4.6 (a,b))

$$E(\mathbf{r}',\omega) \sim sinc\left(\frac{N\pi\omega}{\omega_1(\mathbf{r}')}\right), \tag{4.41}$$

where $sinc(x) = sin(x)/x$ and $\omega_1(\mathbf{r}')$ for the fundamental harmonic is defined by Eq. (4.24). Therefore the angular density of the spectral flux from a single electron is also described by *sinc*-function

$$\frac{d^2F}{d^2\mathbf{r}'} =\sim |sinc\left(\frac{N\pi\omega}{\omega_1(\mathbf{r}')}\right)|^2. \tag{4.42}$$

Approximating the spectral flux in Eq. (4.42) by a Gaussian function

$$\frac{d^2F}{d^2\mathbf{r}'} \sim exp\left(-\frac{\mathbf{r}'^2}{2\sigma_r'^2}\right) \tag{4.43}$$

simultaneously imposing the condition that the integrals over the solid angle of both functions in Eq. (4.42) and Eq. (4.43) give the same result, an intrinsic characteristic of single-electron radiation is obtained [71]

$$\sigma_r' = \sqrt{\frac{\lambda_n}{2L_u}}, \tag{4.44}$$

where σ_r' is angular divergence of single electron radiation, $L_u = N_u\lambda_u$ is the undulator length, and λ_n determined by Eq. (4.24). Approximating the far-field distribution of the electric field of undulator radiation in resonant conditions from a single electron (Eq. (4.41)) by a Gaussian beam, the following expression for the brightness is obtained from Eq. (4.40) [71]

$$\mathcal{B}_G(r, r', z) \sim exp\left(-\frac{1}{2}\frac{(\mathbf{r} - z\mathbf{r}')^2}{2\sigma_r^2} + \frac{\mathbf{r}'}{2\sigma_r'^2}\right), \tag{4.45}$$

where σ_r is the transverse size of the Gaussian beam. Since both characteristics are assumed to be Gaussian, the following relation is satisfied for the characteristics of single-electron radiation for the Gaussian beams

$$\sigma_r\sigma_r' = \frac{\lambda}{4\pi}, \tag{4.46}$$

from which the transverse size σ_r of the single-electron radiation can be found

$$\sigma_r = \frac{\sqrt{2\lambda_n L_u}}{4\pi}. \tag{4.47}$$

Integrating Eq. (4.45) over $\mathbf{r}$ and $\mathbf{r}'$ in Eq. (4.33), the coherent flux of the radiation F_{coh} (i.e. produced by a filament beam with $\varepsilon_e = 0$) may be obtained

$$\mathcal{B}_0 = \frac{F_{coh}}{(2\pi\sigma_r\sigma_r')^2} = \frac{F_{coh}}{(\lambda/2)^2} \tag{4.48}$$

At this point it is worth noticing, that when considering the Wigner function in Eq. (4.40) on the optical axis (i.e. $\mathbf{r}' \to 0$) and the vanishing size of the source (i.e. $\mathbf{r} \to 0$), the correlation function under the integral and corresponding Wigner function takes the maximum value. In this case the integral in the Eq. (4.40) yields simply the integrated intensity $I \sim \int |E(\Delta\mathbf{r}'/2)|^2 d\Delta\mathbf{r}'$ from the coherent source in the narrow cone around the optical axis. The latter, according to Eq. (4.39) describes the coherent flux F_{coh} of the radiation, and implies that $max(\mathfrak{W}) \sim F_{coh}$.

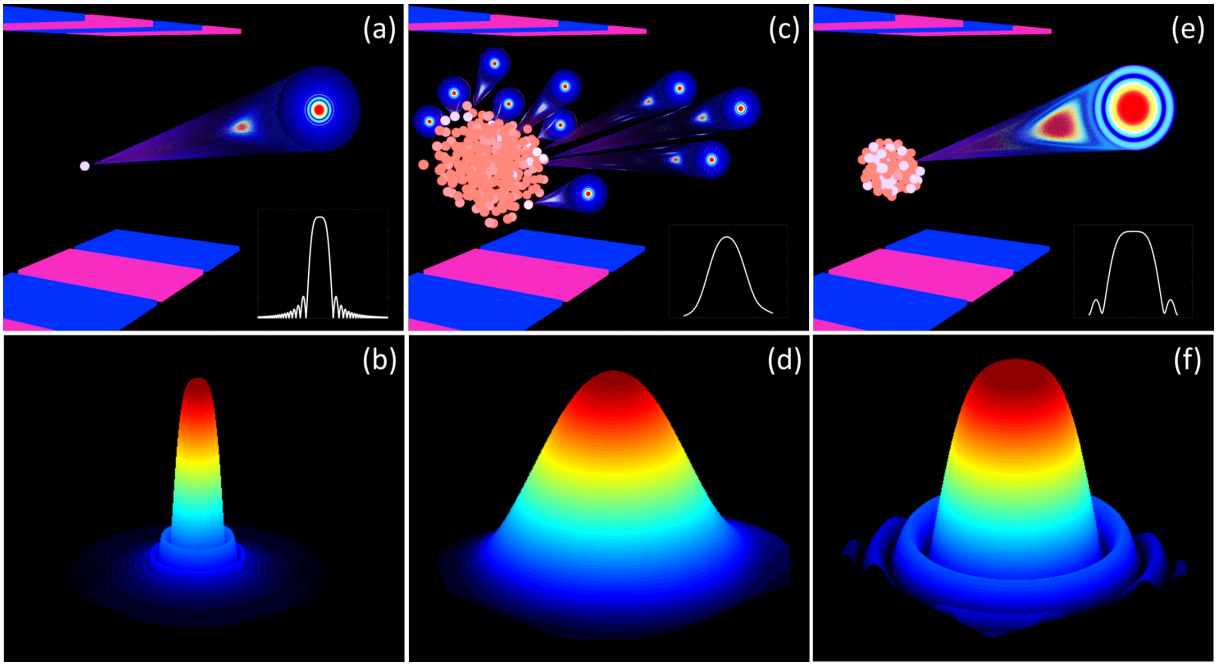

Figure 4.6: Undulator radiation from a single electron (a, b), an electron bunch (c, d), an electron bunch in the DLSR (e, f).

Therefore, it was analytically shown [81] that the brightness of the diffraction-limited source may be represented as the maximum value of the Wigner distribution on axis, which satisfies Eq. (4.45)

$$B_0 = max(\mathfrak{W}) = \left(\frac{2}{\lambda}\right)^2 F_{coh} \tag{4.49}$$

It is also worth mentioning that the size of the photon source σ_r can be calculated without Gaussian approximation of the single-electron radiation function in Eq. (4.40). In this case Gaussian approximation used for the flux per unit surface Eq. (4.34) (which calculation is based on Eqs. (4.40) and (4.41)). This approach gives another value for the transverse size σ_r [82]

$$\sigma_r = \frac{\sqrt{2\lambda_n L_u}}{2\pi}. \tag{4.50}$$

Brightness of the radiation from the total electron bunch may be obtained through a convolution integral of brightness function for a single electron radiation (Eq. (4.45)) and the bunch distribution function $f_e(\mathbf{r}_e, \mathbf{r}'_e)$ defined in Eq. (4.30)

$$\mathcal{B}(\mathbf{r}, \mathbf{r}', 0) \sim \int \mathcal{B}_G(\mathbf{r} - \mathbf{r}_e, \mathbf{r}' - \mathbf{r}'_e, 0) f_e(\mathbf{r}_e, \mathbf{r}'_e) d^2\mathbf{r}_e d^2\mathbf{r}'_e, \tag{4.51}$$

which gives well-known approximation for the brightness of undulator radiation [71, 83].

$$\mathcal{B} = \frac{1}{4\pi^2} \frac{F}{\Sigma_{phx}\Sigma'_{phx}\Sigma_{phy}\Sigma'_{phx}}, \tag{4.52}$$

where F is the spectral photon flux into the central core. In Eq. (4.52) the total photon source

size Σ_{ph} and divergence Σ'_{ph} are defined as

$$\Sigma_{ph} \approx [\sigma_e^2 + \sigma_r^2]^{1/2}, \Sigma'_{ph} \approx [\sigma_e'^2 + \sigma_r'^2]^{1/2}. \tag{4.53}$$

It has also been shown [73], how the Eq. (4.53) may be modified due to effect concerning finite energy distribution $\Delta E_\gamma / E_\gamma$ of the electrons in the bunch. The energy distribution in the electron beam at the synchrotron storage ring obeys Gaussian statistics. As noted in several publications, [73, 82], the effects of electron energy distribution can affect the properties of the synchrotron radiation source. In the Gaussian approximation for each of the transverse directions, the following expressions were obtained for the size and divergence of the beam [73]

$$\Sigma_{ph} \approx \left[\sigma_e^2 + \sigma_r^2 \cdot 4 \cdot Q_a(\rho/8\pi)^{2/3})\right]^{1/2}, \quad \Sigma'_{ph} \approx \left[\sigma_e'^2 + \sigma_r'^2 \cdot Q_a(\rho/2\pi)\right]^{1/2}, \tag{4.54}$$

where $\sigma_r{}'$ and σ_r- internal characteristics of single-electron radiation, defined in the Eqs. (4.44, 4.47). Normalization factor $Q_a(\rho)$ for the energy distribution of electrons in the storage ring in the equations (4.54) defines as

$$Q_a(\rho) = \left[\frac{2\rho^2}{-1 + exp(-2\rho^2) + \sqrt{2\pi}\rho \cdot erf(\sqrt{2}\rho)}\right]^{1/2}. \tag{4.55}$$

where $\rho = 2\pi\sigma_\gamma/\sigma_n$ is proportional to the ratio between the relative value of the spread of electrons in energy $\sigma_\gamma = \Delta E_\gamma / E_\gamma$ and relative bandwidth $\sigma_n = \Delta\lambda/\lambda$ (see Eq. 4.25) of the n-th harmonic of undulator radiation. Subscript 'a' in Eq. (4.55) stands for 'Approximated'. In Eq. (4.55) the Gauss error function defined as

$$erf(\rho) = \frac{2}{\sqrt{\pi}} \int_0^\rho exp(-t^2)dt \tag{4.56}$$

Normalizing function $Q_a(\rho)$ for the zero energy spread of electrons is equal to unity $Q_a(0) = 1$. It should be noted that the effective size of the photon source for the radiation of filament electron beam in formula (4.54) is twice as large as that determined in equations (4.53). The difference in the size of the photon source is due to the fact that the angular profile of radiation from a filament electron beam in the far field is not Gaussian. This fact is taken into account in equations (4.50) and (4.54) by introducing the factor of 2. The total photon emittance of the undulator source is then introduced as

$$\varepsilon_{phx,y} = \Sigma_{phx,y} \cdot \Sigma'_{phx,y}. \tag{4.57}$$

The following important case is considered, when $\sigma_e \gg \sigma_r$ and $\sigma'_e \gg \sigma'_r$. In this case brightness may be approximated as

$$\mathcal{B} \sim \frac{1}{4\pi^2} \frac{F}{\varepsilon_{e,x}\varepsilon_{e,y}}, \tag{4.58}$$

since the total electron emittance is relatively huge, and characteristic parameters of the radi-

ation are dominated by the electron beam parameters. Therefore the total radiation from an electron bunch may be approximated with a Gaussian function (see Fig. 4.6(c,d)). In the opposite case, when $\sigma_e \ll \sigma_r$ and $\sigma'_e \ll \sigma'_r$, the low emittance of the electron bunch defines the low emittance of the photon beam $\varepsilon^{ph}_{x,y}$, and, consequently, the high brightness and high flux of coherent photons from the source,

$$\mathcal{B} \sim \frac{1}{4\pi^2} \frac{F}{\sigma_r^2 \sigma_r'^2}. \tag{4.59}$$

In this case, the total radiation from an electron bunch is hardly approximated by a Gaussian function (see Fig.4.6(e,f)). A common property of all 3rd generation storage rings is a relatively large emittance in the horizontal direction. As a consequence, the photon beam has a low degree of spatial coherence in this direction. Interestingly, from Eqs. (4.53) under approximation of vanishing electron emittance ($\sigma_e = 0$ and $\sigma'_e = 0$) it can be seen, that there is certain limit on minimum achievable photon emittance, which is $\lambda/4\pi$ [78]. The latter means that the wave nature of light determines the minimum value of the photon beam emittance, and the source can be called diffraction-limited when the relation is satisfied

$$\varepsilon_e \leq \varepsilon_{ph} = \frac{\lambda}{4\pi} \tag{4.60}$$

If this relation is satisfied, then the characteristic parameters of the source may be improved by a great amount. Reduction of the electron bunch emittance of the synchrotron facility below the diffraction limited could prove difficult but may be implemented using a multi-bend achromat lattice design of the storage rings at the synchrotron facilities of the 4^{th} generation.

Chapter 5

Modeling and analysis of the 3^{rd} and 4^{th} generation synchrotron sources

As discussed in previous chapters, source brilliance and coherence of the storage rings are the critical parameters for successful synchrotron radiation experiments. However, a better understanding of the source parameters is necessary in order to exploit them properly. Presently, there is a big demand for adequate and effective methods to describe radiation properties from synchrotron sources correctly. It is interesting to note that even basic parameters of synchrotron sources are not very well established nowadays. The cause of this problem is based on the fact that Gaussian distributions cannot describe radiation from a single electron subjected to periodic acceleration.

This problem is easy to overcome at the synchrotron facilities of 3^{rd} generation due to the relatively huge size of the source. It implies that the overall coherence of such source is low and traditional methods of X-ray optics within the framework of partial coherence will provide a sufficient estimate of the radiation properties. On the contrary, ultimate DLSRs are expected to have a high degree of coherence, which means that traditional methods of X-ray tracing will not be sufficient to predict parameters of X-ray source and radiation characteristics at the experimental stations. Effective coherence methods, in this case, should be based on the application of the first- and higher-order correlation functions [20, 23]. At the same time, accurate simulation models based on synchrotron radiation theory and wave optics are necessary. Generally, electrons of the beam current at any synchrotron storage ring, being statistically distributed, can be described in 6-dimensional space, composed of spatial coordinates, angles, electron energy, and time. Therefore, it would be impossible to describe the overall emission by a single wavefront but by statistically distributed wavefronts. In such a way, it is easier to introduce new or take into account peculiar properties of the single electron radiation.

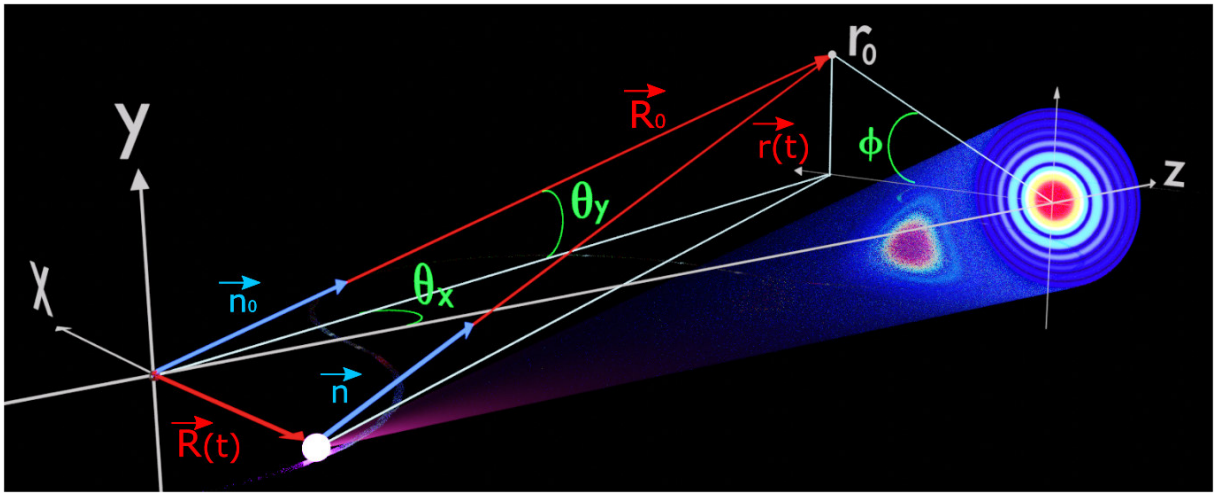

Figure 5.1: (a) Scheme of the electron trajectory and radiation geometry of the undulator field, reproduced from reference [85].

5.1 Modeling of the synchrotron radiation sources. Basic approach

The radiation field of a single electron, moving along trajectory $\mathbf{R}(t)$, in the paraxial approximation in the far zone according to [84] defined as

$$\mathbf{E}(\mathbf{R_0},\omega) = -\frac{i\omega e}{cR_0}\int_{-\infty}^{\infty} dt'[\mathbf{n}\times(\mathbf{n}\times\boldsymbol{\beta}_v(t'))]e^{i\omega(t-\frac{\mathbf{nR}(\mathbf{t}')}{c})} \tag{5.1}$$

In expression (5.1), the following values are used: $R_0 \approx (z_0, r_0)$ is the observation point, $\mathbf{n} = \frac{\mathbf{R_0}-\mathbf{R}(t')}{|\mathbf{R_0}-\mathbf{R}(t')|}$ is the unit vector, directed from the point of motion of the electron towards the observer (see Fig. 5.1). If the observer is at sufficient distance, it is possible to simplify the expression $\mathbf{R_0} - \mathbf{R}(t') = \mathbf{R_0} - \mathbf{n}\cdot\mathbf{R}(t')$. It is assumed that the ultrarelativistic (i.e., $\gamma \gg 1$) approximations for the synchrotron radiation source have been fulfilled, so that $\mathbf{n}\times(\mathbf{n}\times\boldsymbol{\beta}_v)\approx \boldsymbol{\beta}_v - \mathbf{n}$. It is also assumed that the spectrum of wavelengths in the field $E(\mathbf{r},t)$ is given by Eq. (3.8). In this case, the time dependence of a plane wave propagating in the positive direction along the z-axis can be described as follows

$$E(z,\mathbf{r},\omega) = E_0(\mathbf{r})e^{\frac{i\omega z}{c}-i\omega t}. \tag{5.2}$$

Introducing the angles $\theta_x = x_0/z_0$ and $\theta_y = y_0/z_0$, the transverse field components in expression (5.1) in the far zone in the paraxial approximation can be written in the following form

$$\mathbf{E}(z,\mathbf{r},\omega) = -\frac{i\omega e}{c^2 z_0}\int_{-\infty}^{+\infty} dz e^{i\Phi_t}\cdot\Big[(\beta_{v,x}(z)-\theta_x)\mathbf{n_x} + (\beta_{v,y}(z)-\theta_y)\mathbf{n_y}\Big], \tag{5.3}$$

where the total phase Φ_t is written as

$$\Phi_t = \omega\left[\frac{s(z)}{c} - \frac{z}{c}\right] + \frac{\omega}{2c}[z_0(\theta_x^2+\theta_y^2) - 2\theta_x x(z) - 2\theta_y y(z) + z(\theta_x^2+\theta_y^2)]. \tag{5.4}$$

In expressions (5.3) and (5.4) $\beta_{v,x}(z)$ and $\beta_{v,y}(z)$ horizontal and vertical components of the electron transverse velocity, $x(z)$ and $y(z)$ - functions of the longitudinal coordinate denoting the position of the electron in the plane transverse to the motion, $\mathbf{e_x}$ and $\mathbf{e_y}$ unit vectors in the transverse plane, $s(z)$ - longitudinal coordinate along the trajectory of the electron. The electron, in this case, will move at speed v, whose amplitude is constant and equal to $v = ds/dt$. Expression (5.3) can be used to describe the field from a single electron in the far zone moving along any trajectory.

Modeling of the undulator radiation source

In order to find the amplitude distribution of the undulator source, at first, a far filed amplitude distribution can be calculated by knowing the electron trajectory inside the magnetic structure. When the field from a single electron inside the ensemble is known at a certain position z_1, the fields at any other position z_2 can be found by applying a propagator according to the paraxial law

$$\tilde{E}(z_2, \mathbf{r_2}, \omega) = \frac{i\omega}{2\pi c(z_2 - z_1)} \int \tilde{E}(z_1, \mathbf{r_1}, \omega) e^{i\frac{\omega|\mathbf{r_2}-\mathbf{r_1}|^2}{2c(z_2-z_1)}} \tag{5.5}$$

In particular, it is possible to use a propagator to find the radiation field inside the studied magnetic structure. In this case, the field distribution is virtual. In the paraxial approximation, the radiation field of a single electron can be fully characterized if it is known in the transverse plane in one arbitrary position z. However, there is a special position $z = z_0$, where the electric field takes on a simple form, where the wavefront of the field from a single electron is flat. For an undulator source, such a position is in the middle of the magnetic structure, in the waist of the electron beam. Therefore, it is possible to take this position as an initial $z_0 = 0$, or as the position of the source of undulator radiation [81]. In this case, the following relationship is fulfilled between the electric fields of a single electron in the center of the magnetic structure of the undulator and in the far zone

$$\tilde{E}(0, \mathbf{r}, \omega) = \frac{iz_0\omega}{2\pi c} \int \tilde{E}(z_0, \boldsymbol{\theta}, \omega) e^{i\frac{\omega \mathbf{r}\boldsymbol{\theta}}{c}} e^{-\frac{i\theta^2 z_0 \omega}{2c}} d\theta \tag{5.6}$$

$$\tilde{E}(z, \boldsymbol{\theta}, \omega) = \frac{i\omega}{2\pi c z_0} \int e^{\frac{i\theta^2 z_0 \omega}{2c}} \tilde{E}(0, \mathbf{r}, \omega) e^{\frac{-i\omega \mathbf{r}\boldsymbol{\theta}}{c}} d\mathbf{r} \tag{5.7}$$

In the case of single-electron radiation, taking into account the parameters introduced earlier in Eqs. (4.12 - 4.24) and equation (5.3), the well-known expression for the angular distribution of the field of the first harmonic of undulator radiation polarized in the horizontal direction in the far zone at $z \gg L_u$ is derived [85]

$$E(z, \boldsymbol{\theta}) = -\frac{K\omega e L_u}{2c^2 z_0 \gamma} A_{jj} e^{i\frac{\omega z_0 \boldsymbol{\theta}^2}{2c}} sinc(\frac{\omega L_u \boldsymbol{\theta}^2}{4c}), \tag{5.8}$$

where L_u – length of the undulator, and the coupling parameter A_{jj} defines as

$$A_{jj} = J_0(\frac{K^2}{4+2K^2}) - J_1(\frac{K^2}{4+2K^2}), \tag{5.9}$$

where J_n is n-order Bessel functions of the first kind. Function $\tilde{E}(z_0, \mathbf{r_0}, \omega)$ in the expression (5.3) is symmetric about the undulator axis. Therefore function $E(z_0, \theta)$ in Eq. (5.8) can be written as a function of a single angle $\theta^2 = \theta_x^2 + \theta_y^2$, where angles θ_x and θ_y determined from the undulator z-axis in the horizontal and vertical directions.

To characterize the parameters of an undulator source, the field distribution from the ensemble of electrons is required. In this case, the virtual source may completely characterize the radiation field from the ensemble of electrons, where each electron has a given displacement $\mathbf{l}$ relative to the optical axis of the undulator and angle deviation $\boldsymbol{\eta}$ upon entering the undulator (see Fig. 4.4 (a)). The displacement of electrons relative to the optical axis of the undulator and the angular deviation obey a Gaussian distribution and are determined by the transverse phase space of the ensemble of electrons $f(\mathbf{l}, \boldsymbol{\eta})$. When considering an electron entering the undulator at a small angle $\boldsymbol{\eta}$ and small deviation from its axis $\mathbf{l}$, with fixed energy defined by the Lorentz factor γ, the following expression for the angular distribution of the field is obtained [81]

$$E(\boldsymbol{\theta}) = -\frac{K\omega e L_u}{2c^2 z\gamma} A_{jj} e^{i\frac{\omega}{c}(\frac{z\boldsymbol{\theta}^2}{2} - \boldsymbol{\theta}\mathbf{l})} sinc\left(\frac{\omega L_u |\boldsymbol{\theta} - \boldsymbol{\eta}|^2}{4c}\right) \tag{5.10}$$

Distribution of the field in the position of the source itself, i.e., at the center of the undulator, can be obtained using the propagator by applying equation (5.6)

$$E_0(\mathbf{r}) = \frac{i\omega z}{2\pi c} \int E(\boldsymbol{\theta}) e^{\frac{i\theta^2 z_0 \omega}{2c}} e^{\frac{-i\omega \mathbf{r}\boldsymbol{\theta}}{c}} d\mathbf{r} \tag{5.11}$$

The total distribution of the field in the far zone from the ensemble of electrons is obtained as the convolution of the single electron radiation (Eq. (5.10)) with a full electron beam

$$E_{total}(\theta_x, \theta_y) = \int E(\theta_x, \theta_y) f_{\eta_x}(\eta_x) f_{\eta_y}(\eta_y) f_{l_x}(l_x) f_{l_y}(l_y) d\eta_x d\eta_y dl_x dl_y \tag{5.12}$$

using the folowing functions

$$\begin{aligned} f_{\eta_x}(\eta_x) &= \frac{1}{\acute{\sigma_e}\sqrt{2\pi}} exp\left(-\frac{\eta_x^2}{2\acute{\sigma_e^2}}\right), f_{\eta_y}(\eta_y) = \frac{1}{\acute{\sigma_e}\sqrt{2\pi}} e\left(-\frac{\eta_y^2}{2\acute{\sigma_e^2}}\right), \\ f_{l_x}(l_x) &= \frac{1}{\sigma_e\sqrt{2\pi}} exp\left(-\frac{l_x^2}{2\sigma_e^2}\right), f_{l_y}(l_y) = \frac{1}{\sigma_e\sqrt{2\pi}} exp\left(-\frac{l_y^2}{2\sigma_e^2}\right). \end{aligned} \tag{5.13}$$

where $f_{\eta_x}(\eta_x), f_{\eta_y}(\eta_y)$ are the Gaussian electron angular distribution functions and $f_{l_x}(l_x), f_{l_y}(l_y)$ are distribution functions of a deviation from the undulator axis. This procedure implies that an individual electron in the beam acquires an arbitrary deviation in angle and spatial deviation from the optical axis of the undulator within the size of the emittance of the electron beam. The total field distribution in the center of the undulator at the source position is obtained using a propagator (see Eq. (5.11)), where $E(\boldsymbol{\theta})$ is replaced with $E_{total}(\boldsymbol{\theta})$.

5.2 Modeling of the 3^{rd} generation SSR in soft X-rays

In this section, the analysis of the coherence properties of 3^{rd} generation synchrotron source in the soft X-ray range of photon energies is given. The effect of soft X-ray beamline optics on the coherence properties of radiation is analyzed as well. The simulations of the synchrotron undulator radiation, as well as beamline optics, are performed utilizing a semi-analytical approach given in sections 3.1.4, 5.1, and X-ray Tracing Software (XRT) [86], which is primarily meant for modeling synchrotron sources, beamlines, and beamline optics (see A.1).

The starting point of the analysis is the selection of the simple substitution model, an appropriate analysis method, and the radiation treatment approach. Taking into account relation in Eq. (4.60) and knowing the electron beam parameters ($\varepsilon_{e,x} \approx$ 1nmrad and $\varepsilon_{e,y} \approx$ 10 pm rad) of the present storage ring like PETRA III, it can be concluded that present third-generation x-ray sources should be described as partially coherent sources

$$\varepsilon_{e,x} \gg \varepsilon_{e,y} > \varepsilon_{ph} = \frac{\lambda}{4\pi}. \tag{5.14}$$

The substitutional model, in this case, is represented by a Gaussian-Schell model. The coherence analysis may be completed in the frame of GSM and compared to the analysis of correlation functions within the semi-analytical approach, which includes calculations of the radiation field from the undulator source. Knowing the amplitude distribution of the source, one may easily calculate the coherence properties of the beam by methods of statistical optics (see section 3.2). On the other side, if only photon source parameters Σ_{ph} and Σ'_{ph} are known, then in the frame of basic coherence theory, one can get a reasonable estimate of the coherence properties of the radiation produced by 3^{rd} generation synchrotron sources.

As an example of the 3^{rd}generation synchrotron source, simulation of the high-brilliance synchrotron source PETRA III at DESY was performed. Simulations took into account storage ring and undulator parameters usually exploited for the generation of soft X-rays in the photon range of 500 eV to 4keV. PETRA III storage ring operates at an electron beam energy of 6 *GeV* with emittance $\varepsilon_{e,x} = 1$ nm rad in the horizontal direction and the emittance $\varepsilon_{e,y} = 10$ pm rad in the vertical direction due to 1% coupling. The photon energy of 1.2 keV is considered, produced by a 5 m long undulator at the first harmonic. Storage ring and undulator parameters are summarized in Table 5.1.

5.2.1 Coherent fraction of the radiation

In order to calculate the value of the coherent fraction of the synchrotron radiation, turning to the basic theory of synchrotron radiation is necessary. A simple estimation based on synchrotron radiation theory implies that a coherent fraction of the radiation ζ^{CF}, which shows the amount of coherent flux within the total flux

$$\zeta^{CF} = \frac{F_{coh}}{F}, \tag{5.15}$$

Table 5.1: Parameters of third generation synchrotron ring and undulator, used in simulations.

Parameter	Value
Electron energy	6 GeV
Beam current, mA	100 mA
Horizontal electron beam emittance $\varepsilon_{e,x}$	1 nm rad
Vertical electron beam emittance $\varepsilon_{e,y}$	10 pm rad
Horizontal betatron functions, β_x,	20 m
Vertical betatron functions, β_y	2.36 m
Undulator length Lu	5 m
Undulator period	65.6 mm
Number of undulator periods	76
Photon energy	1.2 keV
Number of electrons	$5{\cdot}10^3$

may be estimated taking into account Eqs. (4.48), (4.52). Therefore, the required definition of the coherent fraction of synchrotron radiation defined as

$$\zeta^{CF} = \frac{F_{coh}}{F} = \left(\frac{\lambda}{2}\right)^2 \frac{1}{\varepsilon^x_{ph}\varepsilon^y_{ph}} = \frac{\varepsilon_r^2}{\varepsilon^x_{ph}\varepsilon^y_{ph}}. \tag{5.16}$$

Strictly speaking, this expression is valid only for Gaussian radiation with the parameters determined in Eqs. (4.53, 4.57). A more precise estimation of the coherent fraction may be obtained within the framework of statistical optics (Eq. (3.75)), where the F_{coh} is defined by the normalized weight of the zero mode of the radiation. It can be shown that this equation (3.75) satisfies the definition of the coherent fraction Eq. (5.15). Indeed, the total flux of radiation F may be represented through the spectral density integrated over the solid angle (see Eq. (4.39))

$$F(\omega) = \int S(\mathbf{r}', \omega) d\mathbf{r}'. \tag{5.17}$$

The spectral density may be decomposed into a sum of modes according to Eq. (3.71), which are orthonormal. Performing angular integration in this expression (5.17) will lead to a sum of mode eigenvalues.

$$F(\omega) = \int \sum \beta_j(\omega) E_j^*(\mathbf{r}', \omega) E_j(\mathbf{r}', \omega) d\mathbf{r}' = \sum \beta_j. \tag{5.18}$$

Following the same arguments, the coherent flux F_{coh} may be represented as a weight of the zero mode

$$F_{coh}(\omega) = \beta_0. \tag{5.19}$$

Such the value of the coherent fraction is obtained directly from the spectral density of the radiation. However, for the synchrotron sources of the 3^{rd} generation, simple estimation by use of Eq. (5.16) is sufficient. For instance, coherent fraction, calculated according to Eq. (5.16) for

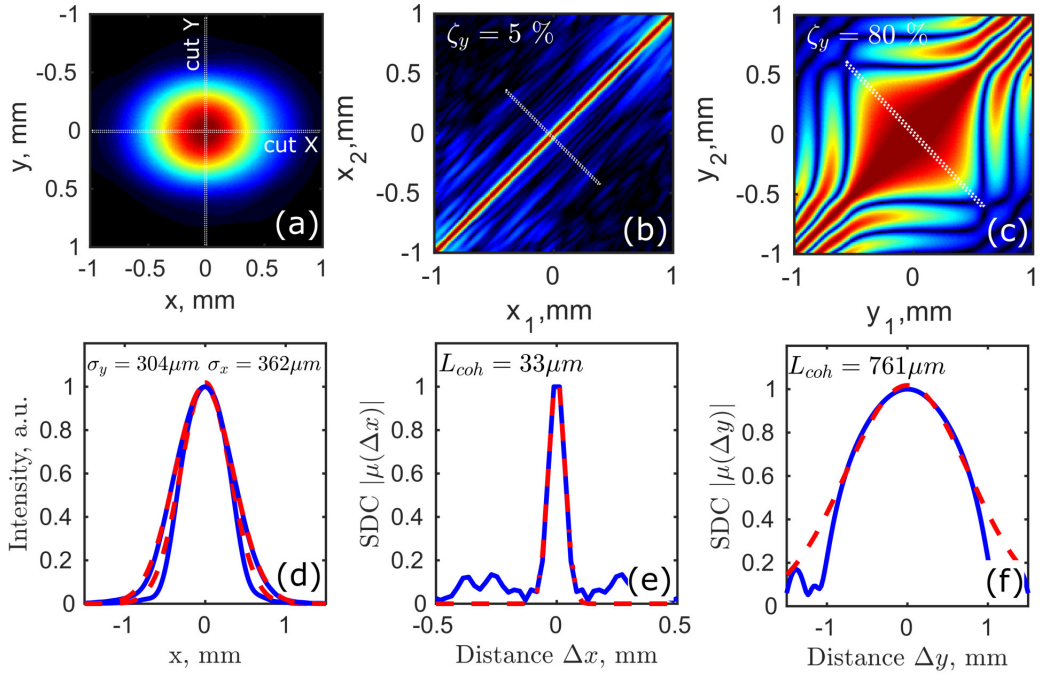

Figure 5.2: (a) Intensity distribution of the soft X-ray undulator radiation and (d) it cuts in horizontal and vertical directions, fitted by the Gaussian function. Absolute values of the normalized SDC function $|\mu(x_1, x_2)|$ (b) and $|\mu(y_1, y_2)|$ (c) with the calculated degree of coherence $\zeta_{i=x,y}$ and its cut (e,f) along the anti-diagonal line shown in (b,c) as a function of the separation of two points $|\mu(\Delta r = \Delta x, \Delta y)|$, fitted by a Gaussian function.

the radiation at a photon energy of 1.2 keV produced by the electron beam with parameters specified in Table. 5.1, is $\zeta_y^{CF} = 0.82$ and $\zeta_x^{CF} = 0.05$ in the vertical and horizontal directions, respectively. The value of the coherent fraction of the radiation ζ_y^{CF} in the vertical direction, calculated according to Eq. (5.16) is underestimated. In reality, ζ_y^{CF} for the monochromatic radiation in soft X-ray range at SSR of the 3^{rd} generation should be higher. In section 5.5.2 it will be shown how Eq. (5.16) can be rewritten, to get a more accurate estimation. However, in the horizontal direction, the coherence is poor, and estimation via Eq. (5.16) is sufficient. Such a low value of the horizontal coherent fraction is explained directly from the Eq. (5.16), namely due to huge electron emittance in this direction compared to the vertical one. More adequate analysis of coherence properties of the radiation is obtained in the frame of statistical optics in the next section.

5.2.2 Degree of coherence

For the simulation of the undulator source employing a semi-analytical approach and the XRT software, parameters given in Table 5.1 were used. Initially, the amplitude distribution at the distance of 27.9 m ($N_F \approx 0.01 \div 0.68$ according to Eq. 3.24), was calculated according to Eqs. (5.10)-(5.13) within the semi-analytical approach and by XRT software. Knowing the amplitude distribution of the source, one may easily calculate the coherence properties of the

beam in the frame of basic coherence theory (see section 3.2.3). Both simulation methods give similar results, which are shown in Fig. 5.2.

The intensity distribution of the beam at 27.9 from the undulator source is shown in Fig. 5.2 (a). The rms sizes of the intensity distribution are σ_x =362 μm in the horizontal direction and σ_y = 304 μm in the vertical direction. For the direct correlation analysis according to Eqs. (3.55-3.62) in transverse x and y directions, a thin cut of the central amplitude distribution in the corresponding direction was taken (see Fig. 5.2 (a)). The absolute value of the normalized SDC function $|\mu(\Delta r = \Delta x, \Delta y)$ for the horizontal and vertical directions is shown in Fig. 5.2 (b,c).

The analysis of the correlation function shows a relatively high degree of coherence in the vertical direction around 80%. This value was calculated directly according to Eq. (3.63) without the assumption of functional dependence of correlation functions and amplitude distributions of the undulator radiation. In the horizontal direction, due to huge electron emittance $\varepsilon_{e,x}$, the degree of coherence is only 5%. Fitting of the $|\mu(\Delta r = \Delta x, \Delta y)|$ function (see Fig. 5.2 (e,f)) with the Gaussian function Eq. (3.78), the corresponding coherence length of the radiation in the vertical and horizontal direction was obtained $\xi_y = 761\ \mu m$ and $\xi_x = 33\ \mu m$. In the frame of the GSM model, knowing the beam size $\sigma_{x,y}$ and the coherence length $\xi_{x,y}$, the degree of coherence may be calculated according to Eq. (3.81). In this case, calculated values of the degree of coherence are slightly lower $\zeta_x = 78\%$ in the vertical direction and $\zeta_x = 4.6\%$ in the horizontal direction. It also should be noted here, due to highly coherent radiation in the vertical direction at 1.2 keV photon energy, the functional dependence of $|\mu(\Delta y|$ is non-Gaussian (see Fig. 5.2 (f)).

As the result of this analysis, the undulator source at a soft photon energy of 1.2 keV possesses a high degree of coherence in the vertical direction and comparably low in the horizontal. However, the 'balance of powers' can be reversed by introducing optical elements in the way of field propagation. Such, by implementing apertures, which cut the radiation tales, coherent fraction and degree of coherence may be increased. On the contrary, adding absorbent elements, optical elements with distorted surfaces, and elements that cause optical aberrations may significantly reduce the degree of coherence. Such effect of the coherence degradation due to optical aberrations is considered in the next section. A related question arises whether the degree of coherence of the undulator beam can be transported without losses through a beamline.

5.2.3 Coherence at soft X-ray beamline

Abstracting from the synchrotron source and moving on to an overview of coherent properties at the 3^{rd} generation facility in the soft X-ray region, simulations of the beamline similar in type to P04 beamline at PETRA III were completed. The coherence characteristic of the photon beam transported through the beamline may significantly deteriorate due to aberrations in the optical system. Since that, a more detailed look at beamline optics is required. The analysis performed in this section is very similar to what is given in the work [87]. The beamline layout used in the simulation is shown in Fig. 5.3.

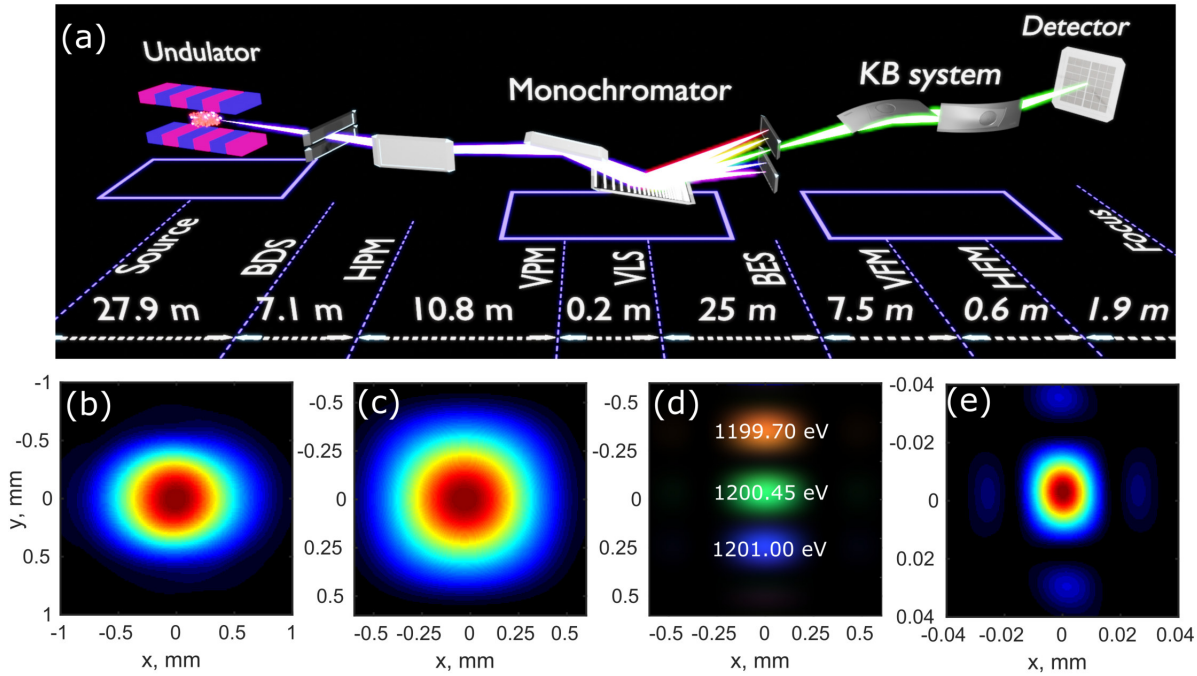

Figure 5.3: (a) Schematic arrangement of the optical elements at the P04 beamline at PETRA III. (b) Simulated intensity distribution from the undulator source is shown at the position of BDS (27.9 m), (c) at the position of BES in zero grating order and (d) +1 order, as well as at the focus position (e)

X-ray radiation at the P04 beamline is generated via a 5 m long APPLE-II type helical undulator. All distances of the optical elements listed further are given downstream from the reference point of the undulator position. Parameters of the simulated optical elements are given in Table. 5.2. A beam-defining slit (BDS) is placed at 27.9 m. The BDS is used to define the angular acceptance of the beamline and select a coherent volume of the beam. The horizontal plane mirror (HPM) at 35 m switching the photon beam between two branches of the beamline. The beam monochromatization is achieved via varied-line-spacing (VLS) grating at 46 m. The VLS grating disperses the beam vertically and focuses it in the vertical direction into the plane of the beam exit-slit (BES). The BES monochromatizes the beam by spatial filtering of the spectral focal distribution. The maximum resolving power achieved in the simulation by closing BES up to 30 μm is $\approx 2 \cdot 10^4$. The horizontal BES may be used to select the coherent volume of the photon beam in the horizontal direction as well. Finally, the beam is focused in the vertical and horizontal direction by the use of a Kirkpatrick-Baez (KB) mirror system consisting of two plane-elliptical focusing mirrors located 78.5 m (VFM) and 79.1 m (HFM). In the horizontal direction, the undulator source is directly imaged to the focus position by HFM. In the vertical direction, the exit slit of the monochromator is imaged to the focus position by VFM. The minimum achievable focal spot size in the simulation, by closing BES to 30 μm is 7 $\mu m \times 7 \mu m$

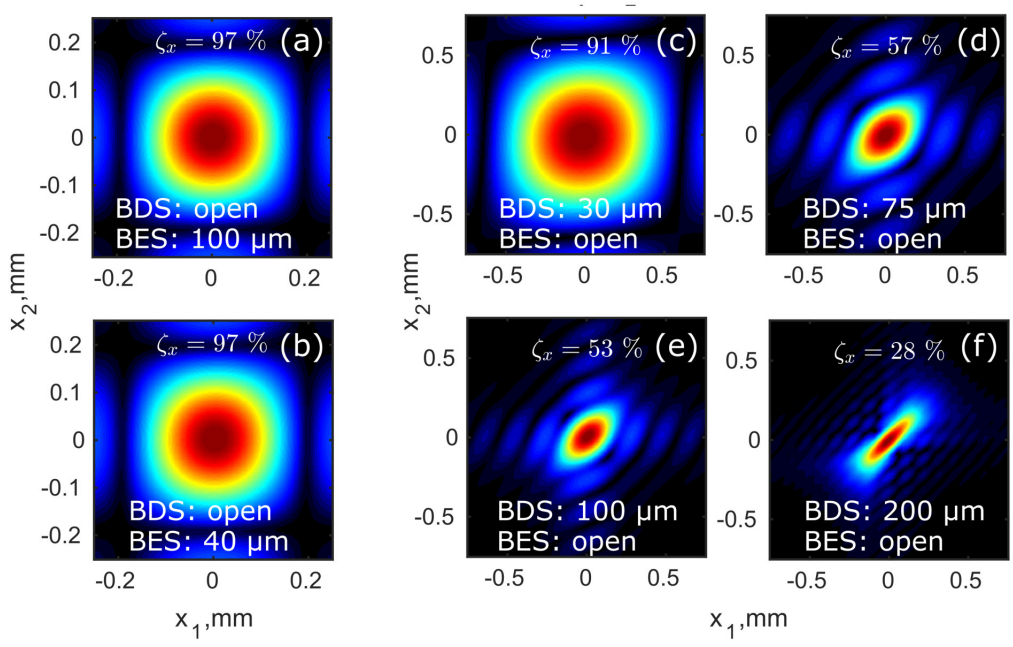

Figure 5.4: Absolute value of the CSD function $|W(x_1, x_2)|^2$ of the radiation at position of VFM upon closed BES to 100 μm while BDS is open (a,b) and closed BDS to 30 μm (c), 75 μm(d), 100μm(e), 200μm (f) while BES is open. In plots (a-f) ζ_x is the horizontal degree of coherence determined in each case according to Eq. (3.81).

5.2.4 Analysis of beamline optics

In order to determine the coherence properties of the beam transported through the optics, several virtual screens were placed along the beamline to record the amplitude and intensity of the radiation. Screens placed after the BDS at the position of VPM and after BES at the position of VFM were used for the correlation analysis. Additional screens were placed to monitor the focal position of the grating (i.e., at BES position) and focus (i.e., at focal position 81 m). The analysis of coherence properties is divided separately into vertical and horizontal parts.

The impact from the BDS and BES on beam characteristics may differ for the beamline setup presented in Fig. 5.3. The BDS located closer to the undulator source may be used as the secondary source, while BES can be used as a spatial filter. In this case, the focal spot size is determined either by the undulator source with open BDS or by secondary source provided by BDS upon closing (see for details [87]).

The first simulation is dedicated to the analysis of the coherence properties of radiation in the horizontal direction. In all following cases of the beamline setup, required coherent characteristics are determined only by the degree of coherence, calculated directly according to Eq. (3.81) using the recorded CSD function $W(r_1, r_2)$ at different positions along the beamline. The CSD function, in this case, simultaneously provides the degree of coherence and gives a rough estimation of the size of the incoming beam at the virtual screen.

In order to see the impact upon closing BDS and BES on coherence properties of the beam, in the initial simulation, BDS was fully opened while BES was closed up to 40 - 100 μm. Results of the analysis are shown in Fig. 5.4 (a,b). The degree of coherence in the horizontal direction, in

Table 5.2: Parameters of the simulated optical elements. Distance is defined from the source position. For the elliptical mirrors focal and defocal lenghts are defined as "q" an "p" accordingly

Parameter	Distance, m	Grazing angle, °	p /q /focus, m	Material coating
HPM	35	0.8	-/ -/	Pt
VPM	45.796	2.11	-/ -/	Pt
VLS	46	2.7	-/ -/25	Au
VFM	78.5	0.58	7.5/2.5/-	Pt
HFM	79.1	1	79.1/1.96/-	Pt

Table 5.3: Parameters of the VLS grating. The groove density is described as $N(z) = N_0(1 + 2b_2z + 3b_3z^2)$, where the density in the center is N_0 =1200 mm^{-1}

Parameter	Value
Groove density parameters	b_2=6.05 $\cdot$ 10^{-5}, b_3=−1.97 $\cdot$ 10^{-9}
Duty ratio (groove size/grating period)	0.65
Groove depth	9 nm

this case, is raised by 0.92 from the initial and reaches the value of 0.97. Closing BES further than 100 μm did not change the degree of coherence. Next, BES in horizontal direction stayed fully open, while BDS was varying from 30 to 200 μm (see Fig. 5.4). The degree of coherence, in this case, was also changing from 0.91 to 0.28. Thus, a maximum degree of coherence, achievable at the soft X-ray beamline in the horizontal direction, is very close to unity to the detriment of the radiation flux. The maximum degree of coherence in the horizontal direction, achievable under reasonable BDS parameters, providing sufficient flux is 0.53 - 0.57.

The next part of the simulation concerns vertical direction. In these simulations, BDS slits in the vertical direction were closed to 30-100 μm, and the correlation function is recorded at the VPM position.

Since the undulator source at photon energy 1.2 keV provided the radiation with 0.8 of coherence, after closing the BDS, it improved up to unity in both cases (see Fig. 5.5 (a,d)). Since the maximum value of the degree of coherence is achieved, in this case, closing BES would not improve the coherence of the radiation at VFM position and further downstream, which stays at unity at any BES separation (see Fig. 5.5 (b,c,e,f)). Therefore, a maximum degree of coherence, achievable at the soft X-ray beamline, is equal to unity to the detriment of the radiation flux.

Another related question concerns the possible degradation of radiation characteristics at the beamline and its origin. Reduction of the spatial degree of coherence may originate from diverse sources within the beamline, such as optical elements which embodying vibration-induced effects, dispersive effects and effects concerning the surface quality. Vibrations of optical elements can have a significant impact on the spatial coherence properties of the beam. It can be explained due to a significant increase of the virtual source size caused by optics vibrations, which immediately influences spatial coherence. Undulator photon source in the horizontal direction is already relatively huge in comparison to the vertical due to the enlarged

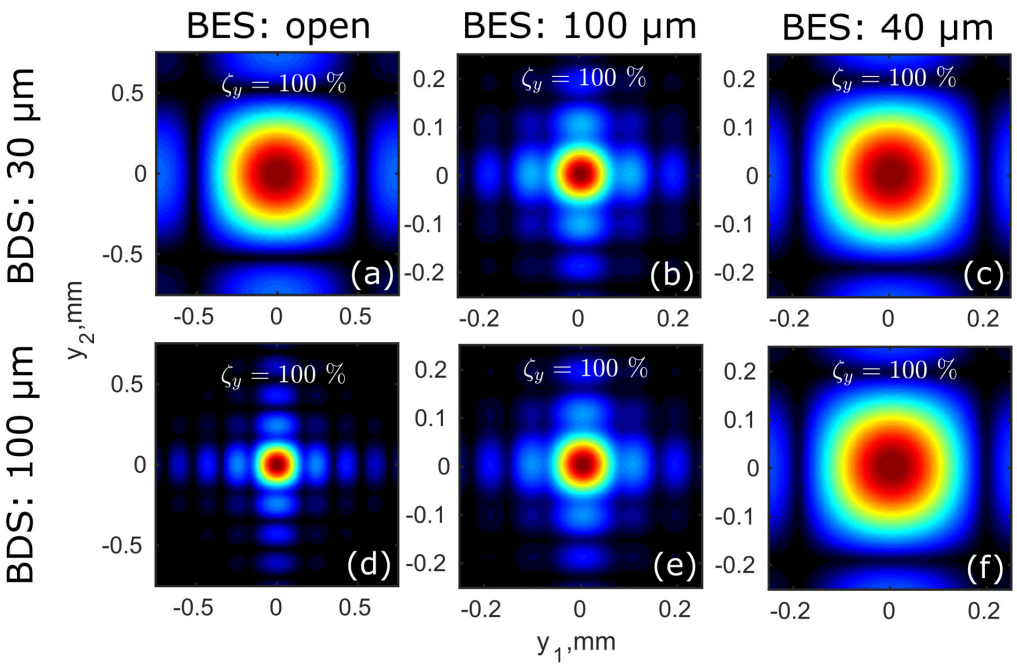

Figure 5.5: Absolute value of the CSD function $|W(y_1, y_2)|^2$ of the radiation at position of VPM upon closing BDS to 30 μm (a) and 100 μm (d). Absolute value of the CSD function $|W(y_1, y_2)|^2$ of the radiation at position of VFM upon closing BDS to 30 μm at the same time BES to 100 μm (b) and to 40 μm(c), as well as upon closing BDS to 100μm at the same time BES to 100 μm (e) and to 40 μm(f). In plots (a-f) ζ_y is the vertical degree of coherence determined in each case.

electron beam emittance. Since then, vibrational effects on the horizontal coherence properties have been negligible. Due to the fact that simulations are performed with ideal optics, the only elements that can harm the coherence of radiation in the vertical direction by means of their vibration are VPM, VLS, VFM, and HFM. Among these elements, the vibrational effect of VLS on coherence in vertical direction should be considered carefully. In addition, due to the vibration of this optical element, an energy variation effect is superimposed since the dispersive plane of the grating is in the vertical direction.

The effect of energy dispersion on the coherence properties of the beam will require additional simulations and will not be present here (see A.6). However, if the energy bandwidth is small, the vibration effect may be considered within the framework of statistical optics in the quasi-monochromatic regime (see Chapter 3). In this case, only the effect of virtual source enlargement will play a dominant role. It is interesting to note, due to the monochromator design, where VPM is redirecting beam to the VLS, the effect of the source enlargement due to VPM vibrations is doubled and also should be considered for completeness.

A frequency analysis of photon beam vibrations, performed at soft X-ray beamline P04 [87] at the focal position using the beam diagnostic tool, showed vertical photon-beam vibrations with frequencies of 13 Hz, 18 Hz, 25 Hz, and 50 Hz. In this case, to analyze the effect on coherence properties of the final radiation in the presence of the vibrational impacts from optical elements, simulations may be carried out at least by two methods. The first headlong method implies calculations of the amplitude distribution at the focal position, propagated through the

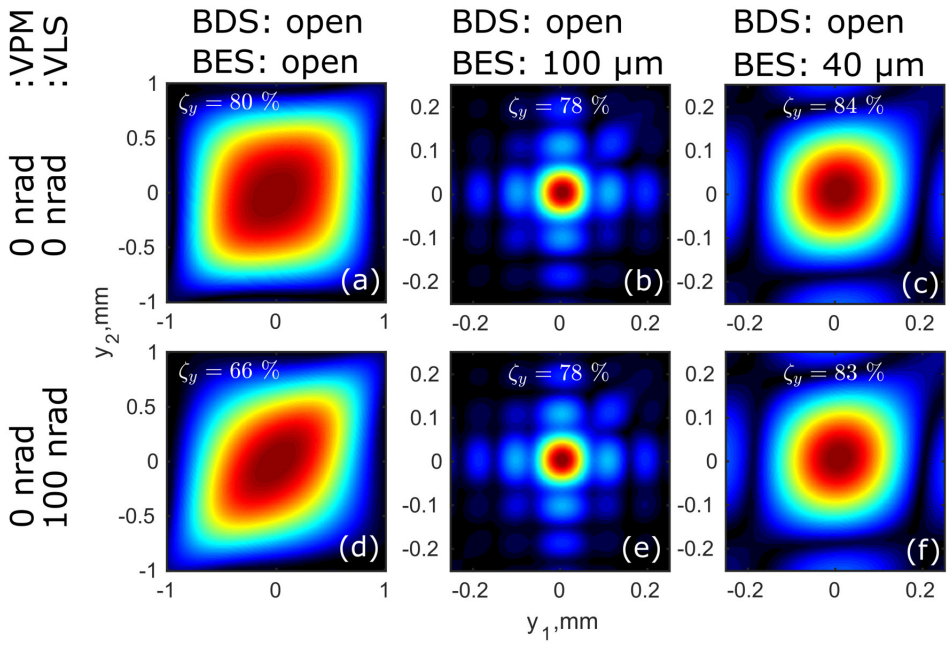

Figure 5.6: (a,d) Absolute value of the CSD function $|W(y_1, y_2)|^2$ of the radiation at position of VPM upon fully opened BDS for different pitch vibrations, written in the left column. Absolute value of the CSD function $|W(y_1, y_2)|^2$ of the radiation at position of VFM upon closed BES to 100 μm (b,e) and to 40 μm (c,f) for different pitch vibrations. In plots (a-f) ζ_y is the vertical degree of coherence determined in each case.

optical and diffraction elements. In addition, besides that final amplitude of the undulator radiation source at the desired position is obtained as a convolution integral with the electron bunch distributions (Eqs. (5.12), (5.12)), the angular distribution of the pitch vibration of each optical element should be added to the integral as well. In order to exclude errors of the simulation, it should be repeated several times until the simulation results differ for each transmitted radiation by 1-5%. Such a procedure is time-consuming and computationally is hardly beneficial. Another method is to obtain the amplitude distribution of the source, the same as for the case with vibration effects but for static optical elements. In this case, simulation can be completed with static elements but for an enlarged effective source. Therefore, the method implies calculation of the effective source size. This can be done by running a calculation of the field propagation through the setup at two opposite (maximum) possible deviations of optical elements following the specified value. After that, the backpropagation of the calculated field gives the effective source size. The size of the source can also be calculated analytically by the following equation, which gives the same result for the effective source size Σ^y_{vib} [87, 88]

$$\Sigma^y_{vib} = \sqrt{\Sigma^2_{ph,y} + (2\sigma_{VPM} \cdot z_{VPM})^2 + (2\sigma_{VLS} \cdot z_{VLS})^2}, \tag{5.20}$$

where σ_{VPM} and σ_{VLS} is the VPM and VLS rms values of the pitch vibrations accordingly, z_{VPM} is the distance from the undulator source to VPM, z_{VLS} is the distance from the undulator source to VLS, and $\Sigma_{ph,y}$ is the size of the source. Therefore, in the simulation, to save computational power, the vibration effect was modeled as an enlargement of the photon source for

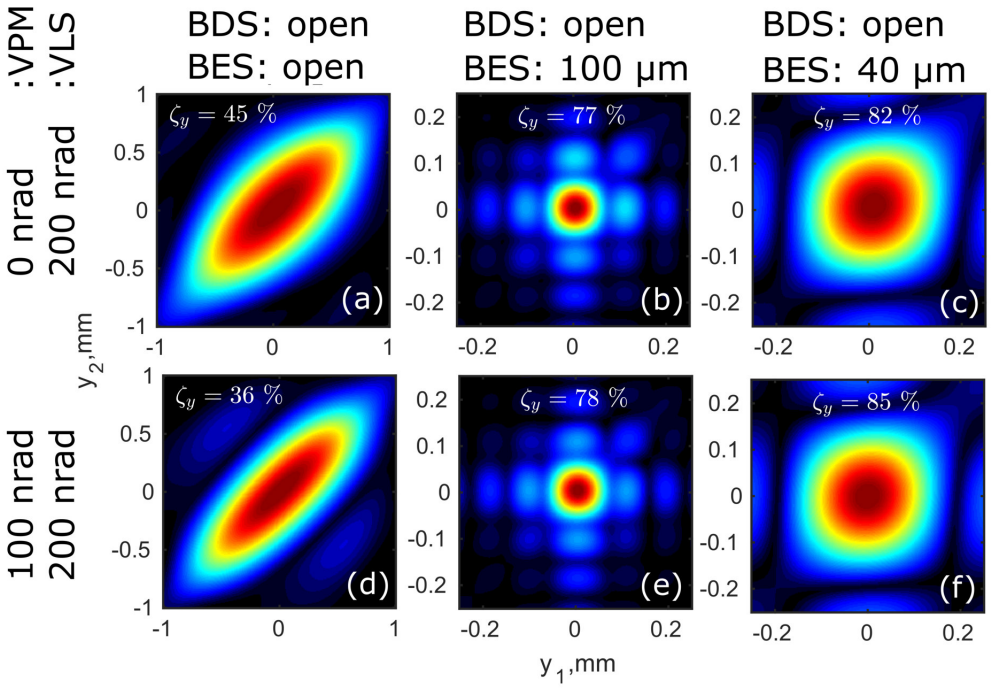

Figure 5.7: (a,d) Absolute value of the CSD function $|W(y_1, y_2)|^2$ of the radiation at position of VPM upon fully opened BDS for different pitch vibrations. Absolute value of the CSD function $|W(y_1, y_2)|^2$ of the radiation at position of VFM upon closed BES to 100 μm (b,e) and to 40 μm (c,f) for different pitch vibrations. In plots (a-f) ζ_y is the vertical degree of coherence determined in each case. Pitch vibrations of the VPM and VLS are written in the left column.

static optical elements. The pitch vibration of the VLS was varying in the range from 0 to 800 nrad and of the VPM from 0 to 200 nrad. Results of these simulations are shown in Fig. 5.6, Fig. 5.7 and Fig. 5.8. For the fully open BDS, the degree of coherence in vertical direction at position of VPM was significantly dropped from initial 80% to 13% at pitch vibration values of VPM and VLS in the range from $\sigma_{VPM} = 0$, $\sigma_{VLS} = 0$ to highest vibration $\sigma_{VPM} = 200$ nrad and $\sigma_{VLS} = 800$ nrad (see Fig.5.6 (a,d), 5.7 (a,d) and Fig. 5.8 (a,d,g)). However, under the same pitch vibrations, while the BES is closed to 100 μm the degree of coherence in the vertical direction at the VFM position slightly changed from 80% to 73% (see Figs. 5.6 (b,e) - 5.8 (b,e,h). Moreover, when the BES is closed down to 40 μm, the lowest degree of coherence achieved in the vertical direction at the VFM position with the highest pitch vibration of VPM and VLS is 82% (5.8 (i)). This underlines the important function of the BES and BDS in spatial filtering of the synchrotron radiation and imaging of the source at the focal position. If both slits are set correctly at the beamline, providing sufficient flux to the focal position, then large deviations of the coherent vertical fractions obtained in the experiments [89] in comparison with the theoretical values cannot be described only by optics vibrations.

Results of this analysis for the degree of coherence in a vertical direction depending on optics vibrations are given in Table. 5.4. As mentioned earlier, the degradation of X-ray beam coherence can be due to complex phase changes caused by the imperfection of optics. In this case, significant imperfections of optical elements will play the role of secondary sources, fur-

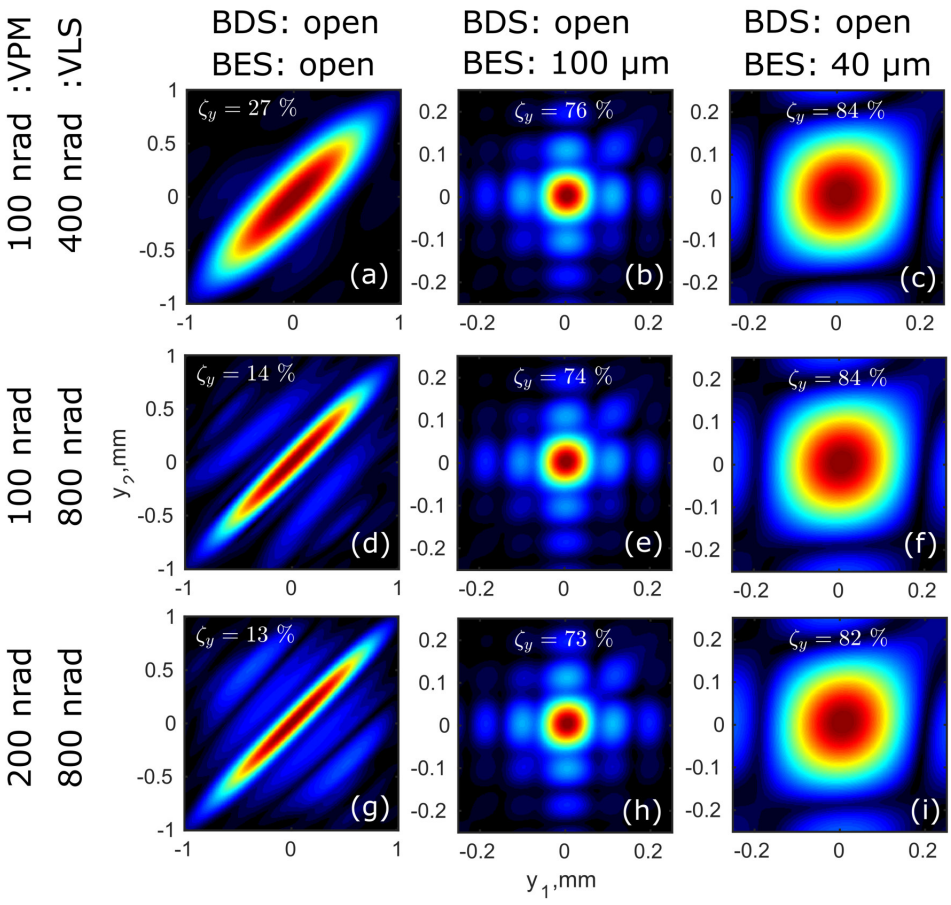

Figure 5.8: (a,d,g) Absolute value of the CSD function $|W(y_1, y_2)|^2$ of the radiation at position of VPM upon fully opened BDS for different pitch vibrations. Absolute value of the CSD function $|W(y_1, y_2)|^2$ of the radiation at position of VFM upon closed BES to 100 μm (b,e,h) and to 40 μm (c,f,i) for different pitch vibrations. In plots (a-i) ζ_y is the vertical degree of coherence determined in each case. Pitch vibrations of the VPM and VLS are written in the left column.

Table 5.4: Degree of coherence in vertical direction under different BDS/BES configuration and elemnts pitch vibrations.

VPM pitch vibration	VLS pitch vibration	BDS open	BES 100μm	BES 40μm
Total vibration		Degree of coherence		
0	0	0.8	0.78	0.84
0	100	0.66	0.78	0.83
0	200	0.45	0.77	0.82
100	200	0.36	0.78	0.85
100	400	0.27	0.76	0.84
100	800	0.14	0.74	0.84
200	800	0.13	0.73	0.82

ther degrading the beam quality [87].

5.2.5 Summary of the analysis

In summary, it was shown that coherence properties of the 3^{rd} generation synchrotron source might be calculated with reasonably good accuracy within the framework of statistical optics as well as conventional phase space methods.

The analysis of the beam at soft X-ray beamline showed important functions provided by the beamline apertures and outlined negative influence on coherence characteristics of the beam from the vibrational optical elements. It was found that the horizontal degree of coherence may be significantly increased from the original values by closing BDS or BES while maintaining a sufficient amount of flux.

On the contrary, in the vertical direction, due to vibration of optical elements, the degree of coherence may significantly drop down by 67%. However, in this case, closing the BES to the detriment of flux may raise the coherence values to the original level and beyond. In order to maintain high coherence in the vertical direction, the VLS pitch vibration should not exceed 100 nrad in the case of fully open BDS. The effects of surface imperfections of the optical elements on the radiation's coherence properties and energy shifts due to vibration of dispersive elements require additional studies.

In conclusion, understanding the coherence properties of the radiation and effects concerning their conversation are of vital importance for the design and optimization of future beamlines at 4^{th} generation synchrotron facilities.

5.3 Modeling of the DLSR sources

For the analysis of coherence properties of the DLSRs, a starting point should be modeling the synchrotron source at vanishing electron emittance or the filament electron beam. The next step is a generalization to the full electron beam case by applying statistical methods. Each of the electrons, in this case, will contribute to the total radiation, providing the final beam with certain characteristics, whether it is beam size, coherence, or brightness. As a result, simulation of the synchrotron radiation source by such an approach is more effective and less time-consuming. The simulations presented in the following sections are completed within the described approach, based on the theoretical works [90, 91].

Equation (5.12) does not include detuning or energy-spread effects on the radiation beam. However, for diffraction-limited rings, studying the influence of energy spread of undulator radiation properties is becoming more important because of the ultra-low electron emittance. Therefore, it is interesting to study energy spread effects on the brightness of undulator radiation, avoid the Gaussian beam approximation, and define the brightness function through the Wigner distribution. It will also be quite helpful to study the effects on brightness together with effects on coherence.

In order to take into account the effect of electron energy distribution, it is required to introduce a correction to the Lorentz factor in expression (5.8). When considering an electron entering the undulator at a small angle $\boldsymbol{\eta}$ and small deviation from its axis $\mathbf{l}$, with energy defined by the Lorentz factor γ, but different from the ensemble mean γ_0, the following expression is obtained for the angular distribution of the field [90]

$$E(\boldsymbol{\theta}) = -\frac{K\omega e L_u}{2c^2 z\gamma} A_{jj} e^{i\frac{\omega}{c}\left(\frac{z\boldsymbol{\theta}^2}{2} - \boldsymbol{\theta}\mathbf{l}\right)} sinc\left(\frac{\omega L_u |\boldsymbol{\theta} - \boldsymbol{\eta}|^2}{4c} + \frac{2\pi N_u(\gamma - \gamma_0)}{\gamma_0}\right). \tag{5.21}$$

This equation is similar to Eq. (5.10), except for the last part, accounting for the electron energy spread. The total distribution of the field in the far zone is obtained in a similar way, namely by taking the convolution of the radiation of a single electron (Eq. (5.21)) with a full electron beam and electron energy spread distribution

$$E_{tot}(\theta_x, \theta_y) = \int E(\theta_x, \theta_y) f_{\eta_x}(\eta_x) f_{\eta_y}(\eta_y) f_{l_x}(l_x) f_{l_y}(l_y) f_{\gamma_e}(\gamma_e) d\eta_x d\eta_y dl_x dl_y d\gamma_e \tag{5.22}$$

using the same distributions, as introduced in Eq. (5.13) and the Gaussian energy distribution of the electron beam

$$f_{\gamma_e}(\gamma_e) = \frac{1}{\sigma_\gamma \sqrt{2\pi}} e^{-\frac{\gamma_e^2}{2\sigma_\gamma^2}}. \tag{5.23}$$

The described method implies that an individual electron in the beam, besides acquiring an arbitrary deviation in angle and spatial deviation from the optical axis of the undulator within the size of the emittance of the electron beam, additionally gets an arbitrary energy shift within the value of the total energy spread. Distribution of the field in the position of the source it-

Table 5.5: Parameters of the storage ring and undulator, used in the analysis.

Parameter	Value
$\varepsilon_{e\,x,y}$, pm rad	10
$\beta_{x,y}$, m	1
Electron bunch energy, GeV	6
Undulator period λ_u, mm	65.6
Number of undulator periods N_u	76
Photon energy, keV	0.58 and 4

self, i.e., at the center of the undulator, can be obtained using the propagator by applying the equation (5.11). In the case when the required parameters of the function cannot be calculated within the Gaussian approximation, it is suggested to calculate its variance values instead (second moment in Eq. 3.38). For instance, in order to determine the size and divergence of the photon source, with the distribution other than a Gaussian, the following equations can be used

$$\Sigma^2_{ph_x} = \frac{\iint x^2 |E(x,y)|^2 dxdy}{\iint |E(x,y)|^2 dxdy}, \quad \Sigma'^2_{ph_x} = \frac{\iint \theta_x^2 |E(\theta_x,\theta_y)|^2 d\theta_x d\theta_y}{\iint |E(\theta_x,\theta_y)|^2 d\theta_x d\theta_y} \tag{5.24}$$

where $E(x,y)$ and $E(\theta_x,\theta_y)$ are the amplitude distribution of the photon source at the source position and in the far region accordingly.

Further, the analysis of the coherence properties may be performed by utilizing methods given in sections 3.2.3, 3.3, 3.6. The analysis of the DLSR radiation source parameters was divided into three parts depending on electron beam emittance: filament electron beam (i.e., $\varepsilon_e = 0$), vanishing electron emittance ($\varepsilon_{e\,x,y} \approx 1 - 10$ pm rad) and the wide range of electron emittance values $\varepsilon_{e\,x,y}$ from 10 pm rad to 300 pm rad. The photon energy considered in the analysis lies in the range from 500 eV to 50 keV. The analysis dedicated to studying coherence properties of SR from the filament electron beam and the beam with vanishing emittance (section 5.4) is generalized and given in normalized units.

5.4 Diffraction-limited storage ring. Vanishing electron emittance

For studying the effect of the vanishing electron emittance and the energy spread effect, the DLSR, operating at 6 GeV (for parameters of the source see Table 5.5) was considered as an example. The basic value for the vanishing electron emittance was considered 10 pm rad both in the vertical and horizontal direction by that considering a round beam shape.

5.4.1 Source amplitude and intensity distribution

The considerations in this section, being fully general, apply to other magnetic systems as well. Derivations of the formulas are based on the works [63, 81] For the analysis of SR coherence properties at vanishing electron emittance, the following normalized units [90]

Table 5.6: Converted values of basic functional parametrs in accordance with the source parameters defined in Table 5.5. Note ± sign corresponds to a positive/negative detuning

Parameter/ Normalized value	0	±1	±2
Energy spread detuning ξ_E	0	$\mp 10^{-3}$	$\mp 2.1 \cdot 10^{-3}$
rms value of the energy spread distribution $\sqrt{\Delta_E}$	0	10^{-3}	$2.1 \cdot 10^{-3}$
Photon energy of 580 eV			
Spatial coordinate $\hat{r}$	0	$\pm$ 0.1 mm	$\pm$0.2 mm
Angle $\hat{\theta}$	0	$\pm$20 μrad	$\pm$41 μrad
Photon energy of 4000 eV			
Spatial coordinate $\hat{r}$	0	$\pm$40 μm	$\pm$79 μm
Angle $\hat{\theta}$	0	$\pm$7.7 μrad	$\pm$15.7 μrad

$$\begin{aligned} \hat{\boldsymbol{\eta}} = \frac{\boldsymbol{\eta}}{(\lambda/L_u)^{1/2}}, \hat{\boldsymbol{\theta}} = \frac{\boldsymbol{\theta}}{(\lambda/L_u)^{1/2}}, \\ \hat{\mathbf{r}} = \frac{\mathbf{r}}{(\lambda L_u)^{1/2}}, \hat{\mathbf{l}} = \frac{\mathbf{l}}{(\lambda L_u)^{1/2}}, \\ \hat{\xi}_E = -4\pi N_u \frac{\gamma - \gamma_1}{\gamma_1}, \end{aligned} \tag{5.25}$$

and normalized parameters

$$\begin{aligned} N_{x,y} = \frac{\sigma_{x,y}^2}{\lambda L_u}, D_{x,y} = \frac{{\sigma'_{x,y}}^2}{\lambda/L_u}, \\ \Delta_E = (4\pi N_u \sigma_{\Delta\gamma/\gamma})^2, \end{aligned} \tag{5.26}$$

are used for the electron beam distributions given in Eq. (5.13) and (5.23). In Eqs. (5.25), (5.26) $\sigma_{\Delta\gamma/\gamma} = (\gamma - \gamma_1)/\gamma_1$ and the normalization is shown for the angles to the diffraction angle $\sqrt{\lambda/L_u}$ of single-electron emission, sizes to the diffraction size $\sqrt{\lambda L_u}$, and the energy deviation to the undulator resonant bandwidth.

Considering Eqs. (5.25) and (5.26), far-zone amplitude of the single electron radiation in Eq. (5.21) in normalized units can be written as [90]

$$\hat{E}(\hat{\boldsymbol{\theta}}) = \frac{1}{\hat{z}} exp\left(i\frac{\hat{z}\hat{\theta}^2}{2} - i\hat{\boldsymbol{\theta}} \cdot \hat{\mathbf{l}}\right) sinc\left(\frac{|\hat{\boldsymbol{\theta}} - \hat{\boldsymbol{\eta}}|^2}{4} + \frac{\hat{\xi}_E}{2}\right) \tag{5.27}$$

where $\hat{z} = z/L_u$. Using the Eq. (5.6), it is possible to calculate the analogous field at the virtual source as [90]

$$\hat{E}(\hat{\mathbf{r}}) = -iexp\left[i\hat{\boldsymbol{\eta}} \cdot (\hat{\mathbf{r}} - \hat{\mathbf{l}})\right] \times \int_0^\infty d\hat{\theta}\hat{\theta} J_0\left(\hat{\theta}|\hat{\mathbf{r}} - \hat{\mathbf{l}}|\right) sinc\left(\frac{\hat{\xi}_E}{2} + \frac{\hat{\theta}_E}{4}\right) \tag{5.28}$$

In the panels (a,b) of Fig. 5.9 amplitude $\hat{z}\hat{E}(\hat{\theta})/exp(i\hat{\theta}^2\hat{z}/2)$ and intensity $\hat{z}^2|\hat{E}(\hat{\theta})|^2$ functions are shown, i.e. the well known far-field profiles for $\hat{\mathbf{l}} = 0$ and $\hat{\boldsymbol{\eta}} = 0$ (which is azimuthal-symmetric) as a function of $\hat{\theta}$ for different values of the electron energy detuning $\hat{\xi_E}$, while in the panels (c,d) the field at the virtual source for the same choices of the detuning parameter

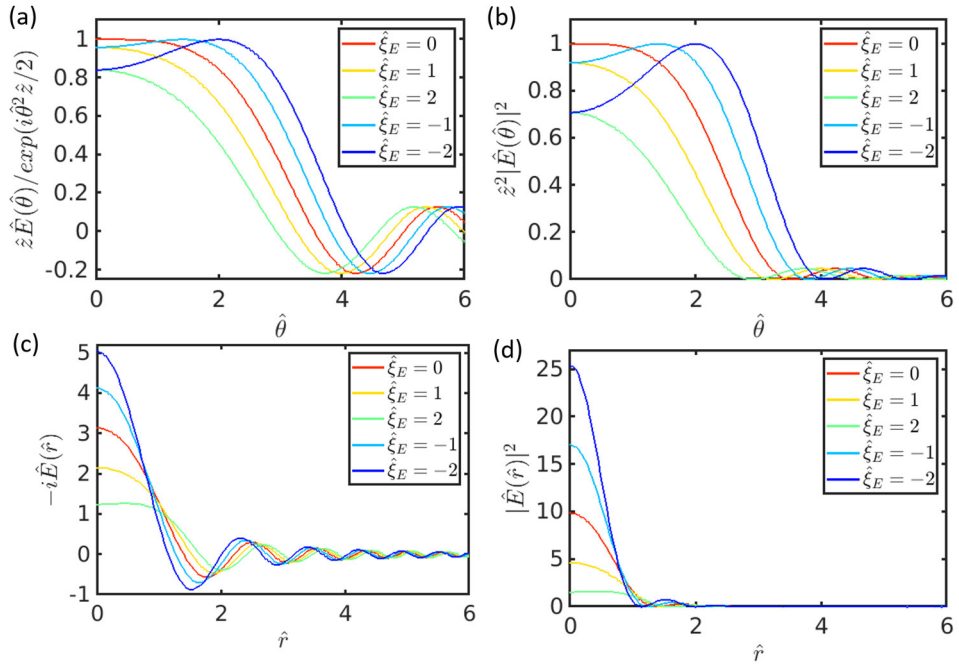

Figure 5.9: Functions (a) $\hat{z}\hat{E}(\hat{\theta})/exp(i\hat{\theta}^2\hat{z}/2)$ and (b) $\hat{z}^2|\hat{E}(\hat{\theta})|^2$, the field in the middle of the undulator, $-i\hat{E}(\hat{r})$ (c), and intensity $|\hat{E}(\hat{r})|$ (d) are drawn for different values of $\hat{\xi}_E$. Here $\hat{\mathbf{I}} = 0$ and $\hat{\boldsymbol{\eta}} = 0$. For a more explicit assessment and comparison with existing sources, the values of the electron beam energy detuning, angles, and positions are given in Table 5.6

are shown. Corresponding intensity distributions in panels (b,d) are shown for comparison with amplitude distribution in (a,c). It can be shown that for negative values of $\hat{\xi}_E$, the maximum intensity at the source increases and tends to 'saturate' for large negative values while it remains constant in the far zone.

Also, even at $\hat{\xi}_E = 0$, the intensity distribution at the virtual source and in the far zone is not Gaussian. Therefore, any Gaussian approximations for the source amplitude should be taken with caution. In this regard, it is important to note that the intensity distribution in the far zone and at the virtual source are related by the laws of field propagation in free-space. One may fit the intensity at the virtual source with a Gaussian, but in this case, the real intensity in the far-zone does not match the propagated Gaussian beam. Or vice versa, one may fit the intensity in the far zone with the Gaussian, but in this case, the intensity at the virtual source does not match the backpropagated Gaussian beam.

In other words, there is some freedom in applying the Gaussian approximation. As it was discussed in section 4.4, different methods of approximation can be found in the literature (see, for example, [71], [72], [73]).

5.4.2 Cross - spectral density, spectral degree of coherence and brightness

Cross-spectral density function for the source amplitude distribution in the far field $\hat{E}(\hat{\boldsymbol{\theta}})$ in normalized units accoding to Eq. (3.68), may be written in the following way

$$\hat{G}(\hat{\boldsymbol{\theta}},\Delta\hat{\boldsymbol{\theta}}) = \left\langle \hat{E}(\hat{\boldsymbol{\theta}}+\Delta\hat{\boldsymbol{\theta}}/2)\hat{E}^{*}(\hat{\boldsymbol{\theta}}-\Delta\hat{\boldsymbol{\theta}}/2)\right\rangle, \tag{5.29}$$

where $\hat{\boldsymbol{\theta}}$ is the vector position at which a two-slits system is introduced to probe coherence, and $\Delta\hat{\boldsymbol{\theta}}$ is the vector describing the separation between the two slits, see Eq. (5.25).

Accordingly, spectral degree of coherence (Eq. (3.69)) for the source amplitude distribution in the far field is defined as

$$\hat{g}(\hat{\boldsymbol{\theta}},\Delta\hat{\boldsymbol{\theta}}) = \frac{\hat{G}(\hat{\boldsymbol{\theta}},\Delta\hat{\boldsymbol{\theta}})}{\left[\hat{G}(\hat{\boldsymbol{\theta}}+\Delta\hat{\boldsymbol{\theta}}/2)\hat{G}(\hat{\boldsymbol{\theta}}-\Delta\hat{\boldsymbol{\theta}}/2)\right]^{1/2}}, \tag{5.30}$$

and the fringe visibility in Eq. (3.70) is given by

$$\hat{V} = \frac{2\hat{G}(\hat{\boldsymbol{\theta}},\Delta\hat{\boldsymbol{\theta}})}{\hat{G}(\hat{\boldsymbol{\theta}}+\Delta\hat{\boldsymbol{\theta}}/2,0)\hat{G}+(\hat{\boldsymbol{\theta}}-\Delta\hat{\boldsymbol{\theta}}/2,0)}, \tag{5.31}$$

The Wigner distribution function in Eq. (3.101) in terms of the CSD in the far-zone in normalized units at the source position is defined as

$$\hat{\mathfrak{W}}(\hat{\mathfrak{r}},\hat{\boldsymbol{\theta}}) = \int d^{2}(\Delta\hat{\theta})exp(i\hat{\mathfrak{r}}\cdot\Delta\hat{\boldsymbol{\theta}})\hat{G}(\hat{\boldsymbol{\theta}},\Delta\hat{\boldsymbol{\theta}}). \tag{5.32}$$

According to Eq. (4.49), the brightness of the filament electron beam with current I is proportional to the maximum of the Wigner distribution

$$B = C\ max(\hat{\mathfrak{W}}). \tag{5.33}$$

Following the work [81], the corresponding result for brightness in dimensional units is found to be linked to equation (5.32) by the constant [90]

$$C = \frac{z^{2}\mathcal{I}K^{2}\omega^{3}\alpha A_{jj}^{2}}{64\pi^{4}ec^{3}\gamma^{2}Lu}, \tag{5.34}$$

with $\alpha = e^{2}/(\hbar c)$ being the fine structure constant, A_{jj}-coupling parameter, and z is the coordinate along the propagation distance.

Substitution of Eq. (5.27) into equation (5.29) gives the following explicit expression for the cross-spectral density in the case of undulator radiation around the fundamental harmonic [90]

$$\begin{aligned}\hat{G}(\hat{\boldsymbol{\theta}},\Delta\hat{\boldsymbol{\theta}}) = {} & \frac{1}{(2\pi)^{3/2}\left(D_{x}D_{y}\Delta_{E}\right)^{1/2}\hat{z}^{2}}exp(-i\hat{z}\hat{\boldsymbol{\theta}}\cdot\Delta\hat{\boldsymbol{\theta}})exp\left(-\frac{N_{x}\Delta\hat{\theta}_{x}^{2}}{2}\right)exp\left(-\frac{N_{y}\Delta\hat{\theta}_{y}^{2}}{2}\right)\\ & \times\int_{-\infty}^{\infty}d\hat{\eta}_{x}\int_{-\infty}^{\infty}d\hat{\eta}_{y}\int_{-\infty}^{\infty}d\hat{\xi}_{E}exp\left(-\frac{\hat{\eta}_{x}^{2}}{2D_{x}}\right)exp\left(-\frac{\hat{\eta}_{y}^{2}}{2D_{y}}\right)exp\left(-\frac{\hat{\xi}_{E}^{2}}{2\Delta_{E}}\right)\\ & \times sinc\left(\frac{\hat{\xi}_{E}}{2}+\frac{|\hat{\boldsymbol{\theta}}-\hat{\boldsymbol{\eta}}+\Delta\hat{\boldsymbol{\theta}}/2|^{2}}{4}\right)sinc\left(\frac{\hat{\xi}_{E}}{2}+\frac{|\hat{\boldsymbol{\theta}}-\hat{\boldsymbol{\eta}}+\Delta\hat{\boldsymbol{\theta}}/2|^{2}}{4}\right)\end{aligned} \tag{5.35}$$

Then, for a Gaussian distribution of energy spread, divergence and size of the electron

beam, the maximum of the Wigner distribution must be at $\hat{r} = 0$ and $\hat{\theta} = 0$, and therefore

$$B = C\hat{\mathfrak{W}}(0,0) = C\int d^2(\Delta\hat{\theta})\hat{G}(0,\Delta\hat{\boldsymbol{\theta}}) \tag{5.36}$$

5.4.3 Effect of the energy spread on brightness

In order to investigate the effect of the energy spread on brightness, first, the simplest case of a beam with vanishing electron emittance was considered. Equation (5.35) simplifies accordingly, and substitution into equation (5.36) gives the following expression for the brightness [90]

$$\begin{aligned} B = \frac{\sqrt{2\pi}C}{\sqrt{\Delta_E}\hat{z}^2}\int_0^\infty d(\Delta\hat{\theta})\Delta\hat{\theta}\int_{-\infty}^\infty d\hat{\xi}_E exp\left(-\frac{\hat{\xi}_E}{2\Delta_E}\right) \\ \times sinc^2\left[\frac{\hat{\xi}_E}{2}+\frac{(\Delta\hat{\theta}/2)^2}{4}\right], \end{aligned} \tag{5.37}$$

where azimuthal symmetry of $\hat{\mathbf{G}}(0,\Delta\hat{\boldsymbol{\theta}}))$ is assumed. The Eq. (5.37) can be rewritten by taking integral over $\Delta\hat{\theta}$

$$B = \frac{\sqrt{2\pi}C}{\sqrt{\Delta_E}\hat{z}^2}\int_{-\infty}^\infty d\hat{\xi}_E exp\left(-\frac{\hat{\xi}_E}{2\Delta_E}\right)F(\hat{\xi}_E), \tag{5.38}$$

where

$$\begin{aligned} F(\hat{\xi}_E) &= \int_0^\infty d(\Delta\hat{\theta})\Delta\hat{\theta}sinc^2\left[\frac{\hat{\xi}_E}{2}+\frac{(\Delta\hat{\theta}/2)^2}{4}\right] \\ &= \frac{4}{\hat{\xi}_E}\left[2+\pi\hat{\xi}_E-2cos(\hat{\xi}_E)-2\hat{\xi}_E Si(\hat{\xi}_E)\right], \end{aligned} \tag{5.39}$$

with $Si(\hat{\xi}_E) = \int_0^{\hat{\xi}_E} dt\ sinc(t)$ being the sine integral function.

By definition, the function $F(\hat{\xi}_E)$ is proportional to the angle-integrated spectral flux from a single electron (compare Eq. (4.42)), and therefore the brightness is proportional to the single-electron angle-integrated spectral flux, averaged over the energy spread distribution.

Also, it is possible to conclude that for zero emittance and symmetric energy spread distribution, there should be no effect of the energy spread on the brightness [90]

$$B = \frac{\mathcal{I}K^2\omega^3\alpha A_{jj}^2 L_u}{8\pi^2 ec^3\gamma^2} \tag{5.40}$$

For the verification of statements above, a simulation was done with the parameters similar by the type to PETRA IV project. The parameters used in the simulation are presented in Table 5.5. The electron emittance was put to zero, and two single-electron cases with resonant energies at 580 eV and 4000 eV were considered. The results are shown in Fig. 5.10. Should be noted that function $F(\hat{\xi}_E)$ is roughly anti-symmetrical with respect to the point $\hat{\xi}_E = 0$. The latter indicates that for zero emittance and symmetric energy spread distribution, the energy spread has no effect on the brightness, in agreement with the analysis of Eqs. (5.37) and (5.39).

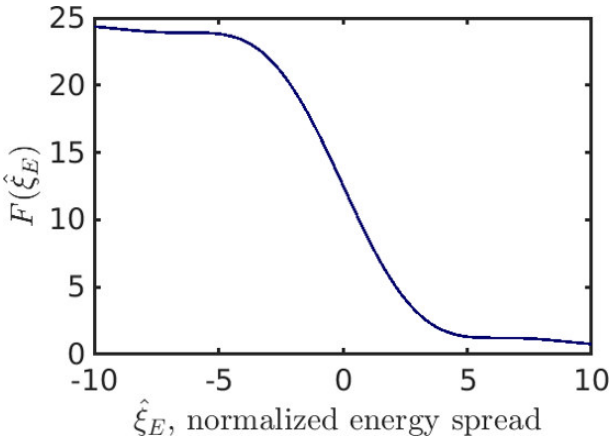

Figure 5.10: Function $F(\hat{\xi}_E)$, calculated for parameters specified in the Table 5.5.

It is also interesting to compare the result in Eq. (5.40) with that from the work of [73], where an approximated formula for the brightness was proposed. The formula was derived from Eq. (4.52), which is the usual expression for the brightness based on Gaussian approximation but includes the impact of a modified spatial and angular profile of the undulator radiation in the presence of electron energy detuning Eq. (4.54). This formula, rewritten in the normalized units, is

$$B_a = \frac{B}{\left[\frac{D}{\pi} + Q_a^2\left(\frac{\sqrt{\Delta_E}}{2}\right)\right]\left[4\pi N + 4Q_A^{4/3}\left(\frac{\sqrt{\Delta_E}}{8}\right)\right]}, \tag{5.41}$$

where $N \equiv N_x = N_y$, $D \equiv D_x = D_y$, and $Q_a(x)$ defined in Eq.(4.55). Subscript 'a' in Eq. (5.41) stands for 'Approximated'.

A comparison of the brightness as a function of the energy spread for zero electron emittance at the two different resonance photon energies of 580 eV and 4000 eV is shown in Fig. 5.11. The main parameters used in the calculation are summarized in Table 5.6. In order to give a dimensional idea of the parameters under investigation, their values were converted and summarized in Table 5.6 as well.

From Fig. 5.11 it is seen that there is a factor of four difference between Eq. (5.41) and Eq. (5.40) in the limit for zero emittance and energy spread. In the frame of [73] approach, this seems to be explained as due to the fact that while the Gaussian approximation was used to determine the angular divergence and source size, the spatial profile was derived by the spatial Fourier transform of the angular distribution of the complex amplitude, leading to a factor of two in the source size. This procedure should not lead to any difference in the brightness in the case of zero emittance and energy spread because the limit is set by Eq. (4.48)

From this, one may conclude that, while Eq. (5.41) may constitute a good approximation in some regions of the parameter space when it comes to the limit for a diffraction-limited beam with non-negligible energy spread, a more detailed study is needed.

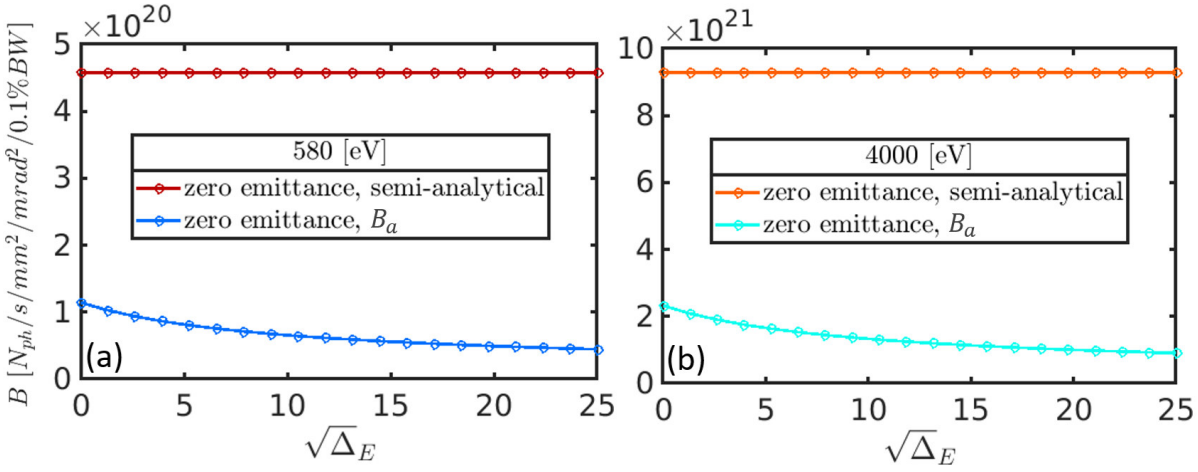

Figure 5.11: A comparison of the brightness as a function of the energy spread for zero electron emittance at two different resonant photon energies (580 eV and 4000 eV) and using different methods: semi-analytical approach and Eqs. (5.41)

5.4.4 Effect of the energy spread on coherence

It is interesting to discuss the possible effects of the energy spread on the coherence properties of undulator radiation. The case for zero emittance will be considered first.

It is seen from Eq. (5.27), that the phase of the field only depends on the electron offset and is fully independent of $\hat{\xi}_E$, i.e., of γ. However, it should be noted that the magnitude and, most importantly, the sign of the field depend on $\hat{\xi}_E$. Below the impact of this sign on the spectral degree of coherence will be shown. A simplified expression in the case of zero emittance for the SDC function according to Eq. (5.29) and Eq. (5.30) can be written as [90]

$$\hat{g}(\hat{\theta},\Delta\hat{\theta}) = \hat{G}(\hat{\theta},\Delta\hat{\theta})exp(-i\hat{z}\hat{\theta}\Delta\hat{\theta}) = exp(-i\hat{z}\hat{\theta}\Delta\hat{\theta})\int_{-\infty}^{\infty} d\hat{\xi}_E\, sinc\left[\frac{\hat{\xi}_E}{2}+\frac{(\hat{\theta}+\Delta\hat{\theta}/2)^2}{4}\right]\times$$
$$sinc\left[\frac{\hat{\xi}_E}{2}+\frac{(\hat{\theta}-\Delta\hat{\theta}/2)^2}{4}\right]exp\left(-\frac{\hat{\xi}_E^2}{2\Delta_E}\right)\Big/\left(\left\{\int_{-\infty}^{\infty} d\hat{\xi}_E\, sinc^2\left[\frac{\hat{\xi}_E}{2}+\frac{(\hat{\theta}+\Delta\hat{\theta}/2)^2}{4}\right]\right. \quad (5.42)$$
$$\left.\times exp\left(-\frac{\hat{\xi}_E^2}{2\Delta_E}\right)\right\}^{1/2}\times\left\{\int_{-\infty}^{\infty} d\hat{\xi}_E\, sinc^2\left[\frac{\hat{\xi}_E}{2}+\frac{(\hat{\theta}-\Delta\hat{\theta}/2)^2}{4}\right]\times exp\left(-\frac{\hat{\xi}_E^2}{2\Delta_E}\right)\right\}^{1/2}\Bigg)$$

This equation is written on the basis of Eq. (5.30), where the limit for zero emittance was taken, and it is assumed, for simplicity, that the two vectors $\hat{\boldsymbol{\theta}}$ and $\Delta\hat{\boldsymbol{\theta}}$ are directed along the same direction. This simplification does not spoil the model but makes it easier to consider. Further on, since the phase of the field in Eq. (5.27) only depends on the electron offset, it is possible to factorize $\hat{g}(\hat{\theta},\Delta\hat{\theta})$ in the product of $\hat{G}(\hat{\theta},\Delta\hat{\theta})$ and of the phase factor $exp(-i\hat{z}\hat{\theta}\Delta\hat{\theta})$.

It is seen from Eq. (5.42) that, when $\sigma_{\Delta\gamma/\gamma}\to 0$, $G(\hat{\theta},\Delta\hat{\theta})$ is different from unity, but $|g(\hat{\theta},\Delta\hat{\theta})| = |G(\hat{\theta},\Delta\hat{\theta})| \to 1$ everywhere. Moreover, on-axis, i.e., for $\hat{\theta}=0$, one has $g = G = 1$, while off-axis ($\hat{\theta}\neq 0$), one has jumps of G from $+1$ to -1 at all values of $\Delta\hat{\theta}$ where $(\hat{\theta}+\Delta\hat{\theta}/2)^2/4$ and $(\hat{\theta}-\Delta\hat{\theta}/2)^2/4$ differ by an odd multiple of π.

First, the case of non-zero energy spread will be considered. Observing function g on-axis at $\hat{\theta} = 0$, from Eq. (5.42), it is seen that $g(\hat{\theta}, \Delta\hat{\theta}) = G(\hat{\theta}, \Delta\hat{\theta}) = 1$. However, off-axis, an interesting phenomenon takes place. The field from different electrons with different detuning $\hat{\xi}_E$ experiences a change in sign at different values of $\Delta\hat{\theta}$. This means that different electrons generate radiation with different wavefronts, and coherence is therefore decreased. This effect is encoded in the function $G(\hat{\theta}, \Delta\hat{\theta})$, while the phase factor $exp(i\hat{\theta}\Delta\hat{\theta})$ cannot change. This mechanism was not considered before, which is at the basis of any possible coherence deterioration related to energy spread effects. It is important to underline that it is present only off-axis, while energy spread alone cannot influence coherence properties on-axis. In the presence of a finite emittance, one must include the effect of different angles $\hat{\boldsymbol{\eta}}$ in Eq. (5.35). Then, even on-axis, different electrons generate radiation with different wavefronts, and coherence deteriorates.

In order to illustrate these statements and to estimate the importance of the effects of energy spread on coherence, semi-analytical calculations for the case of zero emittance were performed. Different values of $\hat{\theta}$ were fixed, and the cross-spectral density G, the spectral degree of coherence g, and the visibility V were calculated in the far-zone as a functions of $\Delta\hat{\theta}$ for different values of the energy spread.

Fig. 5.12 presents results for $\hat{\theta}$ = 0.5 and $\hat{\theta}$ = 1. The definition of used dimensionless units is given in Eq. (5.25) and converted values in Table 5.6. The normalization factor $(\lambda/L_u)^{1/2}$ is of the order of the angular size of the central cone. Therefore, it does not make too much sense to consider values of $\hat{\theta}$ larger than unity. As one immediately sees from the figures, even at $\hat{\theta}$ = 1, the effects of energy spread on coherence deterioration are very small. This is because the first change in the sign for $G(\hat{\theta}, \Delta\hat{\theta})$ happens at $\Delta\hat{\theta} = 2\pi$ (and the second would be at $\Delta\hat{\theta} = 4\pi$). Since there are fewer particular cases when it is interesting to go at such a distance from the axis, the conclusion is made that the effect of energy spread on the degradation of coherence is usually negligible in the far zone for a filament electron beam. It is also interesting to look at the virtual source in the middle of the undulator. In this case, the previous analysis must be repeated using the quantities defined as before but considering Eq. (5.28) instead of Eq. (5.27).

Fig. 5.13 presents results for $\hat{\mathbf{r}}$ = 0.5 and $\hat{\mathbf{r}}$ = 1. This time, the normalization factor $(\lambda L_u)^{1/2}$ in Eq. (5.25) is of the order of the transverse size of the central cone at the virtual source and, by analogy with the far zone, sufficient area for the analysis is up to values of $\hat{\mathbf{r}}$=1. The same remarks made for the far zone hold for the values of the energy spread parameter. Inspection of Fig. 5.13 shows an important effect of the energy spread on coherence properties at the virtual source position. While there is not a simple expression as equation (5.27) at the virtual source position, the mechanism that leads to coherence degradation is the same: namely, there is a change in the sign of the field (see Fig. 5.9). This happens, however, for smaller values of $\hat{\mathbf{r}}$, which leads to degradation already for small values of $\Delta\hat{\mathbf{r}}$, as seen from Fig. 5.13.

The situation becomes more complicated when the finite emittance effects are introduced. In particular, in this section, the two settings of parameters are considered. First setting is for the source with parameters $N_x = N_y = 0.006$, $D_x = D_y = 0.15$, corresponding to a resonant energy of 580 eV, and second setting is for the source with parameters $N_x = N_y = 0.04$, $D_x = D_y = 1.05$, corresponding to a resonant energy of 4000 eV. The values of $\hat{\theta}$ in the far zone and $\hat{r}$ at the virtual

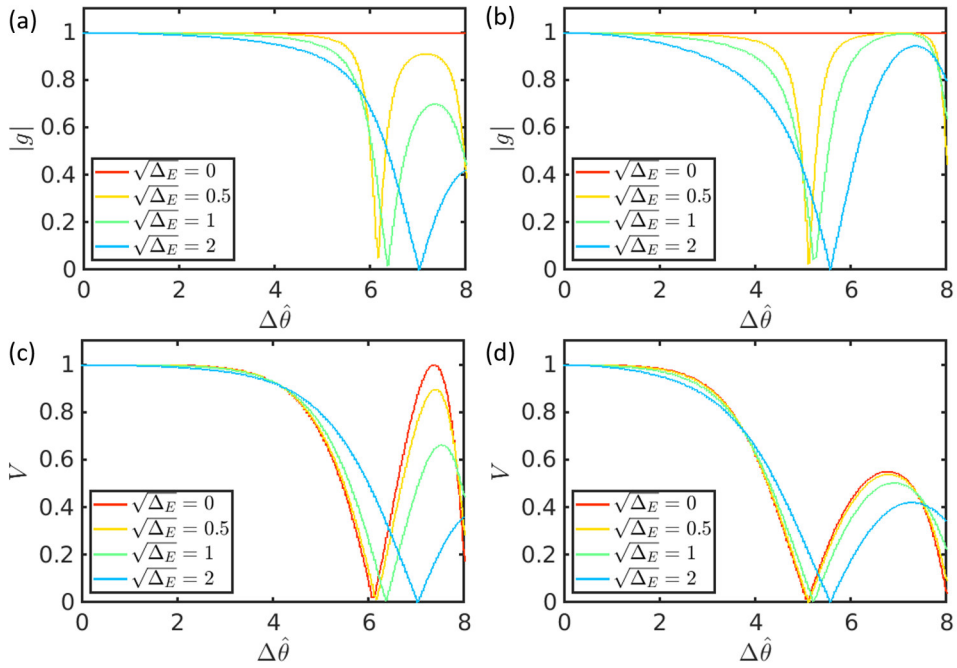

Figure 5.12: Far zone, zero emittance. a) and b) Modulus of the cross-spectral density $|g|$, c) and d) the fringe visibility V as a functions of $\Delta\hat{\theta}$ for different values of the energy spread (see legend). Here in a) and c) shown cut for $\hat{\theta} = 0.5$ and b) and d) for $\hat{\theta} = 1.0$.

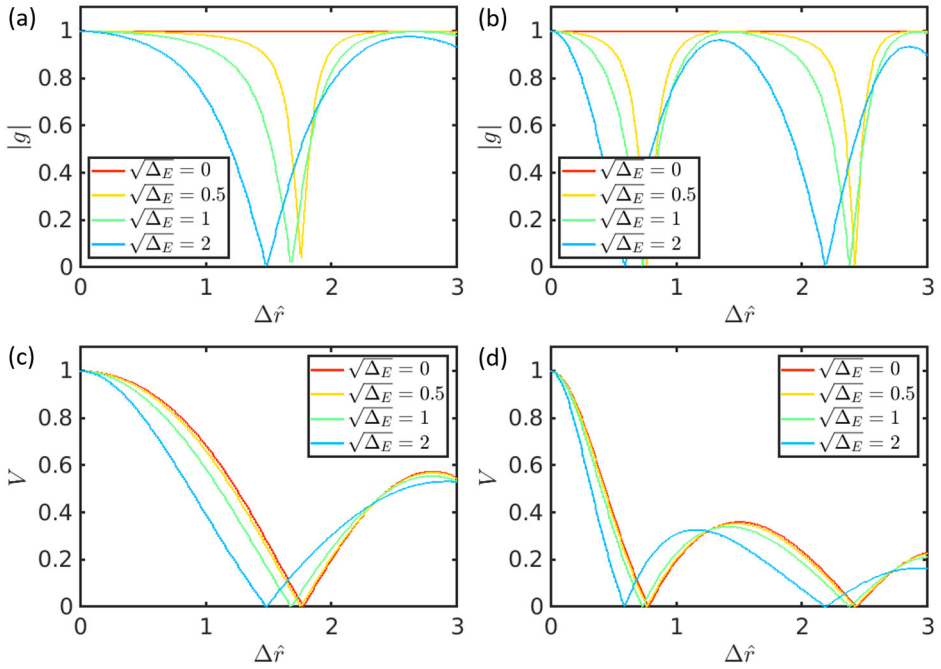

Figure 5.13: Virtual source, zero emittance. a) and b) Modulus of the cross-spectral density $|g|$, c) and d) the fringe visibility V as a functions of $\Delta\hat{r}$ for different values of the energy spread (see legend). Here in a) and c) shown cut for $\hat{r} = 0.5$ and b) and d) for $\hat{r} = 1.0$.

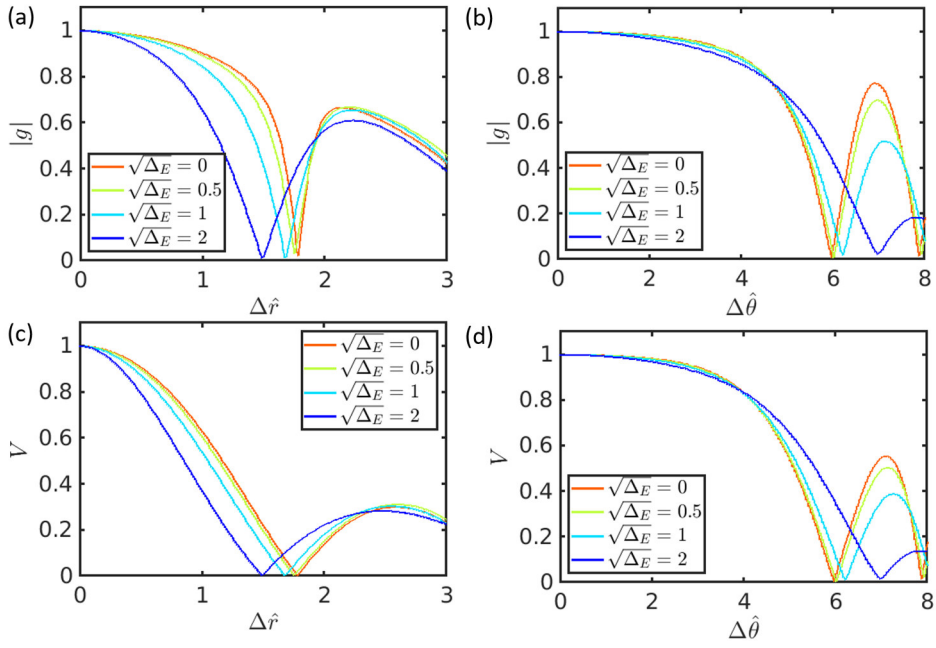

Figure 5.14: Simulations for non-zero emittance case at soft X-ray energy of 580 eV. a) and b) Modulus of the cross-spectral density $|g|$, c) and d) the fringe visibility V as a functions of $\Delta\hat{r}$ and $\Delta\hat{\theta}$ for different values of the energy spread (see legend). Here in a) and c) shown cut for $\hat{r} = 0.5$ and b) and d) for $\hat{\theta} = 0.5$.

source position were setted to $\hat{\theta} = 0.5$ and$\hat{r}$=0. Two functions $|g|$ and V at the virtual source and in the far zone were calculated. Results are shown in Fig. 5.14 and Fig. 5.15. Comparing Fig. 5.13 with Fig. 5.14 and Fig.5.15 one can see how the effects of emittance become more and more important and finally dominate over energy spread effects. One can see coherence degradation already at zero energy spread, both at the virtual source and in the far zone. As is to be expected from the previous discussion, energy spread effects are more visible at the virtual source, while in the far zone, they are much less noticeable but still present.

It should be noticed here that none of the degradation effects on coherence has an impact on the brightness when the electron beam has zero emittance. This fact was also checked by using the expression for CSD $\hat{G}$ to evaluate the brightness according to Eq. (5.36). No deterioration of brightness was found in the case of zero emittance. However, in the case of non-zero emittance, brightness degrades [90].

The fact that the brightness cannot be affected by the energy spread alone, whereas the energy spread alone has an impact on the coherence properties of the radiation, seems amusing. However, it is seen from the fact, that the brightness, according to the definition in Eq. (5.36), is the Wigner distribution on-axis, i.e. at $\hat{\mathbf{r}} = 0$ and $\hat{\theta} = 0$. As one can see from the previous analysis, at $\hat{\mathbf{r}} = 0$ and $\hat{\theta} = 0$ there is no coherence degradation, at any energy spread value. In general, brightness can be spoiled by decreased spectral photon flux, degradation of coherence, or wavefront distortions.

In this section, a mechanism for degradation of coherence off-axis was discussed, while

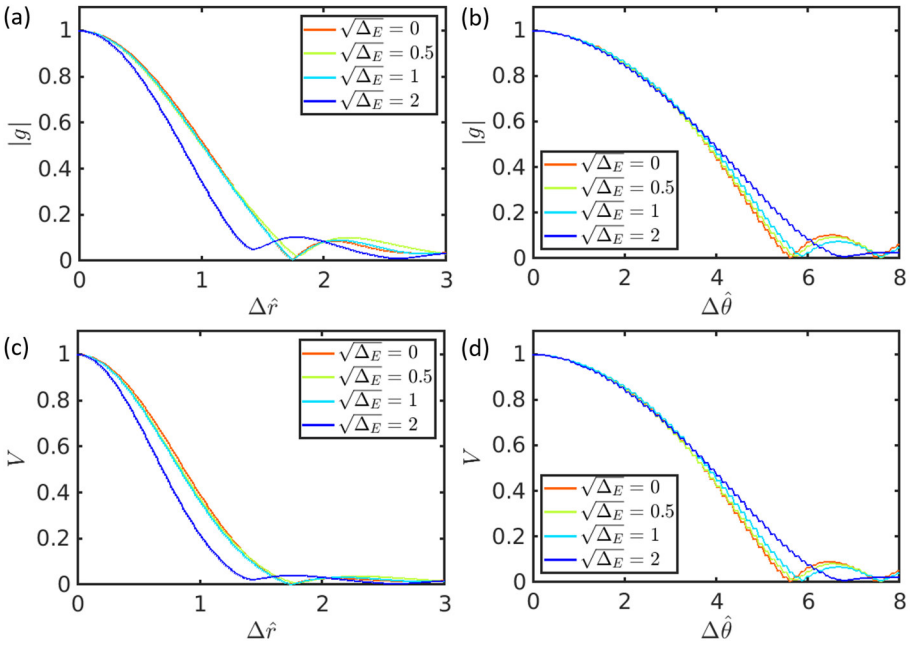

Figure 5.15: Simulations for non-zero emittance case at X-ray energy of 4 keV. a) and b) Modulus of the cross-spectral density $|g|$, c) and d) the fringe visibility V as a functions of $\Delta\hat{r}$ and $\Delta\hat{\theta}$ for different values of the energy spread (see legend). Here in a) and c) shown cut for $\hat{r} = 0.5$ and b) and d) for $\hat{\theta} = 0.5$.

on-axis, it was shown that coherence is preserved. The case of a finite emittance was considered for the coherence and brightness by introducing semi-analytical simulations. The same was done for the enlarged emittance, and its impact on coherence and brightness was studied, showing how it degrades for parameters applicable for diffraction-limited storage rings of the next generation. The spectral degree of coherence is seen to decrease off-axis: this result is in agreement with the conclusion concerning the brightness.

Table 5.7: Storage ring parameters, used in the analysis.

Parameter	Value
Electron energy	6 GeV
Beam current	100 mA
Horizontal and vertical electron beam emittance	10 pm rad
Horizontal and vertical betatron functions, β_x, β_y	2 m
Relative energy spread values	0, $1{\cdot}10^{-3}$, $2{\cdot}10^{-3}$

Table 5.8: Undulator and electron beam parameters, as well as intrinsic characteristics of the photon beam.

Photon energy, keV	0.5	12	24	50
Number of undulator periods, N_u	72	170	170	170
Harmonic number, n	1^{st}	3^{rd}	3^{rd}	5^{th}
Size of single electron radiation σ_r, μm, [Eq. (4.47)]	12.5	2.55	1.79	1.25
Divergence of single electron radiation σ'_r, μrad [Eq. (4.44)]	15.7	3.2	2.3	1.5
Emittance of single electron radiation , pm rad [Eq. (4.46)]	197	8.2	4.1	1.9
Electron beam size [Eq. (4.29)] σ_e, μm	4.47	4.47	4.47	4.47
Electron beam divergence [Eq. (4.29)] σ'_e, μm	2.24	2.24	2.24	2.24
Total photon emittance ε_{ph}, pm rad [Eq. (4.57)]	211	20	15.5	12.5

5.5 Diffraction-limited storage ring. Finite electron beam emittance

5.5.1 Analysis of the photon emittance

In this section, photon beam parameters and coherence of the DLSR source are analyzed for the broad range of electron beam emittance values. Four photon energy values of 500 eV, 12 keV, 24 keV, and 50 keV were considered in the analysis. All simulations in this section were performed according to semi-analytical approach (section 5.3) and backed up with the XRT software [86] (see A.1 for the details).

For an example of the DLSR source, a high-energy storage ring operating at 6 GeV with the parameters close to PETRA IV with an expected electron emittance of 10 pm rad and a new beta β_e function of 2 m is considered. In addition, in order to have a better understanding of the photon properties of the source, a broader range of electron emittance values from 1 pm rad to 300 pm rad is considered. The standard parameters of the DLSR and undulator used for simulations and analysis are given in Table 5.7 and Table 5.8.

The analysis starts from a comparison of natural photon emittance of single-electron radiation with the designed electron emittance of the DLSR $\varepsilon_e = 10$ pm rad. The analysis shows (see Table 5.8) that at the energy of 12 keV, emittance values ε_e and ε_r are comparable, at 500 eV $\varepsilon_e \leq \varepsilon_r$ and at 24 keV as well as at 50 keV $\varepsilon_e > \varepsilon_r$. From this simple estimation, one may expect to reach the diffraction limit at 500 eV and have parameters of radiation close to the diffraction-limited source at 12 keV. It is expected that at higher energies of 24 keV and 50 keV, radiation will be highly coherent but not diffraction-limited.

Table 5.9: Details of XRT simulations and analytical approach. $N_{e,1}$ and $N_{e,2}$ is the number of electrons used in the simulations of photon emittance and simulations of CSD accordingly. The angular mesh, used in the simulation, is given by the number of pixels A_1 for the XRT and semi-analytical simulation of photon emittance, A_2 for the mode decomposition performed by XRT and A_3 for the analytical mode decomposition. D_A is the size of the virtual detector

Photon energy, keV	$N_{e,1}^{XRT}$	$N_{e,1}^{Analyt}$	$N_{e,2}^{XRT}$	$N_{e,2}^{Analyt}$	A_1	A_2	A_3	D_A, mm	Energy spread, 10^{-3}	Fresnel number
0.5	$5{\cdot}10^3$	$5{\cdot}10^3$	$5{\cdot}10^3$	10^5	512	128	256	5.4	0/1/2	0.05/0.05/0.06
12	$5{\cdot}10^3$	10^4	$5{\cdot}10^3$	10^5	512	128	256	2.4	0/1/2	0.09/0.14/0.21
24	$5{\cdot}10^3$	$1.5{\cdot}10^4$	$5{\cdot}10^3$	10^5	512	128	256	1.8	0/1/2	0.13/0.19/0.26
50	$5{\cdot}10^3$	$1.5{\cdot}10^4$	$5{\cdot}10^3$	10^5	512	128	256	1.2	0/1/2	0.19/0.3/0.44

To fully characterize source properties, one needs to know the amplitude and intensity distributions at the source position and in the far-field region, which were calculated within the frame of the semi-analytical approach and simulated utilizing the XRT software. The XRT software calculates an amplitude of the radiation for a single electron from the undulator source at the given photon energy on a given angular mesh (see Table 5.9). The transverse field from each electron gets individual random angular and coordinate offsets within the emittance distribution, assuming Gaussian statistics of the electron bunch. An individual random shift to gamma Lorentz factor within the energy spread is included as well.

Amplitude and intensity calculations in the far-field for all photon energies considered in this section were performed at a distance of 30 m from the undulator source, which corresponds to Fresnel numbers given in Table 5.9. For a defined number of electrons N_e (see Table 5.9), their corresponding amplitudes were stored in the matrix to analyze coherence functions further. The resulting intensity was determined as a sum of intensities of each electron. Angular divergence of the source was determined as the variance value of the intensity distribution at the far-field position (Eq. (5.24)). Transverse positional distribution at the source was obtained by taking the Fourier transform of the angular field distribution in the far-field.

The size of the source was determined as the variance value of the intensity distribution at the source position (Eq. (5.24)). Integration in Eqs. (5.24) was performed over the finite area defined as the detector size D in the far zone or as the size of the source at the source position. In both cases, the area corresponded to 95% of the total recorded intensity at the virtual screen. Total photon emittance was calculated as the product of the source size and source divergence (Eq. 4.57). The error of the performed simulation with the XRT software for each natural electron emittance value was calculated as the standard deviation of the corresponding value.

The photon emittance as a function of the electron beam emittance (from 1 pm rad to 300 pm rad) for different relative energy spread values is presented in Fig. 5.16.

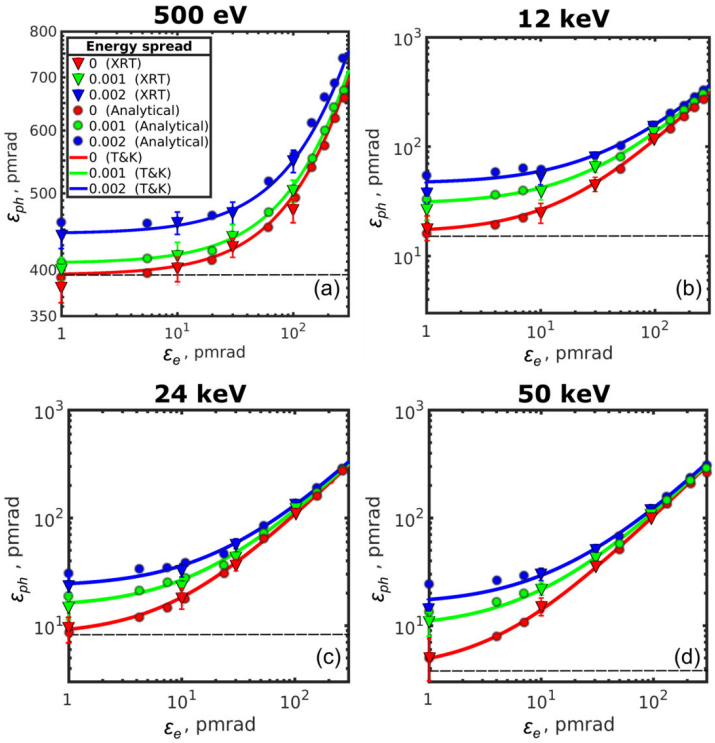

Figure 5.16: Photon emittance ε_{ph} as a function of the electron beam emittance ε_e for the different values of the photon energy and energy spread in one transverse direction. A dashed horizontal line corresponds to the value of the photon emittance of $\lambda/2\pi$.

As a result of these simulations, one may see the lower is electron emittance ε_e, the lower is the photon emittance ε_{ph}. Notably, at 500 eV and 12 keV photon energies and at 10 pm rad electron beam emittance, the photon emittance reaches its asymptotic value (also note different scale for 500 eV photon energy). This is a clear indication that at these energies, the synchrotron source may be considered diffraction-limited.

It is seen that photon emittance increases at larger energy spread values for the same electron emittance. However, the energy spread induced difference does not exceed 12% at 500 eV (10 pm rad), while at higher energy, this difference goes up to 50 %. It can be explained by the fact that at low photon energies, the properties of the beam (source size and divergence) are comparably large, and their small changes caused by the energy spread effect are not noticeable. In contrast, the energy spread effects impact strongly at high energies due to the smaller characteristic sizes of the radiation source. These results were compared with the analytical ones obtained using Eqs. (5.10, 5.11) (circles in Fig. 5.16).

One may see that the results of the analytical approach and simulations performed with the XRT software correspond to each other very well (both for different electron emittance values and for different energy spread values) within the margins of the error bars. Both approaches were also compared with the calculations made according to the approach of Tanaka & Kitamura [73] Eqs. (4.54, 4.55) (shown by lines in Fig. 5.16). It is observed that all three approaches give similar results for three values of energy spread that were considered here.

As can be seen in Fig. 5.16 (see also Table 5.10), the lowest value of the photon emittance

Table 5.10: Photon emittance values determined at different energies and zero electron energy spread using XRT simulations, analytical approach, and Eqs. (4.54, 4.55). Results are presented for the 1 pm rad and 10 pm rad electron emittance values.

Photon energy, keV	0.5	12	24	50
$\varepsilon_{coh} = \lambda/2\pi$, pm rad	395	16.4	8.2	3.9
1 pm rad electron emittance				
ε_{ph}^{XRT}, pm rad	380	20	10	5
$\varepsilon_{ph}^{Analyt}$, pm rad	391	16.3	8.9	5
$\varepsilon_{ph}^{T\&K}$, pm rad	396	17.5	9.3	5
10 pm rad electron emittance				
ε_{ph}^{XRT}, pm rad	398	24.6	18.5	15.2
$\varepsilon_{ph}^{Analyt}$, pm rad	402	24.9	17.7	13.8
$\varepsilon_{ph}^{T\&K}$, pm rad	403	26.5	18.3	13.8

for zero energy spread in the simulations is asymptotically reaching the value of $\lambda/2\pi$, when electron emittance vanishes. This is a strong indication that for low-emittance SSRs, X-ray radiation cannot be approximated as Gaussian, because in this case, the lowest photon emittance should reach the value of $\lambda/4\pi$ as suggested in Ref. [78]. At the same time, these results are in concordance with the other results (see, for example, [73, 82]), where non-Gaussian behavior of synchrotron radiation of a single electron was considered.

5.5.2 Coherent fraction. Basic approach

According to a new asymptotic limit for the photon emittance, it is useful to determine a coherent fraction of radiation, similar to Eq. (5.16), at vanishing electron emittance. If one will use conventional expression (5.16) with the emittance values ε_{ph} shown in Fig. 5.16 coherent fraction values would reach an asymptotic value of 0.5 and would never reach unity. Concerning this, the previous expression was slightly redefined to the new one

$$\zeta^{CF} = \frac{F_{coh}}{F} = \frac{\varepsilon_{coh}^2}{\varepsilon_{ph}^x \varepsilon_{ph}^x} \tag{5.43}$$

where ε_{coh}=$\lambda/2\pi$ and ε_{ph} are photon emittance values obtained through different simulations.

The results of simulations in one transverse direction are presented in Fig. 5.17. First, coherent fraction from the XRT simulations (triangles) was determined by using expression (5.43) and the results of emittance simulations shown in Fig. 5.16. Then these results were compared to the analytical calculation. Expression (5.10) was used to calculate the wave field amplitudes in the far-field region. Eqs. (5.24) were applied to determine the source parameters. Using the same expression (5.43) analytical values of coherent fraction (circles) were obtained (see Fig. 5.17) Finally, the expressions (4.54) and (4.55) were used in equation (5.43) (lines) with the help of Eq. (4.57).

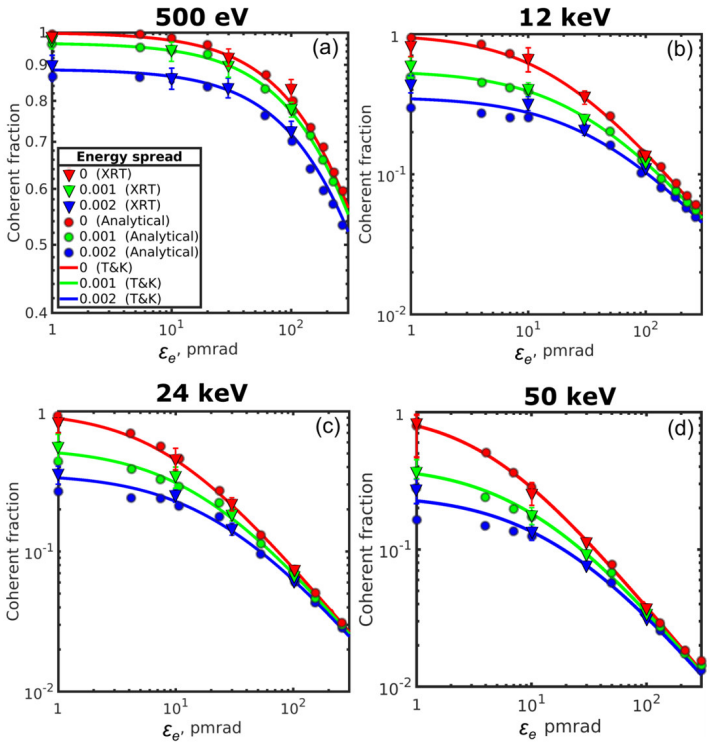

Figure 5.17: Coherent fraction of radiation ζ^{CF} as a function of the electron beam emittance ε_e for the different values of the photon energy and energy spread in one transverse direction calculated according to Eq. (5.43).

It is seen from the figure 5.17 that all three results excellently agree with each other and show the same trend that was observed for emittance. It is important to note that in order to obtain this result, the use of expression (5.43) is necessary instead of commonly exploited Eq. (5.16). A more general definition of coherent fraction through coherent mode decomposition will be discussed in the next section.

5.5.3 Coherent mode representation

As it was discussed in the section 3.3, the four-dimensional CSD function may be decomposed to a sum of two-dimensional coherent modes as given in Eq. (3.71). The XRT software is also providing an opportunity to directly analyze these modes (see A.2).

The mode decomposition of the CSD was performed according to Eqs. (3.71), (3.72), (3.73). The analysis was performed for the studied case of electron beam emittance of 10 pm rad. The mode decomposition was used to determine the shape and contribution of each mode at different photon energies and different values of the relative energy spread.

The first four modes and their normalized weights are shown in Fig. 5.18. An orthogonal set of modes determined by the simulations represents a mixture of Laguerre-Gaussian-type and Hermite-Gaussian-type modes [92] for the whole range of energy spread values from 0 to $2 \cdot 10^{-3}$. These two different sets of modes have different symmetries. Hermite-Gaussian modes may be represented as a product of two separable amplitude functions in the transverse

plane. In contrast, Laguerre-Gaussian modes possess cylindrical modes symmetry and do not allow factorization in two orthogonal directions.

It can also be noticed that the contribution of Laguerre-Gaussian modes is increased for both energies with the increase of the energy spread values. It is interesting to note here that the contribution of Laguerre-Gaussian modes is coming solely from the energy spread effect. It can be shown that if electron offset parameters (entering angle η and axis offset l) are put to zero, then all modes of radiation field may be represented by Laguerre-Gaussian modes (see section 5.6, Fig. 5.28). Therefore, it means that in general, for the diffraction-limited source, it is not possible to factorize CSD function in two orthogonal transverse directions and define the degree of coherence as a product of its values in each direction (see Eq. (3.80)).

The first four coherent modes and their normalized weights for high photon energies of 24 keV and 50 keV for different energy spread values are shown in Fig. 5.19. The behavior of these modes is similar to the ones observed at 500 eV and 12 keV cases (see Fig. 5.18).

The number of modes that contribute dominantly to CSD (Eq. (3.71)) and their spectral densities (Eq. (3.73)) were calculated as well. The weights of different modes normalized to zero mode β_j/β_0 were analyzed, introducing a threshold value of 1%. The values of these mode weights are presented in Fig. 5.20 as a function of the mode number for all photon energies and energy spread values considered in this work. As seen from this figure for 500 eV photon energy and zero energy spread, only three modes contribute significantly. With the increase of the energy spread number of contributing modes increased to only four.

However, for 12 keV photon energy, the number of modes with a contribution higher than 1% is about ten. It is rising with the increased energy spread values reaching 42 modes at $2 \cdot 10^{-3}$ relative energy spread value. The number of modes that contribute dominantly to CSD and spectral density with a threshold of 1% is 19 for 24 keV and 35 for 50 keV in zero relative energy spread case. With the increase of energy spread to the value of $2 \cdot 10^{-3}$, the number of modes contributing dominantly to CSD also increasing to 54 at 24keV and to 90 at 50 keV, which is significantly larger than in the previous case of lower photon energies.

As soon as mode weights were determined, the global degree of coherence was calculated for the considered photon energies and energy spread values according to Eq. (3.74) (see Table 5.11). The global degree of coherence value varies from 90% to 11% for photon energies from 500 eV to 50 keV, respectively. It drops down by 18% - 73% with the increase of energy spread from zero to $2 \cdot 10^{-3}$ for the same range of photon energies.

5.5.4 Coherent fraction. Framework of statistical optics

As soon as the modes are normalized by the sum of all modes $\sum_{j=0}^{\infty} \beta_j(\omega)$, the weight of the first mode naturally gives the coherent fraction of radiation (see Eq. (3.75)). The values of the coherent fraction are presented in Fig. 5.21 for all photon energies considered in this section (shown by triangles) as a function of electron beam emittance for different values of energy spread. It is seen from this figure (see also Table 5.11) that at 10 pm rad one gets very high coherence values about 95% at 500 eV and 55% at 12 keV at zero energy spread. With

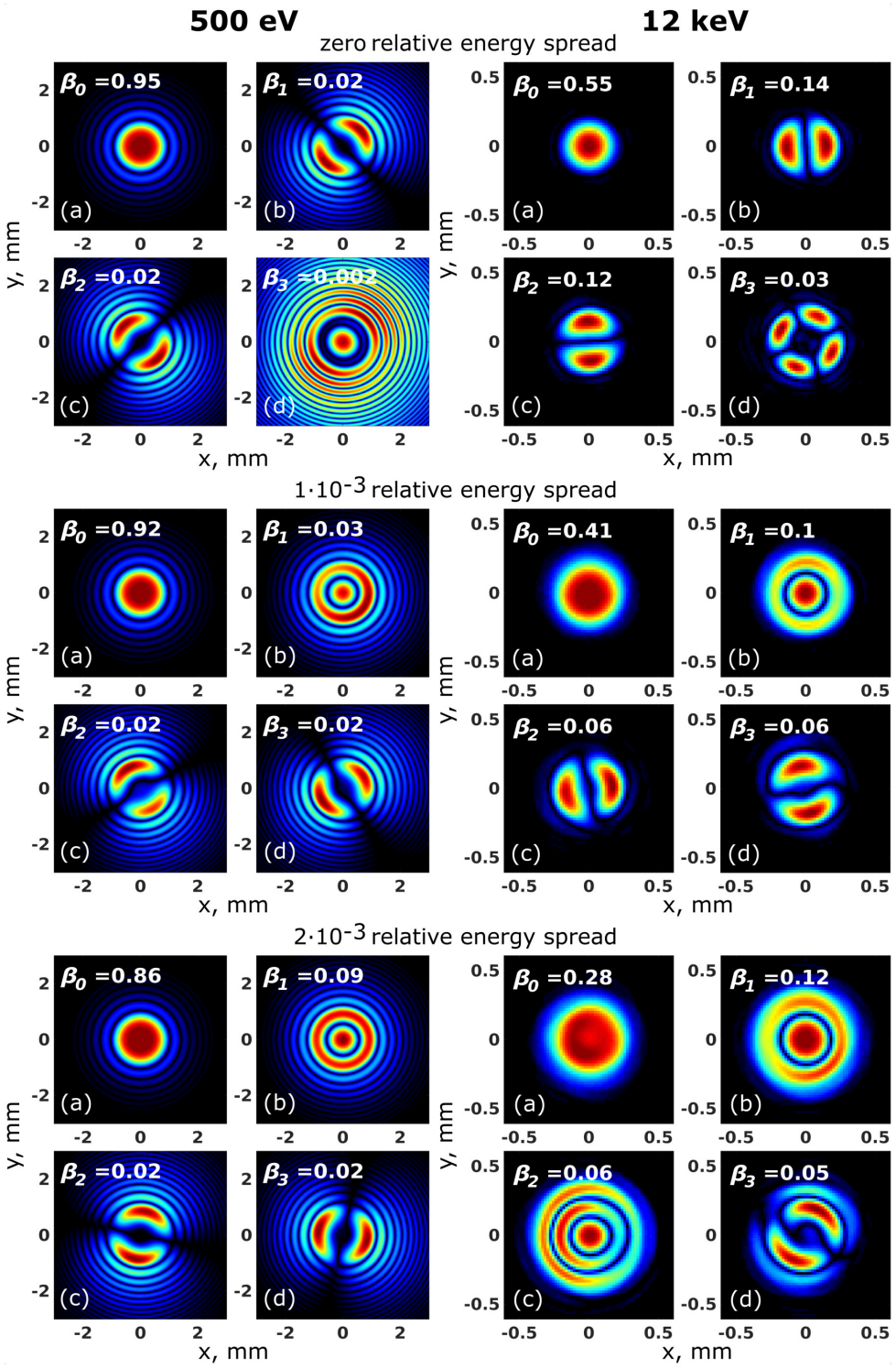

Figure 5.18: First four modes and their normalized weights β_j obtained from the coherent mode decomposition of the CSD at 500 eV (left column) and 12 keV (right column) photon energy for three different relative energy spread values obtained by XRT simulations.

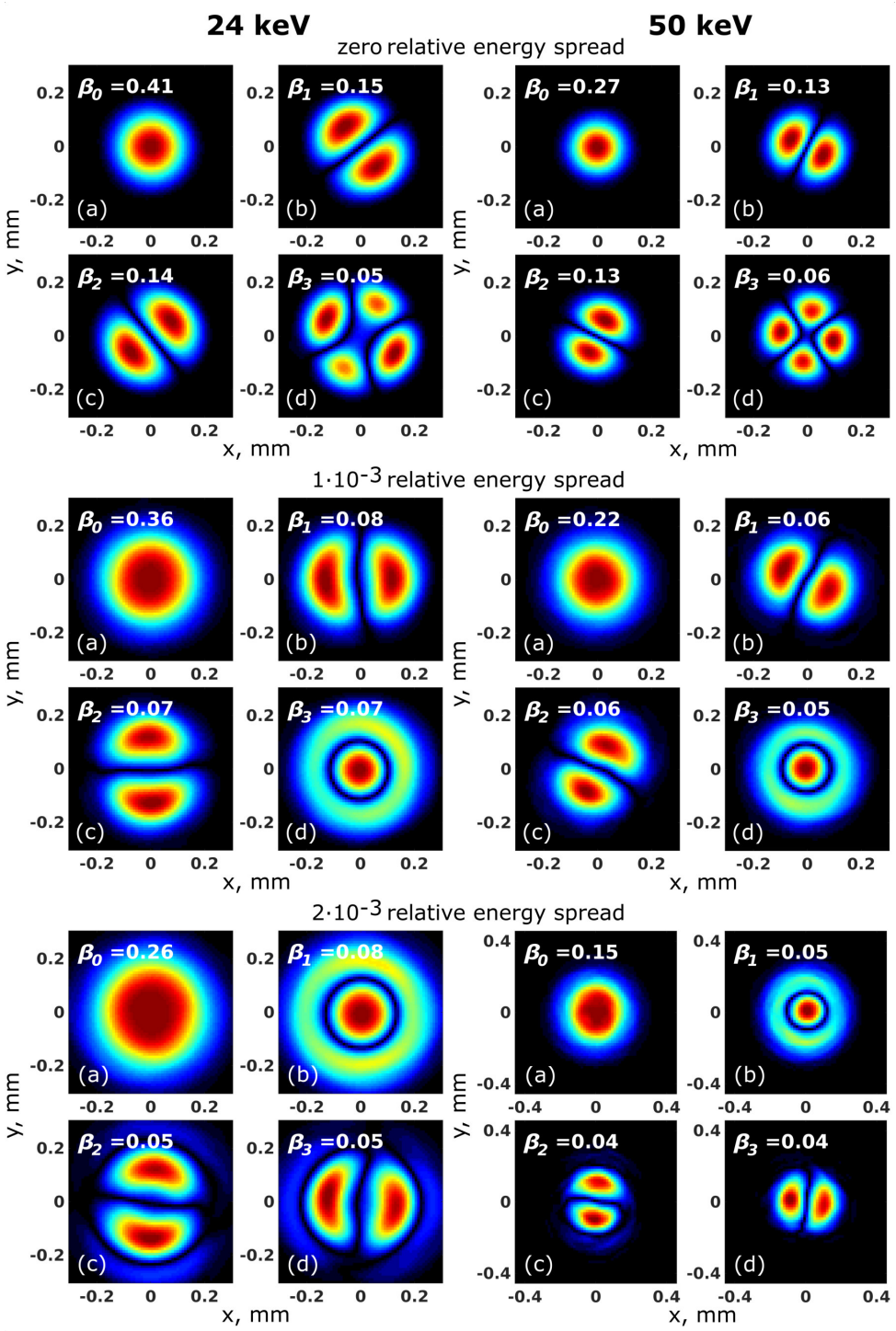

Figure 5.19: First four modes and their normalized weights β_j obtained from the coherent mode decomposition of the CSD at 24 keV (left column) and 50 keV (right column) photon energy for three different relative energy spread values obtained by XRT simulations.

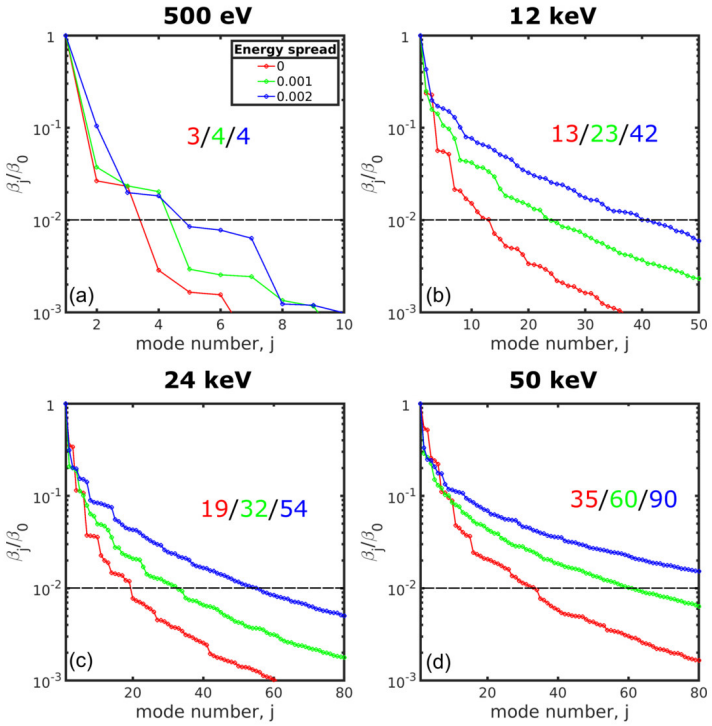

Figure 5.20: Weights of different modes normalized to the weight of a zero-mode β_j/β_0 as a function of the mode number j. Horizontal dashed line corresponds to the value of 1%. Points are connected by lines for better visibility. Number of modes exceeding 1% threshold is given in each panel.

the increase of the energy spread, these values become slightly lower 91% and 41% at $1 \cdot 10^{-3}$ spread and significantly lower at the energy spread values of $2 \cdot 10^{-3}$ (85% and 28%). At higher photon energies, the coherent fraction of the radiation drops from 40% to 26% at 24 keV and from 26% to 15% at 50 keV, while energy spread increases from zero to $2 \cdot 10^{-3}$.

Results of XRT simulations were compared with calculations of coherent fraction in the frame of the analytical approach (shown by circles in Fig. 5.21). Semi-analytical simulations were performed by taking field amplitudes at the source and in the far-field region according to Eqs. (5.10, 5.11). From Fig. 5.21 it is seen that the results of the analytical approach fit well to the results of XRT simulations for all energies and energy spread values considered in this work.

5.5.5 Transverse Cross-spectral density function

Finally, the results obtained in the previous sections were compared with the results of simulations of correlation functions in the single transverse dimension. Coherent-mode representation of correlation functions, being very general, provides an excellent theoretical insight into the problem. At the same time, the shape of the coherent modes is not easy to determine experimentally. Since the cross-spectral density $W(\mathbf{r_1}, \mathbf{r_2})$ is a 4D function, its determination from the experimental data is challenging. In most of the experiments (as Young's double pinhole experiment) correlation functions are determined in each transverse direction separately

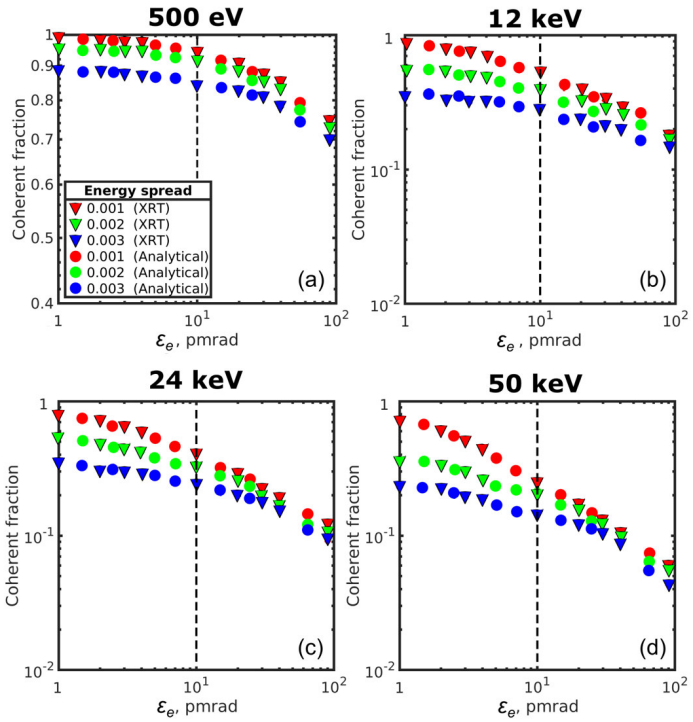

Figure 5.21: Coherent fraction of radiation ζ^{CF} as a function of the electron beam emittance ε_e for the different values of the photon energy and energy spread in one transverse direction. Calculations performed according to Eq. (3.75). A dashed vertical line corresponds to the value of the electron emittance of 10 pm rad. Note the different scale for 500 eV coherent fraction value.

Table 5.11: Degree of coherence (Eq. (3.74)) and coherent fraction (Eq. (3.75)) determined from coherent mode decomposition using XRT software and analytical approach of Eq. (5.10). All simulations are performed at the electron beam emittance value of 10 pm rad for different photon energies and energy spread values.

Photon energy, keV	0.5	12	24	50
Zero energy spread				
Degree of coherence ζ^{DC}_{XRT}	0.90	0.34	0.20	0.11
Coherent fraction ζ^{CF}_{XRT}	0.95	0.55	0.40	0.26
Coherent fraction ζ^{CF}_{Analyt}	0.95	0.56	0.41	0.26
$1 \cdot 10^{-3}$ energy spread				
Degree of coherence ζ^{DC}_{XRT}	0.84	0.20	0.13	0.06
Coherent fraction ζ^{CF}_{XRT}	0.91	0.41	0.35	0.22
Coherent fraction ζ^{CF}_{Analyt}	0.93	0.37	0.3	0.17
$2 \cdot 10^{-3}$ energy spread				
Degree of coherence ζ^{DC}_{XRT}	0.74	0.11	0.07	0.03
Coherent fraction ζ^{CF}_{XRT}	0.85	0.28	0.26	0.15
Coherent fraction ζ^{CF}_{Analyt}	0.89	0.26	0.21	0.12

(see, for example, [64, 89]). Next, it is assumed that the CSD of the whole field may be represented as a product of its orthogonal directions (see Eq. 3.79). This problem was analyzed for the case of the DLSR source.

Simulations of the correlation functions in one transverse direction were performed in the far-field region at a 30 m distance from the source. To determine these functions, the XRT software and analytical expression of the wave field from a single electron in the far-field region (see Eq. (5.10)) were used. The results of these simulations for two photon energies of 500 eV and 12 keV are presented in Table 5.12 and Fig. 5.22 (results of the analytical approach for the same energies are shown in the A.4). The intensity distribution $I(x)$ (Fig. 5.22 (a,b)), the absolute value of the CSD in the horizontal direction $|W(x_1, x_2)|$ (Fig. 5.22 (c,d)), the absolute value of the SDC $|\mu(x_1, x_2)|$ (Fig. 5.22 (e,f)), and the absolute value of the spectral degree of coherence as a function of spatial separation of two points $|\mu(\Delta x)|$ (Fig. 5.22 (g,h)) for both energies are presented in Fig. 5.22. It is well seen from this figure that the functional dependence of these parameters is non-Gaussian for the 500 eV photon energy. But already at 12 keV, these parameters can be successfully described by Gaussian functions (the same is valid for higher energies).

As a general rule, the more modes contribute to the CSD, the more this dependence resembles Gaussian. The rms values $\sigma_{x,y}$ of the intensity distribution were determined in the far-field region as the variance values of corresponding distributions(see Fig. 5.22 (a,b)). The values of the transverse degree of coherence ζ_x^{DC} (see Fig. 5.22 (c,d)) were calculated according to Eq. (3.63). Anti-diagonal cuts of the spectral degree of coherence function (see Fig. 5.22 (e,f)) were used to determine the coherence length of radiation ξ_x as the variance values of corresponding $|\mu\Delta x|$ distribution. As it is seen from Fig. 5.22 results of simulations performed by the XRT software match extremely well to the ones performed analytically (A.4).

As it is seen from simulations, the CSD function $|W(x_1, x_2)|$ has a rectangular shape (see Fig. 5.22 (c,d)) since the coherence length of the beam is much larger than the beam size at this photon energy. This observation is similar to earlier studies of correlation functions described in the work [93]. Also, in this diffraction-limited case, the SDC shows strong oscillations at the tails of the beam profile since the total photon radiation is defined mostly by characteristics of single-electron radiation. In this diffraction-limited case, a Gaussian approximation is not valid, and more careful analysis is required. Similar to the previous studies, a decrease of the transverse degree of coherence with the increase of energy spread was observed. (see Table 5.12).

A similar analysis was completed for higher photon energies of 24 keV, 50 keV in the frame of the semi-analytical approach and XRT software. The results of the analysis are shown in section A.3 (Fig. A.2 and Fig. A.3) and section A.4 (Fig. A.6 and A.7).

Note, although Gaussian approximation fits nicely for the spectral degree of coherence profile as well as for cross-spectral density at higher energies, the global degree of coherence is not equal to the product of transverse coherence values $\zeta \neq \zeta_x\zeta_y$ (compare Tables 5.11 and 5.12). This observation also highlights that correlation functions for synchrotron radiation close to the diffraction limit cannot be factorized in the two transverse directions.

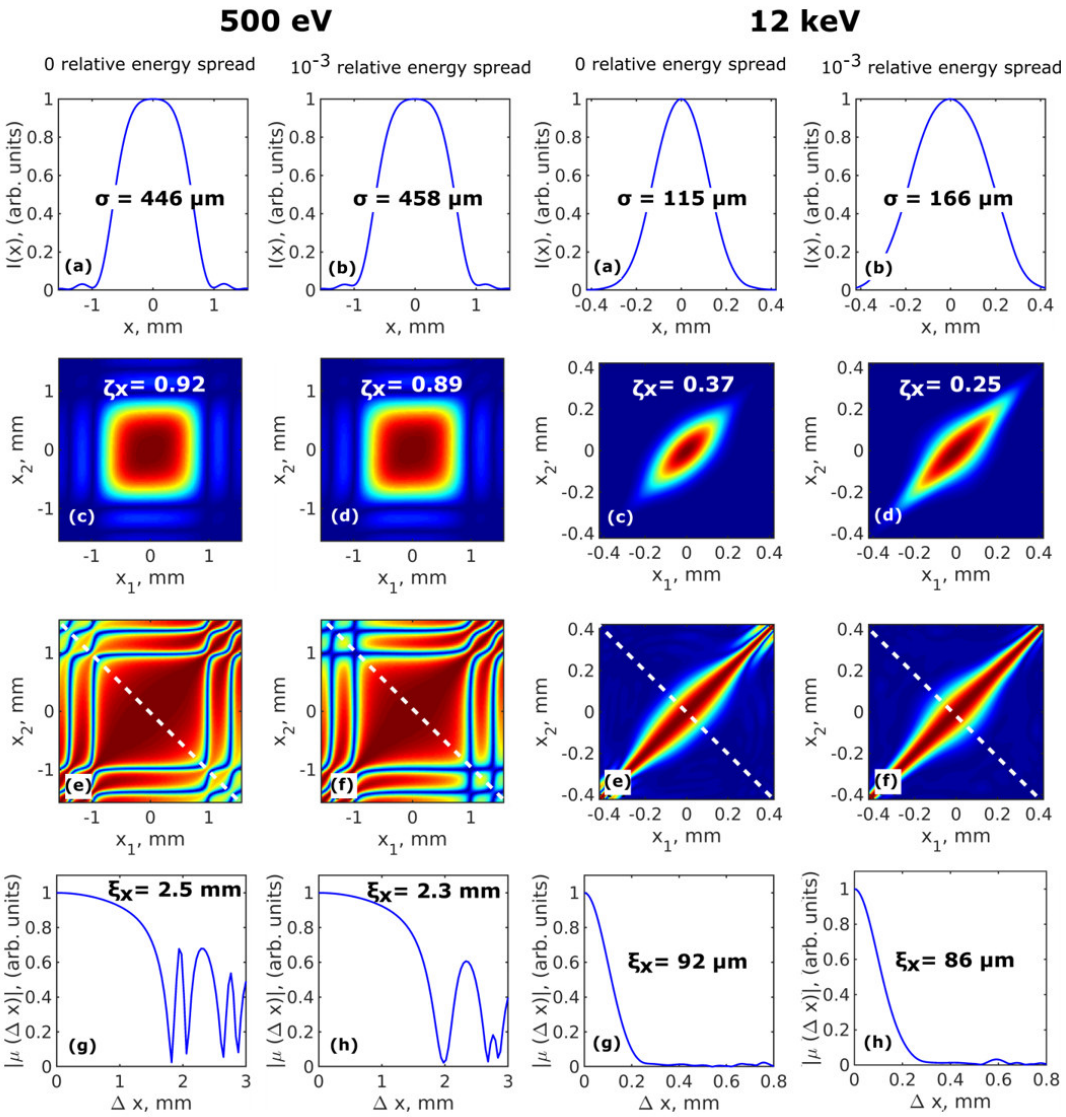

Figure 5.22: Simulations of the correlation functions in horizontal direction performed by the XRT software for 500 eV (left column) and 12 keV (right column) photon energy. Intensity distribution I(x) (a,b), absolute value of the cross-spectral density in the horizontal direction $|W(x_1, x_2)|$ (c,d), absolute value of the SDC $|\mu(x_1, x_2)|$ (e,f), and absolute value of the spectral degree of coherence along the anti-diagonal line (shown in (e,f)) as a function of separation of two points $|\mu(\Delta x)|$ (g,h) simulated in horizontal direction 30 m downstream from the undulator source. In (a,b) σ is the rms value of the beam size, in (c,d) ζ_x is the transverse degree of coherence, in (g,h) ξ_x is the coherence length determined in horizontal direction.

Table 5.12: Degree of coherence in one transverse direction obtained from the XRT simulations at 10 pm rad electron beam emittance compared with the analytical analysis for the different photon energies and relative energy spread values.

Photon energy, keV	0.5	12	24	50
Zero relative energy spread				
Degree of coherence ζ_x^{XRT}	0.92	0.37	0.26	0.15
Degree of coherence ζ_x^{Analyt}	0.92	0.39	0.25	0.15
Degree of coherence ζ_x^{GSM}	0.87	0.39	0.28	0.16
$1 \cdot 10^{-3}$ relative energy spread				
Degree of coherence ζ_x^{XRT}	0.89	0.25	0.17	0.11
Degree of coherence ζ_x^{Analyt}	0.89	0.23	0.17	0.09
Degree of coherence ζ_x^{GSM}	0.85	0.29	0.19	0.11
$2 \cdot 10^{-3}$ relative energy spread				
Degree of coherence ζ_x^{XRT}	0.82	0.17	0.12	0.07
Degree of coherence ζ_x^{Analyt}	0.80	0.15	0.12	0.07
Degree of coherence ζ_x^{GSM}	0.84	0.21	0.14	0.09

5.6 Undulator detuning

The effect of the undulator detuning will be discussed in this section. The detuned energy for the maximum flux defined as [82]

$$\omega' = \omega_n(1 - 1/nN) \tag{5.44}$$

Knowing the amplitude distribution of the detuned undulator source, the coherence properties of the beam can be calculated in the frame of the basic coherence theory. As it was discussed in the section 3.3 the four-dimensional CSD function may be decomposed to a sum of two-dimensional coherent modes as given in Eq. (3.71) in the case of the detuned energy as well. As shown previously, such an approach gives a more accurate estimation of the coherence properties of the source in the diffraction limit since the radiation field cannot be approximated by Gaussian functions. The mode decomposition of the CSD was performed according to Eqs. (3.71). The analysis was done for the studied case of the electron beam emittance of 10 pm rad. The mode decomposition was used to determine the shape and contribution of each mode at different photon energies and at different values of relative energy spread at the resonant and detuned to maximum flux photon energy.

The first four modes and their normalized weights for the detuned energy of 492.3 eV are shown in Fig. 5.23. Similar to the resonance case, an orthogonal set of modes determined by the simulations, for the whole range of energy spread values from 0 to $2 \cdot 10^{-3}$, represents a mixture of Laguerre-Gaussian-type and Hermite-Gaussian type modes [92]. One should note that the modes only look similar to Laguerre-Gaussian and Hermite-Gaussian type of modes, simultaneously being neither one nor the other, but the orthogonal set. For the detuned energy first coherent modes slightly differ from the modes for the resonant energy, forming a more

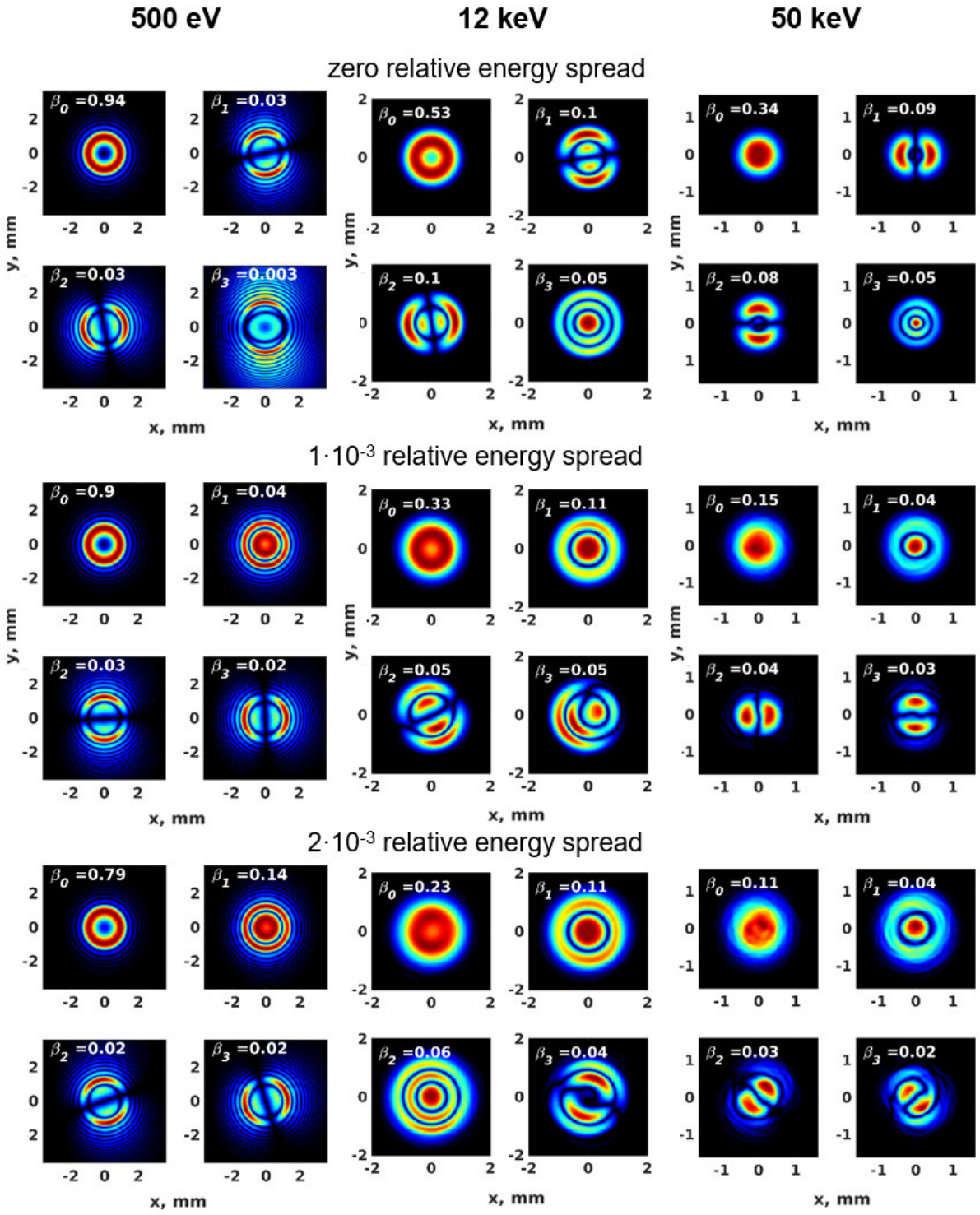

Figure 5.23: The first four modes and their normalized weights β_j obtained from the coherent mode decomposition of the CSD for the detuned energy of 492.3 eV (left column) 11.97 keV (middle column) and 49.97 keV (right column) for three different relative energy spread values.

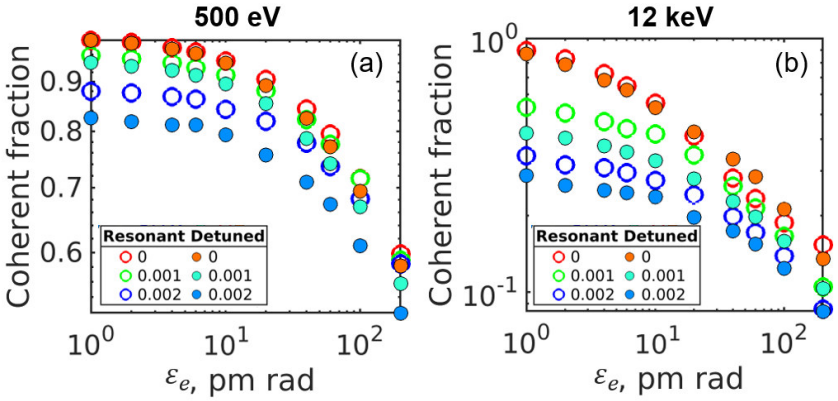

Figure 5.24: Coherent fraction of radiation ζ^{CF} (global, calculated in both transverse directions) as a function of the electron beam emittance ε_e for the different values of the photon energy (resonant and detuned) and energy spread. Donuts are simulations performed at the resonant energy, and circles are simulation performed at the detuned energy. Red, green, and blue color correspond to 0, $1 \cdot 10^{-3}$, and $2 \cdot 10^{-3}$ relative energy spread values, respectively.

donut shape profile (see β_0 at detuned in Fig. 5.23). The latter usually occurs for the radiation source tuned to maximum photon flux [82]. The same conclusion as in the case without detuning can be made from the mode analysis performed for the detuned energy. Since the modes possess different symmetry, the analysis and applied models using factorability of functions in different transverse directions should be used with caution. For the detuned energy, Laguerre-Gaussian-type modes are coming naturally from the decomposition of cross-spectral density function without contribution of energy spread. When the energy spread of the electrons is present, the contribution of the Laguerre-Gaussian-type modes is increased even more. It can be shown by setting electron offset parameters (entering angle $\boldsymbol{\eta}$ and axis offset $\mathbf{l}$) to zero (see Fig. 5.28 in the red dashed square). Another interesting observation is that due to the soft photon energies and high divergences of the beam in this region, the oscillatory shape of the modes is occuring, indicating once more a non-Gaussian origin of the source at vanishing electron emittance. In the case of detuned energies, the central spot of the donat is squeezing higher the energy (see Fig. 5.23), and due to the finite electron beam emittance, the mode translates into a more Gaussian shape. In this case, produced coherent beam in the form of a donut with small divergent angles spreads over the emitted cone, and the total radiation smears due to the finite emittance. The coherent fraction in the case of soft X-rays slightly depends on energy spread, but combined with the frequency detuning, it may experience major changes. For example, in the soft x-ray energy range, the CF may drop down by 18% for 0.002 relative energy spread value depending on the electron beam emittance (see Fig.5.24 (a)). In the case of higher photon energies, this difference is even bigger, about 20-70% depending on the electron beam emittance (see Fig. 5.24 (b)) As soon as mode weights were determined during the mode decomposition process, the global degree of coherence for the considered photon detuned energies and energy spread values according to Eq. (3.74) were determined as well. The tendency for the DOC is preserved the same as it was for CF, and with the combination of the energy detuning effect, it may experience significant changes. The DOC values vary for 20% for soft photon resonant

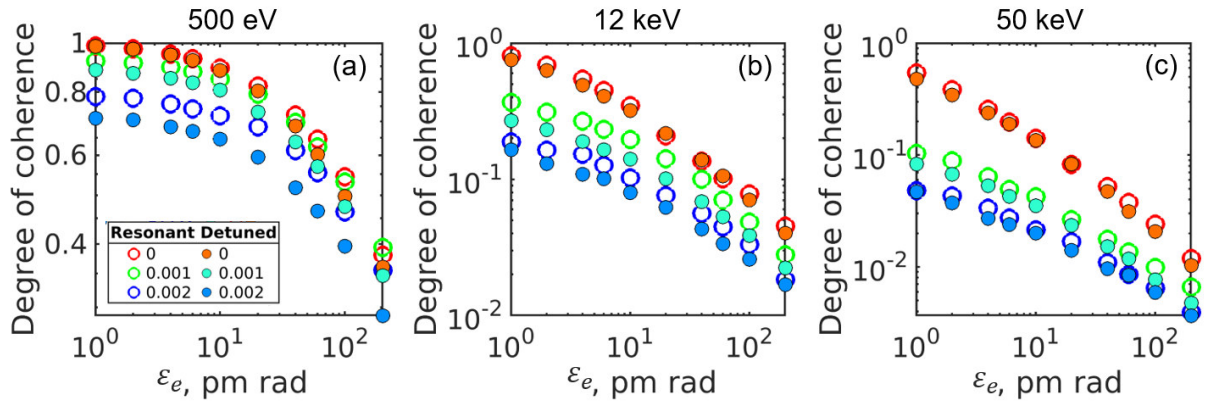

Figure 5.25: Degree of coherence ζ (calculated in both transverse directions) as a function of the electron beam emittance ε_e for the different values of the photon energy (resonant and detuned) and energy spread. Donuts are simulations performed at the resonant energy and circles are simulation performed at the detuned energy. Red, green, and blue color correspond to 0, $1 \cdot 10^{-3}$, and $2 \cdot 10^{-3}$ relative energy spread values, respectively.

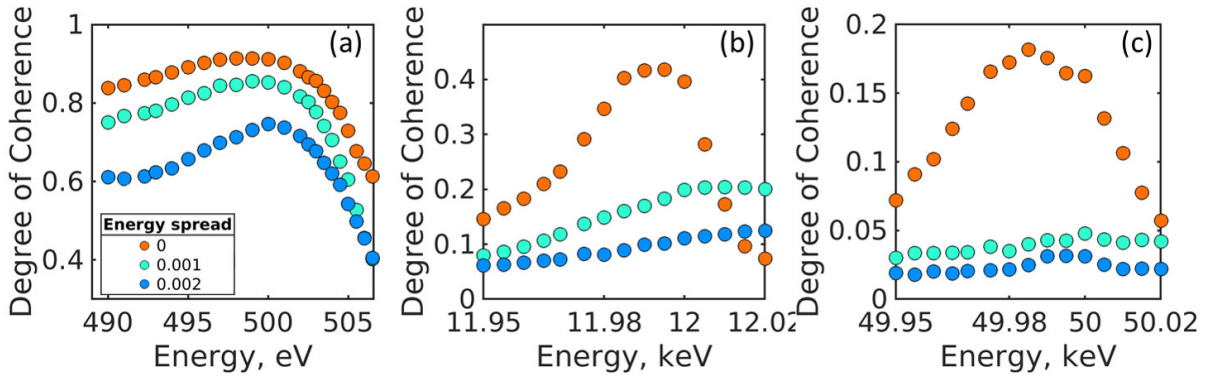

Figure 5.26: Degree of coherence ζ (calculated in both transverse directions) as a function of the photon energy for the different values of the energy spread at 10 pm rad electron emittance. Red, green, and blue color correspond to 0, $1 \cdot 10^{-3}$, and $2 \cdot 10^{-3}$ relative energy spread values, respectively.

and detuned energies depending on electron beam emittance. However, significant change arises again for hard X-rays of 12 keV resonant and 11.93 detuned photon energies with energy spread effect. The DOC values, in this case, may drop down by 20-70%. It is also interesting to look at the dependence of the DOC from the detuned photon energy (see Fig. 5.26). In this case, simulations of the emitted undulator radiation were done around the resonant energy, and the DOC is calculated from the mode weights obtained after the decomposition procedure. One can see from Fig. 5.26 that the highest DOC may be achieved only around the resonant photon energy at zero relative energy spread, while detuning from it may result in degradation of coherent characteristics. For other values of the relative energy spread, the tendency is the same, although small deviations may be seen as well. As it was shown in the section 5.5.1, the energy spread effect results in bigger photon source size and divergence. Therefore, the deviations may happen due to slightly different simulation conditions, as the area of the beam used in the decomposition procedure varies depending on the energy spread. Thus, simulations showed, although detuning from the resonant energy may increase the spectral flux, it will happen at the expense of deterioration of the coherent characteristics of the beam.

While simulating 1D radiation amplitudes, another interesting observation can be made in the case of detuning. For all cases under consideration, the radiation profile is presented in the form of a donut (see Fig. 5.27 (b) in left and right columns), as it was seen before from zero mode (see Fig. 5.23). The hollow of the beam intensity at the central spot may vary depending on the photon energy, relative energy spread value, and electron beam emittance. For higher energy spread values, the hollow at the central part is usually smaller. In the case of hard x-rays, due to the small beam sizes and relatively big electron beam emittance, the beam intensity profile may be smeared, and the hollow may disappear. What is more interesting, that the first-order correlation function in the presence of detuning effects may differ significantly in shape of SDC function $|\mu(x_1, x_2)|$ (see Fig. 5.27 (d,f,h)) and its profile on antidiagonal cut $|\mu(\Delta x)|$ (see Fig. 5.27(j)). Another important observation is that calculated DOC in 2D case is not equal to the product of DOCs obtained in 1D cases (according to Eq. (3.63)) at different transverse directions ($\zeta^{2D} \neq \zeta_x^{1D} \cdot \zeta_y^{1D}$), regardless of whether the resonant energy conditions is satisfied or not. The feasibility of the latter also depends on the electron beam emittance. For relatively big electron beam emittance ($\varepsilon_e > 300$ pm rad) the factorability of the CSD functions is valid, due to the Gaussian distribution of the bunch. Therefore, the condition $\zeta^{2D} = \zeta_x^{1D} \cdot \zeta_y^{1D}$ is fulfilled.

In the case when the electron beam emittance is put to zero $\varepsilon_e = 0$, only effects connected to the energy spread of the electron beam may be studied. As it was shown in the sections 5.4.1 and 5.4.4, the field from various electrons with different energy spread experiences a change in sign at specific distances from the central axis. This effect is encoded in the correlation functions and can be seen directly after the mode decomposition. It can be seen from Fig. 5.28, that as soon as the energy spread effect was introduced immediately, the contribution of the Laguerre-Gaussian-type modes increased (shown by red dashed square). As a result of this analysis, one can see that the method for characterizing the coherence properties based on the mode decomposition is more adequate and contains rich information on the parameters of the source.

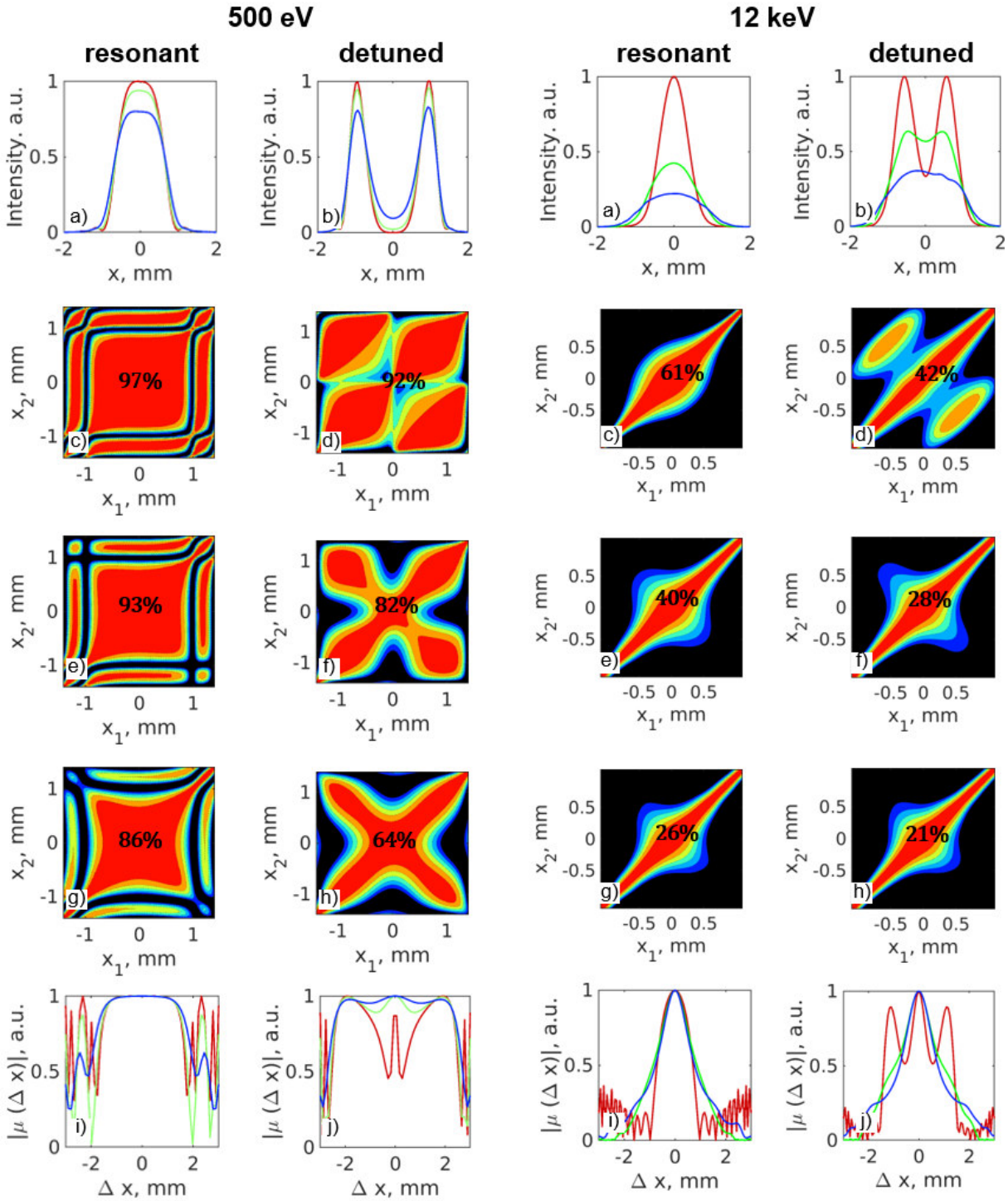

Figure 5.27: Simulations of the correlation functions in horizontal direction for 500 eV (left column) and 12 keV (right column) photon energy. Intensity distribution I(x) (a,b), shown for different values of energy spread (zero (red), $1 \cdot 10^{-3}$ (green) and, $2 \cdot 10^{-3}$ (blue)) .Absolute value of the SDC $|\mu(x_1, x_2)|$ for different energy spread values: zero energy spread (c,d); $1 \cdot 10^{-3}$ energy spread (e,f); $2 \cdot 10^{-3}$ energy spread (g,h), and absolute value of the spectral degree of coherence along the anti-diagonal line (shown in (c-h)) as a function of separation of two points $|\mu(\Delta x)|$ (i,j) simulated in horizontal direction in the far field region. In (c)-(h) the transverse degree of coherence ζ_x is shown.

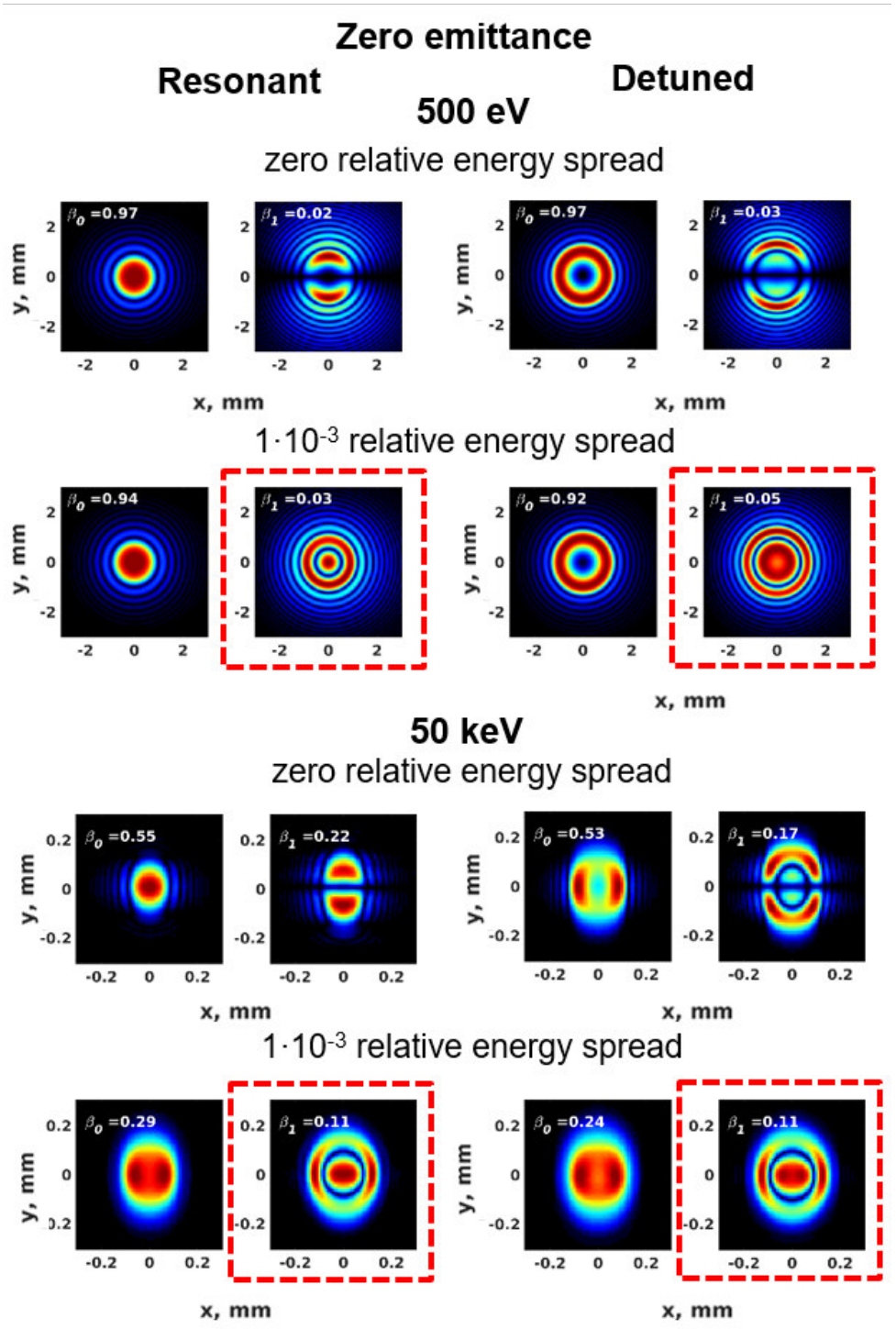

Figure 5.28: First two modes and their normalized weights β_j obtained from the coherent mode decomposition of the CSD for the resonant energy (left column) and detuned (right column) photon energy, for three different relative energy spread values. In the simulation electron beam emittacne is set to zero.

5.7 Summary of the analysis

In summary, a detailed analysis of the coherence properties of a high-energy synchrotron storage ring with ultra-low emittance values near 10 pm rad and a wide range of photon energies from 500 eV to 50 keV was provided. Such low values of electron beam emittance are expected to be reached at PETRA IV facility ([51], [54]). In addition, the effect of electron energy spread on the radiation properties of a DLSR source for the same energy range was analyzed. All simulations were performed within the semi-analytical approach based on equations of synchrotron radiation and compared with the simulations carried out by XRT software. The following important points were discussed during this work. In order to determine the properties of radiation from diffraction-limited sources, an approach based on statistical optics ([62]; [8]) should be used. The single-electron radiation defines the overall photon beam parameters in this low-emittance regime. Consequently, a minimum photon emittance (diffraction limit) that may be reached at such storage rings within the framework of the considered model is rather $\lambda/2\pi$. Another point is that even for such low emittance values as 10 pm rad true diffraction limit will be reached, in fact, only at soft X-ray energies of about 500 eV. In this case, only a few modes will contribute to the radiation field, but already at 12 keV radiation field will consist of about ten modes and approach Gaussian type. This effect will be even more pronounced at high energies. In order to reach the true diffraction limit for hard X-rays, electron emittance at beam focus should be pushed down to about 1 pm rad, which is, unfortunately, out of reach for present technology. The results also show that, for a full description of the radiation properties of these sources, eigenvalue decomposition of the radiation field has to be performed, which offers good theoretical insight and complete generality. It also means that present experimental approaches which measure coherence properties of radiation in each direction separately ([64]; [94]; [95]) should be generalized to 2D methods of coherence determination. Another outcome of this work is the analysis of the electron energy spread effects on the coherence properties of DLSRs. It was demonstrated that this effect becomes more noticeable for low electron beam emittance. The larger the energy spread values, the more the source size and divergence are affected as well as the radiation wavefront. Consequently, the degree of coherence and coherent fraction value of the radiation is decreased. It was shown that, in order to keep high coherence values of radiation, the relative energy spread should not exceed the value of $1 \cdot 10^{-3}$ at the electron emittance values of 10 pm rad. It is also should be noted that at 1 pm rad emittance values the energy spread should be sufficiently smaller than $1 \cdot 10^{-3}$ to keep high coherence of the x-ray beam. It was also shown that the effect related to undulator resonant energy detuning with the combination of the energy spread effect may significantly reduce the coherence characteristics of the DLSR source. Finally, the results demonstrate that the coherence properties of the future diffraction-limited sources will be outstanding ([46]; [53]). It is believed that the general approach and new tools for an adequate description of the coherence properties of synchrotron sources provided in this chapter will be helpful for the design and planning of future diffraction-limited sources worldwide.

Chapter 6

X-ray free-electron lasers

Over several decades, femtosecond lasers, operating in the near-infrared and visible regions, have been available. They allowed the investigation of many processes with characteristic times below a picosecond, such as vibrational motions in molecules or generation of the exciton. However, the resolution of lasers is limited to a few hundred nanometers, and the power is by the wavelengths in use. On the other side, structural information retrieved by X-rays is on the atomic scale. However, the generation of focused X-ray pulses with a small duration (down to a few femtoseconds), very intense, and utterly coherent from the synchrotron storage facilities is challenging. This difficulty has been overcome by the invention of the so-called X-ray free electron laser (XFEL), which can operate in the far ultraviolet and X-ray modes.

The invention of the XFELs allowed increasing coherence up to 95% [93, 97, 98] and peak brightness by ten orders of magnitude, up to $10^{35} ph/(s\ mm^2\ mrad^2\ 0.1\%BW)$ (see Fig. 6.1). The first FELs demonstrating SASE principle were FLASH in Hamburg [99] operating in the extreme ultraviolet photon range and LCLS at SLAC [100], operating in hard X-rays. Soon many other SASE XFELs such as SACLA [101], European XFEL [102], Swiss FEL [103] and PAL-XFEL [104] started their operation.

Producing extremely bright and short pulses of X-ray radiation, XFELs are based on an entirely new concept, which Madey initially suggested in 1971 [105], and the working source was demonstrated in the infrared domain in 1977 [106]. With the improved concept of Self-Amplified Spontaneous Emission (SASE) process, proposed by A. Kondratenko and E. Saldin in 1980 [107] and R. Bonifacio, C. Pellegrini, L. M. Narducci, and J. Murphy in 1984 [108], [109], construction of FELs in the X-ray range providing extremely short pulse durations become possible. The basic principle [105, 107] makes use of the fact that an electron beam passing a long undulator magnet amplifies an initially produced radiation field.

Figure 6.1: Examples of Free-Electron Lasers, operating in tender and hard X-rays with the given parameter of the electron beam energy. The bottom right plot shows a comparison in the peak brightness of FELs (adapted from [96])

6.1 Basic concept of the XFEL machine

6.1.1 Electron beam

Photocathode RF gun is generally used for XFEL machines because they require high-quality injection electron beams with a low emittance to improve FEL generation. The electron beam of the initial condition represents the shot noise signal driven from the photo-injector. Due to extraction by a laser beam, the obtained electron signal has quantum random fluctuations (Poisson process). Such random fluctuations in the beam current correspond to intensity modulation of the beam current at all frequencies simultaneously – including the frequency to which the undulator is tuned. When the electron beam enters the undulator, the presence of the beam modulation at frequencies close to the resonance frequency initiates the process of radiation. It is assumed that the input current has homogeneous spectral distribution since all possible harmonics occur in the shot noise beam. The spectrum of the transversely coherent fraction of radiation is concentrated within the narrow band, $\Delta\lambda$, so that the typical amplification bandwidth of the XFEL is of the order of 0.1% (see Eq. (4.25)).

After extraction, the bunch is accelerated by an electron radio frequency (RF) gun and directed towards the linac. In the linac, consisting of a long sequence of superconducting accelerating modules, magnets for beam focusing, and diagnostic equipment, the electrons are accelerated to energies from a few up to tens of GeV. Next, electron bunches passing through the undulators channeled down to the beamlines.

6.1.2 Microbunching and Self-Amplified Spontaneous Emission

Due to the interaction between the radiation field and the electron bunch in the presence of the undulator's magnetic field, a density modulation (microbunching) of the electron bunches at the electro-magnetic wavelength builds up. This results in the enhanced power and coherence of radiation during the passage of the bunch through the undulator.

In general, the electron-radiation interaction, during the process of microbunching, described by the Lorentz force, according to Eq. (4.7) with the help of Maxwell's equations (Eqs. (3.1)-(3.4)), accounting for charge and current density, which are solved within the method of a self-consistent radiation field. However, a simple picture of the process may be described within the standard framework of the synchrotron radiation mechanism. Electrons propagate along a sinusoidal path and emit synchrotron radiation in a narrow cone in the forward direction (see Fig. 4.2 (a,c)). When an electron beam goes through an undulator, it emits radiation at the resonance wavelength (Eq. (4.24)). Moving with the speed of light, an electromagnetic wave is always faster than the electrons, and a resonant condition occurs when the radiation is ahead of the electrons by a distance λ after one undulator period. The fields produced by the moving charges in one part of the electron bunch react on moving charges in another part of the bunch, causing a small perturbation. Due to that, occurred tail-head instability leads to a growing concentration of particles. In general, the Coulomb forces between the electrons prevent the formation of a strong electron density modulation. However, the radiation produced

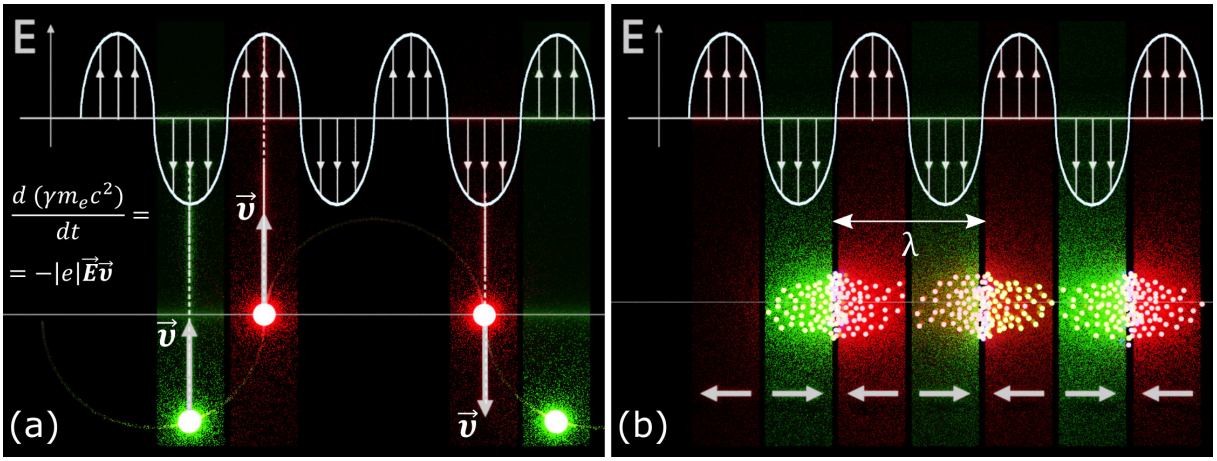

Figure 6.2: (a) Electron energy modulation (gain energy - green area and loss - red area). The rate of change of the electron energy can be described according to Eq. (4.7) (b) Density modulation, where redistribution of particles occurred due to electron energy exchange and ponderomotive forces (for inhomogeneous fields).

by the electron bunch itself is strong enough to slow down some of the electrons and accelerate others, finally redistributing them into smaller microbunches at distances equal to the resonant radiation wavelength. Redistribution takes place under the electron energy exchange, between particles emitted the radiation and particles accelerated by the emitted radiation (see Fig. 6.2 (a)).

Thus, this collective instability in the electron beam produces an exponential growth (along the undulator) of the electron density modulation on the scale of undulator radiation wavelength (see Fig. 6.2 (b)). Before the micro-bunching occurs, all N_e electrons are treated as individually radiating charges, and the resulting spontaneous emission power is proportional to N_e (as in the case of bending magnet, wiggler, and undulator radiation). Within a micro-bunched beam, all electrons radiate almost in phase. This leads to a radiation power growth as N_e^2, and thus, to amplification of many orders of magnitude with respect to spontaneous emission of the undulator (typical number of electrons in the microbunch is around $10^8 - 10^9$).

Stronger the electromagnetic radiation produced by such a bunch, stronger microbunching is occurring and so on, which in fact form a positive feedback loop so that the process only amplifies with propagation distance. This regime of FEL operation is called 'Linear Regime' (LR), and the radiation produced during the amplification process Self-Amplified Spontaneous Emission (see Fig. 6.3). The name originates from the fact that the magnitude of an electromagnetic field is still proportional to the starting signal during the amplification process, which is spontaneous undulator radiation. Therefore, the statistical properties of SASE FEL in the linear regime are close to spontaneous undulator radiation and obey Gaussian statistics [111]. In addition, if the beam is perfectly microbunched the phase of the radiation field is constant across the beam, so that the longitudinal coherence length is eqaual to the lenght of the electron beam.

$$L_{coh,\,z} \approx L_{e\ beam} \tag{6.1}$$

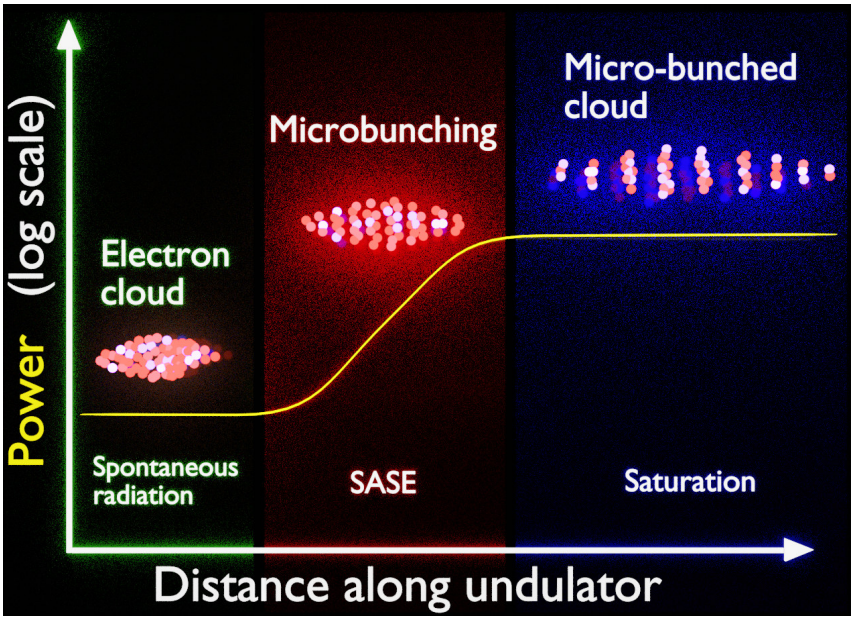

Figure 6.3: Michrobunching process and the power radiated by an electron bunch as it propagates through a long undulator (reproduced from [110]).

At a certain point, the microbunches are fully formed, and the exponential power growth stops. It is called FEL saturation (see Fig. 6.3). In this regime, most of the electrons are out of the resonant bandwidth of the radiation. Beyond this point radiation power can be extracted at best linearly as a function of the undulator length by properly adjusting unduator paramter K (undulator tapering) to maintain the resonant condition as the electron beam loses energy:

$$\frac{1+K(z)^2}{2\gamma(z)^2} = \text{constant} \tag{6.2}$$

The radiated power produced at FEL is closely connected to the FEL parameter (Pierce parameter) or efficiency parameter ρ, which describes the energy transfer efficiency between electrons and photons. If the peak electron beam power P_{peak}, defined as

$$P_{peak} = \frac{\gamma m_e c^2 \mathcal{I}}{e}, \tag{6.3}$$

then the peak saturation power P_{sat} at which no further power improvement can be achieved at FELs is proportional to P_{peak} through the efficiency parameter

$$P_{sat} \approx \rho P_{peak}. \tag{6.4}$$

The efficiency parameter is introduced as [111]

$$\rho = \left[\frac{\mathcal{I}}{\gamma^3 \mathcal{I}_A} \frac{\lambda_u^2}{2\pi\sigma_{e,x}\sigma_{e,y}} \frac{(KA_{jj})^2}{32\pi}\right]^{1/3}, \tag{6.5}$$

where A_{jj} is the coupling parameter defined in Eq. (5.9) and $\mathcal{I}_A$ is the Alfvén current accounting

for electron beam self-interaction. It is seen from Eq. 6.5, that for the best FEL performance, high electron beam current, small transverse beam emittance, and a small energy spread σ_γ are required. The method of a self-consistent radiation field in the 1D FEL theory imposes constrain on the magnitude of the efficiency parameter (should be much smaller than the unity) [111]. Usually, ρ is on the order of 10^{-3} and defines such FEL characteristic parameters as the gain length L_g and the cooperation length L_c. Gain length is a characteristic length defining power growth of the pulse in the undulator with the propagation distance in the linear regime

$$L_g = \frac{\lambda_u}{4\pi\rho}, \tag{6.6}$$

so that power dependence is determined as

$$P(z) \sim exp\left(\frac{z}{L_g}\right). \tag{6.7}$$

The cooperation length L_c is describing a slippage of photons in comparison to electrons in one gain length, introduced as

$$L_c \approx \frac{\lambda}{\lambda_u} L_g. \tag{6.8}$$

The resonance condition imposes that radiation slips forward with respect to the electron beam, one wavelength every undulator period. Slippage implies how far during the propagation the radiation pulse profile will slip from the envelope of the axial electron beam profile at a distance of the gain length L_g [111]. Therefore, the parameter L_c describes the distance at which radiation from microbunches is still interfering. Usually, the electron bunch length is much larger than the cooperation region. Electrons emit radiation coherently within this region, but phase differences between any two of them are uniformly distributed. It results in multiple longitudinal modes of radiation in both time and frequency domains. Therefore, L_c can be used to estimate the coherence time of the radiation $\tau_c = L_c/c$. Thus, the buildup of longitudinal correlation of the electric field during the FEL process is limited to the scale of the number of wavelengths multiplied by the number of undulator periods within a gain length. Finally, through the FEL parameter, the saturation length can be calculated

$$L_{sat} \approx \frac{\lambda_u}{\rho}. \tag{6.9}$$

6.2 Seeding

Although the radiation from SASE FEL is spatially highly coherent, it may have a very spiky temporal structure, which may spoil the temporal (or longitudinal) coherence. Still, there is a way to clean the spectrum of FEL SASE radiation, achieving relatively high coherence and peak brightness. This method is called ”seeding” since the beam is seeded with a highly temporally coherent source during the amplification process. ”Direct seeding” refers to any method where the seed signal has the same wavelength as the resonance wavelength of the FEL with a power

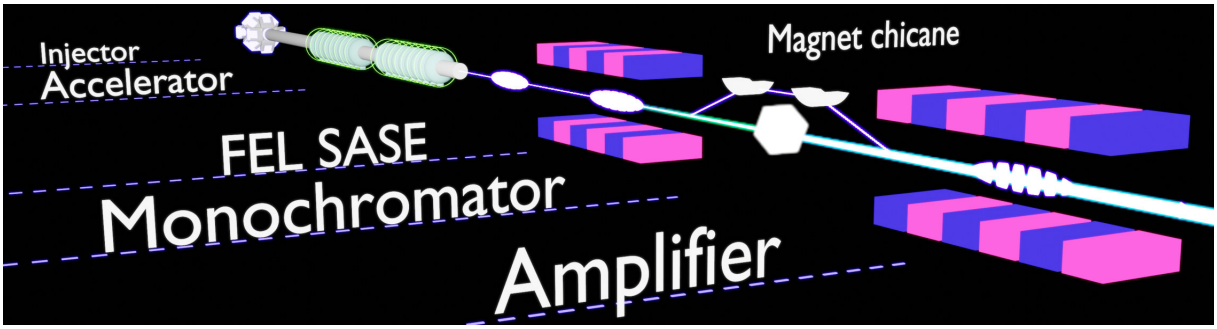

Figure 6.4: Main components of the XFEL facility. For instance, a self-seeding scheme utilizing hard X-rays is shown.

level above the shot noise power but below saturation power of the FEL. For instance, seed radiation at the resonant wavelength can be obtained via infra-red Ti: sapphire laser [112, 113].

One of the main challenges in seeding FEL externally is the temporal synchronization of the FEL electron bunch. This problem is solved if the same electron bunch creates a highly temporally coherent source (seeding radiation) and amplifies the latter. This concept is called" self-seeding", which was first proposed utilizing soft X-rays [114] (SXRSS) and thereafter hard X-rays [115] (HXRSS).

In the self-seeding scheme, initially, the undulator is operating in the SASE regime, then the photon beam is filtered through a monochromator and is used as a seed. The scheme requires two undulators tuned at the same radiation wavelength. The SASE radiation is generated by the first undulator before reaching saturation. Then it passes through the narrowband monochromator. In the case of the SXRSS, a grating is used, while in HXRSS, the FEL pulse is monochromatized with a single diamond crystal. The initial self-seeding concept as described in Ref. [116], required a long electron bypass line, where control over the electron beam properties was achieved by many quadrupole and sextupole magnets. The problem of a long electron bypass was successfully solved by Geloni, Kocharyan, and Saldin in 2011 [117]. They proposed using the transmission around the stopband of a Bragg reflection. In this case, after FEL SASE radiation is generated, it is spectrally filtered by passing through a diamond crystal (see Fig. 6.4). After that, the bandwidth of the radiation is reduced. In order to violate the density modulation of the electron bunches produced by the first SASE FEL and at the exact time match entering of the bunch into the second undulator section, the electron beam is forced through a magnetic chicane. Thus a narrow band photon pulse, which overlaps the electron bunch when they enter the second undulator, provides the necessary seed to induce coherent amplification in this second FEL amplifier stage. The self-seeding method was successfully realized at LCLS in both soft and hard x-ray regimes [116, 118], and this allowed to increase the temporal coherence of the beam.

6.2.1 High-gain harmonic generation

FEL can be seeded by the formation of a coherent bunching of the electron beam at the resonant wavelength. This scheme implies electron beam manipulation and is called High-

gain harmonic generation (HGHG). In the HGHG scheme, the beam is first modulated by an external seed laser. The modulation occurs in the first undulator section due to the ponderomotive force resulting from the external seed laser. Ponderomotive force describes a nonlinear force that a charged particle experiences in an inhomogeneous oscillating electromagnetic field, which causes the particle to move towards the area of the weaker field strength. Further, the energy modulation is converted into a current modulation by a dispersion magnet. In the dispersion section, particles with higher energy will be deflected less effectively and thus travel short paths than those with lower energy. As a result, the electron beam will be bunched. This bunched beam induces bright coherent radiation at a higher harmonic when it passes through the next undulator, which is tuned to this resonance harmonic. The HGHG scheme can be generalized to a cascade system with more than one harmonic multiplication. This scheme was first proposed by Yu [119] and tested in Brookhaven [120]. Later the first seeded-FEL source FERMI operating with wavelength down to 4 nm was commissioned at the Sincrotrone Trieste Laboratory [121]. The limitation of the HGHG seeding scheme is the lack of power of the conventional lasers, which makes it impossible to seeding at x-ray wavelength. This problem was partly solved by the invention of the so-called echo-enable harmonic generation (EEHG) FEL scheme [122, 123]. In this scheme, a more complex configuration with two modulators and dispersive sections is used to achieve strong overcompression of the electron beam. Consequently, much higher harmonics conversion in the HGHG stage occurs, providing smaller wavelengths but no smaller than 1 nm in practice.

6.3 Science at the XFELs

The highest goals of imaging single molecules and obtaining molecular movies were the cause of the construction of XFELs. The whole concept of imaging at the FEL is based on recording diffraction patterns before the inevitable destruction of the samples in the form of a Coulomb explosion occurs. The increased pulse rate, short pulse itself, and its transverse coherence are the key enabling factors for single-particle X-ray diffractive imaging [24], which implies averaging the weak diffraction signal from single biological particles during multiple measurements. In such dedicated imaging experiments performed at XFEL sources, hundreds of thousands of coherent X-ray pulses interact with differently oriented replicas of the target sample in order to determine its three-dimensional structure with the highest resolution.

Conduction of the pump-probe experiments is another application of the ultrashort XFEL pulses, where the conventional infrared laser first pumps a sample, and after some time delay, the dynamics is measured by the probe pulse. This kind of experiment is used to reveal the dynamics of plasma–matter interactions [30, 124], ultrafast phase transition, and laser-induced molecular dynamics [31]. Using time-resolved small-angle x-ray scattering in pump & probe experiments at XFELs, it is possible to study topological phases of matter (like skyrmions) or highly non-trivial configurations of the electronic or spin system, which often result in exotic and previously unimaginable material properties [125].

Exploiting incoherent X-ray radiation (artificially deteriorated at FELs) with the application

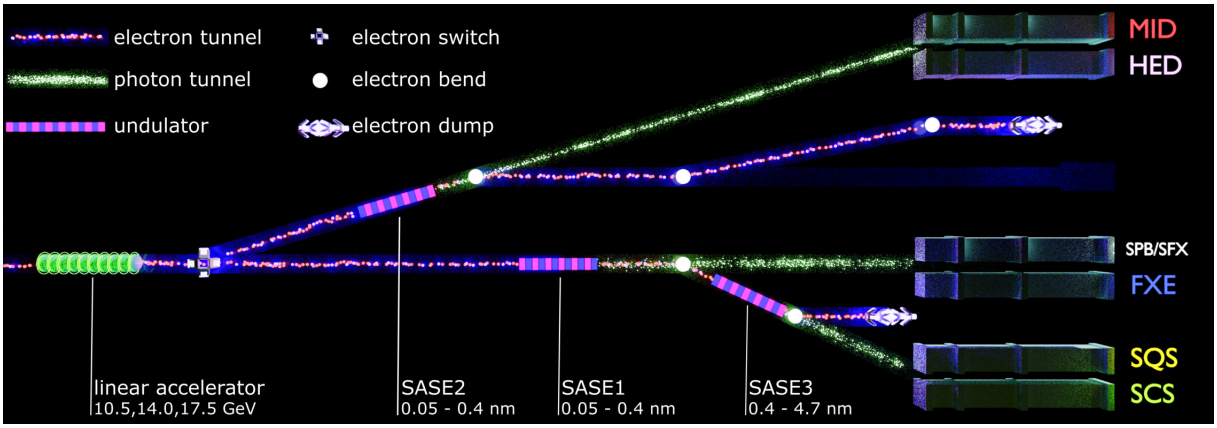

Figure 6.5: Schematic layout of the EuXFEL instruments.

of higher-order photon correlation techniques, the incoherent source or irradiated sample may be resolved as well [126–130]. At the same time, applying higher-order photon correlation techniques, statistical properties of the XFEL beams may be studied [94, 126, 131–133]. The obtained results from these works pave the way towards exploiting high coherent properties, short pulse duration, and repetition rate of XFELs.

6.3.1 Science at the European XFEL

The European XFEL induces novel studies in physics that haven't been considered before. The dynamics and kinetics which occur on sub-microsecond and ultrafast timescales are difficult to probe experimentally. With the construction of XFEL, such experiments became available via collecting series of diffraction patterns at repetition rates of up to several MHz. Using the EuXFEL pulsed source, with such high repetition rate, it is possible to determine the structure of viruses on the atomic level, trace ultrafast energy transfers within molecules, take three-dimensional images of the nanoscale objects, film chemical reactions, and probe the characteristics of extreme states of matter.

Opening up opportunities for new experiments, the European XFEL facility possesses three different light sources (undulators SASE1-SASE3), providing X-ray radiation with the best properties directed to the instruments in the facility's experiment hall (see Fig. 6.5). Research is possible at various complex experiment stations in the hard X-ray range (MID, HED, SPB, SFX, FXE) or soft x-rays (SQS, SCS) utilizing advanced methods such as pump-probe [134].

The arrangement of SASE1 undulators represents the radiation source for the Materials imaging & dynamics (MID) and High Energy Density Science (HED) end stations. The MID beamline [135] pertains to scientific research for condensed matter physics (glass formation and magnetism research), as well as for soft and biological material (colloids, cells, and viruses) employing X-ray scattering, imaging [136] and pump-probe techniques. The latter is possible due to the highly coherent beam, increased flux, and ultrashort duration of the X-ray pulses. Recent studies conducted at the MID instrument showed interesting behavior and anomalous dynamics in the soft matter utilizing X-ray photon correlation spectroscopy (XPCS) [137–139] as

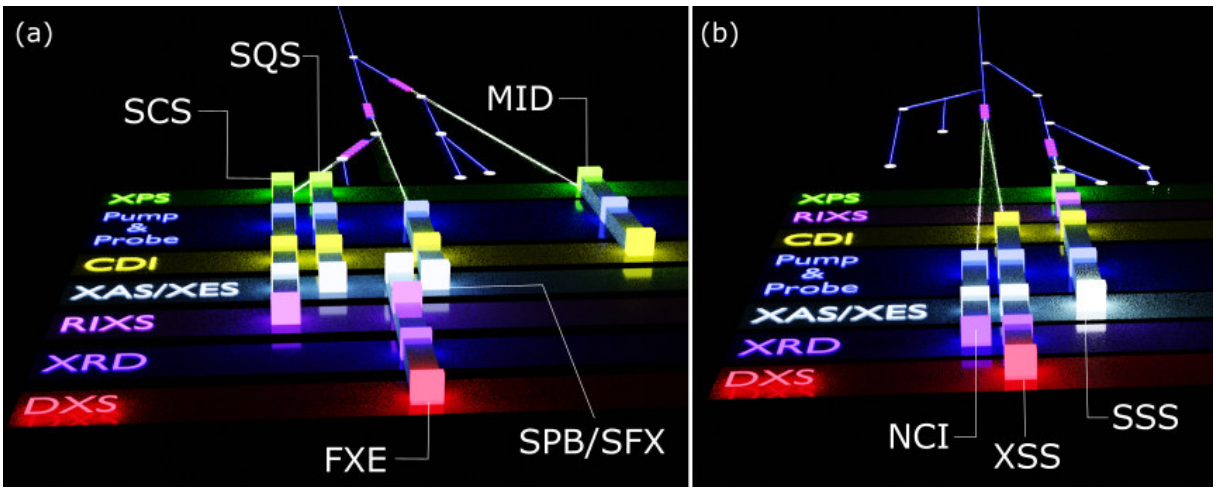

Figure 6.6: Map of techniques and methods available at various beamline stations of the EuXFEL (a) and PAL-XFEL (b) facilities.

well as revealed the transition regime of the heat diffusion due to ultrafast laser interaction with solids [140]. Such studies became possible due to pump-probe methods available at EuXFEL at the MID station.

The HED instrument at the EuXFEL is a unique platform for experiments combining hard X-ray FEL radiation and the capability to generate matter under extreme conditions of pressure [141], temperature, or electric field. Experiments and available *in situ* studies at the beamline, equipped with high-precision X-ray diffraction setup [142], provide the information on the new extreme-pressure phases and solid-density plasmas, structural phase transitions of complex solids in high magnetic fields. Recent studies at the HED beamline revealed an unexpected cubic symmetry in Si materials [143], captured the process of new material synthesis at high pressures [144], as well as structural changes in silicate, melts under extreme pressure [145]. Such material studies under extreme temperature and pressures are becoming possible at high-power XFEL facilities.

From the other side, in the soft X-ray branch of the EuXFEL (undulator source SASE3, see Fig. 6.5), scientific objectives include the understanding and control of complex materials, the investigation of ultrafast magnetization processes on the nanoscale, and the real-time observation of chemical reactions in liquids, by means of Resonant X-ray Emission Spectroscopy (XES), CDI and XPS. Combined with femtosecond laser pulses, it is possible to induce phase transitions and unexpected transient states of matter on ultrafast timescales. Recent studies at the SCS with a single-shot infrared pump–X-ray probe measurements captured the topological switching dynamics in the skyrmion phase in real time [146]. An exceptional sensitivity to the process is achieved due to the short X-ray pulse duration and reciprocal-space resolution available at the SCS instrument.

SPB/SFX instrument is primarily dedicated to diffractive imaging and structure determination of micrometer-scale and smaller objects at atomic or near-atomic resolution. The instrument implies research on biological objects, organelles, and cells, as well as viruses and crystals

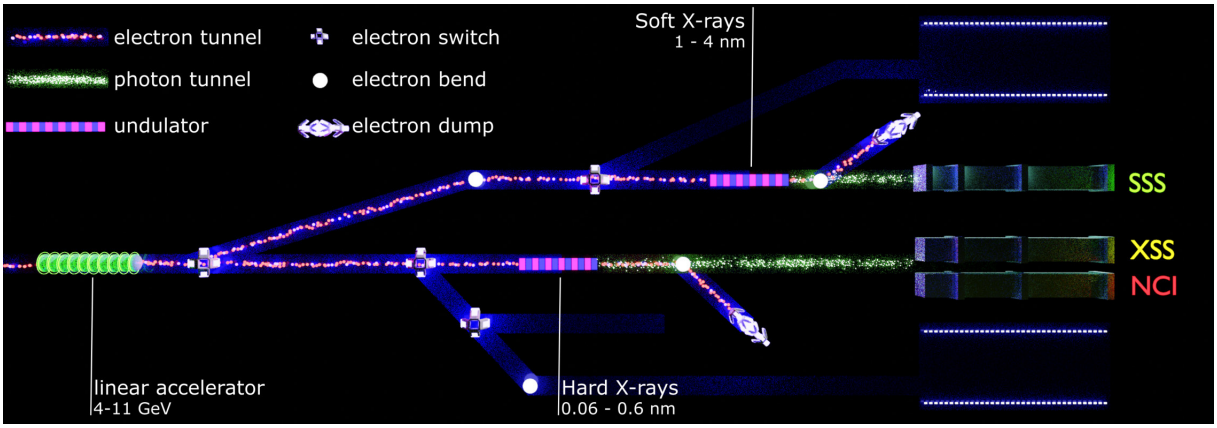

Figure 6.7: Schematic layout of the PAL-XFEL instrumnets.

of macromolecules.

The FXE instrument's primary research is devoted to dynamic studies of chemical and biochemical reactions in liquids. With enabling laser pump source, femtosecond time resolution studies are available, exploiting different techniques (XRD, X-ray diffuse scattering, wide-angle X-ray scattering X-ray emission, and absorption spectroscopies).

6.3.2 Science at the PAL-XFEL

X-ray free-electron laser at Pohang Accelerator Laboratory can provide transversely coherent X-ray pulses with tens of GW (10^9 W) power scales and the duration of few tens of femtosecond (10 -15 fs, for SASE operation mode). Although the transverse coherence is excellent, the longitudinal coherence is poor due to the limitation of the SASE mode that starts from the shot noise of the electron beam. To improve longitudinal coherence, the harmonic lasing self-seeding is applied at FEL (HLSS FEL) (see section 6.2). The first Hard X-ray Self-Seeded beam was provided by PAL-XFEL at a photon energy of 9.0 keV. The beam has an extremely narrow spectrum band characteristic compared to the conventional self-amplified spontaneous emission (SASE) method and is effective in experiments using a monochromatic beam. Such SS X-ray beams will be effective to use in the experiments, concerning resonant Auger effect [147], two-photon absorption [148], electronic quantum dynamics [149], nanocrystallography [27]. The current self-seeding X-ray energy available at PAL-XFEL varies from 5.0 keV to 14 keV. On the other hand, SASE beams cover the photon range from 2.8 keV to 14 keV.

The hard x-ray branch of PAL-XFEL is dedicated to x-ray scattering, spectroscopy, imaging, and crystallography experiments in a wide range of x-rays. The XSS (X-ray Scattering and Spectroscopy) consists of FXS (Femtosecond X-ray Scattering) and FXL (Femtosecond X-ray Liquidography) endstations. The NCI (Nano Crystallography and coherent Imaging) consists of CXS (Coherent diffraction Imaging/Scattering and Spectroscopy), SFX (Serial Femtosecond Crystallography) endstations (see Fig. 6.7).

The FXS (Femtosecond X-ray Scattering) induces researches on ultrafast dynamic phenomena in solid-state materials by means of XRD, DXS, X-ray absorption, and emission spec-

troscopy [150]. The optical laser pump source is available at the station, with an estimated temporal resolution of 40 femtoseconds.

The FXL (Femtosecond X-ray Liquidography) instrument is designed for the study of ultrafast electronic and molecular structural dynamics of samples by means of SAXS/WAXS and X-ray absorption and emission spectroscopy for capturing the laser-induced changes in the sample.

The CXS (Coherent X-ray Imaging/Scattering and Spectroscopy) endstation is designed for structure determination by means of SAXS, CXI, and XAS.

Serial Femtosecond Crystallography (SFX) experimental endstation offers advanced sample environments, including microcrystal delivery systems and sample chambers to perform macromolecular structure studies. Besides the conventional sample delivery techniques using liquid streams, 1D and 2D fixed target scanning systems are available. The X-ray focusing is achieved to the area of about $5 \times 5\ \mu m^2$. The achievable resolution using the detector is about 1.4 Å. Applicable optical pumping instruments for structural dynamics are fs- and ns-lasers.

Soft X-ray Spectroscopy and Scattering (SSS) Beamline at PAL-XFEL covers soft X-ray energy range (250 – 1200 eV), utilizing for direct observation the transition of valence electrons. Spectroscopy tools and time-resolved methods are available at the station. There are three endstations in the SSS beamline: XAS/XES, RSXS, FTH.

It is seen from the name that XAS/XES stations perform time-resolved spectroscopy experiments on the conduction and valence bands materials.

RSXS endstation allows investigating the complex electronic ordering (charge/spin/orbital) using time-resolved resonant soft X-ray scattering experiments on quantum materials and strongly correlated systems.

FTH/Forward scattering endstation allows time-resolved imaging experiments as well as X-ray absorption spectroscopy.

Chapter 7

Hanbury Brown and Twiss interferometry

The development of quantum optics has not been without interference and intensity correlation experiments. In 1956, Hanbury Brown and Twiss, who were eager to develop a new method to determine the size of stars, stirred up optical physics with the observation of a new form of interference produced by correlations of the intensity fluctuations of light from a chaotic source [151]. Their stellar interferometer collected light produced by independent sources on the disc of a star and detected at two different detectors on Earth [152]. The observation of a second-order interference effect in this configuration was intriguing because, at that time, it appeared that classical and quantum theories of light offered different predictions. The fact that initially unrelated photons, emitted from the disc of a star (or even different stars), would exhibit a bunching effect provoked much disputation among the prominent physicists of the time, despite having a sufficient interpretation [153]. A quantum-mechanical description of photon correlations and further generalization of the concept of optical coherence, which is based on the analysis of correlation functions of higher order, were introduced by R. J. Glauber. Ever since, this effect has motivated extensive studies of higher-order correlations and their quantum counterparts in optics, as well as in condensed matter and particle physics [154]. Nowadays, The Hanbury Brown–Twiss effect is universally accepted and, being so fundamental, embodies many subtleties of our understanding of the nature of light.

Figure 7.1: Schematic representation of the HBT experiment.

7.1 HBT experiment

Different methods are generally applied for the experimental characterization of the radiation source. For instance, double pinholes or non-regular arrays of slits at FELs and third-generation synchrotron sources [89, 98] utilized to measure the spatial coherence of radiation. Usually, such methods exploit diffraction elements to get an interference pattern. For instance, in the Young interferometry experiment, double slits with several sets of distances between apertures are used. In the case of a non-regular array, interference occurring from all pinholes simultaneously at all distances present in the array. The conventional approach implies using Michelson type interferometry [94, 155] to determine longitudinal coherence. The most exotic of these experiments is Hanbury Brown and Twiss (HBT) intensity interferometry. Information provided by the HBT interferometry connected to the second-and higher-order statistical properties of the source. A schematic representation of the HBT experiment is shown in Fig. 7.1.

Initially, Hanbury Brown demonstrated the effect by measuring the angular size of the two intense sources in the Cygnus and Cassiopeia constellations [156]. Afterward, Hanbury Brown and Twiss proposed the interferometry method [157], and were able to demonstrate the existence of the excess fluctuations from laboratory source [12]. As the result of the experiment, Hanbury Brown and Twiss discovered the so-called "photon bunching" of thermal light, which was further explained by Purcell [153] as a "photon clump" (a tendency of photons to arrive on the detector together). For instance, the probability of detecting a photon at position $\mathbf{r}_1, t_1$ given that a photon is recorded at position $\mathbf{r}_2, t_2$ revealed by the second-order photon correlation function $G^{(2)}(\mathbf{r}_1, t_1, \mathbf{r}_2, t_2)$

$$G^{(2)}(\mathbf{r}_1, t_1, \mathbf{r}_2, t_2) =< I(\mathbf{r}_1, t_1) I(\mathbf{r}_2, t_2) > . \tag{7.1}$$

In this case interference may occur in the absence of first-order coherence, and the information about incoherently emitting objects can still be extracted. The effect is described in the frame of quantum statistics as a pair-correlation between bosons caused by their indistinguishability [153].

In HBT intensity interferometry, the transition between the initial and final states involves the emission and absorption of two indistinguishable photons at two detectors. The overall result of the HBT experiment is obtained through these two (in reality $\approx 10^6$ pixels for a modern detector) distinct channels. By measuring and collecting statistics, one can study the correlation between signals and get information about the source. It was shown [151] that the correlation is fully preserved even in the process of photoelectric emission (photoemissive detectors). During the coincidence detection in the HBT interferometry experiment, the concept of photon bunching implies that photodetection is more likely to occur at the same time, or very close together than farther apart in time. In this case, the probability function (section 3.2.1) of joint photoelectric detection $\mathfrak{p}(t, t+\tau)$ clearly shows a photoelectric bunching within the range of coherence time, with the maximum at $\tau = 0$ [8]. In more general cases, the photoelectric detections are correlated not only in time but also in space within the range of coherence length [8]. Therefore, it is convenient to consider such practical parameter as the degeneracy parameter $\delta\omega$, which shows the number of photons N_{ph} in the coherence volume V_{coh}. The parameter describes the average number of photons in one quantum state, consequently enables interference. It can be determined from Heisenberg's uncertainty relations Eq. (3.47) for longitudinal direction and Eq. (3.48) for transverse direction, where the phase space volume is given

$$V = \Delta\mathbf{p}\Delta\mathbf{r}\Delta E\Delta t \geq \left(\frac{\hbar}{2}\right)^3. \tag{7.2}$$

Therefore, the coherence volume comes naturally from Eq. (7.2) as $V_{coh} = (\hbar/2)^3$, so that the degeneracy parameter can be defined as

$$\delta = \frac{N_{ph}V_c}{V} \tag{7.3}$$

Thus, the basic idea of HBT interferometry is to explore the correlation of intensities at different spatial or temporal positions, i.e., to perform measurements of the second-order correlation functions. For example, if measurements are carried out in the spatial domain, this leads to the following normalized second-order correlation function

$$g^{(2)}(x_1, x_2) = \frac{< I(x_1)I(x_2) >}{< I(x_1) >< I(x_2) >} \tag{7.4}$$

where $I(x_1)$, $I(x_2)$ are the intensities of the wave field recorded at two spatial positions x_1, x_2 and averaging, denoted by brackets $< \ldots >$, is performed over a large ensemble of different realizations. If radiation is cross-spectrally pure and obeys Gaussian statistics, which is typical for chaotic fields, then $g^{(2)}$-function can be expressed as [8]

$$g^{(2)}(x_1, x_2) = 1 + \zeta(D_\omega)|g^{(1)}(x_1, x_2)|^2 \tag{7.5}$$

where $g^{(1)}(x_1, x_2) = \mu(x_1, x_2) =< E^*(x_1)E(x_2) > / \sqrt{(I(x_1)I(x_2))}$ is the first-order correlation function and $\zeta(D_\omega)$ is the contrast function, which depends on the radiation bandwidth D_ω.

7.2 Application of Gaussian Schell-model in HBT interferometry at FELs

The HBT method for the FEL pulses may be described in the frame of the Gaussian Schell-model (GSM). In this case the cross-spectral density in the spatial-frequency domain can be written as [65, 158, 159]

$$W_{in}(x_1, x_2; \omega_1, \omega_2) = W_0 W(x_1, x_2) W(\omega_1, \omega_2), \tag{7.6}$$

where W_0 is the normalization constant and spatial dependence is defined by the function

$$W(x_1, x_2) = exp\Big[- \frac{x_1^2 + x_2^2}{4\sigma_i^2} - \frac{(x_2 - x_1)^2}{2L_{coh}^2} \Big]. \tag{7.7}$$

Here σ_I is the root mean square (rms) size and $L_coh = \xi$ is the spatial coherence of the incoming beam. The frequency dependence is defined by

$$W(\omega_1, \omega_2) = exp\Big[- \frac{\omega_1^2 + \omega_2^2}{4\Omega^2} - \frac{(\omega_2 - \omega_1)^2}{2\Omega_c^2} \Big], \tag{7.8}$$

where Ω_c is the rms spectral width of radiation, Ω_c is the spectral coherence, and it is assumed that the frequency is counted from the central frequency ω_0. Together with the cross-spectral density $W_{in}(x_1, x_2; \omega_1, \omega_2)$ in Eq. (7.6) the spectral density functions both in spatial and frequency domains can be introduced as

$$S_{in}(x) = W_{in}(x, x), \quad S_{in}(\omega) = W_{in}(\omega, \omega). \tag{7.9}$$

It should be mentioned here that the cross-spectral density in spatial $W_{in}(x_1, x_2)$ and frequency $W_{in}(\omega_1, \omega_2)$ domains is defined through its first-order correlation functions, $g_{in}^{(1)}(x_1, x_2)$ and $g_{in}^{(1)}(\omega_1, \omega_2)$, respectively, as

$$\begin{aligned} W_{in}(x_1, x_2) &= [S_{in}(x_1)]^{1/2} [S_{in}(x_2)]^{1/2} g_{in}^{(1)}(x_1, x_2), \\ W_{in}(\omega_1, \omega_2) &= [S_{in}(\omega_1)]^{1/2} [S_{in}(\omega_2)]^{1/2} g_{in}^{(1)}(\omega_1, \omega_2). \end{aligned} \tag{7.10}$$

Here, the first-order correlation functions are defined as

$$g_{in}^{(1)}(x_1, x_2) = \frac{< E_{in}^*(x_1) E_{in}(x_2) >}{\sqrt{|E_{in}(x_1)|^2} \sqrt{|E_{in}(x_2)|^2}}, \quad g_{in}^{(1)}(\omega_1, \omega_2) = \frac{< E_{in}^*(\omega_1) E_{in}(\omega_2) >}{\sqrt{|E_{in}(\omega_1)|^2} \sqrt{|E_{in}(\omega_2)|^2}}, \tag{7.11}$$

where $E_{in}(x)$ and $E_{in}(\omega)$ are the amplitudes of the incoming fields. The parameters Ω and Ω_c in Eq. (7.8) can be also expressed through the rms values of the pulse duration σ_T and coherence time τ_c of the pulse in front of the monochromator as [158, 159]

$$\Omega^2 = \frac{1}{\tau_c^2} + \frac{1}{4\sigma_T^2}, \quad \Omega_c = \frac{\tau_c}{\sigma_T} \Omega \tag{7.12}$$

For the SASE pulses at XFELs in most of the cases the coherence time τ_c is much shorter than the pulse duration σ_T ($\tau_c \ll \sigma_T$). Taking this into account we have from Eqs. (7.12)

$$\Omega \approx \frac{1}{\tau_c}, \;\; \Omega_c \approx \frac{1}{\sigma_T} \tag{7.13}$$

In this limit, taking into account Eqs. (7.6-7.10), one can rewrite the spectral density in frequency domain as

$$S_{in}(\omega) = S_0 exp\Big[- \frac{\tau_c^2 \omega^2}{2} \Big] \tag{7.14}$$

and the second-order correlation function as

$$g^{(2)}(\omega_2 - \omega_1) = exp\Big[- \frac{\sigma_T^2 (\omega_2 - \omega_1)^2}{2} \Big]. \tag{7.15}$$

In the next section, deriviations accroding to [59] will be presented of the second-order correlation functions taking into account the finite energy resolution of the monochromator unit. Hereafter, frequency and spatial domains will be considered separately.

7.3 Second-order correlation functions in frequency domain and the monochromator resolution

The normalized second-order correlation function $g^{(2)}(\omega_1, \omega_2)$ in frequency domain can be defined as

$$g^{(2)}(\omega_1, \omega_2) = \frac{< S(\omega_1) S(\omega_2) >}{< S(\omega_1) >< S(\omega_2) >}, \tag{7.16}$$

where $S(\omega)$ is a spectral density. As it is shown in [59] (see appendix B), this $g^{(2)}$-function for chaotic light can be expressed through the correlation functions of the beam incoming on the monochromator unit as

$$g^{(2)}(\omega_1, \omega_2) = 1 + \zeta g_{in}(\omega_1, \omega_2) \tag{7.17}$$

Here ζ is the degree of spatial coherence of the incoming X-ray beam [68]

$$\zeta = \frac{\int\int |W_{in}(x', x'')|^2 dx' dx''}{[\int S_{in}(x) dx]^2} \tag{7.18}$$

and

$$g_{in}(\omega_1, \omega_2) = \frac{\int\int R(\omega_1 - \omega') R(\omega_2 - \omega'') |W_{in}(\omega', \omega'')|^2 d\omega' d\omega''}{\int R(\omega_1 - \omega') S_{in}(\omega') d\omega' \int R(\omega_2 - \omega') S_{in}(\omega') d\omega'}, \tag{7.19}$$

where $R(\omega)$ is the resolution function of the monochromator. In the following, the resolution function is considered to be a Gaussian function with the root mean square (rms) value σ_r

$$R(\omega) = exp\Big(- \frac{\omega^2}{2\sigma_r^2} \Big). \tag{7.20}$$

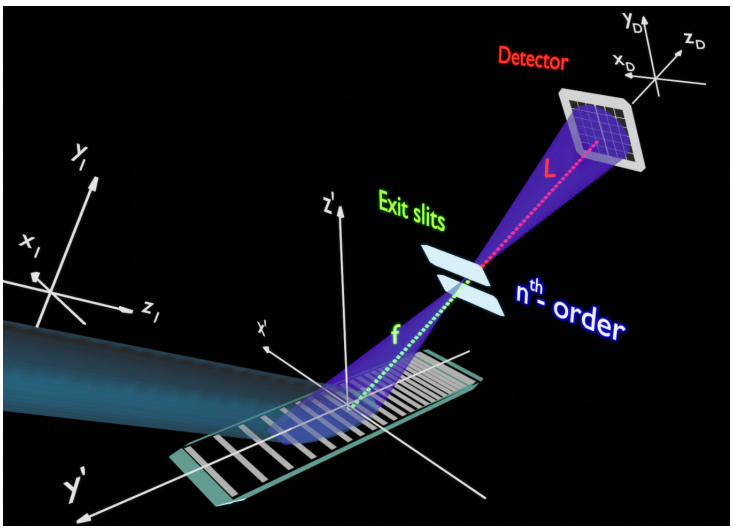

Figure 7.2: Schematic layout of the HBT experiment performed at the XFEL facility. The incoming beam is scattered on the VLS grating. The exit slits are positioned at the focal plane of the VLS grating at the grating order n. The second-order spatial correlation measurements are performed by the pixelated detector positioned far from the monochromator unit to resolve spatial modes of the incoming x-ray pulses. The coordinate systems for the incoming beam, the grating, and detector are shown.

It can be shown [59], that in the case of Gaussian Schell-model pulses the function $g^{(1)}_{in}(\omega_1, \omega_2)$ in Eq. (7.19) can be expressed as

$$g^{(1)}_{in}(\omega_1, \omega_2) = \frac{exp\left[- \frac{\sigma_T^2}{1+4\sigma_r^2\sigma_T^2}(\omega_2 - \omega_1)^2 \right]}{(1 + 4\sigma_r^2\sigma_T^2)^{1/2}} \tag{7.21}$$

Equation (7.21) was obtained in the limit $\sigma_r \tau_c \ll 1$. This condition is well satisfied for the typical SASE pulses of an XFEL. Equations (7.16-7.21) were used in the analysis of the EuXFEL pulses in frequency domain. Here, it should be noted, that if one can neglect the monochromator resolution (by putting $\sigma_r = 0$) then the function $g^{(1)}_{in}(\omega_1, \omega_2)$ in Eq. (7.21) can be expressed through the function $g^{(1)}_{in}(\omega_2 - \omega_1)$ defined in Eq. (7.15) as

$$g_{in}(\omega_1, \omega_2) = exp[-\sigma_T^2(\omega_2 - \omega_1)^2] = |g^{(1)}_{in}(\omega_2 - \omega_1)|^2. \tag{7.22}$$

7.4 Second-order correlation functions in spatial domain

In the HBT experiment at the FELs the intensities measured at the detector, if located far from the monochromator unit $I_D(x^D)$ (x^D are coordinates at this detector), may be correlated to determine the normalized second-order correlation function as

$$g^{(2)}(x_1^D, x_2^D) = \frac{< I_D(x_1^D) I_D(x_2^D) >}{< I_D(x_1^D) >< I_D(x_2^D) >} \tag{7.23}$$

The intensities $I_D(x^D)$ are determined after projecting the intensities measured on the two-dimensional pixelized detector along the vertical (dispersion) direction. It can be shown [59], that the $g^{(2)}$-function defined in Eq. (7.23) can be related to the statistical properties of the incoming on the monochromator unit pulses as

$$g^{(2)}(x_1^D, x_2^D) = 1 + \zeta_{in}(D_\omega)|g_{in}(x_1^D, x_2^D)|^2. \tag{7.24}$$

In this expression, the contrast function $\zeta_{in}(D_\omega)$, which depends on the radiation bandwidth D_ω, is defined as

$$\zeta_{in}(D_\omega) = \frac{\iint \tilde{T}_{sl}(\omega_1)\tilde{T}_{sl}(\omega_2)|W_{in}(\omega_1,\omega_2)|^2 d\omega_1 d\omega_2}{[\int \tilde{T}_{sl}(\omega)S_{in}(\omega)d\omega]^2} \tag{7.25}$$

In Eq. (7.25) the function $\tilde{T}_{sl}(\omega)$ is determined as

$$\tilde{T}_{sl}(\omega) = T_{sl}^2(\omega) \otimes R(\omega) = \int T_{sl}^2(\omega')R(\omega-\omega')d\omega' \tag{7.26}$$

where $\otimes$ is the convolution sign. The transmission function of the slits $T_{sl}(\omega)$ in Eq. (7.26) is defined as a finite window in the spectral domain of the size of the spectral bandpass D_ω^{sl} as

$$T_{sl}(\omega) = rect\left[\frac{\omega}{D_\omega^{sl}}\right], \tag{7.27}$$

where $rect(x)$ is the rectangular function. The expression (7.26) means that when the spectral bandpass of the slits D_ω^{sl} is much wider than the resolution function,$D_\omega^{sl} \gg \sigma_r$, then the bandpass will be defined by the bandpass of the slits D_ω^{sl}. In the opposite case, when $D_\omega^{sl} \ll \sigma_r$, the bandpass will be determined by the resolution function $R(\omega)$. This means that by closing the slits one can reduce the bandwidth up to some limit defined by the resolution function of the monochromator unit. In Eq. (7.24) the correlation function $g_{in}(x_1^D, x_2^D)$ is determined by

$$g_{in}(x_1^D, x_2^D) = \frac{\iint P_{f+L}^*(x_1^D - x_1)P_{f+L}(x_2^D - x_2)W_{in}(x_1,x_2)dx_1dx_2}{[S_D(x_1^D)]^{1/2}[S_D(x_2^D)]^{1/2}}, \tag{7.28}$$

where

$$S_D(x_i^D) = \iint P_{f+L}^*(x_i^D - x_1)P_{f+L}(x_i^D - x_2)W_{in}(x_1,x_2)dx_1dx_2 \tag{7.29}$$

and i=1,2. In Eqs. (7.28,7.29)

$$P_L(x-x') = \left(\frac{-ik}{2\pi L}\right)^{1/2} exp\left[i\frac{k}{2L}(x-x')^2\right] \tag{7.30}$$

is the propagator of the field in free space for the distance L, $k = 2\pi/\lambda$ is the wavenumber, and λ is the wavelength of X-ray radiation. In Eqs. (7.28, 7.29) f is the focal distance from the VLS grating to the focal position (see Fig. 7.2) of this grating and L is the distance from the exit slits (that are positioned in the focal plane of the VLS grating) to the detector.

It can be shown [59] , that in the case of Gaussian Schell-model the contrast function $\zeta_{in}(D_\omega)$ in Eq. (7.25) can be expressed as

$$\zeta_{in}(D_\omega) = \frac{\int_{-\infty}^{\infty} F(\omega)|g_{in}^{(1)}(\omega)|^2 d\omega}{\left[\int_{-\infty}^{\infty} \tilde{\tilde{T}}(\omega)d\omega\right]^2}, \tag{7.31}$$

where $F(\omega)$ is the autocorrelation function

$$F(\omega) = \int_{-\infty}^{\infty} \tilde{\tilde{T}}(\omega')\tilde{\tilde{T}}(\omega'+\omega)d\omega' \tag{7.32}$$

the function $\tilde{\tilde{T}}(\omega)$ is defined as

$$\tilde{\tilde{T}}(\omega) = S_{in}(\omega)\tilde{T}_{sl}(\omega) \tag{7.33}$$

and the function $g_{in}^{(1)}(\omega)$ is defined in Eq. (7.15).

In the HBT interferometry the contrast values are determined directly from the experiment for different exit slit opening from the relation (7.24). In order to estimate the pulse duration, these contrast values should be fitted by Eq. (7.31).

7.5 Coherence time

According to Wiener–Khinchin theorem, the complex degree of coherence may be determined through the average spectral density $S(\omega)$ as

$$\gamma(\tau) = \frac{\int_0^\infty S(\omega)e^{-i\omega\tau}d\omega}{\int_0^\infty S(\omega)d\omega}. \tag{7.34}$$

In the statistical optics coherence time is defined through the complex degree of coherence $\gamma(\tau)$ as [8, 55]

$$\tau_c = \int_{-\infty}^{\infty} |\gamma(\tau)|^2. \tag{7.35}$$

In this way, the coherence times may be determined for simple spectrum shapes [55]. For example, if the spectrum has a rectangular shape, then $\tau_c = 2\pi/D_\omega$, where D_ω is the width of the spectrum; if the spectrum is Gaussian then $\tau_c = \sqrt{\pi}/\sigma_\omega$, where σ_ω is the rms value of the Gaussian spectrum.

In the case, when the spectral density maybe presented in the form of a sum of two Gaussian functions,

$$S(\omega) = A_1 exp\left[-\frac{(\omega-\omega_1^0)^2}{2\sigma_1^2}\right] + A_2 exp\left[-\frac{(\omega-\omega_2^0)^2}{2\sigma_2^2}\right], \tag{7.36}$$

where A_1 and A_2 are scaling coefficients, ω_1^0 and ω_2^0 are the centers of each Gaussian line and σ_1 and σ_2 are their rms values, the coherence time may be found using Eqs. (7.35)- (7.36) as

$$\tau_c = \frac{\sqrt{\pi}}{[A_1\sigma_1 + A_2\sigma_2]^2}\left\{A_1^2\sigma_1 + A_2^2\sigma_2 + \frac{2\sqrt{2}A_1A_2\sigma_1\sigma_2}{\sqrt{\sigma_1^2+\sigma_2^2}} exp\left[\frac{\Delta\omega_0^2}{2(\sigma_1^2+\sigma_2^2)}\right]\right\}, \tag{7.37}$$

where $\Delta\omega_0 = \omega_2^0 - \omega_1^0$.

Chapter 8

Hanbury Brown and Twiss interferometry at EuXFEL

One of the most challenging tasks for the XFEL photon diagnostics is the precise determination of the photon source parameters. Understanding the properties of recently constructed XFEL facilities [100, 101, 160, 161] appears vital as many experiments rely on the high degree of coherence and short pulse durations of these sources. The radiation source at XFEL possesses a unique temporal structure. Therefore, there is a significant demand for developing adequate and effective methods that correctly describe radiation properties from such ultimate facilities.

An excellent approach and the analysis method, providing the information about the photon source, lies within the framework of statistical optics. Various phenomena occurring with light propagating in free space, interaction with optical systems, extended media, and particle bunching are discussed within this framework. In general, an approach within statistical optics includes rigorous mathematical methods applicable for the statistical analysis of a photon source.The first-order coherence properties of these sources were determined in double pinhole Young's experiments [94, 98] or by the speckle contrast analysis [162, 163]. By performing HBT experiments at XFEL sources, rich information on their statistical properties, such as the degree of spatial coherence and average pulse duration, can be determined [131, 133, 164, 165] (see for review [65]). These experiments may also shed light on the fundamental statistical properties of XFEL sources and clearly indicate whether an FEL behaves as a true single-mode laser source or rather as a chaotic source of radiation [132]. This chapter is dedicated to a comprehensive statistical analysis of experimental results for the high-power European XFEL (EuXFEL) radiation utilizing HBT interferometry. The HBT method was applied in both the spectral and spatial domains. As a result, three XFEL operation modes were characterized, involving linear (LT) and quadratic (QT) undulator tapering at saturation, as well as the operation in the linear gain regime (LR). Finally, the degree of coherence and characteristic pulse durations for all three regimes were determined.

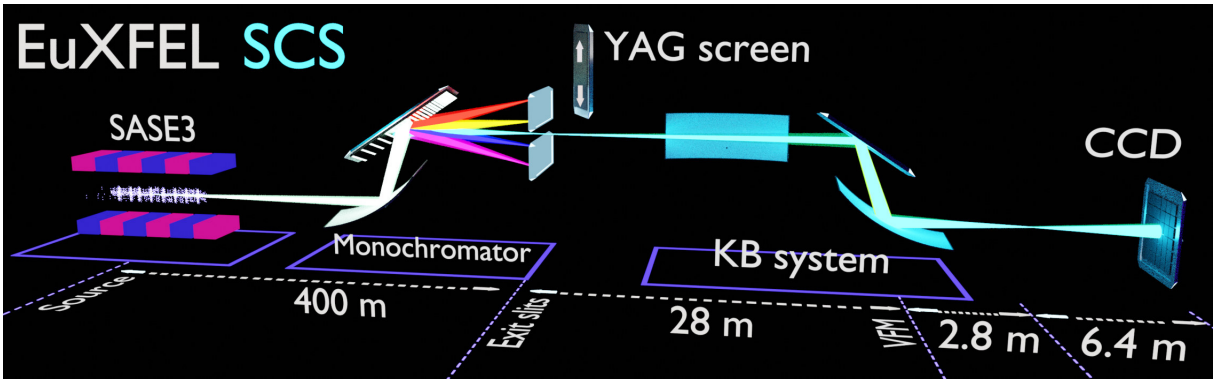

Figure 8.1: Schematic layout of the experiment. The monochromator focuses the SASE3 undulator source located about 300 m upstream onto the exit slits (ES) located 100 m downstream. Vertical focusing mirror (VFM), part of a variable bending mirrors Kirkpatrick-Baez (KB) system, located 28 m downstream from the ES, refocuses the x-ray beam at 2.8 m downstream from this mirror. The measurements were taken at a distance of about 6.4 m from the focal position. Horizontal KB focusing mirror located 1.35 m upstream of the VFM, refocuses the intermediate horizontal focus located at 374 m after the undulator source.

8.1 Experiment

The HBT experiment was carried out at the European XFEL's Spectroscopy and Coherent Scattering (SCS) instrument. The EuXFEL linac was operated at 14 GeV electron energy with an electron bunch charge of 250 pC in a single bunch mode at a 10 Hz repetition rate. The SCS instrument is located at the SASE3 undulator beamline, producing intense X-ray pulses in the soft X-ray photon energy range (250 eV - 3000 eV). A schematic representation of the beamline is shown in Fig. 8.1. The experiment was performed at 1.2 keV photon energy with three undulator configurations, i.e., LT and QT at saturation which are dedicated settings to provide high power radiation, and a configuration for operating the XFEL in the LR with the average pulse energies of 1.2 mJ, 6.5 mJ, and 0.117 mJ, respectively (see Fig. 8.2 for details).

The SCS instrument is equipped with a variable line spacing (VLS) diffraction grating monochromator [166, 167]. The monochromator was operating in the second diffraction order, corresponding to a photon energy dispersion of 2.69 eV/mm in the exit slit (ES) plane along the vertical direction. The experimental resolution at this energy was estimated to be better than 0.3 eV at the full-width at half maximum (FWHM) (theoretical resolution at this energy is 0.2 eV [167]). In the case of spectral measurements, the spectral distribution of XFEL pulses were acquired in the ES plane of the monochromator. This was achieved by introducing a YAG:Ce crystal just behind the fully opened ES and detecting the optical luminescence from this crystal by a charge coupled device (CCD) gated by a microchannel plate (MCP) detector.

Spatial second-order correlation measurements were performed using a back-illuminated CCD detector (Andor iKon-M 934, 1024×1024 pixels, pixel size of 13×13 μm^2) with 8 pixels binned in the vertical direction and no binning in the horizontal direction. The detector was located at the end of the beamline at a distance of about 6.4 m from the X-ray beam focus. The bending of the horizontal Kirkpatrick-Baez (KB) mirror was adjusted for QT and LT/LR measurements, thus changing the horizontal size of the beam on the detector (Fig. 1). In the

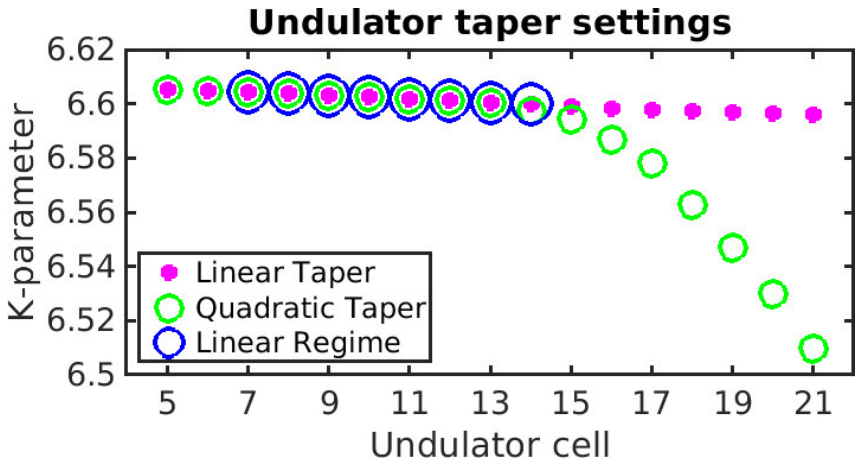

Figure 8.2: K-values of the SASE3 undulators, used during the HBT experiment at EuXFEL. For linear (magenta dots) and quadratic (green circles) tapering in saturation regime cells 5-21 were used and in linear regime (blue circles) cells 7-14 were used.

case of spatial correlation measurements, the bandwidth of X-ray radiation at the CCD detector was controlled by the size of the monochromator ES opening.

8.1.1 Undulator settings explored in the experiment

The soft X-ray undulator beamline SASE3 of the European XFEL consists of 21 undulator cells each being 6.1 m long. The magnetic structures are 5 m long followed by a 1.1 m long intersection with a quadrupole magnet, a phase shifter, horizontal and vertical air coil correction magnets as well as a beam position monitor. The K-parameter of the individual cells can be changed by the variable gaps of the undulators. The undulator period length is 68 mm [168]. All measurements of this experiment have been carried out with a photon energy of 1.2 keV. This required the undulator gaps between 15.73 mm and 16.2 mm depending on the undulator cells position as well as on the taper setting. The gaps of the first 4 undulator cells were not closed during the whole experiment. The undulator cells 5-21 were used for the first two measurement steps with the linear (LT) and quadratic (QT) tapering. These 17 cells delivered sufficient pulse energy as well as a single spot on a downstream FEL imager with no halos, which is an indication that the beams trajectory through the undulator is straight. For the LT and QT, the undulator cells 5 to 13 were tapered linearly using the same K-parameters. The taper settings differ only in the cells 14 to 21 as shown in Fig. 8.2. The respective tapering settings were found by optimization of the SASE pulse energy signal, first with linear tapering only, and then including the quadratic taper starting from cell 14. The measurement in the linear gain regime (LR) was carried out using the undulator cells 7 to 14 with a LT as presented in Fig. 8.2.

8.1.2 Monochromator at the SCS instrument

The experiment has been performed at the SASE3 undulator beamline of European XFEL in the monochromatic mode of operation. The SASE3 beamline is equipped with a plane grating

monochromator which consists of elliptical focusing mirror and the plane variable line spacing (VLS) grating [169]. The elliptical mirror focuses the undulator source located at about 300 m upstream onto the exit slit located 100 m downstream, and the grating disperses the beam in the vertical plane. Presently, the monochromator is equipped with a provisional 140 mm long grating [167] which cuts the beam vertically. In this experiment about 1.4 – 2 rms values of the vertical beam size have been transmitted by the grating. In the horizontal direction, where spatial correlation measurements were performed, the beam was not cut by the monochromator. The monochromator was operating at 1200 eV in the 2-nd diffraction order. The grazing angle of incidence and diffraction were 18.03 mrad and 21.97 mrad, respectively. Thus, the grating of 140 mm length was transmitting 2.52 millimeters of the vertical beam size. The FWHM of the vertical beam size at the grating position was estimated to be about 4.2 mm for LT, 3.4 mm for QT, and 2.5 mm for LR. This would lead to geometrical cut by the grating in the vertical direction to about of 1.4 rms of the vertical beam size for LT, 1.8 for QT, and 2.4 for LR, respectively. Note that the beam was not centered on the grating vertically.

8.2 Spectral analysis

Single-pulse spectra were recorded for all three regimes of the EuXFEL operation prior to spatial measurements by introducing YAG screen (see Fig. 8.1). Each run consisted of about $3{\cdot}10^3$ pulses for each operating condition of the EuXFEL. Below the results of spectral and spatial measurements for all regimes are presented. As shown in Fig. 8.3 (a,c,e), one can observe a multimodal structure in the single pulse spectrum intensity distribution for all operating regimes of the EuXFEL. The number of spectral modes varies depending on the operation conditions. As it is well seen in Fig. 8.3 (a,c,e), the average spectrum does not resemble a single Gaussian function but is rather a sum of two distributions, which applies for all operating conditions. The FWHM of the average normalized spectrum was estimated directly from the experimental data which was in the range of 0.7% - 1% from the resonant energy, depending on the experimental conditions (see Table 8.1). This spectrum is about three times wider than the theoretically predicted one for the SASE3 undulator [170], which may be affected by the energy chirp of the beam (see simulation section C). The knowledge of the average spectrum allows one to estimate the coherence time of X-ray radiation as according to Eq. 7.35. The average spectrum was fitted by the sum of two Gaussian functions to determine the coherence time in each operating condition of the SASE3 undulator. For all three operation conditions the coherence time was in the range from 200 as to 300 as.

To determine the bandwidth of single spike spectral lines the autocorrelation analysis of the spectra was performed. The result of this analysis for all regimes is shown in Fig. 8.3 (b,d,f). This was done in the following way: the autocorrelation function for each pulse spectral line was evaluated first and then it was averaged over all pulses. Similar features are observed for the autocorrelation functions determined in such a way for all three regimes of SASE3 operation. In Fig. 8.3 (b,d,f) one can observe a sharp peak, corresponding to the averaged single spike spectral lines, positioned on the top of a broad peak, which corresponds to the average

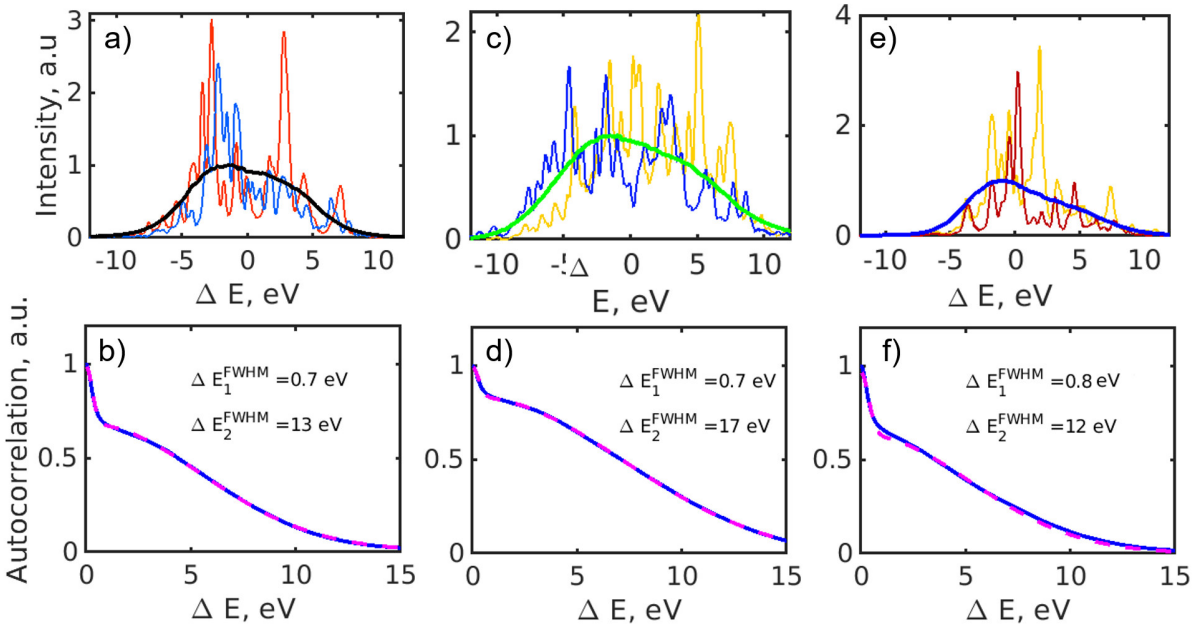

Figure 8.3: (a, c, e) Typical single shot spectra for different operation regimes of SASE3 beamline and an average spectrum of about $3 \cdot 10^3$ pulses. (b, d, f) Autocorrelation function of individual spectral lines averaged over $3 \cdot 10^3$ pulses (blue solid line) and the fit with the sum of two Gaussian functions (magenta dashed line). The FWHM values of the Gaussian fits are also given. Here (a, b) refer to LT, (c, d) to QT, and (e, f) to LR of the SASE3 undulator settings.

spectrum. By fitting these peaks with Gaussian functions one can determine an average width of both spectral lines. An average width of the peaks in spectra ΔE is related to the width of the peaks determined from the autocorrelation function ΔE_{ACF}, by $\Delta E = \Delta E_{ACF}/\sqrt{2}$. The narrowest value of the sharp peak was measured in the regime of QT with the value of 0.45 eV, which, in this case, is close to the monochromator resolution of 0.3eV. Therefore, in this regime the limit of sufficient resolution for the fine structure of the spectrum was reached. The bandwidth of radiation was determined from the autocorrelation analysis of the spectra by Gaussian fit of the broad peaks. For the LT and LR the radiation bandwidth is almost the same, 9.3 eV and 8.7 eV, respectively, and for the regime with QT it is 12 eV (see Table 8.1). The values of the FWHM of both peaks corrected for the factor of $\sqrt{2}$ are provided in Table 8.1.

The average pulse duration in spectral domain was determined by performing correlation analysis [59] (according to Eq. 7.16). The second-order correlation functions in the frequency domain for all cases are presented in Fig. 8.4. In Fig. 8.4 (b,d,f) the behavior along the white dashed diagonal line of the second-order correlation function in Fig 8.4 (a,c,e) is shown. Note, that the contrast value is below unity for all three undulator settings due to the finite degree of coherence in spatial domain and monochromator resolution function (see Appendix Eqs. (7.17-7.19).

These profiles were fitted by expressions (7.17) and (7.21) assuming the FWHM resolution function $R(\omega)$ of 0.3 eV. The values of the degree of coherence ζ_{in} were determined from the spatial analysis discussed below, but set to unity during the fitting procedure. The latter was done due to artifacts from spectrometer, influencing the contrast values. As a result of this

Table 8.1: Results of the analysis in spectral and spatial domains for LT, QT, and LR operation regimes. Parameters determined from the analysis of autocorrelation function are noted as "ACF". Parameters specified from the HBT analysis in spectral and spatial domains are indicated as 'spec' and 'spat' accordingly.

Operation regime	LT	QT	LR
Photon energy, eV	1205	1205	1202
Spectral analysis			
FEL bandwidth (FWHM), eV	10.0 ± 0.1	12.6±0.1	8.8±0.1
Width of spectrum from^{ACF} (FWHM), eV	9.2±0.1	12.0±0.1	8.5±0.1
Width of spike spectral lines^{ACF} (FWHM), eV	0.49±0.02	0.49±0.02	0.57±0.02
Coherence time (rms), as	309±7	235±5	316±7
Pulse duration T_{spec} (FWHM), fs	6.56±0.2	5.86±	4.86±0.1
Spatial analysis			
Average beam size (FWHM), mm	2.3±0.03	1.7±0.02	2.2±0.03
Coherence length (rms), mm	2.4±0.1	1.3±0.4	2.6±0.2
Degree of spatial coherence, %	91.6±3	71±5	89±3
Pulse duration T_{spat} (FWHM), fs	8.5±1.1	12.8±1.5	7.3±1.2

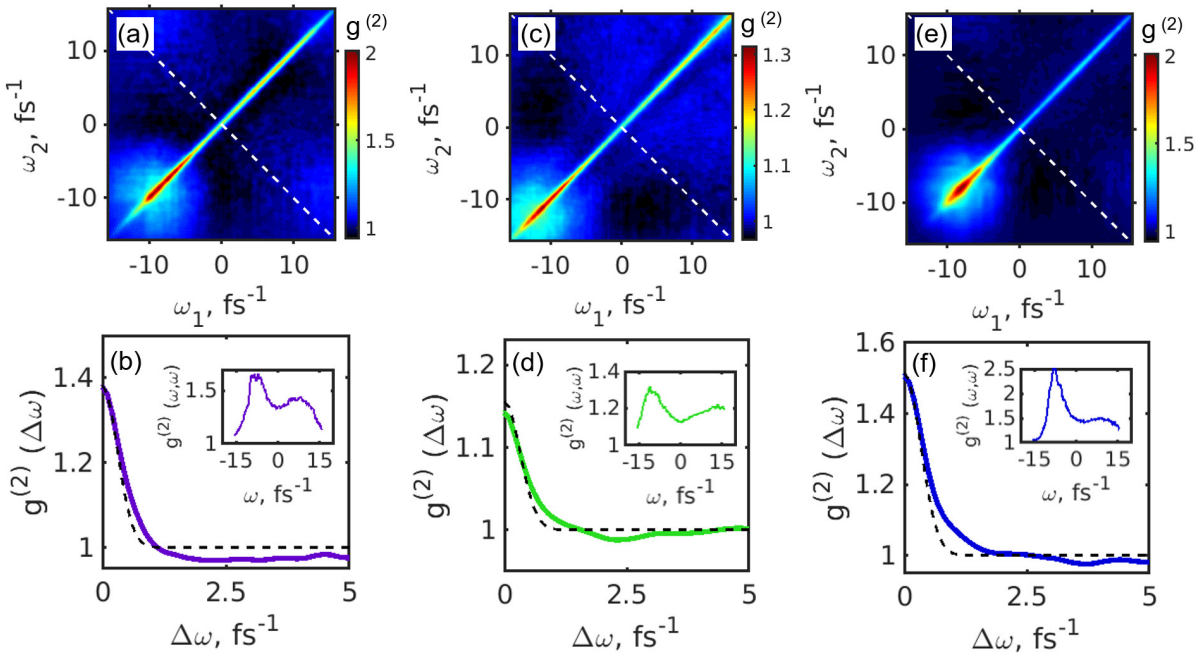

Figure 8.4: (a, c, e) Intensity correlation functions of spectra $g^{(2)}(\omega_1, \omega_2)$. (b, d, f) Cut along the anti-diagonal lines shown by the white dashed lines in (a, c, e) and its fit with the profile given in Eqs. (7.17, 7.21) (black dashed line). In the inset the profiles along the diagonal of the $g^{(2)}(\omega, \omega)$ function in (a, c, e) are shown. Here (a, b) refer to LT, (c, d) to QT, and (e, f) to LR of the SASE3 undulator settings. In the analysis the assumed resolution of the monochromator unit is 0.3 eV (FWHM).

fitting by Eq. (7.21) (see Fig. 8.4 (b,d,f)) we determined the rms values σ_T of an average pulse duration, from which the FWHM values ($T_{FWHM} = 2.355\sigma_T$) were deduced. The FWHM values ($T_{FWHM} = 2.355\sigma_T$) lie in the range from 4.9 fs to 6.6 fs depending on the undulator setting (see Table 8.1). The measurements were performed by the YAG:Ce crystal positioned behind the fully opened exit slits of the monochromator. The optical luminescence from this crystal was detected by a charge coupled device (CCD) gated by a microchannel plate (MCP) detector. This scheme does not provide high resolution measurements, especially for the QT regime, when a non-linear response of the detection system may affect the results of the measurements. Due to this detection scheme adapted at the EuXFEL values of the transverse degree of coherence and the contrast were set to unity in the expression (7.17) during the fitting procedure. The histogram of the pulse intensities was evaluated for the linear regime of operation from the spectral measurements (see Fig. 8.5). This histogram was compared with the Gamma probability distribution function which describes statistical behavior of the FEL SASE radiation in the linear regime of operation

$$p\left(\frac{I}{< I >}\right) = \frac{M^M}{\Gamma(M)}\left(\frac{I}{< I >}\right)^{M-1} exp\left(-M\frac{I}{< I >}\right), \tag{8.1}$$

where I is the integrated intensity at the spectrometer camera for a single pulse, $< I >$ is the intensity averaged over many pulses, and M is the number of longitudinal modes of radiation. According to the FEL theory [111], the number of modes M is inversely proportional to the normalized dispersion of the intensity distribution

$$M = < I >^2 / \sigma_I^2, \tag{8.2}$$

where σ_I is the standard deviation of the intensity distribution. The number of modes obtained by this method in the linear regime of SASE3 undulator was M = 21. The Gamma probability distribution function with this number of modes is shown in Fig. 8.5. The intensity histogram is well described by the Gamma probability distribution in Eq. (8.1). It should be noted here that the observed spectrum of radiation from the SASE3 undulator is substantially wider than it was theoretically predicted [170]. It is attributed to a possible frequency chirp of radiation that will be further analyzed by simulations.

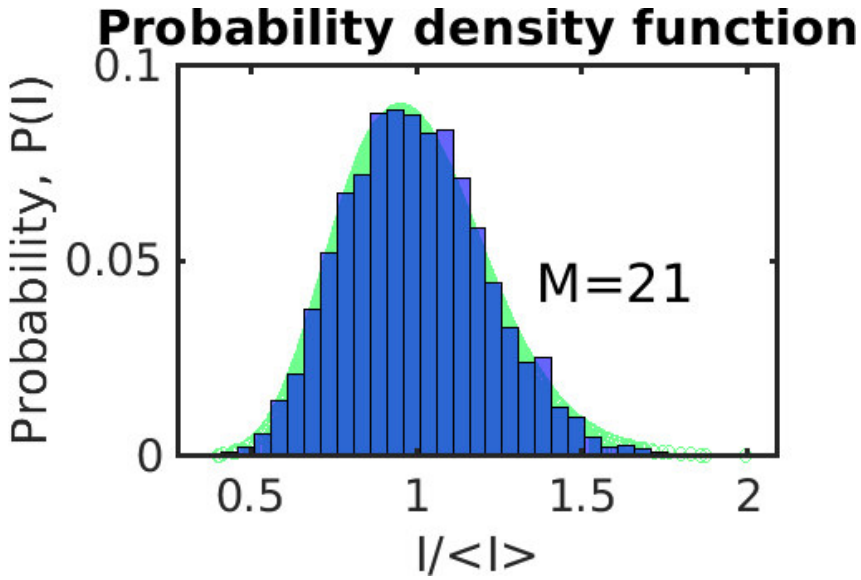

Figure 8.5: Histogram of the spectral pulse intensity distribution for the linear regime of the SASE3 operation. The green background corresponds to the Gamma probability distribution function with the number of modes M=21 that is inversely proportional to the normalized dispersion of the power distribution.

8.3 Transverse coherence properties at the EuXFEL

Transverse coherence properties at the EuXFEL were determined via spatial analysis from recorded intensity distributions (see Fig. 8.6).

In order to perform intensity correlation analysis, first, the CCD detector background (average dark signal) was determined and subtracted from all measured 2D intensities for each pulse. This led to the appearance of sparse negative values in the intensity distribution for some pulses. These 2D intensity distributions were then projected along the vertical (dispersion) direction and thus 1D intensity distributions were obtained. Next, the same constant intensity value was added to each pulse, in order to have values always larger or equal to zero. This constant value was determined as the maximum negative value in the 1D intensity distribution. These intensity distributions were used for the further spatial correlation analysis (see Eqs. (7.23, 7.24)). It should be noted that such data correction procedure does not change correlation between pulses.

Typical intensity distributions of individual pulses, measured with small and wide ES's width, are shown in Fig. 8.6. A visual inspection of the individual pulses reveals that between one and five spectral spikes were present in the XFEL beam at 2.5 mm wide ES's (see Fig. 8.6 (d-f)). For further intensity correlation analysis, these intensity distributions were projected along the vertical (dispersion) direction and correlation analysis was performed in the horizontal direction according to Eq. 7.4 for about 10^4 XFEL pulses.

The average pulse intensity distribution for different monochromator ES's width and typical intensity correlation $g^{(2)}$-function for the smallest ES's width of 0.02 mm in the LT mode are shown in Fig. 8.7. The growth of the average pulse intensity is clearly observed with the in-

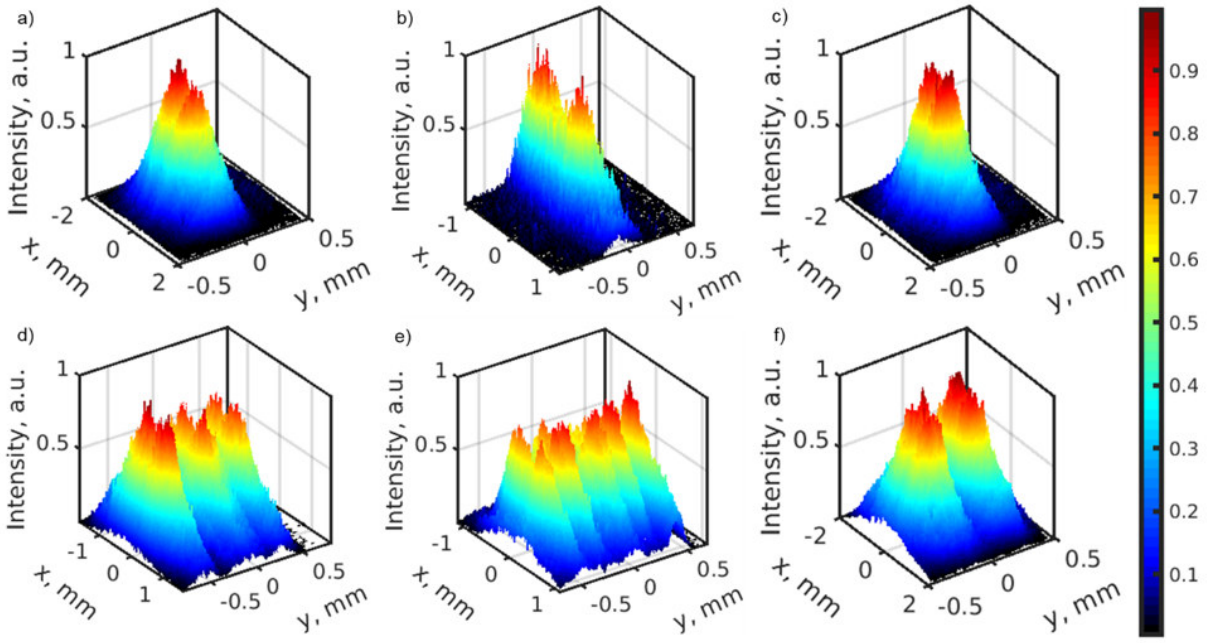

Figure 8.6: Typical intensity distribution of single pulses measured by the CCD detector for the slit opening of 20 μm (a-c) and slit opening 2.5 mm (d-f). Here (a, d) is LT, (b, e) is QT, and (c, f) is LR of the SASE3 undulator settings.

crease of the monochromator ES's width. The non-Gaussian shape of these intensity profiles is due to the slope error of the beam transport mirrors. The FWHM of the beam size was directly estimated from these profiles which was in the range from 1.7 mm to 2.3 mm, depending on the KB mirror settings and mode of the undulator operation (see Table 8.1).

As it can be seen from 8.7 (d, f) (see Fig. 8.7) the shape of the $g^{(2)}$)-function resembles a flat-top function. Such form of the $g^{(2)}$-function is typical for highly coherent radiation when the coherence length of radiation is much larger than the size of the beam (see section 3.2.3 and [91, 132].

In Fig. 8.8(a) the results of intensity correlation analysis for the LT mode as a function of the monochromator ES's width are presented (see Fig. 8.9 and Fig. 8.10 for the other operation regimes). The intensity correlation functions determined along the white dashed lines in Fig. 8.8(a) are presented in Fig. 8.8(b) for different ES's width. One can see that the larger the ES's width the lower is the contrast $\zeta(D_\omega)$ in Eq. (7.5) (that is the maximum value of the $g^{(2)}(\Delta x)$ function), which obeys the typical behavior predicted by this equation for a Gaussian chaotic source. Should be noted that for the separation of two points of about $\Delta x = 4$ mm, the correlation function $g^{(2)}(\Delta x)$ takes values below unity. These features are attributed to low values of intensity at these separations and to positional jitter of the beam [131].

A more detailed analysis of the $g^{(2)}$-function for each monochromator exit slit opening in QT and LR regimes of the SASE3 undulator operation is presented in Figs. (8.9)-(8.10). As it can be seen from Fig. 8.8 and Fig. 8.10, the $g^{(2)}$-function behaves in a similar way for the LT and LR. As a consequence, one can observe similar behavior of the contrast function and degree of coherence in these regimes of operation. When XFEL operates with QT of undulator settings,

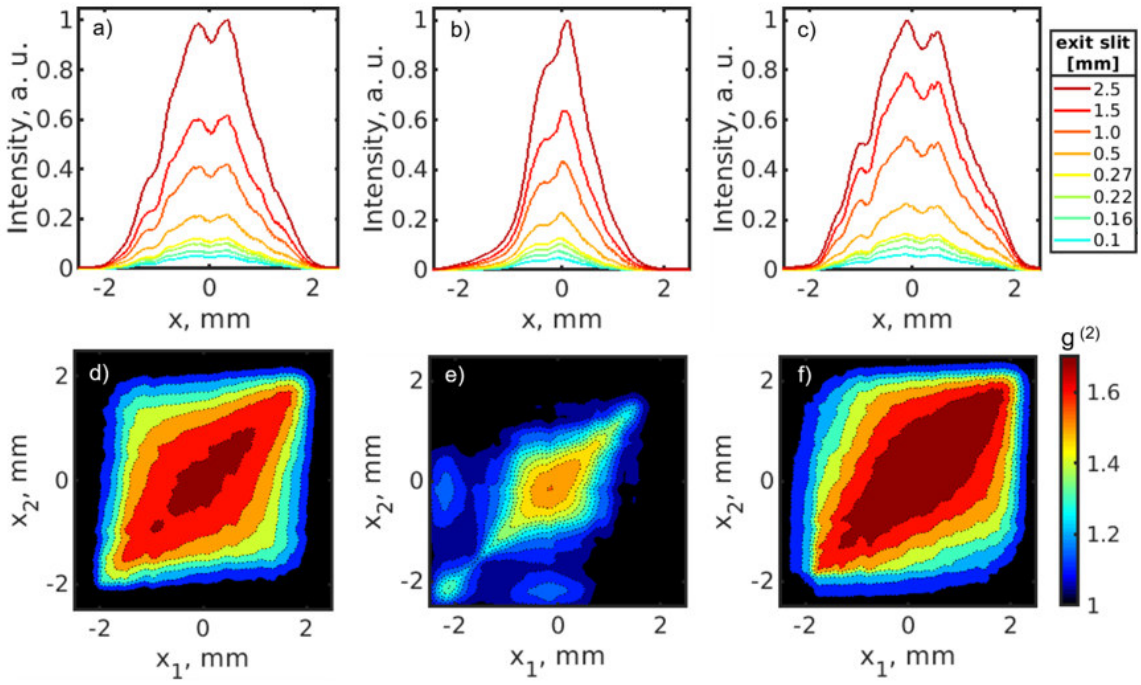

Figure 8.7: (a-c) Pulse intensities averaged over the vertical (dispersion) direction as a function of the slit opening. The top curve corresponds to the slit opening of 2.5 mm and the lowest one to the slit opening of 0.1 mm. (d-f) Intensity correlation function $g^{(2)}(x_1, x_2)$ for the exit slit opening of 0.02 mm measured by the CCD detector. Here (a, d) corresponds to LT, (b, e) to QT, and (c, f) to the LR of the SASE3 undulator settings.

the $g^{(2)}$-function looks more Gaussian (see Fig. 8.9). In this case the degree of coherence is slightly lower, but the behavior of the contrast as a function of the monochromator exit slit opening remains the same as for the LT and LR (see Fig. 8.11 (c-e)), which is typical for a chaotic source.

Next, the degree of spatial coherence ζ (according to Eq. (3.63) for definition) and the coherence length L_{coh} as a function of coherence time for all three undulator settings were determined (see Fig. 8.11). The coherence length L_{coh} was obtained as the variance value of the $g^{(2)}(\Delta x)$ function for different ES's width. The coherence time was determined according to Appendix Eqs. ((7.35), (7.34)), in which the spectral density $S(\omega)$ was substituted by the function $\tilde{T}_{sl}(\omega)$ defined in Eq. (7.26) that accounts for the finite monochromator resolution [59]. The first observation here is that the degree of spatial coherence and coherence length essentially do not depend on the coherence time, being practically constant in the range of coherence times from 1 fs to 12.8 fs. Second, one can see that the value of coherence length for the LT and LR settings was about the FWHM width of the corresponding beams. For the QT slightly smaller values of the coherence length were observed, which were also lower than the corresponding beam sizes (see Table 8.1). From these observations one may conclud that the degree of spatial coherence reaches high values of about 85-95% for the LT and LR modes. In the case of QT mode a slightly lower degree of spatial coherence of about 70% was observed. The values of contrast $\zeta(D_\omega) = g^{(2)}(x, x) - 1$ taken at x=0 as a function of coherence time for all three settings of the

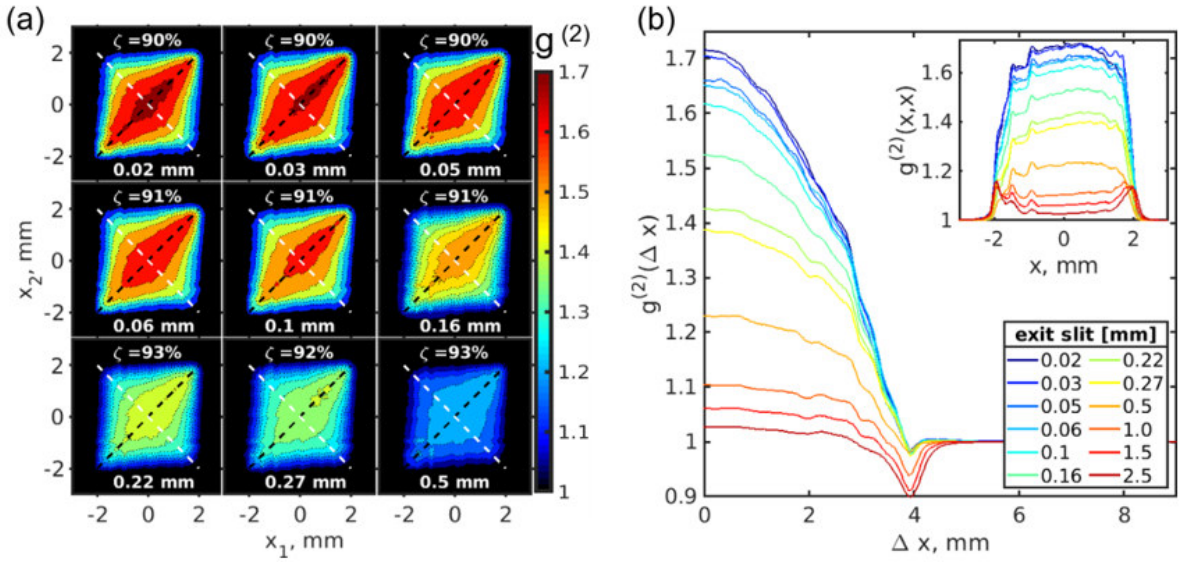

Figure 8.8: (a) Second-order intensity correlation functions $g^{(2)}(x_1, x_2)$ determined in measurements in the LT mode. Each panel corresponds to a certain width of the monochromator ES's. (b) Profiles of the $g^{(2)}(\Delta x)$ function taken along the white dashed anti-diagonal lines shown in panel (a) as a function of the ES's width. In the inset the corresponding $g^{(2)}(x, x)$-functions taken along the black dashed diagonal lines in panel (a) are shown.

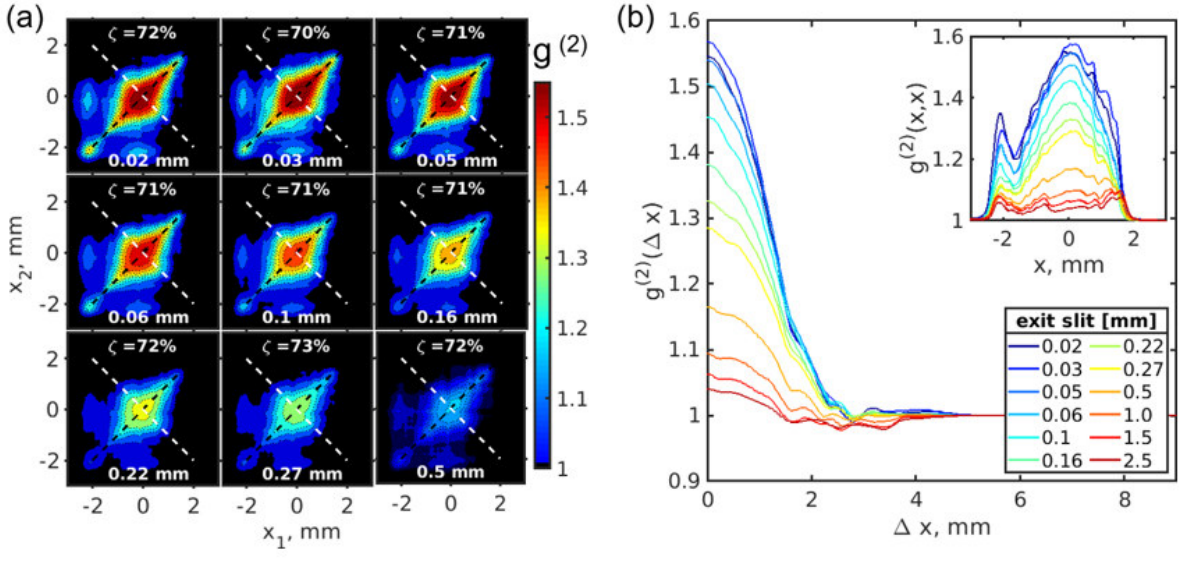

Figure 8.9: (a) Intensity correlation functions $g^{(2)}(x_1, x_2)$ measured by the CCD detector in the QT regime of the undulator settings, for different openings of the exit slit of the monochromator. (b) Profiles of the $g^{(2)}(\Delta x)$-function taken along the white dashed anti-diagonal lines shown in panel (a) as a function of the slit opening. In the inset the corresponding autocorrelation functions $g^{(2)}(x, x)$ taken along the black dashed diagonal lines in panel (a) are shown.

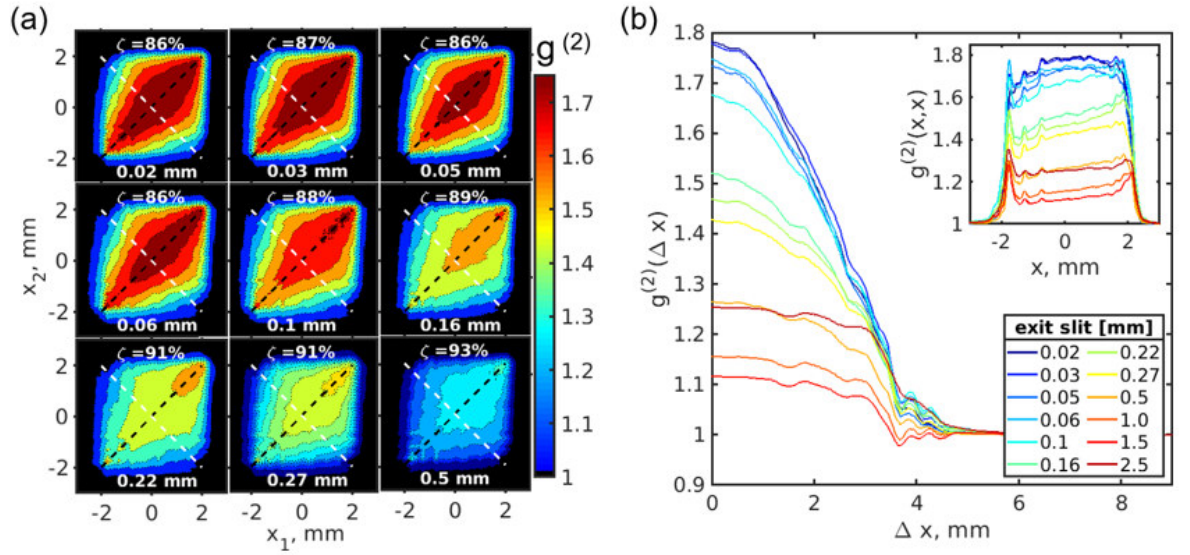

Figure 8.10: (a) Intensity correlation functions $g^{(2)}(x_1, x_2)$ measured by the CCD detector in the QT regime of the undulator settings, for different openings of the exit slit of the monochromator. (b) Profiles of the $g^{(2)}(\Delta x)$-function taken along the white dashed anti-diagonal lines shown in panel (a) as a function of the slit opening. In the inset the corresponding autocorrelation functions $g^{(2)}(x, x)$ taken along the black dashed diagonal lines in panel (a) are shown.

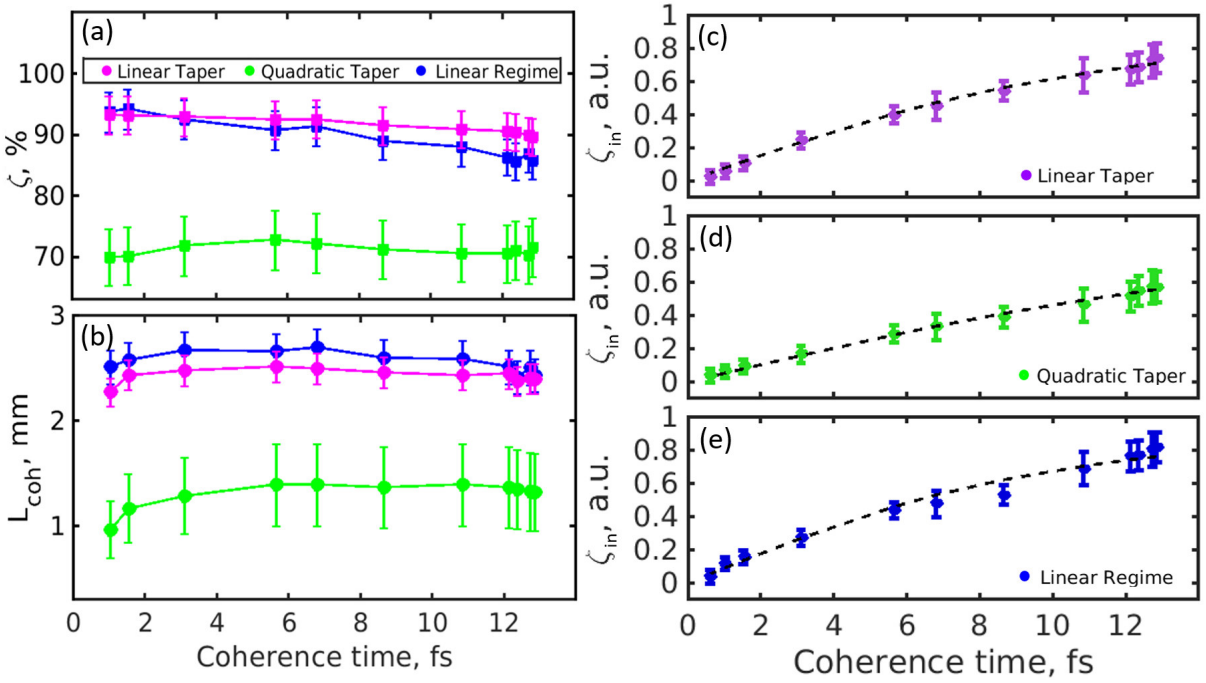

Figure 8.11: Degree of coherence (a) and coherence length (b) as a function of coherence time for different undulator operation modes. (c-e) Contrast values as a function of coherence time for different modes of undulator settings. (a) LT, (b) QT, and (c) LR of the undulator operation. Circles represent experimental points. Errors are calculated as the standard deviation of the contrast. The black dashed lines are the fit over all experimental data points according to Eq. (7.31)

undulators were evaluated in the last turn. As it is clearly visible from Fig. 8.11 (c-e) the values of contrast strongly depend on coherence time and show the typical behavior of a chaotic source [131, 133]. One may observe in Fig. 8.11 (c-e) that the contrast values do not reach the maximum value of unity at saturation, which is due to the finite resolution of the monochromator. Fitting the obtained contrast values with Eq. (7.31) and, assuming the resolution of the monochromator unit $R(\omega)$ to be 0.3 eV (see Eq. (7.20)), provides us with the average pulse duration values from about 7 fs to 13 fs for the different SASE3 undulator settings of the EuXFEL (see Table 8.1).

Additional simulations were carried out to investigate statistical properties of the SASE3 undulator at the EuXFEL and the behavior of the intensity correlation $g^{(2)}$-functions. These simulation were performed in the time-frequency domain according the proposed work [171] (see C.1.1 for the details). As the result of these simulations the significant broadening of the spectrum and spectral spikes for the chirped pulses was confirmed. It was also shown that the number of modes does not depend on the resolution function or chirp effects and stays about the same for all considered simulations. It was possible to get a correct pulse duration applying HBT method in spectral domain in simulations, for unchirped pulses and pulses affected by the monochromator resolution (see C.1.2).However, the fit gave twice shorter pulse durations, for the chirped pulses. This is related to the broadening of the spectrum twice from its nominal initial value. From this one can conclude that the HBT spectral analysis in the case of chirped pulses provides only the lower boundary for a possible pulse duration. Similar results were obtained using HBT spatial analysis (see C.1.3), where the correct values of pulse durations were determined for unchirped pulses and pulses affected by the monochromator resolution. Simulations show that in the case of chirped pulses the spatial analysis also will provide only the lower boundary for the pulse duration.

8.4 Summary of the HBT interferometry at EuXFEL

By performing HBT interferometry it was possible to determine not only the degree of spatial coherence, but also the average pulse duration of radiation before the monochromator unit. The determined values of the pulse duration both in spectral and spatial domains were on the order of 10 fs (except of QT mode of operation) (see Tables 8.1). These short pulse durations should be considered with the certain caution. The nominal pulse duration of the European XFEL was about 20 fs as determined for the electron bunch. The spectral bandwidth of the SASE3 undulator in the performed experiment was 1% and thus about 2-3 times larger than the baseline parameter, i.e. 0.35% at 1200 eV [170]. The observed broadening of the spectral profiles including individual spikes may be caused by the finite monochromator resolution as well as frequency chirp of the X-ray pulses. As soon as the broadening due to monochromator resolution is about 3%, most of the observed broadening was attributed to the frequency chirp. The frequency chirp of the X-ray pulses is a result of the electron bunch chirp in the accelerator modules. As it follows from the simulations, the spectral width, as well as the spectral spikes width, may change significantly due to the frequency chirp effects. This may cause an apparent lower pulse duration obtained from both spectral and spatial measurements from the nominal one. Thus, pulse durations upstream of the monochromator can be about twice longer, lying in the range of 10 fs to 20 fs, than deduced from the analysis. As such, performed measurements provide the lower boundary for the pulse durations of the European XFEL at different modes of operation. From this discussion it is clear that additional measurements with a controlled frequency chirp of radiation will be an important step in understanding the properties of the EuXFEL radiation. It will be also important to carry out measurements using complementary methods, for example, gas ionization at the same photon energy of 1.2 keV at the Small Quantum Systems (SQS) instrument [172] that is sharing the same undulator SASE3 at the EuXFEL facility.

Chapter 9

Hanbury Brown and Twiss interferometry at PAL-XFEL

This chapter is devoted to one of the first high-energy FELs, producing hard X-rays in the self-seeding regime. The XFEL is located in Pohang, Korea, and named accordingly Pohang Accelerator Laboratory X-ray Free-Electron Laser (PAL-XFEL) [160],[173], [174].

At the PAL-XFEL, the self-seeding regime is provided by the HLSS scheme, which consists of two undulator parts. In the first undulator part, the fundamental and third harmonic FELs are generated then pass through the second undulator part. In the second part, the resonance is set to the third harmonic, so only the third harmonic is amplified, while the fundamental is suppressed using the optimized phase shifters setting. At PAL-XFEL HLSS scheme has been successfully demonstrated [175] at a soft X-ray with the highest photon energy up to 1250 eV. As a result, the longitudinal coherence was improved, and a 170% increase of the spectral flux was achieved compared to that of the SASE mode. In general, this HLSS scheme can be employed for existing and planned X-ray FEL facilities with gap-tunable undulators to generate a stable and high brightness X-ray FEL.

The self-seeding regime at PAL-XFEL was demonstrated in the broad range of photon energies starting from 3.5 keV to 14.6 keV with the highest peak brightness of 3.2×10^{35} $ph/s/mm^2/mrad$ /0.1%BW at 10 keV [176]. PAL-XFEL facility provides an amazing X-ray beam with 0.19 eV bandwidth and the peak spectral brightness 40 times higher than in the SASE regime. It was shown that the use of such seeded XFEL pulse results in high-quality serial femtosecond crystallography. Therefore, many experiments conducted at PAL-XFEL will rely on the stable, highly coherent source, providing strongly intense short pulses. It is clear that these pulsed sources, in principle, cannot be treated as stationary ones and, hence, such properties as spatial and temporal coherence have to be revised.

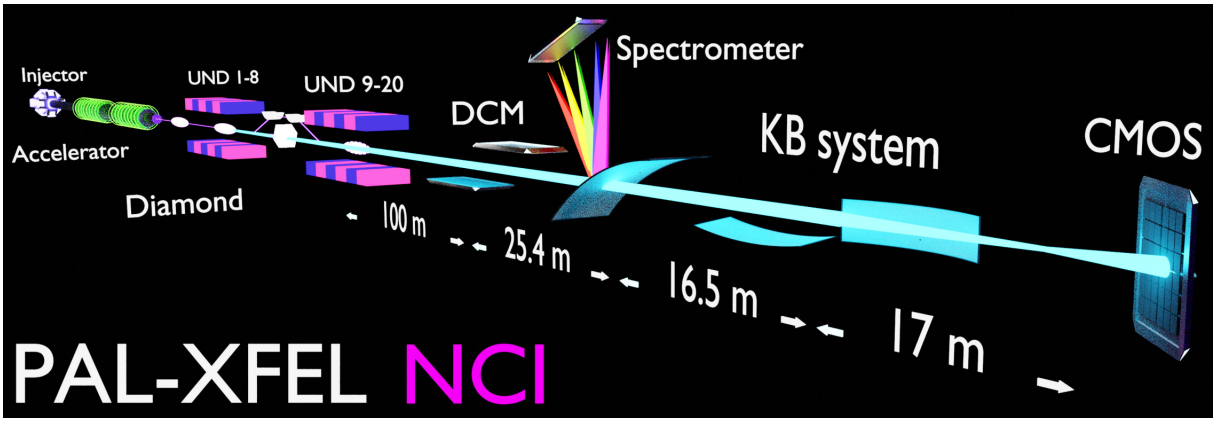

Figure 9.1: Schematic layout of the experiment. The PAL-XFEL source consist of 20 undulator cells. Seeding is provided by including the diamond crystal between 8 and 9 cells. Each optical components were aligned as shown in the figure. The measurements were taken at a distance of about 11.5 m from the focal position. Horizontal KB focusing mirror located 5.37 m upstream from the focus.

9.1 Experiment setup

At the PAL-XFEL, a transmitting Bragg scattering method (see section 6.2) is utilized in the SS scheme. This Brag scattering section is located after 8 undulator sections, where x-ray beams become monochromatic by passing through the Bragg section. The seeded X-ray beam is then amplified as it passes through the remaining 12 undulator sections and delivered to the beamline.

The HBT interferometry experiment at PAL-XFEL was conducted at Nano-Crystallography and Coherent Imaging (NCI-CXI) hard X-ray beamline [160, 177] (see Fig. 6.7). The standard operational electron energy at PAL XFEL is around 10 GeV, with electron bunch charges of 120 pC - 200 pC at 30 Hz repetition rate. The schematic representation of the experimental set-up is shown in Fig. 9.1. The PAL-XFEL source under the investigation is represented as the 5 m undulators combined into 20 cells [104]. Provided by such a source, the X-ray photon energy that used for the experiment was 10 keV (λ = 1.24 $\AA$). Three main regimes of PAL-XFEL operation with different bunch charges were studied: Self-Seeding regime (SS), SASE regime with the broad radiation bandwidth (PINK), and the monochromatic regime (MONO). The latter implies the use of the double-crystal monochromator (DCM) unit at the NCI-CXI instrument.

The standard operation mode of high radiation power at saturation implies 20 undulator cells while in the top-linear (TL) gain regime around 12-13 cells, depending on the electron bunch charge. Saturation and TL operation modes were studied in the SASE regime to compare the FEL source's statistical properties.

For the MONO operation, DCM was installed at 99.84 m downstream from the source point. For the SS operation, the forward Bragg diffraction (FBD) diamond crystal was used, placed after the eight undulators, and monochromatizing the x-ray beam for the last twelve undulators downstream [176].

In order to retrieve the spectral distribution of the PAL-XFEL pulses in-line spectrometer,

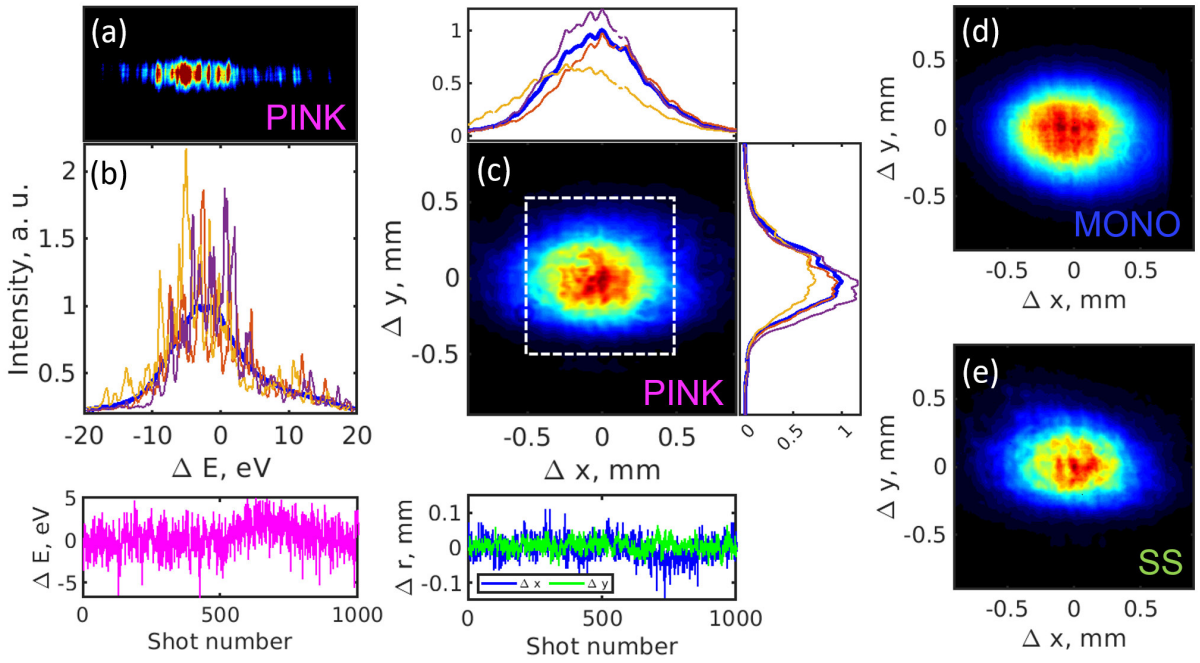

Figure 9.2: (a) Typical spectral intensity distribution of single pulse measured by the Andor CCD detector, and its projection (b) on horizontal axis. (c)Typical spatial intensity distribution measured by Hamamatsu detector, and its projections on horizontal and vertical axes. The bottom pictures show COM jitter of photon energy and intensity distribution. All examples showed in the figure attributed to the studied SASE PINK operating regime with 180 pC bunch charge. Due to mirror imprint effect on the Hamamatsu detector, the region of interest for the correlation analysis in spatial domain was selected, which is shown in (c) by white dashed square. Typical measured spatial intensity distributions in the MONO and SS regimes are shown in (d) and (e).

consisting of the Si bend crystal and the CCD detector was used. The crystal was tuned to Si (333) Bragg reflection and placed after 25.4 m from the DCM. The estimated spectrometer resolution was 0.1 eV. The CCD detector, Andor ZYLA5.5X-FO (2560 × 400 pixels, pixels size of 6.5 × 6.5 μm^2), placed at 1.17 m from bend crystal [104].

All spatial data were recorded by Hamamatsu X-ray sCMOS Camera (2048 × 2048 pixels, pixels size of 6.5 × 6.5 μm^2) with 600 × 600 pixels cropped area. The Hamamatsu detector was placed at 11.5 m downstream from the beam focus, provided by Kirkpatrick-Baez (KB) mirrors located 5.37 m upstream (see Fig. 9.1). To prevent the beam damage of the detectors, a silicon 0.28 mm thick attenuator was placed in front of the in-line spectrometer, as well as 1.175 mm - 1.5 mm attenuators in front of the Hamamatsu detector depending on beam conditions. Typical spectral and spatial intensity distributions of the single pulse, recorded by both detectors, are shown in Fig. 9.2

To characterize the source in full, spatial measurements were performed in parallel to the spectral ones. In the hard X-ray range, it is unlikely to perform the same analysis as it was done at the SCS instrument at Soft X-rays, where the contrast as a function of bandwidth was controlled to retrieve the beam pulse duration. The value of the pulse duration, in this case, may be retrieved only from spectral data by calculating correlation functions in the spectral domain. As it was shown in section 7.3 and derived in B the analysis in spectral-domain relies on

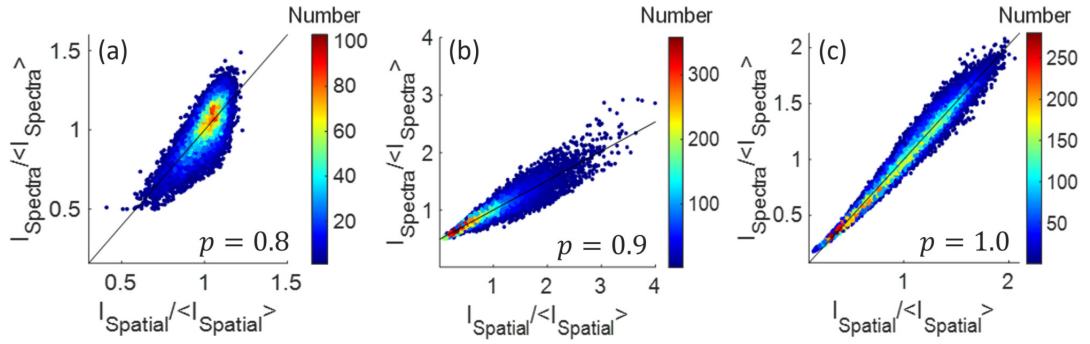

Figure 9.3: Pearson correlation of the measured spatial and spectral data in the case of SASE PINK (a), MONO (b) and SS (c) regimes of operation. The Pearson correlation coefficient p varies in the range from 0.8 to 1, depending on the operating regime in the case of 180 pC charge.

the results from the analysis of the spatial domain. Therefore, a good correspondence between the measured data in spatial and spectral domains is expected. The correspondence of the measured spatial (I^{spat}) and spectral (I^{spec}) data was checked by the simple Pearson correlation

$$p = \frac{\sum_{i=1}^{n}(I_i^{spat} - < I^{spat} >)(I_i^{spec} - < I^{spec} >)}{\left[\sum_{i=1}^{n}(I_i^{spat} - < I^{spat} >)^2 \sum_{j=1}^{n}(I_j^{spec} - < I^{spec} >)^2\right]^{1/2}}, \tag{9.1}$$

where p is the Pearson correlation coefficient. According to the analysis, the Pearson correlation coefficient p lies in the range from 0.8 to 1, which shows the good correspondence of the measured data (see Fig. 9.3).

9.2 Spectral analysis

In order to reach sufficient statistics for the intensity correlation analysis $9{\cdot}10^3$ to $2{\cdot}10^4$ pulses were collected in each operating condition. Prior to the analysis, each spectral and spatial 2D image was corrected by subtracting the background (dark image averaged over 1,000 dark signal shots). This led to the appearance of sparse negative values in the intensity distribution for some pulses. The one-dimensional spectral intensity distribution was obtained by projecting along the vertical direction from the 2D spectrum image (see Fig. 9.2 (b)). In order not to break the intensity-intensity correlations and dispose of the negative values additionally, the same constant was added to each spectral distribution. This constant value was determined as the maximum negative value in the 1D intensity distribution. Note, such data correction procedure may slightly change the correlation between pulses and reduce the contrast value, determined from the $g^{(2)}$-function if the constant value is higher than 1% of the maximum average intensity distribution.

A comparison between spectra and its mean is shown in Fig. 9.4. As expected, the highest intensity in narrow bandwidth is provided in the SS regime. In the MONO regime, the narrowband pulses were provided as well, however, the mean intensity is ten times lower than in the SS regime. A comparison between spectral distributions of individual pulses measured for

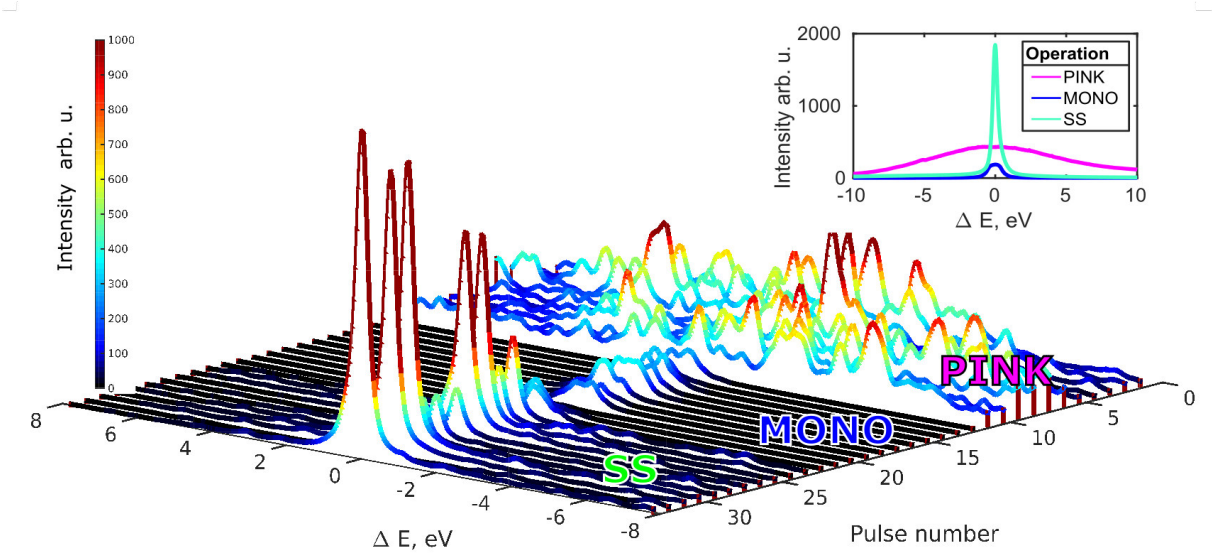

Figure 9.4: Comparison of the spectral intensity for 30 random pulses. In the inset, the average spectrum of each PAL-XFEL operation regime is shown.

all operating regimes is shown in Fig. 9.5 (a,c,e). The multimodal structure in the single pulse spectrum intensity distributions is observed for operating regimes except for the self-seeding case Fig. 9.5 (e), where the presence of the single mode is expected. The number of spectral spikes in other cases varies depending on the operating conditions. In the case of monochromatic SASE beam, only 3 to 4 spectral spikes are presented 9.5 (c), indicating on a small number of spectral modes, while for the PINK SASE beam from 30 to 40 spectral spikes are observed Fig. 9.5 (a).

As it is well seen in Fig. 9.5, for some of the studied operating conditions, the average spectrum does not resemble a single Gaussian function but is rather a sum of two distributions. In order to get the bandwidth of single spike spectral lines and the FWHM width of the average spectrum, the autocorrelation analysis was performed. Each operation mode of SASE PINK, MONO, and SS showed similar shapes of the autocorrelation function regardless of the bunch charge. For SASE PINK, it was possible to distinguish between a single spike and a broad peak of the autocorrelation function ACF (see Fig. 9.5). On the contrary, for the case of the monochromatic and SS beam, the average spectral spike and the average spectrum were hardly distinguishable (see Fig. 9.5 (d). The Gaussian fitting of the autocorrelation functions allowed to extract the FWHM widths of the average spectrum and single spike spectral lines. The values of the FWHM of both peaks corrected for the factor of $\sqrt{2}$ are provided in Table 9.1. The width of the single spike lines, determined from the ACF, lies in the range from 0.48 eV to 0.5 eV (see Table 9.1). The width of the average spectrum lies in the range from 0.5 eV to 12.6 eV. The coherence time was determined according to Eq. (7.35). The second-order correlation functions in the frequency domain for various operation modes are presented in Fig. 9.6 (a,c,e).

In Fig. 9.6(b,d,f) its behavior was analyzed along the white dashed diagonal line shown in Fig. 9.6 (a,c,e). Note that the contrast value is below unity for SASE PINK operation mode

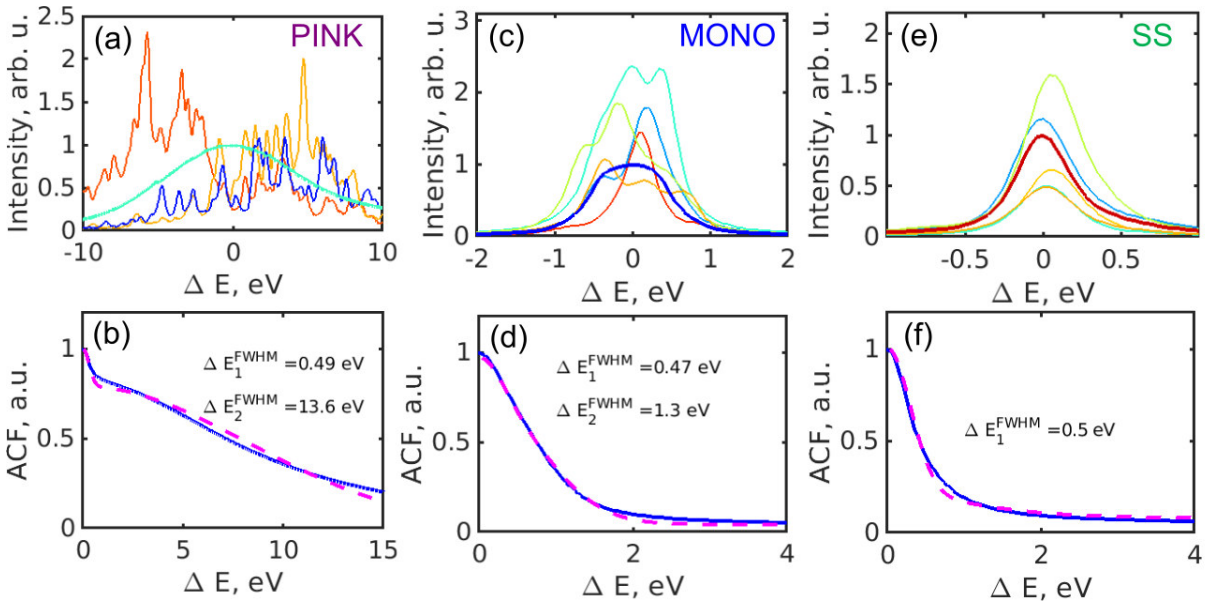

Figure 9.5: Spectral distributions of random shots and average spectrum (a,c,e), the average autocorrelation function of the spectrum (b,d,f). The following regimes of operation are presented: SASE PINK (a,b), MONO (c,d), and SS (e,f) at 180 pC bunch charge.

Table 9.1: Results of the analysis in spectral domain for the operation mode with 180 pC bunch charge. Width of spectrum and spectral spike were determined from the analysis of ACF.

Operation regime	PINK	MONO	SS
FEL bandwidth (FWHM), eV	12.5 ± 0.2	1.2±0.1	0.43±0.01
Width of spectrum from (FWHM), eV	12.6±0.1	1.3±0.02	0.5±0.02
Width of spectral spike (FWHM), eV	0.48±0.02	0.48±0.02	0.5±0.02
Coherence time (rms), fs	0.17±0.02	2.48±0.28	4.19±0.2
Pulse duration T (FWHM), fs	7.0±0.23	8.77±0.22	-
Contrast	0.26±0.02	0.47±0.07	0.32±0.02

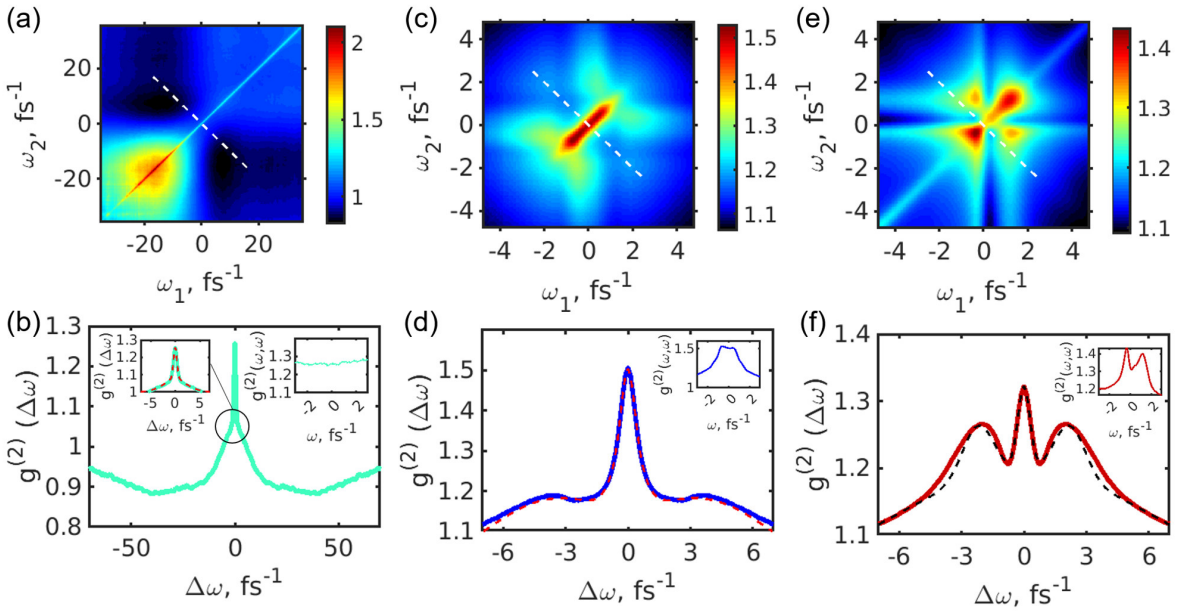

Figure 9.6: (a, c, e) Intensity correlation functions of spectra $g^{(2)}(\omega_1, \omega_2)$. (b, d, f) Cut along the anti-diagonal lines shown by the white dashed lines in (a, c, e) and its fit with the profile given in Eqs. (7.17, 7.21) (dashed line), taking into account additional background. In the inset the profiles along the diagonal of the $g^{(2)}(\omega, \omega)$ function in (a, c, e) are shown. Here (a, b) refer to SASE PINK, (c, d) to MONO, and (e, f) to SS operation regimes.

due to the finite degree of coherence in the spatial domain, monochromator resolution function (see Eq. (7.17)) and Ref. [59]), as well as possible energy jitter [131]. On the contrary, for the monochromatic and self-seeding cases, the contrast values always above unity and $g^{(2)}(\Delta\omega)$-function experiences major distortions. The origin of this distortion, which manifests itself in the form of the additional wide peaks and the pedestal in $g^{(2)}(\Delta\omega)$-function, may be attributed to the variation of the pulse duration from shot to shot in combination with energy jitter (see section C.2.1). Fitting this profile with a function, which takes into account resolution of the monochromator $\sigma_{res} = 0.26$ eV (defined by Eq. (7.21)), as well as additional background gave the root mean square (rms) values σ_T of average pulse duration, from which were deduced the FWHM values $T = 2.355 \cdot \sigma_T$. The values lie in the range from 7.0 fs to 9.0 fs for all three operating settings (see Table 9.1). The pulse duration in the self-seeding operation mode is about 7 fs (see section 9.4.2 for the details).

The same analysis in the spectral domain was carried out for the electron bunch charge of 120 pC and 200 pC (see C.3). In this case, the Pearson correlation analysis showed good correspondence of the data in the case 120 pC bunch charge, while due to higher instabilities of the beam with 200 pC charge, the correlation coefficient is reduced in the SASE regime of operation (see Fig. C.9 and Fig. C.10). The pulse duration for different operational regimes in the case of 200 pC charge was deduced from the $g^{(2)}(\omega_1, \omega_2)$ correlation function as well (C.11). The determined values of the pulse duration are in the range from 6.4 fs (in the MONO case) to 10.3 fs (in the SS case).

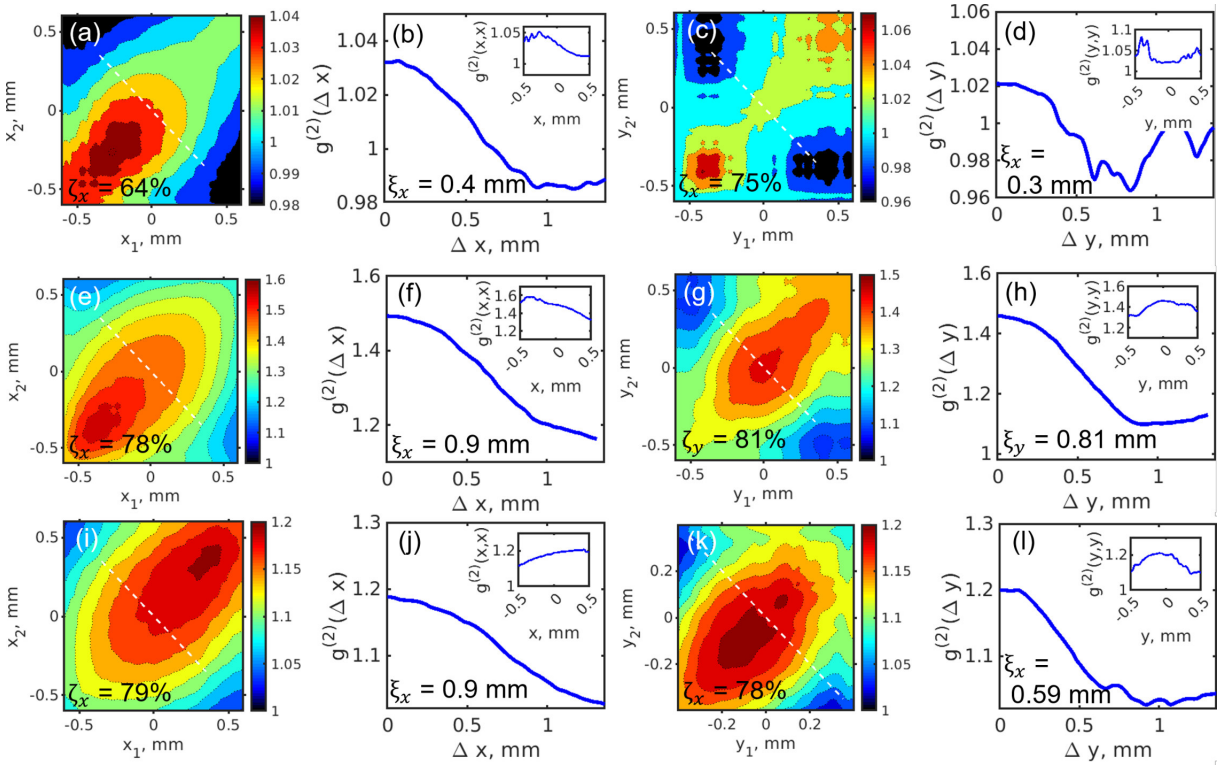

Figure 9.7: Intensity correlation functions $g^{(2)}(x_1, x_2)$ (a,e,i) and $g^{(2)}(y_1, y_2)$ measured by the Hamamatsu detector in the horizontal and vertical directions accordingly. Profiles of the $g^{(2)}(\Delta x)$ (b,f,j) and $g^{(2)}(\Delta y)$ (d,h,l) - functions taken along the white dashed anti-diagonal lines shown in panels (a,e,i) and (c,g,k) accordingly. In the inset the corresponding autocorrelation functions $g^{(2)}(x, x)$ taken along the diagonal lines of $g^{(2)}(r_1, r_2)$- function are shown. Here results for the SASE PINK operating regime shown in (a-d), SASE MONO radiation in (e-h) and SS regime in (i-l). In order to get an average beam size on the Hamamatsu detector, the projected intensities were fitted with the Gaussian function (results shown in Table 9.2).

9.3 Transverse coherence properties at the PAL-XFEL

The typical spatial intensity distribution of individual pulse, measured for the case of SASE operating regimes with 180 pC bunch charge, is shown in Fig. 9.2 (c,d). It is seen from the figure that the average beam is nicely shaped in the Gaussian form, but some small artifacts and distortions are present, which is attributed to the imperfections of mirrors. Due to the mirror imprint effect on the Hamamatsu detector during the measurement, the region of interest (ROI) for the correlation analysis in the spatial domain was selected, which is shown in Fig. 9.2 (c) by white dashed square. The ROI for the analysis was about 1 mm^2. For further intensity correlation analysis, these intensity distributions were projected either along the vertical or horizontal directions, and correlation analysis was performed in the horizontal or vertical direction accordingly, by use of Eq. (7.4) for about $9{\cdot}10^3$ to $2{\cdot}10^4$ XFEL pulses.

In Fig. 9.7 the results of intensity correlation analysis for the SASE PINK operating regime (a-d), SASE MONO beam (e-h), and SS regime (i-l) with 180 pC bunch charge are presented. (see C.3 for the other bunch charges). The intensity correlation functions determined along the white dashed lines in Fig. 9.7 (a,c,e,g,i,k) are shown in Fig. 9.7 (b,d,f,h,j,l) accordingly. One can

Table 9.2: Results of the analysis in spatial domain for the operation mode with 180 pC bunch charge

Operation regime	PINK	MONO	SS
Horizontal direction, x			
Average beam size (FWHM), mm	0.74±0.01	0.75±0.01	0.72±0.01
Coherence length (rms), mm	0.41±0.03	0.9±0.03	0.9±0.02
Degree of spatial coherence, %	64.0±1.2	78±2.7	79±1.3
Contrast	0.03±0.01	0.5±0.08	0.19±0.01
Vertical direction, y			
Average beam size (FWHM), mm	0.48±0.01	0.52±0.01	0.46±0.01
Coherence length (rms), mm	0.28±0.01	0.81±0.03	0.59±0.01
Degree of spatial coherence, %	75±0.9	81±0.8	78±1.7
Contrast	0.02±0.01	0.48±0.07	0.20±0.01

see that the obtained $g^{(2)}(i_1, i_2)$-functions (where i=x,y) in both directions are shaped in the unusual form, as well as $g^{(2)}(i, i)$ - function maxima position shifts and intensity variations along the diagonal. It was also noticed that for the separation of two points of about Δx=1 mm in the anti-diagonal direction, the correlation function $g^{(2)}(\Delta x)$ takes values slightly below unity. All these observable features indicate on positional jitter effect (Δr see Fig. 9.2), as well as the possible presence of multiple sources in the beam. This phenomenon was studied in the work of O. Y. Gorobtsov et al. [131]. Interesting to note, that the $g^{(2)}(i_1, i_2)$-function has slight ripples, very similar to ones, observed in the average intensity shown in Fig. 9.2 (c,d,e). The intensity ripples are attributed to the mirror imperfections projected on the detector during the measurement. The use of such distorted intensity patterns in the correlation analysis led the $g^{(2)}(i_1, i_2)$- function take the form of the checkered pattern. The contrast value for various operating regimes deduced directly from the $g^{(2)}(i_1, i_2)$- function as the maximum value on the diagonal cut ζ_i = $g^{(2)}(i, i)$-1 at i=0. The contrast values for the monochromatic SASE and the self-seeding radiation lies in the range from 0.02 to 0.4 (values are listed in Table 9.2). Despite the fact, that the $g^{(2)}(\Delta x = 0)$ in the SASE operating regime is very close to unity (ζ_i = 0.02), which may give an idea of laser type source [132], the number of spikes in the spectral distribution is still large, which is typical for a chaotic source [133],[131].

Next, the degree of spatial coherence ζ_i in each transverse direction and the corresponding coherence length were determined. The degree of spatial coherence was calculated according to Eq. (3.63). Depending on the operating regimes, electron bunch charge, and the transverse direction under the investigation, the degree of spatial coherence took values in the range from 64% to 81% (see Fig.(9.7) and Table 9.2). In the SASE operating regime with the bunch charge of 180 pC the degree of coherence has taken a relatively small value around 65%, compared with the case of MONO and SS ($\approx$ 80%). Interestingly, the SS beam shows slightly better spatial coherence than the monochromatic beam in the horizontal direction but the opposite in the vertical direction.

The coherence length L_{coh} was obtained as the variance value (second moment in Eq. (3.38)) of the distribution of the $g^{(2)}(i_1, i_2)$-function at anti-diagonal cut. The obtained values of the

coherence length for the SASE, MONO, and self-seeding beams lie in the range from 0.3 to 0.9 mm depending on electron bunch charge and transverse direction (see Table 9.2).

9.4 Modeling of the FEL SASE pulse

In order to understand the statistical properties of the undulator source at the PAL-XFEL and the behavior of the intensity correlation $g^{(2)}$-functions, additional simulations were done, combining several effects, similar to those, described in section C.1.1. Paying attention to the fact that the FEL is a complicated machine, many instabilities may arise during the electron bunch acceleration and radiation amplification process. Results of such instability can manifest themselves in the resonant energy jittering effect. In order to study the energy jitter effect on the intensity correlation functions through the simulation, the resonant energy of 10 keV, which was used in the initial simulation, was allowed to have variation within 5 eV (rms) photon energy according to Gaussian distribution. As the result of simulation, deeps and additional maxima were also observed in the correlation function similar to the obtained in the experiment at PAL-XFEL, indicating possible energy jittering effects (see C.2.2 for the details).

As mentioned earlier, instabilities arising during the acceleration or radiation amplification process, such as an energy jitter, complicate determining the pulse duration. But it is very often that these effects, in turn, do not come alone. Along with the energy jitter, another effect that may affect the correlation functions and make it difficult to determine beam parameters is the pulse duration jitter. The latter means that there is a variation of the pulse duration, which may change from shot to shot. In order to study this effect, the rms value for the Gaussian time filter on the modeling stage allowed to have variation within 1 fs from shot to shot according to Gaussian distribution. As the result of the simulation, a slight broadening of the spectral correlation function is appeared (see C.2.3 for the details). The presence of such a bump in correlation functions obtained from experimental data may indicate a possible pulse variation effect.

The last studied effect, which may arise from the mentioned instabilities and influence the outcome of the HBT interferometry method and the performance of the XFEL, is the effect of multiple beam sources. In this case, performed simulations with small source inhomogeneities still affect results of the HBT interferometry, where $g^{(2)}(\Delta\omega)$-function gives slightly reduced values of the pulse duration (see C.2.4 for the details).

9.4.1 Modeling of the FEL SASE monochromatic pulse

Results for monochromatic radiation and $g^{(2)}$-function of the FEL pulses were simulated as well. In this case a bandwidth of ΔE=1.9 eV in frequency domain (see Fig. 9.8) was applied for the generated pulses. Only two modes were obtained in the distribution of modes, that considerably contribute to the result. For the $g^{(2)}(\omega_1, \omega_2)$-correlation function result shown in Fig. 9.8(c) were obtained, that is similar to the experimental result for monochromatic case (see Fig. 9.6 (c)).

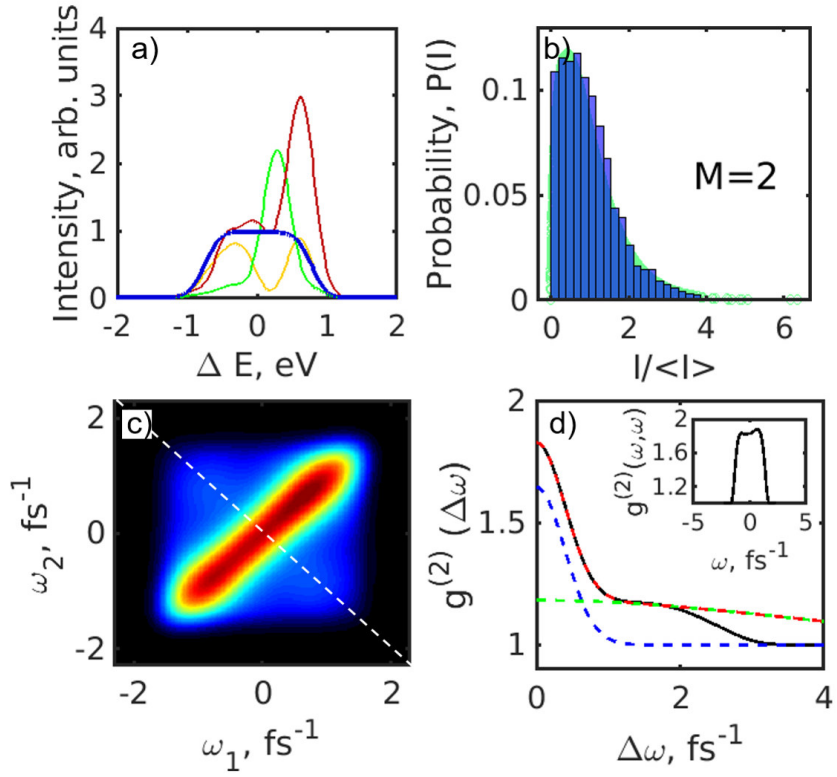

Figure 9.8: Spectral analysis simulation with the monochromator installed in the beamline. (a) Simulated profiles of single pulse intensities and an averaged spectrum (blue line) with the bandwidth of 1.9 eV. (b) Histogram of intensities of single pulses obeying Gamma function distribution (green background) with the number of modes M=2. (c) Second-order intensity correlation function $g^{(2)}(\omega_1, \omega_2)$ of the simulated spectra with the monochromator. (d) Second-order intensity correlation function $g^{(2)}(\Delta\omega)$ (black curve) taken along the white dashed line in (c) and its fit (red dashed line) with Eq. (B.78). In the inset the profile of $g^{(2)}(\omega, \omega)$ function along the diagonal in (c) is shown.

9.4.2 Modeling of the FEL seeded pulse

In order to simulated a seeded pulse the same approach (see section C.2.1) was used. The pulse duration was fixed to T=5 fs and, at the same time, the bandwidth of the generated pulses in frequency domain (ΔE=0.4 eV (FWHM)) was reduced until a single mode distribution (see Fig. 9.9 (g)) was obtained. It is interesting to note that each pulse in this simulation has a varying phase both in the energy and time domains that is random from pulse to pulse (see Fig.9.9 (c)). Then the pulses were modified in time domain by putting a constant value to the phases of each pulse and these phases were allowed to change randomly from pulse to pulse (see Fig. 9.9 (d)). In this case the shape of the $g^{(2)}(\omega_1, \omega_2)$-correlation function in the form of the leaf (see Fig. 9.9(e)) was obtained, similar to the results for self-seeding operation mode (see Fig 9.6 (e)). It was shown, that the distance between two maxima along the anti-diagonal line depends on the pulse duration. To analyse this in detail, this distance in frequency $\Delta\omega$ as a function of the pulse duration is calculated and obtained curve is shown in Fig. 9.9(h). From that curve for the distance between two maxima determined from the experiment ($\Delta\omega$=3.5 fs^{-1}) a pulse duration for the self-seeding operation mode was estimated (about 7 fs).

9.5 Summary of the HBT interferometry method at PAL-XFEL

The second-order correlation experiment performed at the PAL-XFEL facility at 10 keV photon energy demonstrated the high degree of spatial coherence of radiation, around 65-80 % in both perpendicular directions. These values agree with the results of experiments carried out on various XFEL sources and are sufficiently high enough considering the energy of X-rays. The HBT interferometry method allowed to determine the degree of spatial coherence and the average pulse duration of radiation. The determined pulse duration values turn out to be in the range of 7-10 fs.

As it follows from the simulations (see section C.2.1), several effects may take the cause of inhomogeneities of the intensity correlation functions. It is hard to determine whether one of the listed effects is presented individually or a combination of the effects modifies the spectral intensity correlation function. The presence of these effects can be confirmed indirectly using additional detectors and complementary absorption methods. These effects may lead to an overestimation (depending on the present effect) of the pulse duration from the nominal one, obtained from spectral analysis.

In summary, the statistical analysis of X-ray radiation by means of HBT interferometry again proves to be a powerful tool to understand the basic properties of the beams generated by the hard X-ray source even in self-seeding mode at the PAL-XFEL. These experiments provide necessary parameters, such as the degree of coherence and pulse duration. It is assumed that results obtained in this work will greatly help the experiments requiring and utilizing the high coherence properties at PAL-XFEL.

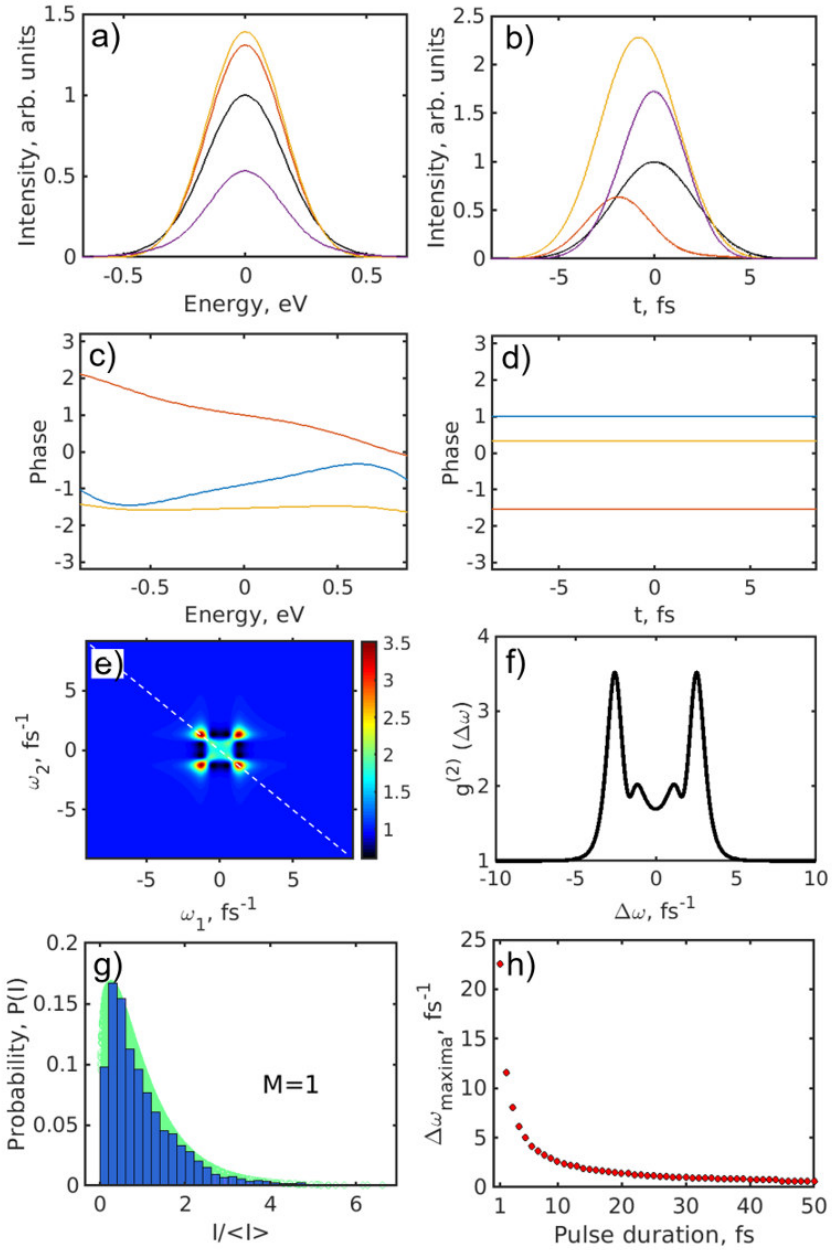

Figure 9.9: Spectral simulations for the seeded beam. (a-d) An example of generated single pulses in (a) energy domain with the bandwidth 0.4 eV and (b) time domain with the pulse duration T=5 fs (FWHM). (c,d) The corresponding phases for these pulses in energy domain (c) and in time domain (d). The phases in time domain were put to a constant value corresponding to phase at T=0. (e) Second-order intensity correlation function $g^{(2)}(\omega_1, \omega_2)$ of the simulated spectra of the seeded beam. (f) Second-order intensity correlation function $g^{(2)}(\Delta\omega)$ (black curve) taken along the white dashed line in (e). (g) Histogram of intensities of single pulses obeying Gamma function distribution (green background) with the number of modes M=1. (h) Distance between two maxima $\Delta\omega_{maxima}$ in $g^{(2)}(\Delta\omega)$-correlation function in (f) as a function of pulse duration.

Chapter 10

Summary

This thesis is devoted to the state-of-the-art XFELs and new generation DLSRs known to be irreplaceable instruments for a wide variety of scientific research fields. It is assumed that the characteristic properties of the XFELs and 4^{th} generation synchrotrons will be outstanding. The photon source of these machines will be recognized as an invaluable research tool. Therefore, the important part of the thesis was dedicated to the performance of these machines and their characterization methods. A general theoretical approach based on the principles of synchrotron radiation and statistical optics was applied to understand the properties of fields generated by DLSRs and XFELs. As a result, the complete procedure is described from the simulation to the analysis of the photon sources at large-scale facilities.

In particular, for the DLSRs with the vanishing electron emittance, a mechanism for degradation of coherence properties was discussed. A detailed analysis of the coherence properties of a high-energy DLSR with emittance values near 10 pm rad operating in a wide range of photon energies from 500 eV to 50 keV is provided. In order to suppress deterioration of brightness and coherence characteristics at DLSRs, proposals were made regarding the effects of beamline optics, energy spread, and detuning from the resonant energy. It was suggested to determine radiation properties from DLSRs sources within the approach based on statistical optics since the single electron radiation defines the overall photon beam parameters. It was shown that in this low-emittance regime, characterization methods based on Gaussian models should be treated with caution. A method based on the radiation field's eigenvalue decomposition was proposed to describe the radiation properties of these sources fully. It was proven that for such low emittance values as 10 pm rad, a true diffraction limit at DLSRs would be reached, in fact, only at soft X-ray energies. It was shown that in order to achieve the same result at higher photon energies, the electron emittance at beam focus should be pushed down to about 1 pm rad. It was also demonstrated that, in order to keep high coherence values of radiation, the energy spread of the electron beam should not exceed the value of $1 \cdot 10^{-3}$ at the emittance values of 10 pm rad, and it should be sufficiently smaller than $1 \cdot 10^{-3}$ at the emittance of 1 pm rad. Applied methods of statistical optics also showed that the effect related to undulator resonant energy detuning, in combination with the energy spread effect, might significantly reduce the coherence characteristics of the DLSR source. In conclusion, it should be noted that understanding

the coherence properties of the radiation and effects concerning their conservation is of vital importance for the design and optimization of future beamlines at 4^{th} generation synchrotron facilities. It is believed that the general approach and new tools for an adequate description of the coherence properties of synchrotron sources provided in this thesis will be helpful for the design and planning of future diffraction-limited sources worldwide.

Regarding the analysis of XFEL machines, methodological improvements of photon beam diagnostics are also given, including treatment of monochromator resolution effects, photon beam frequency chirp, and FEL's pulse jittering. In particular, it was demonstrated how second-order intensity measurements performed in correlation experiments are related to the statistical properties of the x-ray pulses incident on the monochromator unit. Importantly, relations by which coherence properties and average pulse duration may be determined in such experiments were derived. The derivations in this work are quite general and are not limited to the case of soft x-ray beamlines. They will be valid also for hard x-ray beamlines at XFELs as soon as the intensity of the field delivered by the monochromator is expressed through its resolution function by a convolutional integral. The proposed method based on these derivations was applied to characterize photon source properties at large-scale facilities such as European XFEL and PAl-XFEL in different operation conditions. At the EuXFEL, by performing HBT interferometry, it was possible to determine the degree of spatial coherence of the source and the average pulse duration of radiation under different settings of the undulator tapering. Additional simulations were carried out to understand how the results of the HBT interferometry method will change in the presence of limited monochromator resolution and frequency chirp effect. A similar analysis was completed for the PAL-XFEL, where the studied cases concern SASE regime with the wide bandwidth beam, filtered monochromatic beam, and the regime of Self-Seeding with highly intense radiation. Effects of energy and pulse jittering on the outcome of the HBT interferometry were analyzed through additional simulations. It was possible to determine the average pulse duration under different operating conditions and the degree of spatial coherence of the source. As a result, the intensity-intensity correlation analysis has proved to be an efficient method for measurements of FEL statistical behavior.

In conclusion, this thesis proposes an adequate approach within the framework of statistical optics concerning applications for the determination of photon source parameters at large-scale facilities. The thesis may represent a sufficient contribution to the methodology development. Hopefully, these methods will help better utilize coherent beams by beamline scientists and experimentalists and provide an accurate description of the photon source at the experimental stations.

Acknowledgements

I would like to thank Prof. Ivan Vartaniants and Prof. Alexey P. Menushenkov for their excellent guidance and most significant support during the Ph.D. project. I am grateful to Prof. Ivan Vartaniants, Prof. Alexey P. Menushenkov, and Prof. Christian Schroer for agreeing to be my supervisors for this thesis. I also thank Prof. Edgar Weckert for the guidance, essential comments, and opportunity to complete my doctoral studies and Prof. Christian Schroer for the opportunity to continue on the work of most significant interest.

I am grateful to Evgeny Saldin for guidance and many hours of productive discussions in the field of optics, relativity, synchrotrons, XFELs, space, and time.

I am grateful to the Department of Solid State Physics and Nanostructures at NRNU MEPhI, particularly A. P. Menushenkov, V. V. Popov, V. A. Kashurnikov, A. V. Kuznetsov, A. A. Ivanov, I. A. Rudnev, P. F. Kartsev, S. N. Starikov, I. P. Sipailo, Y. M. Popov, A. V. Litvinov, O. B. Mavritskij as well as A. A. Sinchenko and V. N. Sobakin for the preparation and education in the relevant field of the specialty at the highest level. I thank Michael Sprung for being my mentor at DESY and A. Yaroslavtsev, Ya. V. Zubavichus, my first mentors at NRNU MEPhI and Kurchatov Institute.

I am grateful to the former members of the Coherent X-ray Scattering and Imaging group at DESY Max Rose, Luca Gelisio, Young Yong Kim, Jerome Carnis, Alexandr Ignatenko, Anatoly Shabalin, Oleg Gorobtsov, Ivan Zaluzhnyy, Sergey Lazarev, Dmitry Dzhigaev, Ilya Besedin, Petr Skopintsev, Oleksandr Yefanov, Ruslan Kurta, and Andrej Singer for establishing scientific and computing base of great relevance in the group, and introducing me to the world of hardcore scientific programming, crazy experiments and instrumentation as well as for the tremendous scientific support.

I want to express gratitude to Gianluca Geloni, Kai Bagschik, and Svitozar Serkez for productive discussions on the physics of synchrotrons and FELs and joyful collaborative projects.

I want to thank Konstantin Klementiev and Roman Chernikov for their collaboration, excellent support in scientific computing, and insightful comments.

I want to thank the team of the SCS instrument at EuXFEL and accelerator specialists N. Gerasimova, G. Mercurio, L. Le Guyader, B. E. Van Kuiken, M. Teichmann, A. Yaroslavtsev, M. Scholz, and A. Scherz for the opportunity to carry out the experiment and excellent support during it.

I also would like to express gratitude to the team of NCI instrument at PAL-XFEL, accelerator specialists S. Kim, D. Nam, I. Nam, G. Kim, C. H. Shim, H. Yang, M. Cho, C.-K. Min, C. Kim, for the support during the experiment, and H-S. Kang for the opportunity to perform the experiment.

I want to thank the Russian-speaking band in Hamburg: Nastasia Mukharamova, Dameli Assalauova, Maria Naumova, Sergei Levcenko, Dmitry Lapkin, Rustam Rysov, Dina Sheyfer, Taisiia Cheremnykh, Andrei Trebushinin, Vadim Belov, Anton Sokolov, Vsevolod Chestnov, Radik Batraev, Andrey Fedulin, Sergei Riabchuk, Semyon Goncharov and Ivan Sobolev for many wonderful tea time discussions, for traveling and having a great time together, for many

activities during the Ph.D. and joyful moments at work and beyond.

I want to thank my colleagues at NRNU MEPhI and the Russian band: Bulat Gaynanov, Artur Gabdullin, Katya Meshcheryakova, Roman Voronkov, Pavel Demyanenko, Sergey Zhedulov, Ruslan Yaparov, Ruslan Rakhimov, Ilya Karpov, Alexey Neibauer, Alina Makshanova, Sergey Panarin, Sergei Tikhonov, Mark Ulybkin, Denis Kirillov, Nikita Sivakov, Ilya Karavatsky, Danila Tsvetkov, Sergey Derevyashkin, Vlad Tinyaev, Mikhail Leontev, Anton Lavrov, Alyona Shander, and Denis Guryev for spending unbelievably beautiful times together, that I would strive to repeat.

I would like to thank friends and families from the origins Kirill Bulygin, Yerlan Tanmurzinov, Maria Smirnova, Danil Moshkin, Rinat Valeev, Renat Anvarov as the Universe has thrown the dice, placed us together at the very beginning of our journey.

I acknowledge Ludmila A. Sozykina, Alla. Yu. Lapina, Ludmila. S. Kibardina, Rita R. Khavalieva, Gulnara. M. Yunusova, Nadezhda I. Meshkova, Alfiya Ya. Abzalimova, Zubarzhyat M. Iskhakova, Lilia G. Khamidullina, Larisa M. Khabibrakhmanova, and Elena A. Muratova for setting the path, allowing me to take the first steps in the crucial and ruthless world of nature.

And, of course, I thank my family for supporting me throughout my life.

List of Abbreviations

2D	Two-dimensional
3D	Three-dimensional
ACF	Autocorrelation function
BDS	Beam-defining slit
BES	Beam exit-slit
CDI	Coherent Diffraction Imaging
CDC	Complex degree of coherence
CSD	Cross-spectral density
CXDI	Coherent X-ray Diffraction Imaging
CRL	Compound refractive lenses
DBA	Double-bend-achromat
DOC	Degree of Coherence
DLSR	Diffraction-limited storage ring
EEHG	Echo-enable Harmonic Generation
EuXFEL	European X-ray Free-electron Laser
FEL	Free-electron Laser
FWHM	Full Width at Half Maximum
GSM	Gaussian Schell-model
HBT	Hanbury Brown and Twiss (interferometery)
HFM	Horizontal focusing mirror
HGHG	High-gain Harmonic Generation
HPM	Horizontal plane mirror
LCLS	Linac Coherent Light Source

LHC	Large Hadron Collider
LIGO	Laser Interferometer Gravitational-Wave Observatory
LR	Linear regime
LT	Linear tapering
MBA	Multi-bend-achromat
MCF	Mutual coherence function
MOI	Mutual Optical Intensity
PAL-XFEL	Pohang Accelerator Laboratory - X-ray Free-electron Laser
PCA	Principal component analysis
PW	Plane waves
QT	Quadratic tapering
RF	Radio frequency
RMS	Root mean square
SASE	Self Amplification of Spontaneous Emission
SDC	Spectral degree of coherence
SPI	Single Particle Imaging
SS	Self-Seeding
SSR	Synchrotron storage ring
VFM	Vertical focusing mirror
VLS	Variable-line-spacing (grating)
VPM	Vertical plane mirror
XES	X-ray Emission Spectroscopy
XFEL	X-ray Free-electron Laser
XPCS	X-ray photon correlation spectroscopy
XRT	X-ray Tracer (software)

List of commonly encountered variables

c	Speed of light in vacuum
e	Elementary charge
$\mathbf{k}$	Wavevector
λ	Wavelength of radiation
m_e	Electron mass
ω	Radiation frequency
I	Intensity
$\mathcal{F}$	Fourier transform
$\mathbf{r}$	Vector of spatial coordinates
$\mathbf{r}'$	Vector of angular coordinates
t	Time
x, y, z	Spatial coordinates
x', y', z'	Angular coordinates
$\mathbf{F}$	Force
$\mathbf{n}$	Unit vector
$\hbar$	Planck constant
$\mathbf{E}$	Electric field
$\mathbf{B}$	Magnetic field
ϵ	Electric permitivity

Chapter 1

E_γ	Energy of the particle
γ	Lorentz factor
v	Speed of the particle
β_v	Relative speed of the particle with respect to speed of light
$\varepsilon_{x,y}$	Electron beam emittance in horizontal and vertical directions

Chapter 3

P	Propagator
N_F	Fresnel number
T	Transmission function
n	Complex refractive index
δ	Decrement
β_{abs}	Absorption coefficient
$\mathcal{E}$	Photon energy
τ	Pulse duration
τ_c	Coherence time
Γ	Mutual coherence function
γ	Complex degree of coherence
W	Cross-spectral density
S	Spectral density
μ	Spectral degree of coherence
ζ	Degree of coherence
J	Mutual optical intensity
G	Modifed cross-spectral density
g	Modifed spectral degree of coherence
V	Visibility

β_j	Eigenvalue
ζ^{CF}	Coherent fraction
$\sigma_{x,y}$	RMS source size
$\xi_{x,y}$	Transverse coherence length
H_j	Hermite polynomial
F_ω	Radiant intensity
Ω	Solid angle
$\mathcal{B}_\omega$	Spectral radiance or brightness
$\mathfrak{W}$	Wigner function

Chapter 4

E_γ	Energy of the particle
γ	Lorentz factor
v	Speed of the particle
β_v	Relative speed of the particle with respect to speed of light
m	Mass of the particle
λ_u	Undulator period
m_e	Mass of the electron
B_0	Magnetic field in the undulator
K	Undulator deflection parameter
N	Number of the undulator periods
n	Harmonic number
ε_e	Electron beam emittance
σ_e	Electron beam rms size
σ'_e	Electron beam rms divergence
β_e	Beta (optical) function
F	Photon beam flux

$\mathcal{B}$	Brightness
$\mathbf{S}$	Poynting vector
$\mathcal{P}$	Radiation power
N_{ph}	Number of photons
N_e	Number of electrons
$\mathcal{I}$	Electron beam current
$\mathbf{r}$	Vector of spatial coordinates
$\mathbf{r}'$	Vector of angular coordinates
ω_1	Fundamental harmonic
σ'_r	Angular divergence of the single-electron radition
σ_r	Transverse size of the single-electron radiation
F_{coh}	Coherent flux
L_u	Length of the undulator magnetic period
$\mathcal{B}_0$	Brightness of the filament electron beam
$\mathcal{B}_G$	Brightness function within the Gaussian approximation
f_e	Electron beam distribution
Σ_{ph}	Photon source size
Σ'_{ph}	Divergence of the photon source
Q_a	Normalization factor
σ_γ	Energy spread of the electron beam
σ_n	Relative bandwidth of the n-th harmonic
ε_{ph}	Photon beam emittance

Chapter 5

$\mathbf{n}$	Unit vector
$\boldsymbol{\beta}_\nu$	Vector of the relative speed
$\mathbf{r}$	Positional vector

$\boldsymbol{\theta}$	Angular vector
J_n	Bessel function of the n^{th} order
L_u	Length of the undulator magnetic period
K	Undulator deflection parameter
$\mathbf{l}$	Vector of transverse displacement
$\boldsymbol{\eta}$	Vector of angular displacement
γ	Lorentz factor
σ_e	Electron beam rms size
σ'_e	Electron beam rms divergence
ε_{ph}	Photon beam emittance
ε_{coh}	Diffraction-limitted photon emittance
ε_e	Electron beam emittance
F_{coh}	Coherent flux
F	Total Flux
ζ^{CF}	Coherent fraction
ζ	Degree of coherence
ζ^{2D}	Global degree of coherence
ζ^{1D}	Degree of coherence in one transverse direction
ξ	Coherence lenght
ε_r	Photon emittance of the single-electron radiation
$S(\mathbf{r}', \omega)$	Spectral density
β_j	Eigenvalue (weight) of the mode
β_0	Eigenvalue (weight) of zeroe mode
N_F	Fresnel number
μ	Spectral degree of coherence
W	Cross-spectral density

$\sigma_{x,y}$	RMS sizes of the photon beam
Σ_{ph}	Photon source size
$\sigma_{VPM,VLS}$	RMS pitch vavration of the optical elements
γ_0	Lorentz factor coresponding to resonance energy
σ_γ	RMS size of the energy distribution of the electron beam
$\hat{\mathbf{r}}$	Normalized vector of spatial coordinates
$\hat{\mathbf{I}}$	Normalized vector of transverse displacement
$\hat{\boldsymbol{\eta}}$	Normalized vector of angular displacement
$\hat{\xi_E}$	Normalized parameter of the energy spread detuning
Δ_E	Normalized size of the energy distribution of the electron beam
$\hat{G}$	Modifed cross-spectral density, normalized to difraction sizes
$\hat{g}$	Modifed spectral degree of coherence, normalized to difraction sizes
$\hat{V}$	Normalized visibility to difraction sizes
$\mathfrak{W}$	Normalized Wigner function to difraction sizes
$N_{x,y}$	Normalized size of the electron beam distribution
$D_{x,y}$	Normalized divergence of the electron beam distribution
$\mathcal{I}$	Electron beam current
B	Brightness of the filament electron beam
B_A	Brightness apporximated by Gaussian distributions
$\sigma_{\Delta\gamma/\gamma}$	RMS size of the energy spread distribution of the electron beam
$\beta_{x,y}$	Horizontal/vertical beta (optical) function
D_A	Size of the virtual detector
N_e	Number of electrons

Chapter 6

$\mathcal{I}$	Electron beam current
L_e	Electron beam lenght

$L_{coh,z}$	Longitudinal coherence
γ	Lorentz factor
m_e	Mass of the electron
λ_u	Undulator period
m_e	Mass of the electron
ρ	Efficiency parameter
ω_p	Plasma frequency
r_e	Classical electron radius
n_e	Electron density
L_g	Gain length
L_c	Cooperation length

Chapter 7, 8, 9

V	Phase space volume
V_{coh}	Coherence volume
N_{ph}	Number of photons
$g^{(2)}(\mathbf{r}_1, \mathbf{r}_2)$	Second order correlation function
$\zeta(D_\omega)$	Contrast function
ζ	Degree of coherence
D_ω	Radiation bandwidth
σ_i	Size of the photon beam
ξ	Spatial coherence length of the photon beam
Ω_c	Spectral coherence
Ω	Spectral width of the radiation

W	Cross-spectral density
S	Spectral density
σ_T	Pulse duration
τ_c	Coherence time
σ_r	RMS size of the monochromator reolution function
$R(\omega)$	Resolution function
I_D	Intensity on the spatial detector
T_{sl}	Transmission function of the slits
$\hat{T_{sl}}$	Transmission function of the slits convolved with the monochromator resolution
P_L	Propagator for the distance L
$\gamma(\tau)$	Normalized autocorrelation function of time
Δ_E	Average width of the spectrum and spectral spikes
T	Pulse duration (FWHM)
$< I >$	Average intensity
p	Probability distribution
M	Number of modes
σ_I	Standard deviation of the intensity distribution
L_{coh}	Spatial coherence length

Own publications

Publications directly related to the thesis

1. R. Khubbutdinov, M. Seyrich, K. Bagschik. Soft X-ray grating monochromators as a source of spatial coherence degradation: A wave-optical approach. J. Phys.: Conf. Ser. (2022).

2. Y.Y. Kim, R. Khubbutdinov, J. Carnis, S. Kim, D. Nam, I. Nam, G. Kim, C.H. Shim, H. Yang, M. Cho, C-K. Min, C. Kim, H-S. Kang, and I. A. Vartanyants. Statistical analysis of hard X-ray radiation at PAL-XFEL facility performed by Hanbury Brown and Twiss interferometry. Journal of Synchrotron Radiation **29** (2022).

3. R. Khubbutdinov, N. Gerasimova, G. Mercurio, D. Assalauova, J. Carnis, L. Gelisio, L. Le Guyader, A. Ignatenko, Y.Y. Kim, B.E. Van Kuiken, R.P. Kurta, D. Lapkin, M. Teichmann, A. Yaroslavtsev, O. Gorobtsov, A.P. Menushenkov, M. Scholz, A. Scherz, and I. A. Vartanyants. High spatial coherence and short pulse duration revealed by the Hanbury Brown and Twiss interferometry at the European XFEL. Structual Dynamics **8**, 044305 (2021).

4. I. A. Vartanyants, and R. Khubbutdinov. Theoretical analysis of Hanbury Brown and Twiss interferometry at soft-x-ray free-electron lasers. Physical Review A, **104**, 023508 (2021).

5. R. Khubbutdinov, A.P. Menushenkov, and I. A. Vartanyants. Coherence properties of the high-energy fourth-generation X-ray synchrotron sources. Journal of Synchrotron Radiation **26**, 1851-1862 (2019).

6. G. Geloni, S. Serkez, R. Khubbutdinov , V. Kocharyan, and E. Saldin. Effects of energy spread on brightness and coherence of undulator sources. Journal of Synchrotron Radiation **25**, 1335-1345 (2018).

Publications not directly related to the thesis

1. S. Lazarev, Y.Y. Kim, L. Gelisio, Z. Bi, A. Nowzari, I. Zaluzhnyy, R. Khubbutdinov, D. Dzhigaev, A. Jeromin, T. Keller, M. Sprung, A. Mikkelsen. Influence of contacts and applied voltage on a structure of a single GaN nanowire. Appl. Sci. **11**, (2021).

2. Y.Y. Kim, L. Gelisio, G. Mercurio, S. Dziarzhytski, M. Beye, L. Bocklage, A. Classen, C. David, O. Yu. Gorobtsov, R. Khubbutdinov, S. Lazarev, N. Mukharamova, Yu. Obukhov, K. Schlage, I. Zaluzhnyy, G. Brenner, R. Röhlsberger, J. von Zanthier, W. Wurth and I. A. Vartanyants. Ghost Imaging at an XUV Free-Electron Laser. Phys. Rev. A **101**, 013820 (2020).

3. Assalauova D., Kim Y.Y., Bobkov S., Khubbutdinov R., Rose M., Alvarez R., Andreasson J., Balaur E., Contreras A., DeMirci H., Gelisio L., Hajdu J., Hunter M.S., Kurta R.P, Li H, McFadden M., Nazari R., Schwander P., Teslyuk A., Walter P., Xavier P.L., Yoon C.H, Zaare S., Ilyin V.A., Kirian R.A., Hogue B.G., Aquila A. and Vartanyants I.A. An advanced workflow for single-particle imaging with the limited data at an X-ray free-electron laser. IUCrJ, **7**, (2020).

4. Carnis J. ,Kirner F., Lapkin D, Sturm S, Kim Y.Y., Baburin I.A, Khubbutdinov R., Ignatenko A, Iashina E., Mistonov A., Steegemans T., Wieck T., Gemming T., Lubk A., Lazarev S., Sprung M. and Vartanyants I.A. Ghost Imaging at an XUV Free-Electron Laser. Phys. Rev. A **101**, 013820 (2020).

5. A. Maier, D. Lapkin, N. Mukharamova, P. Frech, D. Assalauova, A. Ignatenko, R. Khubbutdinov, S. Lazarev, F. Laible, R. Löffler, N. Previdi, T. Chassé, M. Fleischer, M. Sprung, F. Schreiber, I.A. Vartanyants, M. Scheele. Structure-transport correlation reveals anisotropic charge transport in coupled PbS nanocrystal superlattices. Advanced Materials, **32**, 2002254 (2020).

6. I.A. Zaluzhnyy, R.P. Kurta, N. Mukharamova, Y.Y.Kim, R.M. Khubbutdinov, D. Dzhigaev, V.V. Lebedev, E.S. Pikina, E.I. Kats, N.A. Clark, M. Sprung and I.A. Vartanyants. Evidence of a first-order smectic-hexatic transition and its proximity to a tricritical point in smectic films. Phys. Rev. E, **98**, 052703 (2018).

Bibliography

[1]N. Bohr, "The quantum postulate and the recent development of atomic theory", Nature **121**, 580–590 (1928).

[2]W. Heisenberg, "Mehrkorperproblem und resonanz in der quantenmechanik", Zeitschrift für Physik **38**, 411–426 (1926).

[3]M. Born, *Optik* (Springer, 1933).

[4]M Born and E Wolf, *Principles of Optics: Electromagnetic Theory of Propagation, Interference and Diffraction of Light* (Cambridge University Press, 1999).

[5]R. J. Glauber, "The quantum theory of optical coherence", Phys. Rev. **130**, 2529–2539 (1963).

[6]E. C. G. Sudarshan, "Equivalence of semiclassical and quantum mechanical descriptions of statistical light beams", Phys. Rev. Lett. **10**, 277–279 (1963).

[7]L. Mandel and E. Wolf, "Coherence properties of optical fields", Rev. Mod. Phys. **37**, 231–287 (1965).

[8]L. Mandel and E. Wolf, *Optical Coherence and Quantum Optics* (Cambridge University Press, 1995).

[9]T. Young, "Experimental demonstration of the general law of the interference of light", Philos. Trans. R. Soc **94**, 1 (1804).

[10]C. J. Davisson and L. H. Germer, "Reflection of electrons by a crystal of nickel", PNAS, Proc. Natl. Acad. Sci. USA **14**, 317 (1928).

[11]A. A. Michelson and E. W. Morley, "On the relative motion of the earth and the luminiferous æther", London Edinburgh Philos. Mag. J. Sci. **24**, 449–463 (1887).

[12]R. H. Brown and R. Q. Twiss, "Correlation between photons in two coherent beams of light", Nature **177**, 27–29 (1956).

[13]R. Q. Twiss, A. G. Little, and R. H. Brown, "Correlation between photons, in coherent beams of light, detected by a coincidence counting technique", Nature **180**, 324–326 (1957).

[14]M. A. Nielsen and I. L. Chuang, *Quantum Computing and Quantum Information*, 2000.

[15]F. Arute, K. Arya, R. Babbush, D. Bacon, J. C. Bardin, R. Barends, R. Biswas, S. Boixo, F. G. Brandao, D. A. Buell, et al., "Quantum supremacy using a programmable superconducting processor", Nature **574**, 505–510 (2019).

[16]B. P. Abbott et al., "Gw151226: observation of gravitational waves from a 22-solar-mass binary black hole coalescence", Phys. Rev. Lett. **116**, 241103 (2016).

[17]K. Akiyama, A. Alberdi, W. Alef, K. Asada, R. Azulay, A.-K. Baczko, D. Ball, M. Baloković, J. Barrett, D. Bintley, et al., "First M87 event horizon telescope results. IV. Imaging the central supermassive black hole", Astrophys. J. Lett. **875**, L4 (2019).

[18]I. A. Vartanyants and O. M. Yefanov, "Coherent x-ray diffraction imaging of nanostructures. In the book *X-ray Diffraction. Modern Experimental Techniques*. Edited by O. H. Seeck and B. M. Murphy.", in (Pan Stanford Publishing, Singapore, 2015), pp. 341–384.

[19]D. Einfeld, M. Plesko, and J. Schaper, "First multi-bend achromat lattice consideration", J. Synchrotron Rad. **21**, 856–861 (2014).

[20]A. Singer and I. A. Vartanyants, "Coherence properties of focused x-ray beams at high-brilliance synchrotron sources", J. Synchrotron Rad. **21**, 5–15 (2014).

[21]C. G. Schroer and G. Falkenberg, "Hard x-ray nanofocusing at low-emittance synchrotron radiation sources", J. Synchrotron Rad. **21**, 996–1005 (2014).

[22]O. G. Shpyrko, "X-ray photon correlation spectroscopy", J. Synchrotron Rad. **21**, 1057–1064 (2014).

[23]L. Mandel and E. Wolf, *Optical coherence and quantum optics* (Cambridge University Press, 1995), 1194 pp.

[24]K. J. Gaffney and H. N. Chapman, "Imaging atomic structure and dynamics with ultrafast x-ray scattering", Science **316**, 1444–1448 (2007).

[25]M. Rose, S. Bobkov, K. Ayyer, R. P. Kurta, D. Dzhigaev, Y. Y. Kim, A. J. Morgan, C. H. Yoon, D. Westphal, J. Bielecki, J. A. Sellberg, G. Williams, F. R. Maia, O. M. Yefanov, V. Ilyin, et al., "Single-particle imaging without symmetry constraints at an x-ray free-electron laser", IUCrJ **5** (2018).

[26]D. Assalauova, Y. Y. Kim, S. Bobkov, R. Khubbutdinov, M. Rose, R. Alvarez, J. Andreasson, E. Balaur, A. Contreras, H. DeMirci, L. Gelisio, J. Hajdu, M. S. Hunter, R. P. Kurta, H. Li, et al., "An advanced workflow for single-particle imaging with the limited data at an x-ray free-electron laser", IUCrJ **7**, 1102–1113 (2020).

[27]H. N. Chapman, P. Fromme, A. Barty, T. A. White, R. A. Kirian, A. Aquila, M. S. Hunter, J. Schulz, D. P. DePonte, U. Weierstall, R. B. Doak, F. R. N. C. Maia, A. V. Martin, I. Schlichting, L. Lomb, et al., "Femtosecond x-ray protein nanocrystallography", Nature **470**, 73–77 (2011).

[28]R. Briggs, M. G. Gorman, A. L. Coleman, R. S. McWilliams, E. E. McBride, D. McGonegle, J. S. Wark, L. Peacock, S. Rothman, S. G. Macleod, et al., "Ultrafast X-ray diffraction studies of the phase transitions and equation of state of scandium shock compressed to 82 GPa", Phys. Rev. Lett. **118**, 025501 (2017).

[29]F. Coppari, R. Smith, J. Eggert, J. Wang, J. Rygg, A. Lazicki, J. Hawreliak, G. Collins, and T. Duffy, "Experimental evidence for a phase transition in magnesium oxide at exoplanet pressures", Nat. Geosci. **6**, 926–929 (2013).

[30]O. Ciricosta, S. Vinko, B. Barbrel, D. S. Rackstraw, T. R. Preston, T. Burian, J. Chalupskỳ, B. I. Cho, H.-K. Chung, G. L. Dakovski, et al., "Measurements of continuum lowering in solid-density plasmas created from elements and compounds", Nat. Commun. **7**, 11713 (2016).

[31]P. Vester, I. A. Zaluzhnyy, R. P. Kurta, K. B. Møller, E. Biasin, K. Haldrup, M. M. Nielsen, and I. A. Vartanyants, "Ultrafast structural dynamics of photo-reactions observed by time-resolved X-ray cross-correlation analysis", Struct. Dyn. **6**, 024301 (2019).

[32]K. Bian, J. J. Choi, A. Kaushik, P. Clancy, D.-M. Smilgies, and T. Hanrath, "Shape-anisotropy driven symmetry transformations in nanocrystal superlattice polymorphs", ACS Nano **5**, 2815–2823 (2011).

[33]P. Lenard, "Ueber kathodenstrahlen in gasen von atmosphärischem druck und im äussersten vacuum", Annalen der Physik **287**, 225–267 (1894).

[34]W. C. Röntgen, "On a new kind of ray, a preliminary communication", Wurzburg Physico-Médical Society **28** (1895).

[35]W. C. Röntgen, "On a new kind of rays", Nature **53**, 274–276 (1896).

[36]W. H. Bragg and W. L. Bragg, "The reflection of X-rays by crystals", Proc. R. Soc. Lond. A Math. Phys. **88**, 428–438 (1913).

[37]J. Stöhr, "Two-photon x-ray diffraction", Phys. Rev. Lett. **118**, 024801 (2017).

[38]S. Sasaki, K. Kakuno, T. Takada, T. Shimada, K. ichi Yanagida, and Y. Miyahara, "Design of a new type of planar undulator for generating variably polarized radiation", Nucl. Instrum. Methods Phys. Res. A: Accel. Spectrom. Detect. Assoc. Equip. **331**, 763–767 (1993).

[39]D. Attwood and A. Sakdinawat, *X-rays and Extreme Ultraviolet Radiation*, 2nd (Cambridge University Press, 2016).

[40]K. Codling and R. Madden, "New Rydberg series in molecular oxygen near 500 $\AA$", J. Chem. Phys. **42**, 3935–3938 (1965).

[41]R. Madden and K. Codling, "New autoionizing atomic energy levels in He, Ne, and Ar", Phys. Rev. Lett. **10**, 516 (1963).

[42]H. Wiedemann, *Synchrotron Radiation* (Springer, 2003).

[43]P. Willmott, *An Introduction to Synchrotron Radiation: Techniques and Applications* (John Wiley & Sons, 2019).

[44]I. A. Vartanyants and A. Singer, "Coherence properties of third-generation synchrotron sources and free-electron lasers", in *Synchrotron light sources and free-electron lasers: accelerator physics, instrumentation and science applications*, edited by E. Jaeschke, S. Khan, J. R. Schneider, and J. B. Hastings (Springer International Publishing, 2018), pp. 1–38.

[45]M Eriksson, "Special issue on Diffraction-Limited Storage Rings and New Science Opportunities", J. Synchrotron Rad **21**, 837–842 (2014).

[46]R. Hettel, "DLSR design and plans: an international overview", J. Synchrotron Rad. **21**, 843–855 (2014).

[47]R. Khubbutdinov, A. P. Menushenkov, and I. A. Vartanyants, "Coherence properties of the high-energy fourth-generation x-ray synchrotron sources", J. Synchrotron Rad. **26**, 1851–1862 (2019).

[48]P. F. Tavares, S. C. Leemann, M. Sjöström, and Å. Andersson, "The *MAX IV* storage ring project", J. Synchrotron Rad. **21**, 862–877 (2014).

[49]T. E. Fornek, *Advanced Photon Source upgrade project preliminary design report*, tech. rep. (Argonne National Laboratory, USA, 2017).

[50]P. Raimondi, *Hybrid Multi Bend Achromat: from SuperB to EBS*, tech. rep. (2017).

[51]C. G. Schroer, I. Agapov, W. Brefeld, R. Brinkmann, Y.-C. Chae, H.-C. Chao, M. Eriksson, J. Keil, X. Nuel Gavaldà, R. Röhlsberger, et al., "PETRA IV: the ultralow-emittance source project at DESY", J. Synchrotron Rad. **25**, 1277–1290 (2018).

[52]A. Rodrigues et al., "Sirius light source status report", in 9th *I*nternational *P*article *A*ccelerator *C*onference (June 2018).

[53]E. Weckert, "The potential of future light sources to explore the structure and function of matter", IUCrJ **2**, 230–245 (2015).

[54]C. G. Schroer, *PETRA IV: upgrade of PETRA III to the Ultimate 3D X-ray microscope. Conceptual Design Report*, edited by R. Roehlsberger, E. Weckert, R. Wanzenberg, I. Agapov, R. Brinkmann, and W. Leemans (Deutsches Elektronen-Synchrotron DESY, Hamburg, 2019).

[55]J. Goodman, *Statistical Optics* (Wiley, 2000).

[56]D. Paganin, *Coherent X-ray Optics* (Oxford University Press, 2006).

[57]J. Goodman, *Introduction to Fourier Optics*, Third Edition (Roberts & Company, 2005).

[58]B. E. A. Saleh and M. C. Teich, *Fundamentals of Photonics* (John Wiley & Sons, 2019).

[59]I. A. Vartanyants and R. Khubbutdinov, "Theoretical analysis of Hanbury Brown and Twiss interferometry at soft-x-ray free-electron lasers", Phys. Rev. A **104**, 023508 (2021).

[60]W. Heisenberg, "Remarks on the origin of the relations of uncertainty", in *The Uncertainty Principle and Foundations of Quantum Mechanics. A Fifty Years' Survey* (Wiley & Sons, 1977), pp. 3–6.

[61]D. Attwood and A. Sakdinawat, "Coherence at Short Wavelengths", in *X-Rays and Extreme Ultraviolet Radiation: Principles and Applications*, 2nd ed. (Cambridge University Press, 2017), 110–147.

[62]J. W. Goodman, *Statistical Optics* (Willey, 1985).

[63]G. Geloni, E. Saldin, E. Schneidmiller, and M. Yurkov, "Transverse coherence properties of x-ray beams in third-generation synchrotron radiation sources", Nuclear Instruments and Methods in Physics Research Section A: Accelerators, Spectrometers, Detectors and Associated Equipment **588**, 463–493 (2008).

[64]I. A. Vartanyants and A. Singer, "Coherence properties of hard x-ray synchrotron sources and x-ray free-electron lasers", New J. Phys. **12**, 035004 (2010).

[65]I. A. Vartanyants and A. Singer, "Coherence Properties of Third-Generation Synchrotron Sources and Free-Electron Lasers", in *Synchrotron Light Sources and Free-Electron Lasers: Accelerator Physics, Instrumentation and Science Applications*, edited by E. J. Jaeschke, S. Khan, J. R. Schneider, and J. B. Hastings (Springer International Publishing, 2020), pp. 987–1029.

[66]F Gori, "Mode propagation of the field generated by collett-wolf schell-model sources", Opt. Commun. **46**, 149–154 (1983).

[67]A Starikov and E Wolf, "Coherent-mode representation of gaussian schell-model sources and of their radiation fields", JOSA **72**, 923–928 (1982).

[68]I. A. Vartanyants and A. Singer, "Coherence properties of third-generation synchrotron sources and free-electron lasers", Synchrotron Light Sources and Free-Electron Lasers: Accelerator Physics, Instrumentation and Science Applications, 987–1029 (2020).

[69]K. A. Nugent, "Coherent methods in the X-ray sciences", Adv. Phys. **59**, 1–99 (2010).

[70]R. Coisson and R. P. Walker, "Phase space distribution of brilliance of undulator sources", in Insertion Devices for Synchrotron Sources, Vol. 582 (International Society for Optics and Photonics, 1986), pp. 24–31.

[71]K.-J. Kim, "Brightness, coherence and propagation characteristics of synchrotron radiation", Nucl. Instrum. Methods Phys. Res. A: Accel. Spectrom. Detect. Assoc. Equip., 71–76 (1986).

[72]K.-J. Kim, "Brightness and coherence of synchrotron radiation and high-gain free electron lasers", Nucl. Instrum. Methods Phys. Res. A: Accel. Spectrom. Detect. Assoc. Equip. **261**, 44–53 (1987).

[73]T. Tanaka and H. Kitamura, "Universal function for the brilliance of undulator radiation considering the energy spread effect", J. Synchrotron Rad. **16**, 380–386 (2009).

[74]D. T. Attwood, P. Naulleau, K. A. Goldberg, E. Tejnil, C. Chang, R. Beguiristain, P. Batson, J. Bokor, E. M. Gullikson, M. Koike, et al., "Tunable coherent radiation in the soft x-ray and extreme ultraviolet spectral regions", IEEE J. Quantum Electron. **35**, 709–720 (1999).

[75]G. Stephenson and C. W. Kilmister, *Special Relativity for Physicists* (Longmans, Green & Co, 1958).

[76]D. F. Alferov, Y. A. Bashmakov, and P. A. Cherenkov, "Radiation from relativistic electrons in a magnetic undulator", Sov. Phys. Uspekhi **32**, 200 (1989).

[77]D. Attwood, *Soft X-Rays and Extreme Ultraviolet Radiation: Principles and Applications* (Cambridge University Press, 1999).

[78]K.-J. Kim, "Characteristics of synchrotron radiation", in Aip conference proceedings, Vol. 184, 1 (American Institute of Physics, 1989), pp. 565–632.

[79]E. Wigner, "On the quantum correction for thermodynamic equilibrium", Phys. Rev. **40**, 749–759 (1932).

[80]D. F. Alferov, Y. A. Bashmakov, and E. G. Bessonov, "Radiation of relativistic particles in an undulator", Sov. Phys. Tech. Phys. **17**, 1540 (1973).

[81]G. Geloni, V. Kocharyan, and E. Saldin, "Brightness of synchrotron radiation from undulators and bending magnets", J. Synchrotron Rad. **22**, 288–316 (2015).

[82]H. Onuki and P. Elleaume, *Undulators, Wigglers and their Applications* (CRC Press, 2002).

[83]K.-J. Kim, "Characteristics of synchrotron radiation", in AIP conference proceedings, Vol. 184 (1989), p. 565.

[84]J. D. Jackson, *Classical Electrodynamics* (John Wiley & Sons, 1962).

[85]G. Geloni, E. Saldin, E. Schneidmiller, and M. Yurkov, "Paraxial green's functions in synchrotron radiation theory", arXiv:physics/0502120 [physics.acc-ph] (2005).

[86]K. Klementiev and R. Chernikov, "Powerful scriptable ray tracing package xrt", in Advances in computational methods for *X*-ray optics *III*, Vol. 9209 (International Society for Optics and Photonics, 2014), 92090A.

[87]K. Bagschik, J. Wagner, R. Buß, M. Riepp, A. Philippi-Kobs, L. Müller, J. Buck, F. Trinter, F. Scholz, J. Seltmann, et al., "Direct 2D spatial-coherence determination using the Fourier-analysis method: multi-parameter characterization of the *P*04 beamline at PETRA III", Optics express **28**, 7282–7300 (2020).

[88]S. Goto, "Effect of beamline optics vibration on the source size and divergence for synchrotron radiation", in Advances in x-ray/euv optics and components x, Vol. 9588 (International Society for Optics and Photonics, 2015), 95880G.

[89]P Skopintsev, A Singer, J Bach, L Müller, B Beyersdorff, S Schleitzer, O Gorobtsov, A Shabalin, R. Kurta, D Dzhigaev, et al., "Characterization of spatial coherence of synchrotron radiation with non-redundant arrays of apertures", J. Synchrotron Rad. **21**, 722–728 (2014).

[90]G. Geloni, S. Serkez, R. Khubbutdinov, V. Kocharyan, and E. Saldin, "Effects of energy spread on brightness and coherence of undulator sources", J. Synchrotron Rad. **25**, 1335–1345 (2018).

[91]R. Khubbutdinov, A. P. Menushenkov, and I. A. Vartanyants, "Coherence properties of the high-energy fourth-generation X-ray synchrotron sources", J. Synchrotron Radiat. **26**, 1851–1862 (2019).

[92]A. E. Siegman, "Lasers university science books", Mill Valley, CA **37**, 169 (1986).

[93]O. Y. Gorobtsov, N. Mukharamova, S. Lazarev, M. Chollet, D. Zhu, Y. Feng, R. P. Kurta, J.-M. Meijer, G. Williams, M Sikorski, et al., "Diffraction based hanbury brown and twiss interferometry at a hard x-ray free-electron laser", Sci. Rep. **8**, 1–9 (2018).

[94]A. Singer, F. Sorgenfrei, A. P. Mancuso, N. Gerasimova, O. M. Yefanov, J. Gulden, T. Gorniak, T. Senkbeil, A. Sakdinawat, Y. Liu, et al., "Spatial and temporal coherence properties of single free-electron laser pulses", Opt. Express **20**, 17480–17495 (2012).

[95]P. Skopintsev, A. Singer, J. Bach, L. Müller, B. Beyersdorff, S. Schleitzer, O. Gorobtsov, A. Shabalin, R. P. Kurta, D. Dzhigaev, O. M. Yefanov, L. Glaser, A. Sakdinawat, G. Grübel, R. Frömter, et al., "Characterization of spatial coherence of synchrotron radiation with non-redundant arrays of apertures", Journal of Synchrotron Radiation **21**, 722–728 (2014).

[96]P. Schmüser, M. Dohlus, J. Rossbach, and C. Behrens, *Free-Electron Lasers in the Ultraviolet and X-Ray Regime* (Springer, 2014), pp. 165–182.

[97]R. Khubbutdinov, N. Gerasimova, G. Mercurio, D. Assalauova, J. Carnis, L. Gelisio, L. Le Guyader, A. Ignatenko, Y. Y. Kim, B. E. Van Kuiken, R. P. Kurta, D. Lapkin, M. Teichmann, A. Yaroslavtsev, O. Gorobtsov, et al., "High spatial coherence and short pulse duration revealed by the Hanbury Brown and Twiss interferometry at the European XFEL", Struct. Dyn. **8**, 044305 (2021).

[98]I. A. Vartanyants, A. Singer, A. P. Mancuso, O. M. Yefanov, A. Sakdinawat, Y. Liu, E. Bang, G. J. Williams, G. Cadenazzi, B. Abbey, H. Sinn, D. Attwood, K. A. Nugent, E. Weckert, T. Wang, et al., "Coherence Properties of Individual Femtosecond Pulses of an X-Ray Free-Electron Laser", PRL **107**, 144801, 144801 (2011).

[99]V. Ayvazyan, N. Baboi, J. Bähr, V. Balandin, B. Beutner, A. Brandt, I. Bohnet, A. Bolzmann, R. Brinkmann, O. Brovko, et al., "First operation of a free-electron laser generating GW power radiation at 32 nm wavelength", Eur. Phys. J. D **37**, 297–303 (2006).

[100]P. Emma, R. Akre, J. Arthur, R. Bionta, C. Bostedt, J. Bozek, A Brachmann, P. Bucksbaum, R. Coffee, F.-J. Decker, et al., "First lasing and operation of an ångstrom-wavelength free-electron laser", Nat. Photon. **4**, 641–647 (2010).

[101]T. Ishikawa, H. Aoyagi, T. Asaka, Y. Asano, N. Azumi, T. Bizen, H. Ego, K. Fukami, T. Fukui, Y. Furukawa, et al., "A compact X-ray free-electron laser emitting in the sub-ångström region", Nat. Photon. **6**, 540 (2012).

[102]M. Altarelli, R. Brinkmann, M. Chergui, W. Decking, B. Dobson, S. Düsterer, G. Grübel, W. Graeff, H. Graafsma, J. Hajdu, et al., "The European X-ray free-electron laser", Technical Design Report, DESY **97**, 1–26 (2006).

[103]R. Ganter, *SwissFEL-conceptual design report*, tech. rep. (Paul Scherrer Institute (PSI), 2010).

[104]I. S. Ko, H.-S. Kang, H. Heo, C. Kim, G. Kim, C.-K. Min, H. Yang, S. Y. Baek, H.-J. Choi, G. Mun, B. R. Park, Y. J. Suh, D. C. Shin, J. Hu, J. Hong, et al., "Construction and Commissioning of PAL-XFEL Facility", Appl. Sci. **7** (2017).

[105]J. M. Madey, "Stimulated emission of bremsstrahlung in a periodic magnetic field", J. Appl. Phys. **42**, 1906–1913 (1971).

[106]D. A. Deacon, L. Elias, J. M. Madey, G. Ramian, H. Schwettman, and T. I. Smith, "First operation of a free-electron laser", Phys. Rev. Lett. **38**, 892 (1977).

[107]A. Kondratenko and E. Saldin, "Generating of coherent radiation by a relativistic electron beam in an ondulator", Part. Accel. **10**, 207–216 (1980).

[108]R. Bonifacio, C. Pellegrini, and L. Narducci, "Collective instabilities and high-gain regime free electron laser", in AIP conference proceedings, Vol. 118, 1 (American Institute of Physics, 1984), pp. 236–259.

[109]J. Murphy and C. Pellegrini, "Generation of high-intensity coherent radiation in the soft X-ray and vacuum-ultraviolet region", JOSA B **2**, 259–264 (1985).

[110]M. Altarelli, R. Brinkmann, and M. Chergui, "The european x-ray free-electron laser. *T*echnical *D*esign *R*eport", (2007).

[111]E. Saldin, E. V. Schneidmiller, and M. V. Yurkov, *The physics of Free Electron Lasers* (Springer, 1999).

[112]G Lambert, T Hara, D Garzella, T Tanikawa, M Labat, B Carre, H Kitamura, T Shintake, M Bougeard, S Inoue, et al., "Injection of harmonics generated in gas in a free-electron laser providing intense and coherent extreme-ultraviolet light", Nature physics **4**, 296–300 (2008).

[113]S. Ackermann, A. Azima, S. Bajt, J. Bödewadt, F. Curbis, H. Dachraoui, H. Delsim-Hashemi, M. Drescher, S. Düsterer, B. Faatz, M. Felber, J. Feldhaus, E. Hass, U. Hipp, K. Honkavaara, et al., "Generation of Coherent 19- and 38-nm Radiation at a Free-Electron Laser Directly Seeded at 38 nm", Phys. Rev. Lett. **111**, 114801 (2013).

[114]J. Feldhaus, E. Saldin, J. Schneider, E. Schneidmiller, and M. Yurkov, "Possible application of X-ray optical elements for reducing the spectral bandwidth of an X-ray SASE FEL", Nuclear Instruments and Methods in Physics Research Section A: Accelerators, Spectrometers, Detectors and Associated Equipment **393**, 162–166 (1997).

[115]E. Saldin, E. Schneidmiller, Y. Shvyd'ko, and M. Yurkov, "X-ray FEL with a meV bandwidth", Nuclear Instruments and Methods in Physics Research Section A: Accelerators, Spectrometers, Detectors and Associated Equipment **475**, 357–362 (2001).

[116]D. Ratner, R. Abela, J. Amann, C. Behrens, D. Bohler, G. Bouchard, C. Bostedt, M. Boyes, K. Chow, D. Cocco, et al., "Experimental demonstration of a soft x-ray self-seeded free-electron laser", Phys. Rev. Lett. **114**, 054801 (2015).

[117]G. Geloni, V. Kocharyan, and E. Saldin, "A novel self-seeding scheme for hard x-ray fels", J. Mod. Opt. **58**, 1391–1403 (2011).

[118]J. Amann, W. Berg, V. Blank, F.-J. Decker, Y. Ding, P. Emma, Y. Feng, J. Frisch, D. Fritz, J. Hastings, et al., "Demonstration of self-seeding in a hard X-ray free-electron laser", Nat. Photon. **6**, 693–698 (2012).

[119]L. H. Yu, "Generation of intense uv radiation by subharmonically seeded single-pass free-electron lasers", Phys.Rev. A **44**, 5178 (1991).

[120]L.-H. Yu, M. Babzien, I. Ben-Zvi, L. DiMauro, A. Doyuran, W. Graves, E. Johnson, S. Krinsky, R. Malone, I. Pogorelsky, et al., "High-gain harmonic-generation free-electron laser", Science **289**, 932–934 (2000).

[121]E. Allaria, D. Castronovo, P. Cinquegrana, P. Craievich, M. Dal Forno, M. Danailov, G. D'Auria, A. Demidovich, G. De Ninno, S. Di Mitri, et al., "Two-stage seeded soft X-ray free-electron laser", Nat. Photon. **7**, 913 (2013).

[122]G. Stupakov, "Using the beam-echo effect for generation of short-wavelength radiation", Phys. Rev. Lett. **102**, 074801 (2009).

[123]D. Xiang and G. Stupakov, "Echo-enabled harmonic generation free electron laser", Phys. Rev. Accel. Beams **12**, 030702 (2009).

[124]N. Mukharamova, S. Lazarev, J.-M. Meijer, M. Chollet, A. Singer, R. P. Kurta, D. Dzhigaev, O. Y. Gorobtsov, G. Williams, D. Zhu, et al., "Probing dynamics in colloidal crystals with pump-probe experiments at LCLS: methodology and analysis", Appl. Sci. **7**, 519 (2017).

[125]K. Gerlinger, B. Pfau, F. Büttner, M. Schneider, L.-M. Kern, J. Fuchs, D. Engel, C. M. Günther, M. Huang, I. Lemesh, L. Caretta, A. Churikova, P. Hessing, C. Klose, C. Strüber, et al., "Application concepts for ultrafast laser-induced skyrmion creation and annihilation", Appl. Phys. Lett. **118**, 192403 (2021).

[126]Y. Y. Kim, L. Gelisio, G. Mercurio, S. Dziarzhytski, M. Beye, L. Bocklage, A. Classen, C. David, O. Y. Gorobtsov, R. Khubbutdinov, S. Lazarev, N. Mukharamova, Y. N. Obukhov, B. Rösner, K. Schlage, et al., "Ghost imaging at an xuv free-electron laser", Phys. Rev. A **101**, 013820 (2020).

[127]R. Schneider, T. Mehringer, G. Mercurio, L. Wenthaus, A. Classen, G. Brenner, O. Gorobtsov, A. Benz, D. Bhatti, L. Bocklage, et al., "Quantum imaging with incoherently scattered light from a free-electron laser", Nat. Phys. **14**, 126–129 (2018).

[128]C. Thiel, T. Bastin, J. Martin, E. Solano, J. von Zanthier, and G. S. Agarwal, "Quantum imaging with incoherent photons", Phys. Rev. Lett. **99**, 133603 (2007).

[129]A. Classen, F. Waldmann, S. Giebel, R. Schneider, D. Bhatti, T. Mehringer, and J. von Zanthier, "Superresolving imaging of arbitrary one-dimensional arrays of thermal light sources using multiphoton interference", Phys. Rev. Lett. **117**, 253601 (2016).

[130]S. Oppel, T. Buttner, P. Kok, and J. von Zanthier, "Superresolving multiphoton interferences with independent light sources", Phys. Rev. Lett. **109**, 233603 (2012).

[131]O. Y. Gorobtsov, G. Mercurio, G. Brenner, U. Lorenz, N. Gerasimova, R. P. Kurta, F. Hieke, P. Skopintsev, I. Zaluzhnyy, S. Lazarev, D. Dzhigaev, M. Rose, A. Singer, W. Wurth, and I. A. Vartanyants, "Statistical properties of a free-electron laser revealed by hanbury brown–twiss interferometry", Phys. Rev. A **95** (2017).

[132]O. Y. Gorobtsov, G. Mercurio, F. Capotondi, P. Skopintsev, S. Lazarev, I. A. Zaluzhnyy, M. B. Danailov, M. Dell'Angela, M. Manfredda, E. Pedersoli, et al., "Seeded x-ray free-electron laser generating radiation with laser statistical properties", Nat. Comm. **9**, 1–6 (2018).

[133]A. Singer, U. Lorenz, F. Sorgenfrei, N. Gerasimova, J. Gulden, O. M. Yefanov, R. P. Kurta, A. Shabalin, R. Dronyak, R. Treusch, V. Kocharyan, E. Weckert, W. Wurth, and I. A. Vartanyants, "Hanbury brown - twiss interferometry at a free-electron laser", Phys. Rev. Lett. **111**, 034802 (2013).

[134]M. Hollstein, K. Mertens, S. Klumpp, N. Gerken, S. Palutke, I. Baev, G. Brenner, S. Dziarzhytski, M. Meyer, W. Wurth, D. Pfannkuche, and M. Martins, "Ultrafast charge redistribution in small iodine containing molecules", New J. Phys. **21** (2019).

[135]A. Madsen, J. Hallmann, G. Ansaldi, T. Roth, W. Lu, C. Kim, U. Boesenberg, A. Zozulya, J. Möller, R. Shayduk, M. Scholz, A. Bartmann, A. Schmidt, I. Lobato, K. Sukharnikov, et al., "Materials Imaging and Dynamics (MID) instrument at the European X-ray Free-Electron Laser Facility", J. Synchrotron Rad. **28**, 637–649 (2021).

[136]C. Kim, M. Scholz, and A. Madsen, "The influence of strain on image reconstruction in bragg coherent x-ray diffraction imaging and ptychography", J. Synchrotron Rad. **28** (2021).

[137]F. Lehmkuhler, F. Dallari, A. Jain, M. Sikorski, J. Moller, L. Frenzel, I. Lokteva, G. Mills, M. Walther, H. Sinn, F. Schulz, M. Dartsch, V. Markmann, R. Bean, Y. Kim, et al., "Emergence of anomalous dynamics in soft matter probed at the European XFEL", PNAS **117**, 24110–24116 (2020).

[138]F. Dallari, M. Reiser, I. Lokteva, A. Jain, J. Möller, M. Scholz, A. Madsen, G. Grübel, F. Perakis, and F. Lehmkühler, "Analysis strategies for mhz xpcs at the european xfel", Appl. Sci. **11** (2021).

[139]F. Lehmkühler, W. Roseker, and G. Grübel, "From femtoseconds to hours–measuring dynamics over 18 orders of magnitude with coherent x-rays", Appl. Sci. **11** (2021).

[140]R. Shayduk and P. Gaal, "Transition regime in the ultrafast laser heating of solids", J. Appl. Phys. **127**, 073101 (2020).

[141]J. Purans, A. Menushenkov, S. Besedin, A. Ivanov, V. Minkov, I. Pudza, A. Kuzmin, K. Klementiev, S. Pascarelli, O. Mathon, A. Rosa, T. Irifune, and M. Eremets, "Local electronic structure rearrangements and strong anharmonicity in YH3 under pressures up to 180 GPa", Nat. Comm. **12** (2021).

[142]H. P. Liermann, Z. Konôpková, K. Appel, C. Prescher, A. Schropp, V. Cerantola, R. J. Husband, J. D. McHardy, M. I. McMahon, R. S. McWilliams, C. M. Pépin, J. Mainberger, M. Roeper, A. Berghäuser, H. Damker, et al., "Novel experimental setup for megahertz X-ray diffraction in a diamond anvil cell at the High Energy Density (HED) instrument of the EuXFEL", J. Synchrotron Rad. **28**, 688–706 (2021).

[143]G. Serghiou, H. J. Reichmann, N. Odling, K. Spektor, A. Pakhomova, W. A. Crichton, and Z. Konôpková, "An unexpected cubic symmetry in group iv alloys prepared using pressure and temperature", Angew. Chem. Int. Ed. **60**, 9009–9014 (2021).

[144]H. Hwang, T. Kim, H. Cynn, T. Vogt, R. J. Husband, K. Appel, C. Baehtz, O. B. Ball, M. A. Baron, R. Briggs, M. Bykov, E. Bykova, V. Cerantola, J. Chantel, A. L. Coleman, et al., "X-ray free electron laser-induced synthesis of e-iron nitride at high pressures", J. Phys. Chem. Lett. **12**, 3246–3252 (2021).

[145]M. Krstulović, A. D. Rosa, N. Biedermann, T. Irifune, and M. Wilke, "Structural changes in aluminosilicate glasses up to 164GPa and the role of alkali, alkaline earth cations and alumina in the densification mechanism", Chem. Geol. **560**, 119980 (2021).

[146]F. Büttner, B. Pfau, M. Böttcher, M. Schneider, G. Mercurio, C. M. Günther, P. Hessing, C. Klose, A. Wittmann, K. Gerlinger, et al., "Observation of fluctuation-mediated picosecond nucleation of a topological phase", Nat. Mater. **20**, 30–37 (2021).

[147]N. Rohringer and R. Santra, "Resonant Auger effect at high x-ray intensity", Phys. Rev. A **77**, 053404 (2008).

[148]G. Doumy, C. Roedig, S.-K. Son, C. I. Blaga, A. D. DiChiara, R. Santra, N. Berrah, C. Bostedt, J. D. Bozek, P. H. Bucksbaum, J. P. Cryan, L. Fang, S. Ghimire, J. M. Glownia, M. Hoener, et al., "Nonlinear atomic response to intense ultrashort x rays", Phys. Rev. Lett. **106**, 083002 (2011).

[149]G. Dixit, O. Vendrell, and R. Santra, "Imaging electronic quantum motion with light", PNAS **109**, 11636–11640 (2012).

[150]V. Popov, A. Menushenkov, A. Ivanov, A. Yastrebtsev, B. Gaynanov, F. d'Acapito, and A. Puri, "A XAFS investigation of amorphous-to-crystalline and fluorite-to-pyrochlore phase transitions in Ln2M2O7 (LnGd, Tb, Dy; MTi, Zr)", Rad. Phys. Chem. **175** (2020).

[151]R. H. Brown and R. Q. Twiss, "Correlation between photons in two coherent beams of light", Nature **177**, 27–29 (1956).

[152]R. H. Brown and R. Q. Twiss, "A test of a new type of stellar interferometer on sirius", Nature **178**, 1046–1048 (1956).

[153]E. M. Purcell, "The question of correlation between photons in coherent light rays", Nature **178**, 1449–1450 (1956).

[154]G. Baym, "The physics of hanbury brown-twiss intensity interferometry: from stars to nuclear collisions", arXiv preprint nucl-th/9804026 (1998).

[155]V. Hilbert, C. Rödel, G. Brenner, T. Döppner, S. Düsterer, S. Dziarzhytski, L. Fletcher, E. Förster, S. Glenzer, M. Harmand, et al., "Spatio-temporal coherence of free-electron laser radiation in the extreme ultraviolet determined by a michelson interferometer", Appl. Phys. Lett. **105**, 101102 (2014).

[156]R Hanbury Brown, R. C. Jennison, and M. K. Das Gupta, "Apparent angular sizes of discrete radio sources.", Nature **170**, 1061–1063 (1952).

[157]R. H. Brown and R. Q. Twiss, "A new type of interferometer for use in radio astronomy", London Edinburgh Philos. Mag. J. Sci. **45**, 663–682 (1954).

[158]H. Lajunen, J. Tervo, J. Turunen, P. Vahimaa, and F. Wyrowski, "Spectral coherence properties of temporally modulated stationary light sources", Opt. Express **11**, 1894–1899 (2003).

[159]P. Paakkonen, J. Turunen, P. Vahimaa, A. T. Friberg, and F. Wyrowski, "Partially coherent gaussian pulses", Opt. Commun. **204**, 53–58 (2002).

[160]H.-S. Kang, C.-K. Min, H. Heo, C. Kim, H. Yang, G. Kim, I. Nam, S. Y. Baek, H.-J. Choi, G. Mun, et al., "Hard x-ray free-electron laser with femtosecond-scale timing jitter", Nat. Photonics **11**, 708–713 (2017).

[161]W. Decking, S. Abeghyan, P. Abramian, A. Abramsky, A. Aguirre, C. Albrecht, P. Alou, M. Altarelli, P. Altmann, K. Amyan, et al., "A mhz-repetition-rate hard x-ray free-electron laser driven by a superconducting linear accelerator", Nat. Photonics **14**, 391–397 (2020).

[162]C. Gutt, P Wochner, B Fischer, H Conrad, M Castro-Colin, S Lee, F Lehmkühler, I Steinke, M Sprung, W Roseker, et al., "Single shot spatial and temporal coherence properties of the slac linac coherent light source in the hard x-ray regime", PRL **108**, 024801 (2012).

[163]F. Lehmkühler, P. Kwaśniewski, W. Roseker, B. Fischer, M. A. Schroer, K. Tono, T. Katayama, M. Sprung, M. Sikorski, S. Song, et al., "Sequential single shot x-ray photon correlation spectroscopy at the sacla free electron laser", Sci. Rep. **5**, 1–9 (2015).

[164]O. Y. Gorobtsov, N. Mukharamova, S. Lazarev, M. Chollet, D. Zhu, Y. Feng, R. P. Kurta, J.-M. Meijer, G. Williams, M Sikorski, et al., "Diffraction based hanbury brown and twiss interferometry at a hard x-ray free-electron laser", Scientific reports **8**, 1–9 (2018).

[165]I. Inoue, T. Hara, Y. Inubushi, K. Tono, T. Inagaki, T. Katayama, Y. Amemiya, H. Tanaka, and M. Yabashi, "X-ray hanbury brown-twiss interferometry for determination of ultrashort electron-bunch duration", Phys. Rev. Accel. Beams **21**, 080704 (2018).

[166]H. Sinn, M. Dommach, B. Dickert, M. Felice, X. Dong, J. Eidam, D. Finze, I. Freijo, N. Gerasimova, N. Kohlstrunk, D. La Civita, F. Meyn, V. Music, M. Neumann, M. Petrich, et al., "The SASE1 x-ray beam transport system", J. Synchrotron Rad. **26** (2019).

[167]N. Gerasimova, *Performance of the SASE3 monochromator equipped with a provisional short grating. Variable line spacing grating specifications*, tech. rep. (EuXFEL Facility GmbH, 2018).

[168]S. Abeghyan, M. Bagha-Shanjani, G. Chen, U. Englisch, S. Karabekyan, Y. Li, F. Preisskorn, F. Wolff-Fabris, M. Wuenschel, M. Yakopov, et al., "First operation of the SASE1 undulator system of the European X-ray Free-Electron Laser", J. Synchrotron Rad. **26**, 302–310 (2019).

[169]H. Sinn, M. Dommach, X. Dong, D. La Civita, L. Samoylova, R. Villanueva, and F. Yang, *Technical Design Report: X-Ray Optics and Beam Transport*, tech. rep. (EuXFEL Facility GmbH, 2012).

[170]E. A. Schneidmiller and M. V. Yurkov, *Photon beam properties at the European XFEL*, tech. rep. (Deutsches Elektronen-Synchrotron, 2011).

[171]T. Pfeifer, Y. Jiang, S. Düsterer, R. Moshammer, and J. Ullrich, "Partial-coherence method to model experimental free-electron laser pulse statistics", Opt. Lett. **35**, 3441–3443 (2010).

[172]T. Tschentscher, C. Bressler, J. Grünert, A. Madsen, A. Mancuso, M. Meyer, A. Scherz, H. Sinn, and U. Zastrau, "Photon beam transport and scientific instruments at the European XFEL", Appl. Sci. **7**, 592 (2017).

[173]H.-S. Kang, H. Yang, G. Kim, H. Heo, I. Nam, C.-K. Min, C. Kim, S. Y. Baek, H.-J. Choi, G. Mun, et al., "FEL performance achieved at PAL-XFEL using a three-chicane bunch compression scheme", J. Synchrotron Rad. **26**, 1127–1138 (2019).

[174]K. Yun, S. Kim, D. Kim, M. Chung, W. Jo, H. Hwang, D. Nam, S. Kim, J. Kim, S.-Y. Park, et al., "Coherence and pulse duration characterization of the PAL-XFEL in the hard x-ray regime", Sci. Rep. **9**, 1–7 (2019).

[175]I. Nam, C.-K. Min, C. Kim, H. Yang, G. Kim, H. Heo, S. Kwon, S. H. Park, and H.-S. Kang, "Soft X-ray harmonic lasing self-seeded free electron laser at Pohang Accelerator Laboratory X-ray free-electron laser", Appl. Phys. Lett. **112**, 213506 (2018).

[176]I. Nam, C.-K. Min, B. Oh, G. Kim, D. Na, Y. J. Suh, H. Yang, M. H. Cho, C. Kim, M.-J. Kim, et al., "High-brightness self-seeded x-ray free-electron laser covering the 3.5 kev to 14.6 kev range", Nat. Photonics **15**, 435–441 (2021).

[177]J. Park, S. Kim, K.-H. Nam, B. Kim, and I. S. Ko, "Current status of the CXI beamline at the pal-xfel", J. Korean Phys. Soc. **69**, 1089–1093 (2016).

[178]*Package X-Ray Tracer documentation*, `http://https://xrt.readthedocs.io/`,

[179]I. Sergueev, R. Döhrmann, J. Horbach, and J. Heuer, "Angular vibrations of cryogenically cooled double-crystal monochromators", Journal of Synchrotron Radiation **23**, 1097–1103 (2016).

[180]Z. Bor, B. Racz, G. Szabo, M. Hilbert, and H. A. Hazim, "Femtosecond pulse front tilt caused by angular dispersion", Optical Engineering **32**, 2501 –2504 (1993).

[181]J Hebling, "Derivation of the pulse front tilt caused by angular dispersion", Optical and Quantum Electronics **28**, 1759–1763 (1996).

[182]F Siewert, J Buchheim, T Zeschke, M Störmer, G Falkenberg, and R. Sankari, "On the characterization of ultra-precise x-ray optical components: advances and challenges in ex situ metrology", Journal of Synchrotron Radiation **21**, 968–975 (2014).

[183]M. Yabashi, K. Tono, H. Mimura, S. Matsuyama, K. Yamauchi, T. Tanaka, H. Tanaka, K. Tamasaku, H. Ohashi, S. Goto, et al., "Optics for coherent x-ray applications", Journal of synchrotron radiation **21**, 976–985 (2014).

[184]Y. Wang, T. Xiao, and H. Xu, "Effect of surface roughness on the spatial coherence of x-ray beams from third-generation synchrotron radiation sources", Journal of Synchrotron Radiation **7**, 209–214 (2000).

[185]X. Meng, X. Shi, Y. Wang, R. Reininger, L. Assoufid, and R. Tai, "Mutual optical intensity propagation through non-ideal mirrors", Journal of Synchrotron Radiation **24**, 954–962 (2017).

[186]C.-C. Cheng and M. Raymer, "Propagation of transverse optical coherence in random multiple-scattering media", Physical Review A **62**, 023811 (2000).

[187]I. Robinson, C. Kenney-Benson, and I. Vartanyants, "Sources of decoherence in beamline optics", Physica B: Condensed Matter **336**, 56–62 (2003).

[188]W. Grizolli, X. Shi, and L. Assoufid, "Influence of optics vibration on synchrotron beam coherence", Optics Letters **44**, 899–902 (2019).

[189]O. Chubar and P. Elleaume, "Accurate and efficient computation of synchrotron radiation in the near field region", in Proc. of the 6th european particle accelerator conference (epac'98) (1998), pp. 1177–1179.

[190]M. Rose, P. Skopintsev, D. Dzhigaev, O. Gorobtsov, T. Senkbeil, A. von Gundlach, T. Gorniak, A. Shabalin, J. Viefhaus, A. Rosenhahn, and I. Vartanyants, "Water Window Ptychographic Imaging with Characterized Coherent X-rays", ArXiv e-prints (2015).

[191]J. Viefhaus, F. Scholz, S. Deinert, L. Glaser, M. Ilchen, J. Seltmann, P. Walter, and F. Siewert, "The variable polarization xuv beamline p04 at PETra iii: optics, mechanics and their performance", Nuclear Instruments and Methods in Physics Research Section A: Accelerators, Spectrometers, Detectors and Associated Equipment **710**, 151–154 (2013).

[192]R Reininger, "The in-focus variable line spacing plane grating monochromator", Nuclear Instruments and Methods in Physics Research Section A: Accelerators, Spectrometers, Detectors and Associated Equipment **649**, 139–143 (2011).

[193]W. B. Peatman, *Gratings, mirrors and slits: beamline design for soft x-ray synchrotron radiation sources* (Routledge, 2018).

[194]S. Akturk, X. Gu, P. Gabolde, and R. Trebino, "The general theory of first-order spatio-temporal distortions of gaussian pulses and beams", Optics express **13**, 8642–8661 (2005).

[195]V. M. Kaganer, I. Petrov, and L. Samoylova, "Resolution of a bent-crystal spectrometer for x-ray free-electron laser pulses: diamond versus silicon", Acta Cryst. A **77**, 268–276 (2021).

[196]M. Born and E. Wolf, *Principles of Optics: 60th Anniversary Edition*, 7th ed. (Cambridge University Press, 2019).

[197]A. Singer, U. Lorenz, F. Sorgenfrei, N. Gerasimova, J. Gulden, O. M. Yefanov, R. P. Kurta, A. Shabalin, R. Dronyak, R. Treusch, V. Kocharyan, E. Weckert, W. Wurth, and I. A. Vartanyants, "Hanbury Brown - Twiss Interferometry at a Free-Electron Laser", Phys. Rev. Lett. **111**, 034802 (2013).

Appendix A

Simulations of 3^{rd} and 4^{th} generation synchrotron sources

A.1 X-Ray Tracing Software

XRay Tracer package (xrt) is a python software library for ray tracing and wave propagation in the x-ray regime. It is primarily meant for modeling synchrotron sources, beamlines, and beamline elements (optical elements, apertures, screens) [86]. For scripting in python, one needs to prepare a script that gives instructions on how to get the wanted ray properties and prepare the graphs. The scripting is different for different backends (backend is a module or an external program that supplies ray distributions). The main advantageous features of XRT are listed below (according to [178]):

1. Rays and waves. Classical ray tracing and wave propagation via Kirchhoff integral. No further approximations, such as thin lens or paraxial. The optical surfaces may have figure errors, analytical or measured. In wave propagation, partially coherent radiation is treated by incoherent addition of coherently diffracted fields generated per electron.

2. Scripting in Python. XRT can be run within Python scripts to generate a series of images under changing geometrical or physical parameters.

3. Synchrotron sources. Bending magnet, wiggler, undulator and elliptic undulator are calculated internally within XRT.

4. Energy dispersive elements. Implemented are gratings (also with efficiency calculations), Fresnel zone plates, Bragg-Fresnel optics. Crystals can work in Bragg or Laue cases, in reflection or in transmission.

5. Materials. The material properties are incorporated using three different tabulations of the scattering factors, with differently wide and differently dense energy meshes. Refractive index and absorption coefficient are calculated from the scattering factors. Two-surface bodies, such as plates or refractive lenses, are treated with both refraction and absorption.

6. Global coordinate system. The optical elements are positioned in a global coordinate system. This is convenient for modeling a real synchrotron beamline. The coordinates in this system can be directly taken from a CAD library. The optical surfaces are defined in local systems for the user's convenience.

7. Beam categories. XRT discriminates rays by several categories: good, out, over and dead. This distinction simplifies the adjustment of entrance and exit slits. An alarm is triggered if the fraction of dead rays (for instance, absorbed or cut) exceeds a specified level.

8. Parallel execution. XRT can be run in parallel in several threads or processes, which accelerates the execution on multi-core computers. It can run on an external server, also without X window system (X11) support.

A.2 Mode decomposition and PCA method

In general, to determine independent coherent modes of radiation or perform coherent mode decomposition, one needs to solve Fredholm integral equation according to Eq. (3.72). Mode decomposition of the CSD in the studied cases was completed according to Eqs. (3.71-3.73). In the XRT software, CSD is calculated according to Eqs. (3.65, 3.66) for the radiation in the far field region for a single electron. The CSD of radiation is, in fact, a four-dimensional (4D) matrix (the CSD function depends on coordinates x1, y1; x2, y2). Effectively in the XRT software, one more dimension is added by including a number of electrons so that the correlation function is saved for each electron, which gives additional dimension. The next step is to compose the 4D CSD matrix from the 5D field distribution and to solve the CSD for eigenvalues and eigenfunctions.

The eigenvalue problem for the CSD matrix in XRT software is reduced to two-dimensional (2D) by applying principal component analysis (PCA) (see Fig. A.1). After the diagonalization of this matrix, the eigenvalues (mode weights) and eigenfunctions (modes) of CSD are obtained. If the mode weights are known, then the global degree of coherence and the coherent fraction of radiation may be calculated according to Eqs. (3.74) and (3.74). It should also be noted that the global degree of coherence according to the PCA method can be obtained without solving a huge eigenvalue problem. The global degree of coherence, in this case, can be calculated as the ratio between traces of the CSD matrix

$$\zeta = \frac{Tr(W_{PCA}^2)}{\left(Tr(W_{PCA})\right)^2},$$

which is equivalent to Eq. (3.74), where W_{PCA} is the rearranged CSD matrix according to the PCA method. The number of electrons used in the coherent-mode simulations is given in Table 5.9.

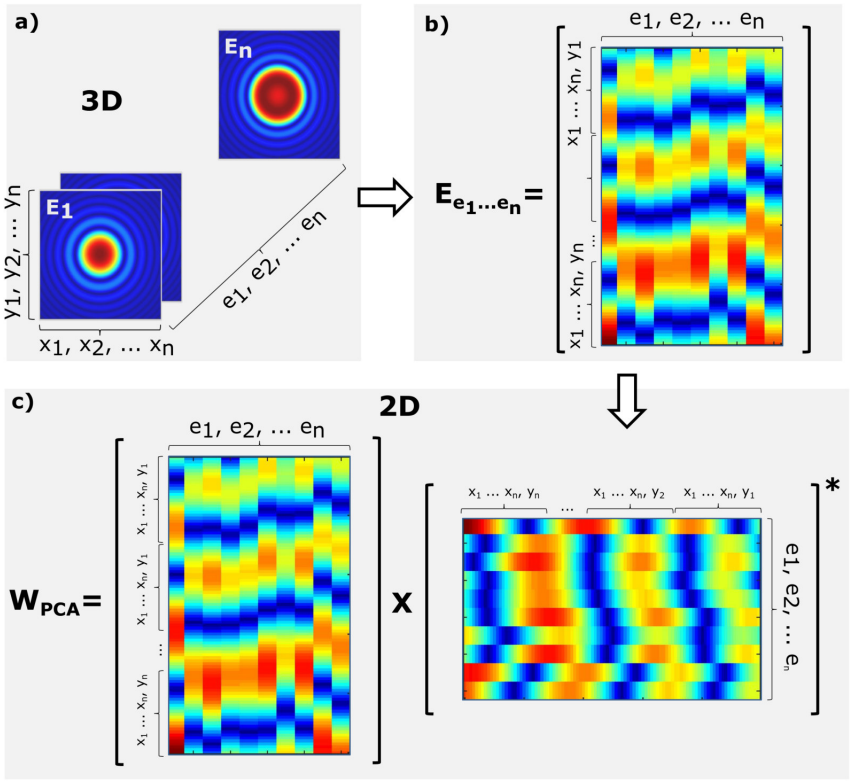

Figure A.1: PCA method used in the coherent mode decomposition. a) 2D amplitudes stored in a 3D matrix for each electron $e_1 \dots e_n$, where 3rd dimension is connected to the number of electrons. b) 3D matrix of amplitudes, rearranged to 2D matrix $E_{e_1-e_n}$, where each column contains all spatial information about an amplitude corresponding to one of the electrons e_i from the electron bunch. c) Cross-spectral density matrix WPCA obtained by multiplication of matrix $E_{e_1-e_n}$ by its complex conjugated and transposed matrix.

A.3 Transverse CSD function at higher photon energies

Simulations of amplitudes and correlation functions in one transverse direction for higher photon energies were performed by XRT software as well. One dimensional CSD function at given photon energy was simulated in the far field region as averaged over an ensemble of electrons according to Eq. (3.66) in the horizontal direction. Results of simulations for high photon energies of 24 keV and 50 keV are shown in Fig. A.2 and Fig. A.3. As it is seen from these figures, energy spread enlarges rms values σ of the intensity distribution (calculated as the variance value of the corresponding distribution) (Fig. A.2, A.3 (a,b,c)), while it narrows the CSD and the spectral degree of coherence in anti-diagonal direction (Fig. A.2, A.3(d-i)), which leads to a decrease of coherence. The values of the degree of transverse coherence in these cases are summarized in Table 5.12. Thus, in the case of higher photon energies, the results are very similar (in the sense of energy spread dependence) to those shown previously for 500 eV and 12 keV photon energies.

A.4 Details of semi-analytical simulations

A.4.1 Source parameters simulation

In the frame of the analytical approach, source properties were calculated as well [81, 90]. In this case, the amplitude $E(\theta_x, \theta_y)$ in the far field region from a single electron was calculated according to Eq. (5.10). Total amplitude in the far field region for the electron bunch was defined according to Eq. (5.12), (5.12). Additionally, the 2D amplitude distribution was saved for each electron into 3D matrix, where the third dimension is connected to the number of electrons. The amplitude at the source position E_0 (x,y) (in the middle of an undulator) was obtained by the use of the propagator, according to Eq. (5.11).

A.4.2 Field amplitude simulation

Calculations of source parameters were done for zero, $1 \cdot 10^{-3}$, and $2 \cdot 10^{-3}$ relative energy spread values. Amplitude and intensity distribution in the far field region at a distance of 30 m from the source for different photon energies were simulated on the same angular mesh, as in the case of XRT simulations (see Table 5.9). Total photon emittance was calculated in the same way as it was done previously according to Eq. (5.24) (see Fig. 5.16 (dots)). Due to the narrowing of divergence of the radiation, higher is the photon energy, more electrons were needed to sample the radiation on the virtual detector in order to obtain uniform intensity distribution. In order to accumulate good statistics and get a uniform intensity distribution number of electrons used in this calculation was increased (see Table 5.9). This adjustment is also valid for larger energy spread values.

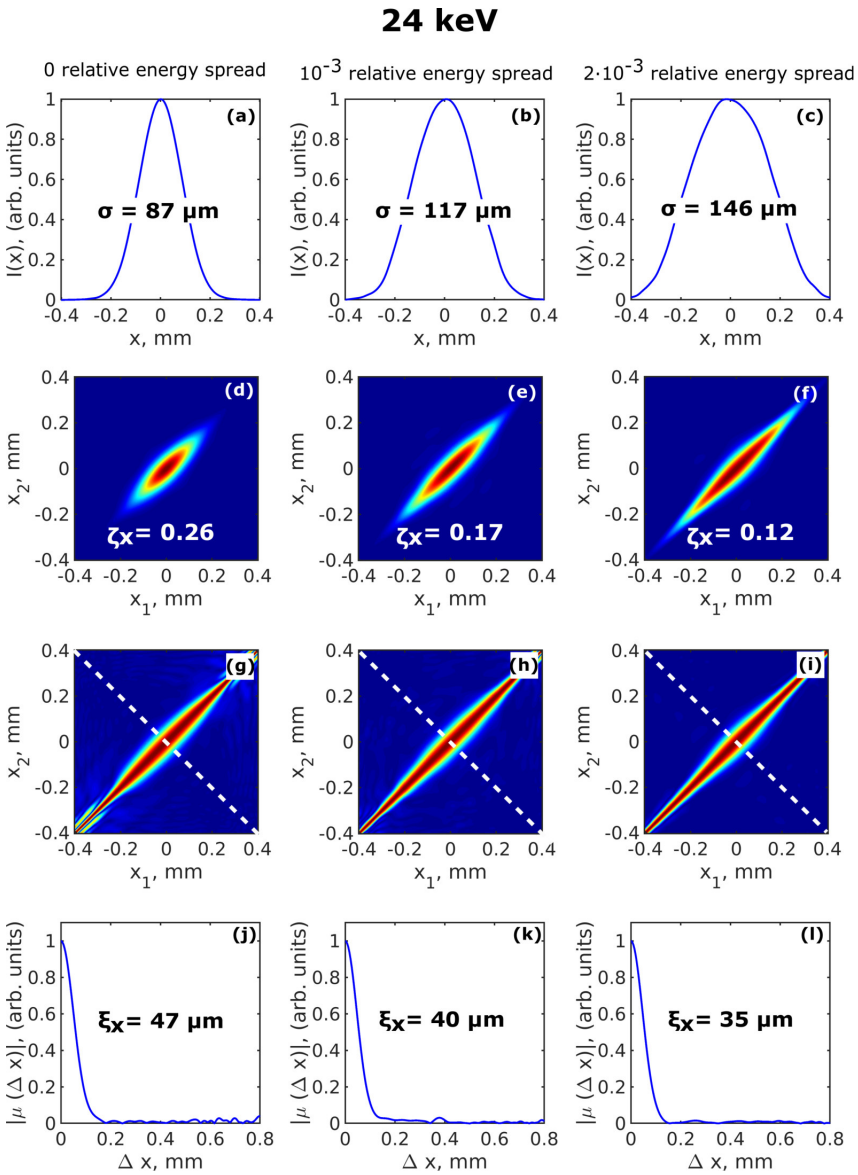

Figure A.2: Simulations of the correlation functions in horizontal direction performed by the XRT software for 24 keV photon energy and different energy spread values. Intensity distribution $I(x)$ (a-c), absolute value of the CSD in the horizontal direction $|W(x_1, x_2)|$ (d-f), absolute value of the SDC $|\mu(x_1, x_2)|$ (g-i), and absolute value of the SDC along the anti-diagonal line (shown in (g-i)) as a function of separation of two points $|\mu(\Delta x)|$ (j-l) simulated in horizontal direction 30 m downstream from the undulator source. In (a-c) σ is the rms value of the beam size, in (d-f) ζ_x is the transverse degree of coherence, in (j-l) ξ_x is the coherence length determined in the horizontal direction.

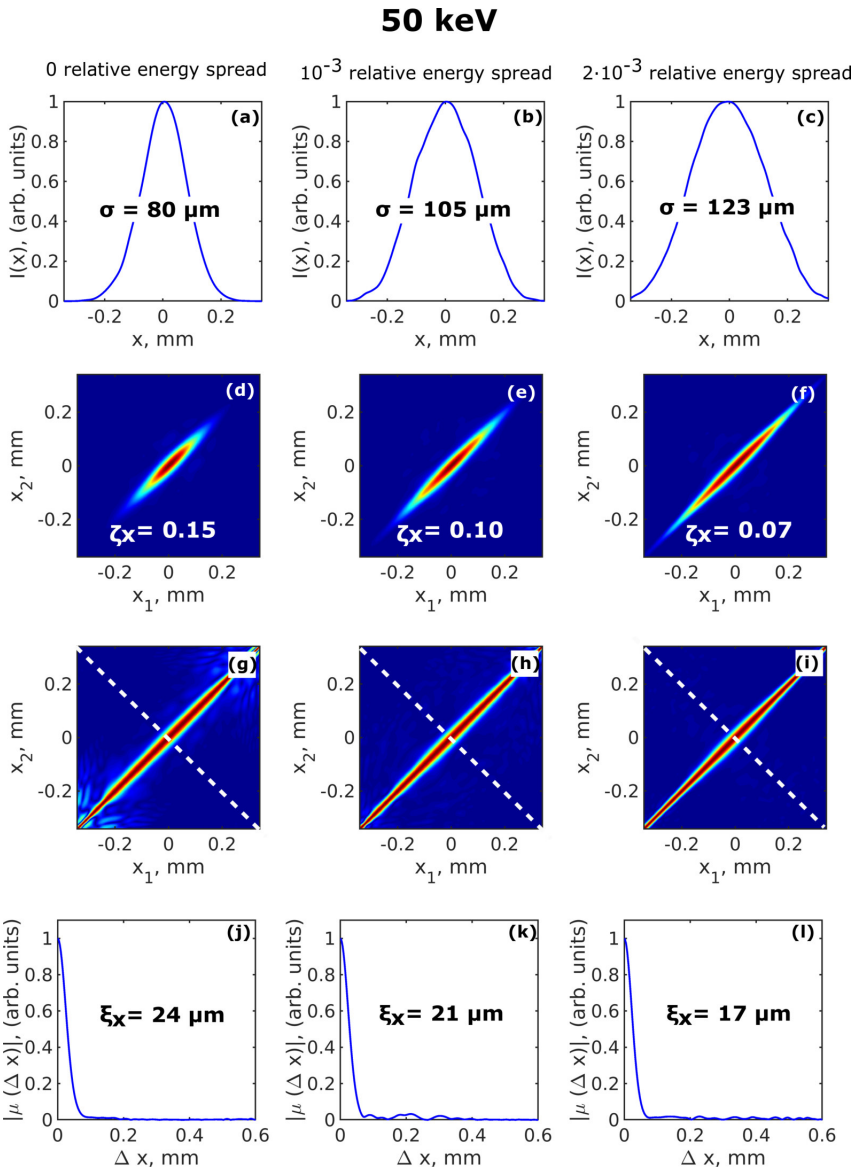

Figure A.3: Simulations of the correlation functions in horizontal direction performed by the XRT software for 50 keV photon energy and different energy spread values. Intensity distribution $I(x)$ (a-c), absolute value of the CSD in the horizontal direction $|W(x_1, x_2)|$ (d-f), absolute value of the SDC $|\mu(x_1, x_2)|$ (g-i), and absolute value of the SDC along the anti-diagonal line (shown in (g-i)) as a function of separation of two points $|\mu(\Delta x)|$ (j-l) simulated in horizontal direction 30 m downstream from the undulator source. In (a-c) σ is the rms value of the beam size, in (d-f) ζ_x is the transverse degree of coherence, in (j-l) ξ_x is the coherence length determined in the horizontal direction.

A.4.3 Coherent-mode representation, coherent fraction and degree of transverse coherence.

The exact parameters of the analytical simulations of the CSD function were used for XRT simulations (see Table 5.8). Correlation functions were calculated and saved for each electron according to Eq. (3.66), with the amplitude distribution calculated according to Eq. (5.10). The eigenvalue problem for the 5D CSD matrix was also reduced to two-dimensional by applying PCA as it was done previously by XRT software. In this case, a coherent fraction of the radiation as a function of electron emittance is shown in Fig. 5.21 (dots). In order to accumulate good statistics, the number of electrons used in this calculation was also increased.

Simulations of the amplitude and CSD were also performed in one transverse direction in the frame of the analytical approach (see Figs. A.4-A.7). One dimensional amplitude distributions for all photon energies considered in this work are shown in Figs. A.4-A.7 (a,b,c). One dimensional CSD was calculated in the far field region as average over an ensemble of electrons according to Eq. (3.66) of the main text in the horizontal direction (see Figs. A.4-A.7 (d,e,f)). The degree of transverse coherence was calculated according to Eq. (3.81). As it is seen from these figures effect of energy spread again enlarges rms values σ of the intensity distribution at the same time it narrows the spectral degree of coherence in anti-diagonal direction, which also leads to a decrease in coherence value as it was already shown by XRT simulations. These results are very close to the results obtained from simulations by XRT software.

Since analytical analysis matches very well to the simulation of correlation functions performed by XRT software (see Fig. 5.21 and Figs. A.4-A.7), it has been extended to other natural electron emittances in a range from 1 to 100 pmrad. The degree of transverse coherence (Eq. (3.81)) calculated in the frame of the analytical approach as a function of natural electron emittance for various relative energy spread values is shown in Fig. A.8. We observe the same tendencies for the degree of transverse coherence as for the coherent fraction of the radiation shown above in Fig. 5.17 and Fig. 5.21. At 500 eV and 12 keV, we reach diffraction-limited case already at 10 pmrad and 1 pmrad respectively. However, at 24keV and 50 keV, even 1 pmrad electron emittance is not sufficient to reach the diffraction limit.

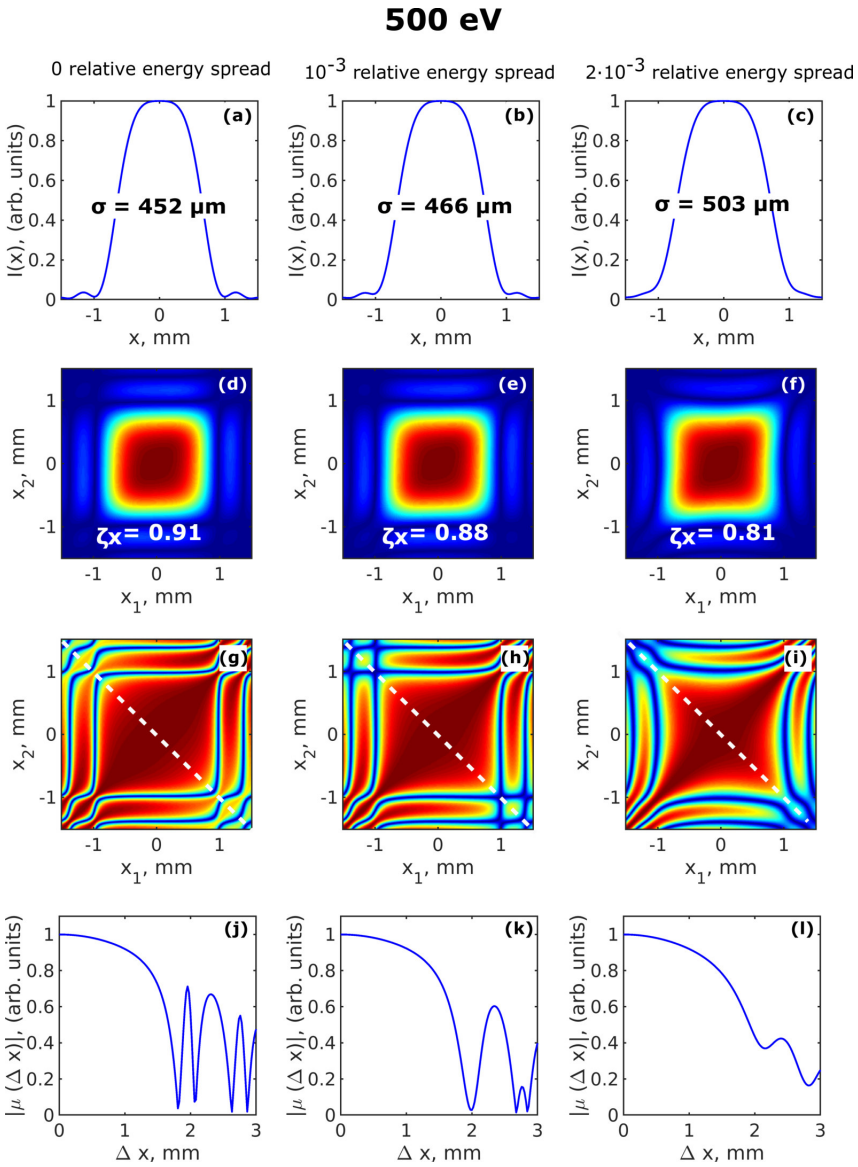

Figure A.4: Simulations of the correlation functions in horizontal direction performed by the analytical approach for 500 eV photon energy and different energy spread values. (a-c) Intensity distribution $I(x)$, (d-f) absolute value of the CSD in the horizontal direction $|W(x_1, x_2)|$, (g-i) absolute value of the SDC $|\mu(x_1, x_2)|$, (j-l) absolute value of the SDC along the anti-diagonal line (shown in (g-i)) as a function of separation of two points $|\mu(\Delta x)|$ simulated in horizontal direction 30 m downstream from the undulator source. In (a-c) σ is the rms value of the beam size, in (d-f) ζ_x is the transverse degree of coherence, in (j-l) ξ_x is the coherence length determined in the horizontal direction.

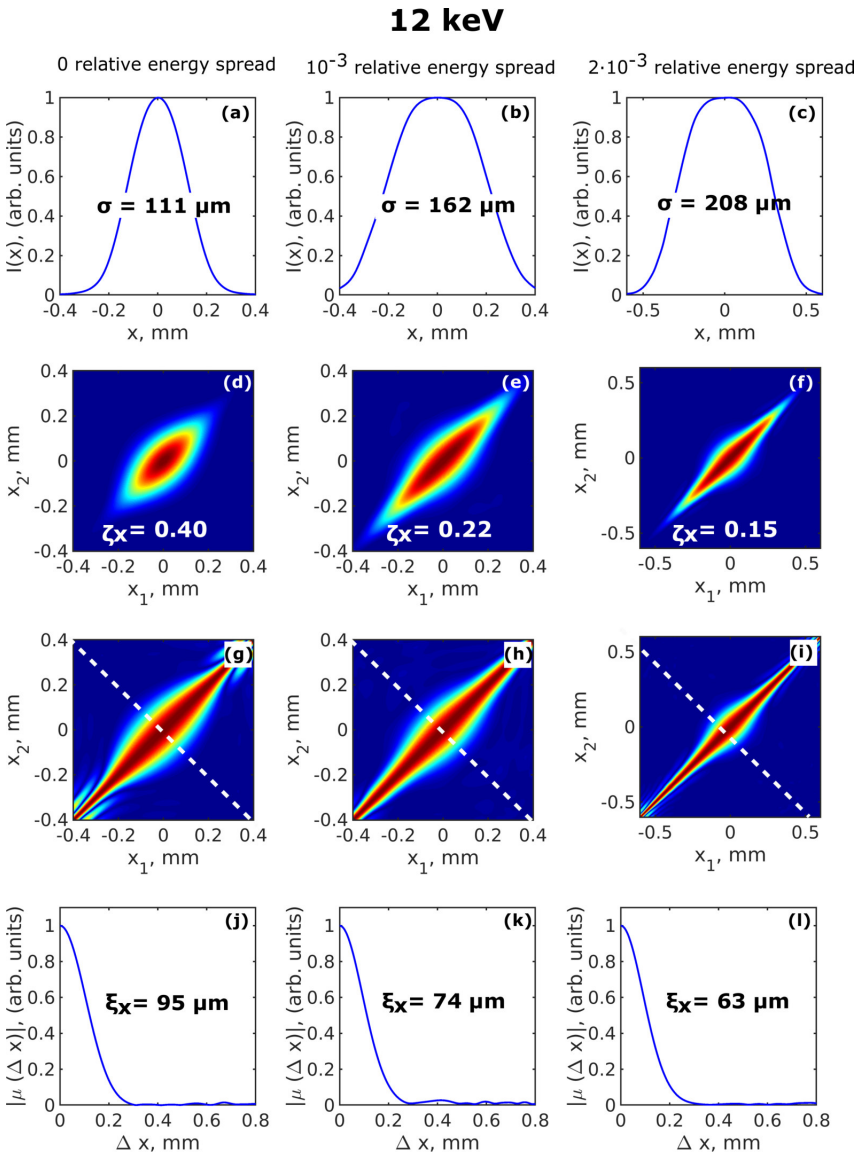

Figure A.5: Simulations of the correlation functions in horizontal direction performed by the analytical approach for 12 keV photon energy and different energy spread values. (a-c) Intensity distribution $I(x)$, (d-f) absolute value of the CSD in the horizontal direction $|W(x_1, x_2)|$, (g-i) absolute value of the SDC $|\mu(x_1, x_2)|$, (j-l) absolute value of the SDC along the anti-diagonal line (shown in (g-i)) as a function of separation of two points $|\mu(\Delta x)|$ simulated in horizontal direction 30 m downstream from the undulator source. In (a-c) σ is the rms value of the beam size, in (d-f) ζ_x is the transverse degree of coherence, in (j-l) ξ_x is the coherence length determined in the horizontal direction.

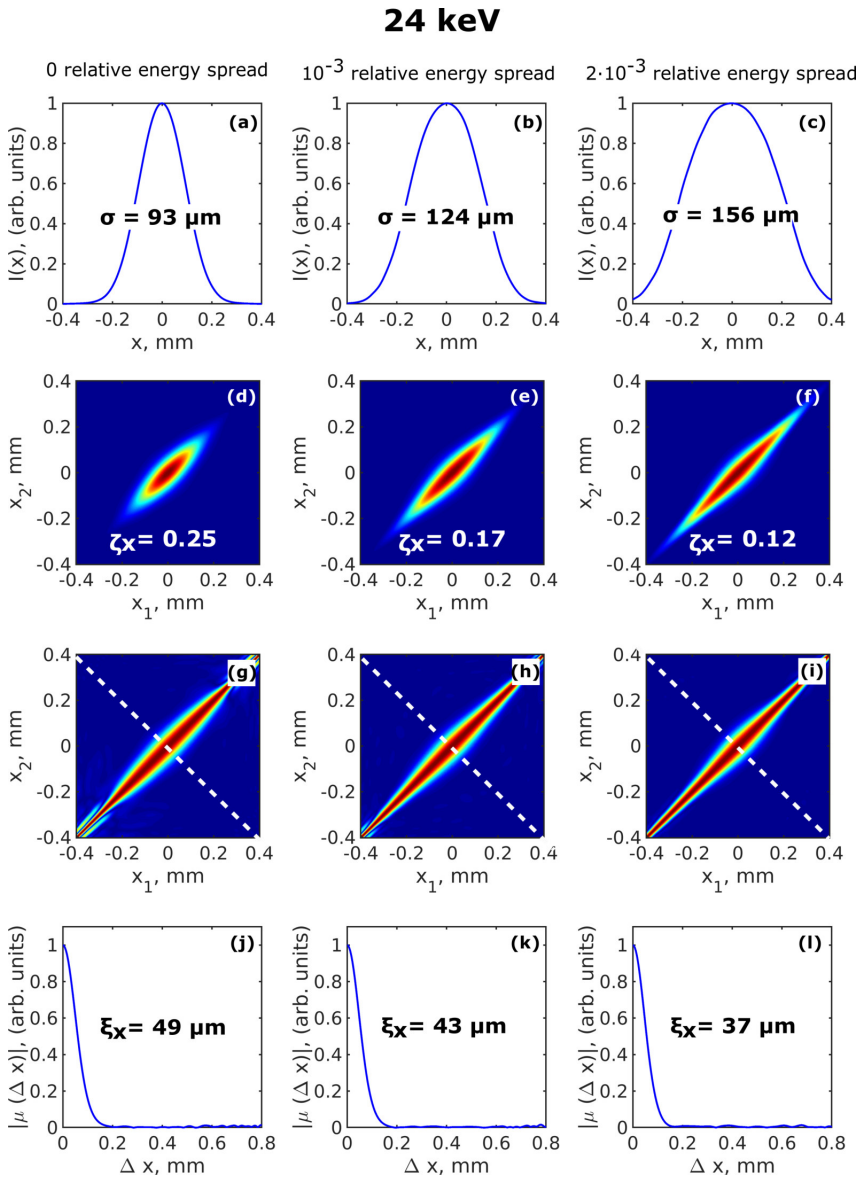

Figure A.6: Simulations of the correlation functions in horizontal direction performed by the analytical approach for 24 keV photon energy and different energy spread values. (a-c) Intensity distribution $I(x)$, (d-f) absolute value of the CSD in the horizontal direction $|W(x_1, x_2)|$, (g-i) absolute value of the SDC $|\mu(x_1, x_2)|$, (j-l) absolute value of the SDC along the anti-diagonal line (shown in (g-i)) as a function of separation of two points $|\mu(\Delta x)|$ simulated in horizontal direction 30 m downstream from the undulator source. In (a-c) σ is the rms value of the beam size, in (d-f) ζ_x is the transverse degree of coherence, in (j-l) ξ_x is the coherence length determined in the horizontal direction.

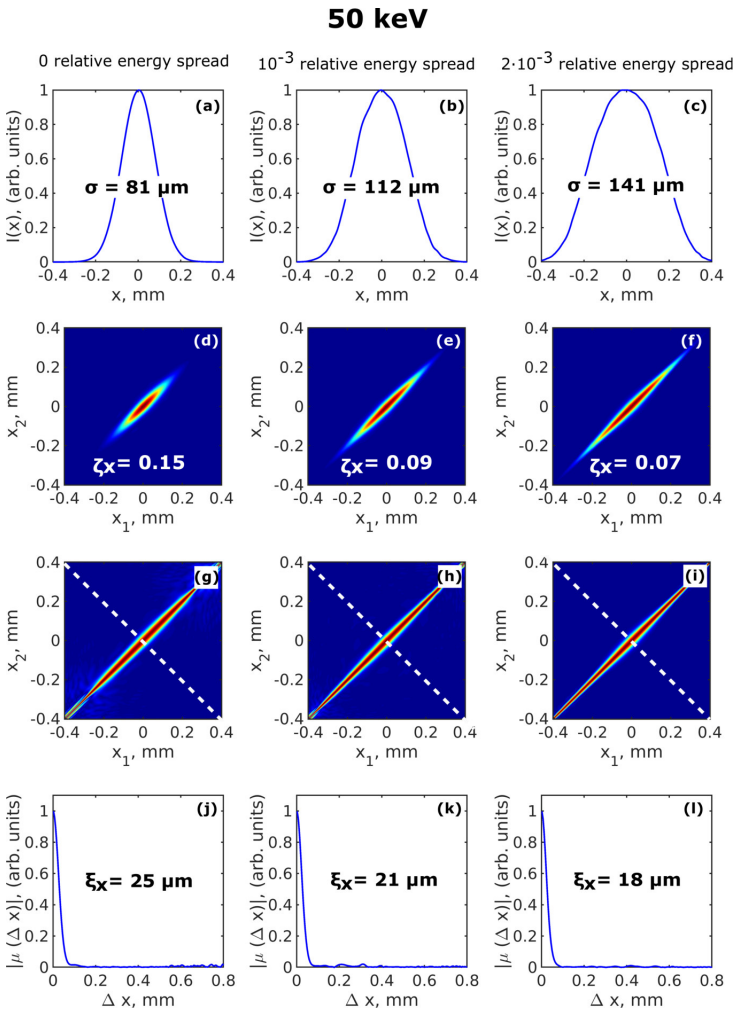

Figure A.7: Simulations of the correlation functions in horizontal direction performed by the analytical approach for 50 keV photon energy and different energy spread values. (a-c) Intensity distribution $I(x)$, (d-f) absolute value of the CSD in the horizontal direction $|W(x_1, x_2)|$, (g-i) absolute value of the SDC $|\mu(x_1, x_2)|$, (j-l) absolute value of the SDC along the anti-diagonal line (shown in (g-i)) as a function of separation of two points $|\mu(\Delta x)|$ simulated in horizontal direction 30 m downstream from the undulator source. In (a-c) σ is the rms value of the beam size, in (d-f) ζ_x is the transverse degree of coherence, in (j-l) ξ_x is the coherence length determined in the horizontal direction.

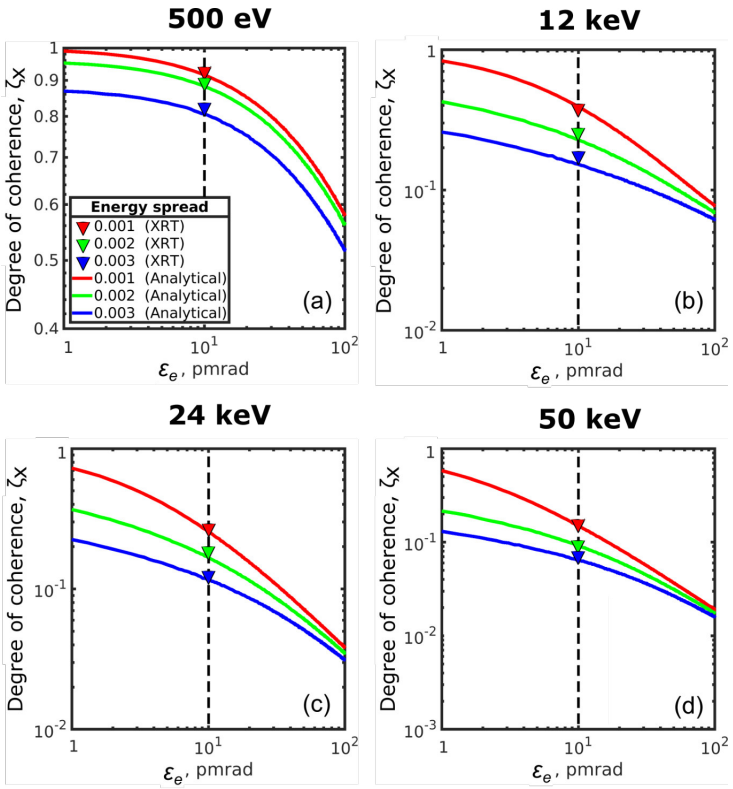

Figure A.8: Simulation of the degree of transverse coherence ζ_x obtained from XRT and analytical analysis (Eq. (3.63)) as a function of natural electron emittance for 500 eV, 12 keV, 24keV, and 50 keV.

A.5 Source and optics vibrations

This chapter provides additional calculations on spatial coherence degradation due to optics vibrations at higher photon energies. In this case, the setup under consideration (presented in Fig. A.9) contains an undulator source, a DCM at 47 meters from the source, and a lens at 3 meters after the DCM.

The first part is dedicated to the vibrations of the DCM and the analysis done according to [179]. The DCM angular vibrations are characterized as root-mean-square (RMS) deviation from the equilibrium position

$$\sigma_m^2 = \frac{1}{T}\int_0^T dt\phi_m^2(t) =< (\phi_{m1}(t) - \phi_{m2}(t))^2 >=< \phi_{m1}^2(t) > + < \phi_{m2}^2(t) > -2 < \phi_{m1}(t)\phi_{m2}(t) >, \tag{A.1}$$

where ϕ_{m1} and ϕ_{m1} are angular vibrations of the DCM crystals. The contribution of the correlation part depends on the type of monochromator. The correlation part almost disappears for a long-arm monochromator with individual angular stages for the crystals. The beam at the position of the lens is broadened by x_l=$\sigma_m(z_0 - z_m)$. Considering Gaussian beams, beam size at the position of the lens accounting for broadening due to DCM vibrations may be calculated as

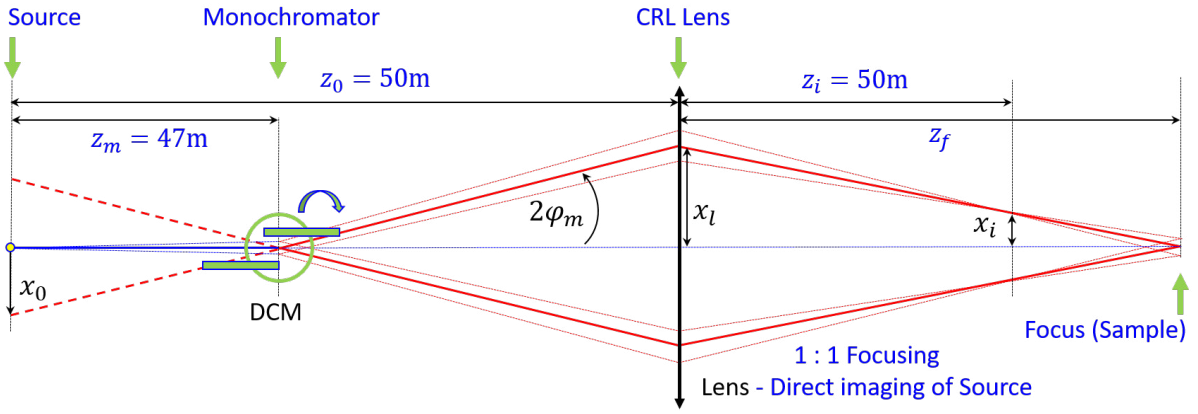

Figure A.9: Diagram of the beam propagation through the optical system which includes the DCM located at z_m = 47 m and the lens at z_0 = 50 m. The beam is turned due to DCM vibration by $\pm 2\phi_m$. Image position is z_i (equals to z_f in the system without vibrations). Deviations from the central axis in lens plane, image and source positions are denoted by x_l, x_i, and x_0 accordingly.

$$\Sigma_L = \sqrt{\Sigma_x^2 + \Sigma_S^2 + \Sigma_x'^2 z_0^2 + \Sigma_S'^2 z_0^2 + \sigma_m^2 (z_0 - z_m)^2}, \tag{A.2}$$

where Σ_x and Σ_x' are source size and divergence defined in Eq.4.54. In Eq. A.2 due to source vibrations, additional broadening of the photon beam is introduced through photon source size Σ_S (transverse movement of the source) and divergence Σ_S' (pointing vibrations of the source). At the source position the size of the beam and divergence may be calculated as

$$\Sigma_0 = \sqrt{\Sigma_x^2 + \Sigma_S^2 + \sigma_m^2 z_m^2}, \tag{A.3}$$

$$\Sigma_0' = \sqrt{\Sigma_x'^2 + \Sigma_S'^2 + \sigma_m^2}. \tag{A.4}$$

The calculated source broadening for the case of E = 12keV photon energy presented in Fig. A.10. The source transverse movement Σ_S was chosen as $0.45\Sigma_x$ in order to get 10% broadening of the photon source without DCM angular vibrations (when $\sigma_m = 0$).

The results show that in order to stay within 20% of beam broadening without source vibrations, the angular pitch vibration of the DCM should not exceed 45 nrad in vertical and 70 nrad in horizontal direction accordingly. Photon source vibration of 10% ($\Sigma_S = 0.45\Sigma_x$) tightens these limitations to 30 nrad vertically and 50 nrad horizontally.

The DCM vibration leads not only to an increase of the beam size but also to a shift of the image position. The position denoted by distance z_f in Fig. A.9 is a new focus position, where the beam deviation from the central axis is zero independent of the amplitude of the vibrations. This is the image position for the virtual source at the monochromator position. In the case without vibrations positions z_i and z_f coincide. In Fig. A.11, the calculation results for different angular pitch vibrations are presented. The shift of the focus and the source broadening due to angular vibrations of the DCM are shown in Fig. A.11(a),(b). When the DCM vibration is zero, the broadening of the focused beam occurs only due to transverse movement of the source(see Fig. A.11 (c),(d)). In this case, the broadening is $1.1\Sigma_x$, and the focus position stays the same

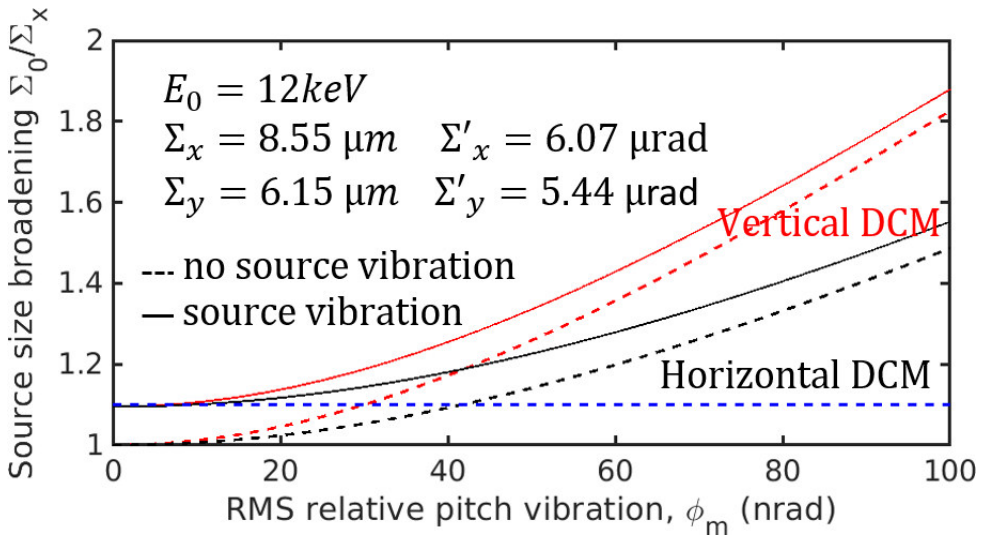

Figure A.10: Relative source size broadening as a function of DCM angular pitch vibrations for the case with and without source vibrations.

z_i=z_f 50 meters.

As a result of the source and DCM vibrations, the coherence properties of the beam may significantly degrade, as shown in Fig. A.12. As can be seen from Fig. A.12, without DCM and source vibrations, the coherent fraction of the beam (calculated from the coherence volume of the beam Σ_{coh}= $\lambda/2\pi$ in Eq. 5.43) is 50% and 33% in vertical and horizontal directions accordingly (Fig. A.12(a), dashed lines). By introducing angular pitch vibrations, the coherent fraction drops to 27% in vertical and 22% in horizontal directions. The coherent fraction drops down further by an additional 4% by raising source vibrations in both directions. The total coherent fraction (assuming Gaussian approximation), without vertical DCM vibrations (only horizontal pitch vibration of the DCM is considered), is shown in Fig. 4(b). In this case, one can see a significant drop in the coherent fraction by 50%, accounting for both angular DCM and source vibrations.

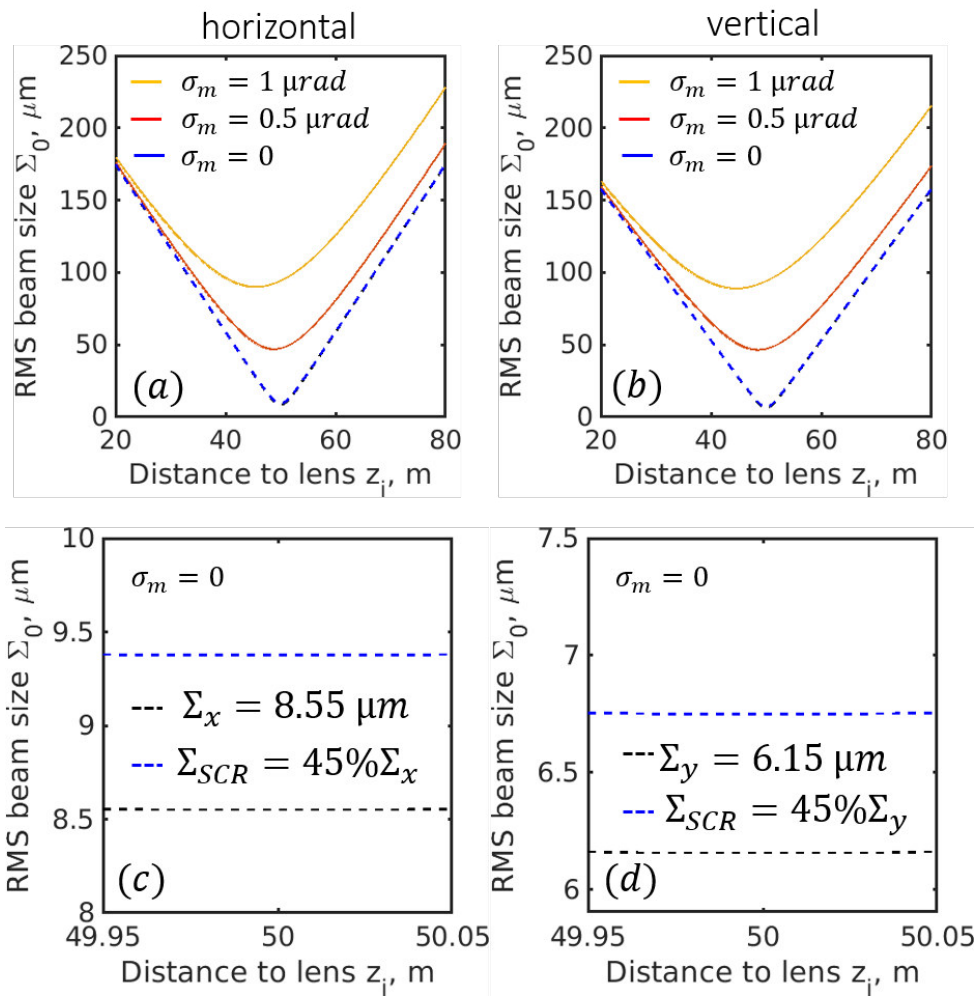

Figure A.11: Beam size RMS value as a function of distance after the lens for different amplitudes of the DCM angular vibrations σ_m.

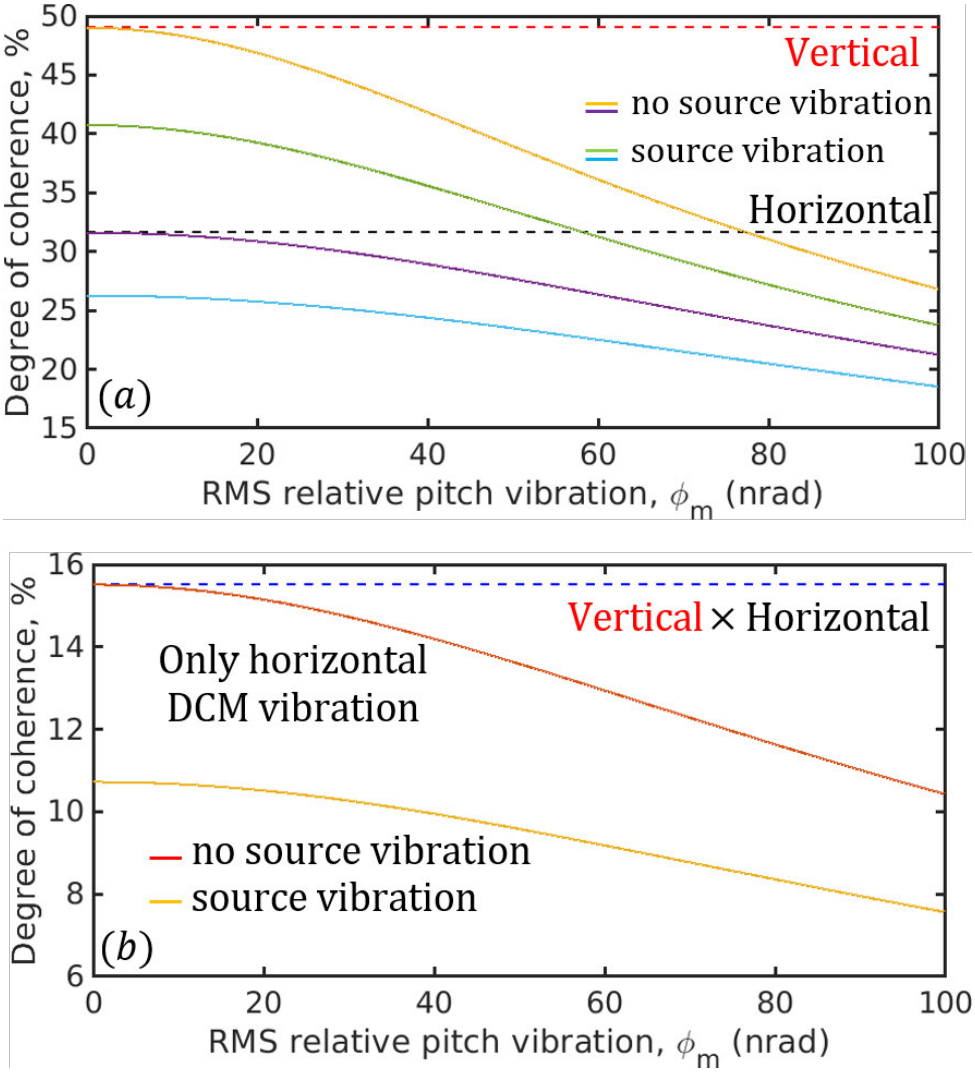

Figure A.12: Transverse coherent fraction (a) and total coherent fraction (b) as a function of DCM angular pitch vibrations for the case with and without source vibrations.

A.6 Soft X-ray grating monochromators as a source of spatial coherence degradation: A wave-optical approach

A wave-optical simulations and coherence analysis of the beam transported through the optics are presented in this section, paying particular attention to a focusing varied line spacing (VLS) plane grating monochromator (PGM). It was shown that this beamline optical element used in several soft X-ray beamlines at synchrotron sources and free-electron lasers can cause a non-negligible spatial coherence degradation. It was demonstrated that the origin of this effect arises from the entanglement between spatial and spectral properties (spatiotemporal coupling [180, 181]) of the photon beam generated by the grating. The latter implies that space and frequency (or space and time) dependencies are not separable into independent functions after such a dispersive element. It was shown which parameters are essential for this effect and how they are linked to each other.

In the soft X-ray range, most existing sources are already diffraction-limited, at least in the vertical direction. However, at this photon energy range, diffraction-limited storage rings are expected to reach a spatial degree of coherence of the total beam close to 100% (see section 5.5) and thus, in terms of spatial coherence, will resemble a laser source. In this case, the photon flux of the source can be considered completely coherent, and thus, the spatial degree of coherence does not need to be increased by, for example, slit systems at the expense of flux. These beam properties not only bring new scientific opportunities, but also pose enormous challenges for the optical layout of the beamlines and the quality of the optics used. The high spatial coherence of the source must be preserved by the photon beam transport system to make it available for the actual experiment at the sample position. It has already been demonstrated that the degradation of the spatial coherence of the source may occur, for example, due to optical surface defects [182–185], incoherent scattering [186, 187], or vibrations of optical elements [87, 88, 188]. The latter effect imposes the most significant influence on spatial coherence so far. This becomes obvious with modern beamline designs and their use of almost exclusively horizontally deflecting optics, which are less susceptible to vibrations.

One way to reproduce measurement or identify the phenomena involving the coherence degradation, as well as clarify their cause, is through wave-optical simulations [86, 189]. Wave-optical simulations allow to explore varies beamline design options including real optical surfaces, vibrations, misalignments and many other aspects. Almost every simulation tool that offers wave-optical calculations also has built-in tools to determine the spatial coherence properties from the obtained wave fields. Many of the coherence analysis tools can also be integrated in existing wave-optical simulation software or the coherence can be calculated externally using the obtained wave fields. The presented results are based on wave-optical simulations with slightly polychromatic light using the software Xrt [86] and are supported by experimental observations [87, 95, 190]. In the following, it is shown that the soft X-ray focussing VLS plane grating monochromator used in many soft X-ray beamlines is a source of spatial coherence degradation and can cause a huge drop in spatial coherence.

A.6.1 Beamline layout and focusing VLS-PGM

The beamline layout used for the wave-optical simulations is based on the layout of the P04 beamline at PETRA III [191] (see figure A.13). The insertion device is an APPLE-II undulator, which delivers photon energies in the range of $E = 250 - 3000$ eV in the first harmonic. The first element of the beamline is a beam-defining aperture 27.9 m downstream from the source. It serves as an angular filter and increases the spatial coherence when the aperture is closed. The monochromator is a focusing VLS-PGM and consists of a plane mirror, a variable line spacing plane (VLS) grating and an exit slit (EXSU). The monochromator is located 46 m downstream from the source. The VLS plane grating spectrally splits the photon beam. Due to the variable line spacing of the grating, the photon beam is additionally focused on the exit slit in the vertical direction, which is located 25 m behind the grating. The exit slit selects a certain bandwidth and together with the VLS grating defines the energy resolution of the monochromator. The plane mirror in front of the grating illuminates the grating at an angle of incidence that simultaneously satisfies the grating equation $nk\lambda = \sin\alpha + \sin\beta$ and the focusing condition of the plane grating $\cos\beta/\cos\alpha = c_{ff}$ [192]. The angles α and β are the angles of incidence and diffraction, n is the diffraction order, λ is the wavelength and k is the line density. When scanning the photon energy with the monochromator, c_{ff} is kept constant, resulting in exact focusing with fixed entrance r and exit arm length r'. The magnification of the VLS grating is defined by [193]:

$$M = \frac{r'}{r \cdot c_{ff}} \tag{A.5}$$

Using the distances shown in figure A.13 and described above, and a $c_{ff} = 2.0$ (PETRA III beamline P04, $k = 1200$ lines/mm grating), the source is demagnified with $M = 0.27$ onto the exit slit. Due to the variable line spacing of the grating, the angular dispersion of the photon beam occurs, implying that each wavelength is focused individually at different z-positions along the exit slit (see figure A.13). Due to the finite resolution function of the monochromator and the finite photon beam size for each wavelength, the individual photon beams also overlap, representing the angular dispersion function of the grating. The spatial extend of the dispersed photon beam at the exit slit position can be determined by the reciprocal linear dispersion [193] and the bandwidth of the illuminating photon beam and is given by:

$$\Delta z[mm] = \frac{1.24 \cdot 10^{-3} \cdot nkr'[m]}{\cos\beta \cdot E^2[eV]} \Delta E[eV] \tag{A.6}$$

A photon beam incident on the VLS grating with a photon energy of E = 1200 eV and an energy bandwidth of $\Delta E = 200$ meV will generate a beam profile with a size of 89 μm (FWHM) at the exit slit position.

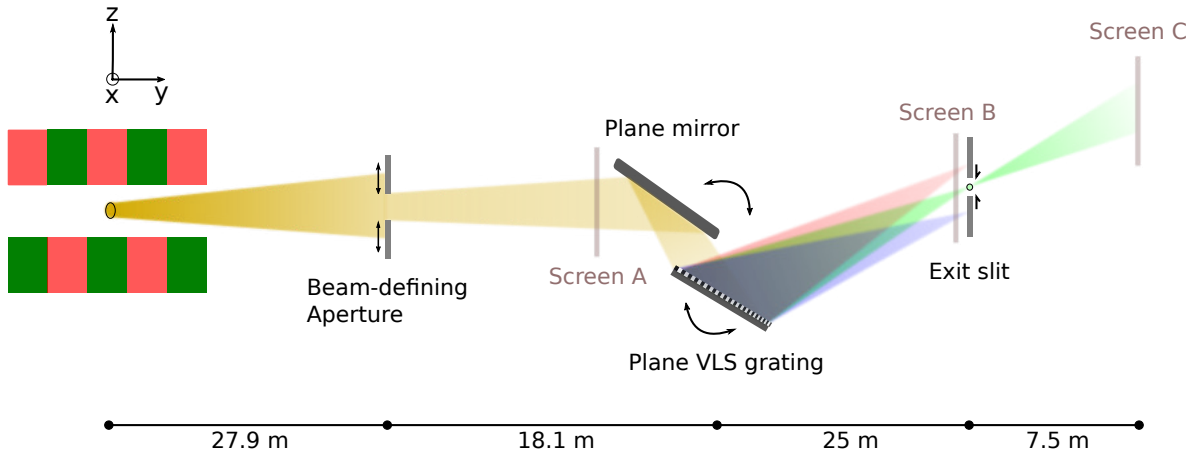

Figure A.13: Beamline Layout used for the wave-optical simulations. The coherence analysis of the wave fields using the standard methods and the CMD is performed at screen A after the beam-defining aperture, at screen B closely before the exit slit, and at screen C after the exit slit.

A.6.2 Wave-optical simulations

For the wave-optical simulations the XRT software [86] was used. For efficiency and performance reasons, a filament electront beam with zero energy spread was employed as the source of radiation. Such a photon source has a spatial degree of coherence of $\zeta = 100\%$. The photon energy has been set to $E = 1200$ eV for all simulations. Furthermore, the size of the beam-defining aperture was chosen to be 50 μm x 400 μm (h x v). In addition, a horizontal size of 50 μm was set for the exit slit.

Assuming that the statistical process is stationary, the calculation of the spatial coherence is based on the standard methods [23] and the use of the coherent mode decomposition (CMD) [47]. As a result, one obtains the spatial degree of coherence ζ (Eqs. (3.63),(3.74)) and the coherent fraction (CF) (Eq. (3.75)) of the investigated wave fields. Both are single values that represent the spatial coherence properties of the total beam. The photon beam energy bandwidth ΔE used for the simulations was selected such that the quasi-monochromatic approximation can be applied for the coherence analysis methods, which is the case if $\Delta E \ll E$. In the simulations, it was ensured that the number of electrons used lead to reasonable statistics where the obtained spatial coherence values converge and does not change anymore with increasing number of electrons. The number of modes was chosen such that the cumulative sum of the mode weights always equals one. These two facts lead to reliable coherence values for the presented simulations.

A.6.3 Results and discussion

To analyse the spatial coherence properties of the photon beam along the beamline and thus the influence of the VLS plane grating monochromator on the spatial coherence properties, the spatial degree of coherence ζ (Eq. (3.74)) was determined at three different positions. The first position (screen A) has been set after the beam-defining aperture and closely before the plane

mirror, the second position (screen B) is after the grating and closely before the exit slit, and the third position (screen C) is after the exit slit (see figure A.13). As mentioned in the previous section, the source generates a fully coherent beam with a spatial degree of coherence of $\zeta = 100\%$. In case of a monochromatic source with just a single photon energy $E = 1200$ eV, the VLS grating monochromator generates a focused beam at the exit slit position with a size of $\sigma_b = 7$ μm (rms) based on the magnification described in equation (A.5). The exit slit size was set to $w_e = 20$ μm in this case. The spatial degree of coherence of the photon beam at screen A, B, and C is $\zeta = 100\%$, as expected. The exit slit size is larger than the beam size at the exit slit and therefore has no effect on the beam size or spatial coherence after the exit slit.

The same analysis was performed for a polychromatic source with a very narrow photon energy bandwidth of $\Delta E = 200$ meV. This bandwidth results in an energy resolution of $\Delta E/E = 1.6 \cdot 10^{-4}$ at 1200 eV. It has been found that at a finite bandwidth of $\Delta E = 200$ meV, the beam at the source and at screen A still has a spatial degree of coherence of $\zeta = 100\%$, this is also true for all bandwidths below $\Delta E = 600$ meV. In this case and at these positions, the spatial coherence properties of the photon beam is therefore decoupled from the spectral properties of the beam, which is to be expected. The photon beam size after the grating is determined by ΔE incident on the grating as described in equation (A.6). Hence, at screen position B spatial and spectral properties are correlated to some extent. When analysing the coherence properties of the photon beam at screen B, it was found that the degree of spatial coherence drops significantly to $\zeta = 17\%$ (at $\Delta E = 200$ meV). This is at first glance a very surprising and unexpected result, since the photon beam at this position is a superposition of several fully coherent single Gaussian beams whose spacing is determined by the dispersion properties of the grating. The coherence properties after the exit slit at screen C were further analysed to investigate the effect of the slit on the spatial coherence properties of this beam. For this, the slit was varied between $w_e = 100$ μm and 8 μm and the spatial degree of coherence of the photon beam at screen C was determined (see figure A.14). It was found that the spatial degree of coherence increases with decreasing slit size, which is an expected result considering the coherence properties of the incident beam. The obtained results are in line with several independent experimental findings which also describe that the assumed fully coherent beam of the source at soft X-ray beamlines in the vertical direction show a rather low spatial degree of coherence in this direction and that it can be increased or decreased with closing or opening the exit slit, respectively [87, 95, 190]. The experimental findings thus support the results of the simulations. Starting from an exit slit size of around $w_e = 20$ μm and going towards smaller exit slit sizes, we see an effect which is opposite to the expected behaviour. Below an exit slit size of $w_e = 20$ μm, the degree of spatial coherence saturates to $\zeta = 56\%$ and remains constant with decreasing exit slit size. Looking at the transmitted ΔE, the same effect is seen. The photon energy bandwidth even remains constant with $\Delta E = 25$ meV. In terms of ΔE, this is an expected behaviour since the minimum photon energy bandwidth achieved is determined by the dispersion properties of the grating and cannot be further reduced by closing the exit slit. The observed phenomena lead to the assumptions that there is a strong correlation between the spatial and the spectral properties of the photon beam after the grating. This effect is related to the first-order spatio-

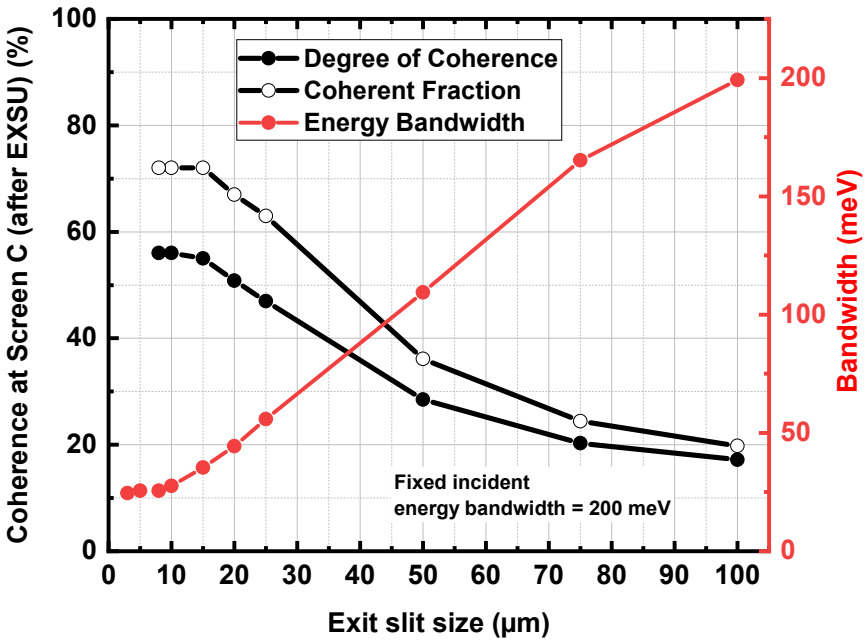

Figure A.14: Spatial degree of coherence and coherent fraction at screen C for different exit slit sizes. The corresponding energy bandwidth at screen C is indicated in red. The incident energy bandwidth has been set to $\Delta E = 200$ meV.

temporal distortions, that is, couplings between spatial (or spatial-frequency) and temporal (or frequency) coordinates, of Gaussian pulses and beams. These distortions include pulsefront tilt, spatial dispersion and angular dispersion [180, 181, 194]. To explore this effect more in detail and to determine its dependencies, a fixed exit slit size of $w_e = 20$ μm was set and ΔE of the source varied (see figure A.15). In figure A.15(a), the degree of spatial coherence at screen B and screen C was compared as a function of ΔE. Figure A.15(b) shows the transmitted photon energy bandwidth at screen C as a function of the incident photon energy bandwidth at screen B. It was found, that in case of $\Delta E = 10$ meV and $\Delta E = 20$ meV, the spatial degree of coherence is similar to the monochromatic case. The photon beam, in this case, is smaller than the 20 μm exit slit size and hence the photon energy bandwidth of the incoming and transmitted beam is the same. At $\Delta E = 50$ meV the size of the photon beam incident on the exit slit is slightly larger than the exit slit size. The transmitted photon energy bandwidth is slightly smaller than the incoming one. In this case, the degree of spatial coherence of the incoming and transmitted beam is different. After the exit slit the spatial degree of coherence is about 10% larger. With increasing ΔE, it was found that the degree of spatial coherence determined at screen C converges to $\zeta = 50\%$ and does not further decrease whereby the degree of spatial coherence at screen B further decreases. This happens exactly at the point where the transmitted ΔE 44 meV does not change anymore due to the finite bandpass of the 20 μm exit slit size.

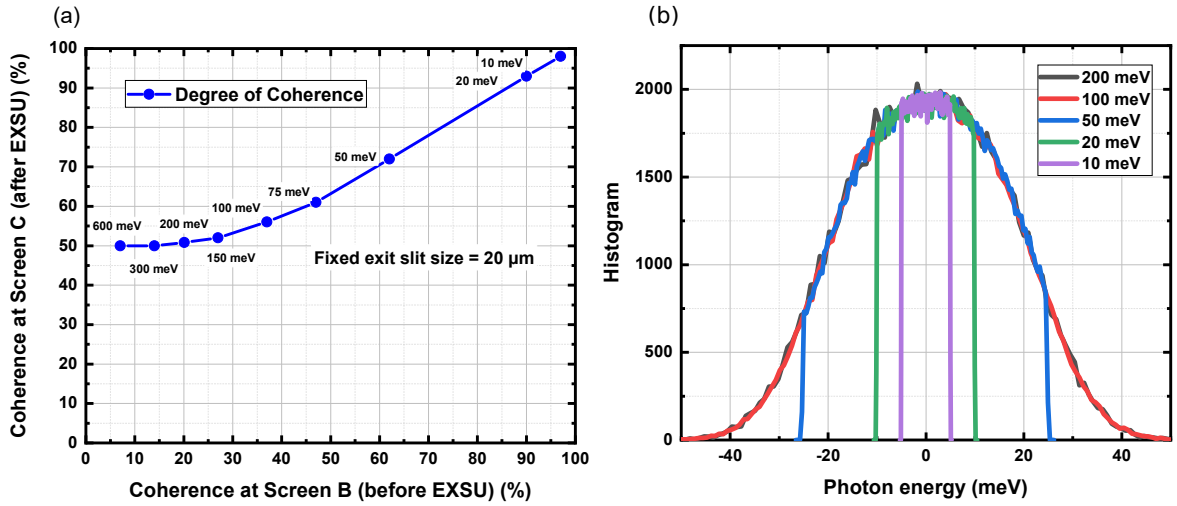

Figure A.15: (a) Comparison of the obtained spatial degree of coherence between the photon beam incident on the exit slit (screen B) and the photon beam after the exit slit (screen C) for different incident photon energy bandwidths (ΔE = 10 meV - 600 meV). The exit slit size has been set to $w_e = 20$ μm. (b) Spectrum of the photon beam at screen C for a set of five different incident photon energy bandwidths.

A.6.4 Theoretical substantiation of the effect.

An attempt to explain this effect is made within the framework of laser physics. In the laser physics and applications of ultrafast pulse optics space and time dependences of an pulse's electric field are often assumed to be factorizable functions

$$E(\mathbf{r}, t) = E(\mathbf{r})E(t) \tag{A.7}$$

Spatio-temporal distortion occurs when such assumption is violated. It was shown [181] that any manifestations associated with angular dispersion automatically include the pulse front tilt (PFT) phenomena [181]. At the synchrotron facility in the soft X-ray range such dispersive optical element is the monochromator consisitng of a grating and the focusing lens or the VLS grating (see Fig. A.16).

Assuming beam propagation in the z-direction and the disperssion in x plane, negletic another transverse direction 'y' the Eq. (A.7) may be rewritten acounting for the PFT in x-z plane

$$E(x, z, t) = E(x, z)E(t - px) \tag{A.8}$$

where p is the PFT introduced as [181]

$$p = \frac{dk_x}{d\omega} \tag{A.9}$$

Using the Fourier transform and the Shift theorem of Eq.(A.8) with respect to t yields an additional factor corresponding to the PFT

$$E(x, z, \omega) = E(x, z)E(\omega)e^{-ipx\Delta\omega}, \tag{A.10}$$

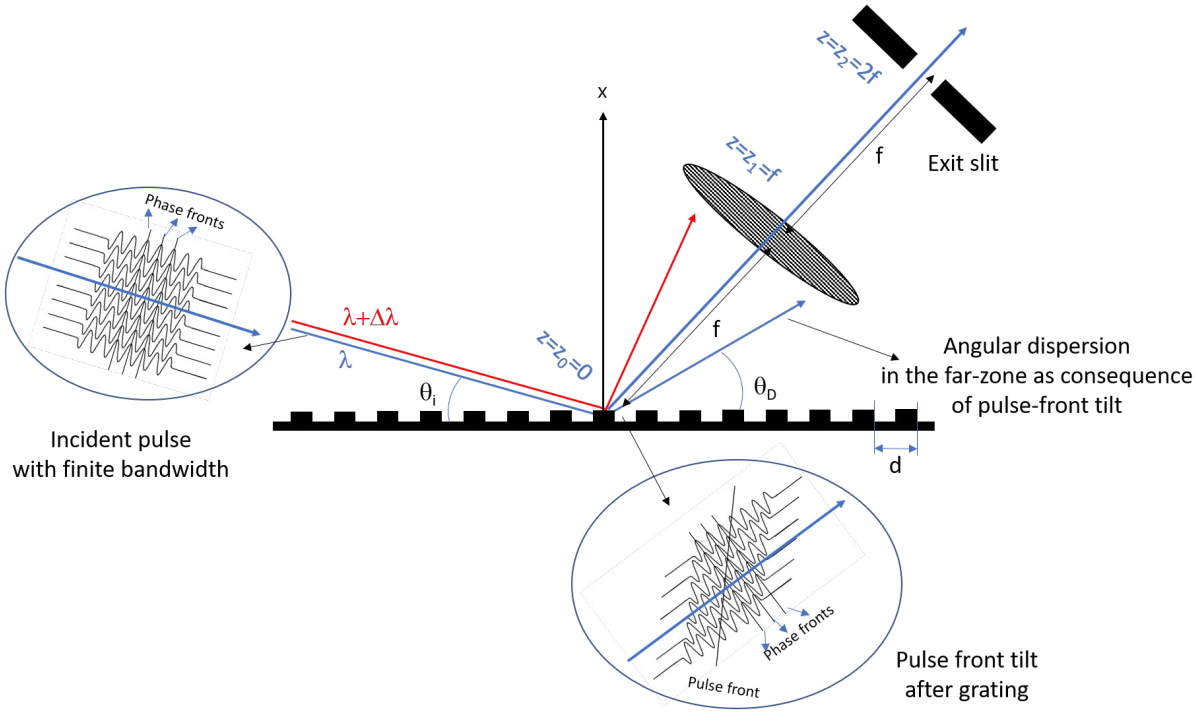

Figure A.16: A beam propagating through a grating monochromator undergoes a pulse-front tilt. After propagation in the far zone, the pulse-front tilt results in angular dispersion. After free-space propagation, the beam may enter an optical system, here a lens.

where $\Delta\omega$ is counted from the center frequency ω_0 of the diffracted beam if the dispersive element, such as grating, is considered (see Fig. A.17). Applying the second Fourier transform and the Shift theorem one obtains components of the electric field in the k-ω domain

$$E(k_x, k_z, \omega) = E(k_x + p\Delta\omega, k_z)E(\omega) \tag{A.11}$$

Thus, without additional effects of spatial or frequency chirp, the Eqs. (A.8), (A.11) show the translation between the components of the electic filed from x-t to k-ω domain. The translation may be used in order to calculate spatial coherence fuction. It should be taken into account that the pulse front and phase front after the dispersive optical element may have a certain angle between them (see Fig. A.16).

In oder to charecterize spatial properties of the pulse in the dispersive x direction acounting for PFT the basic theory of optical coherence is used. Assuming stationary process and the ergodicity of the process, the ensemble average in Eq. (3.58), may be replaced by the time average

$$\Gamma(x_1, x_2) = \int_{-\infty}^{\infty} E^*(x_1, t)E(x_2, t)dt \tag{A.12}$$

It is more convinient to work in the frequency domain, utilizing CSD function, assuming that the quasi-monochromatic approximation is valid and the ensemble averaged replaced by the

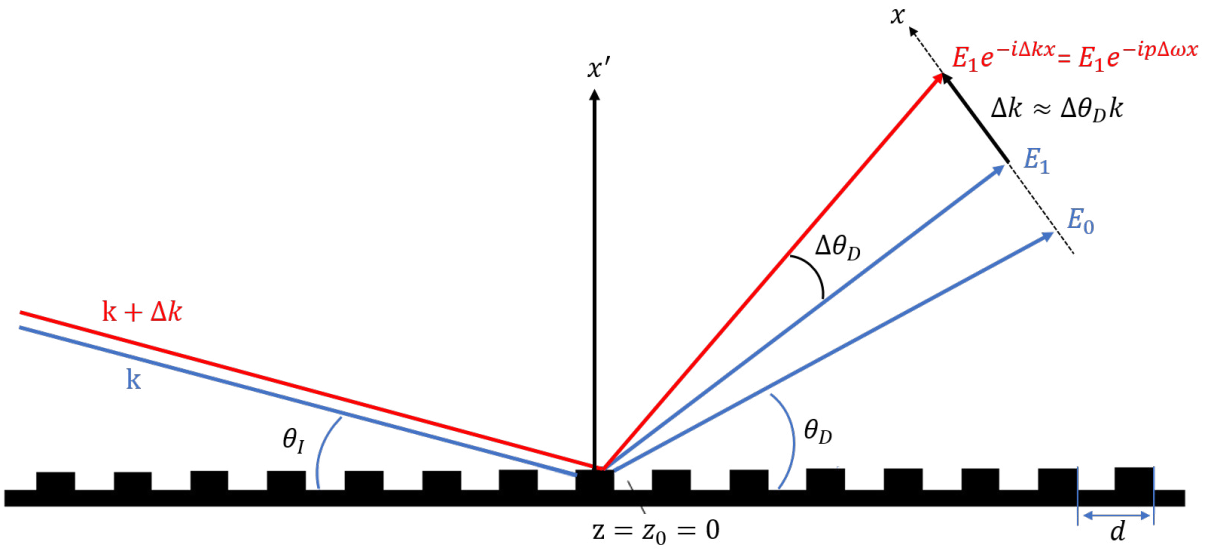

Figure A.17: A beam propagating through a grating monochromator results in angular dispersion.

average over narrow frequency distribution $\Delta\omega$.

$$J(x_1, x_2) = \int_{-\infty}^{\infty} E^*(x_1, \Delta\omega) E(x_2, \Delta\omega) d\Delta\omega \tag{A.13}$$

A Gaussian spatial profile of the beam with the PFT is assumed,

$$f(x) = e^{\frac{-x^2}{2\sigma_x^2}}, \tag{A.14}$$

with a certain bandwidth

$$S(\omega) = |f(\omega)|^2 = e^{\frac{-\Delta\omega^2}{2\sigma_\omega^2}}. \tag{A.15}$$

For the calculation of the CSD function for the beam with the PFT at a certain z position, z-dependence was omitted. Taking into account Eq. (A.10) and Eqs. (A.14) and (A.15) one can write the CSD function for the beam with PFT

$$\begin{aligned} J(x_1, x_2) &= f(x_1) f(x_2) \int_{-\infty}^{\infty} |f(\Delta\omega)|^2 e^{-i\Delta\omega p(x_2 - x_1)} d\Delta\omega \\ &= e^{\frac{-x_1^2}{2\sigma_x^2}} e^{\frac{-x_2^2}{2\sigma_x^2}} \int_{-\infty}^{\infty} e^{\frac{-\Delta\omega^2}{2\sigma_\omega^2}} e^{-i\Delta\omega p(x_2 - x_1)} d\Delta\omega \\ &= \sqrt{2\pi}\sigma_\omega e^{-\frac{x_1^2 + x_2^2}{2\sigma_x^2} - \frac{p^2\sigma_\omega^2 (x_2 - x_1)^2}{2}} \\ &= \sqrt{2\pi}\sigma_\omega e^{-(x_1^2 + x_2^2)(\frac{1}{\sigma_x^2} + p^2\sigma_\omega^2) + 2p^2\sigma_\omega^2 x_1 x_2} \end{aligned} \tag{A.16}$$

Integration with respect to x1 in Eq. (3.63)

$$I_1 = \int_{-\infty}^{\infty} |J(x_1, x_2)|^2 dx_1 = \frac{2\pi^{3/2}\sigma_\omega^2\sigma_x}{\sqrt{1 + p^2\sigma_\omega^2\sigma_x^2}} e^{\frac{x_2^2}{\sigma_x^2}(\frac{1}{1 + p^2\sigma_\omega^2\sigma_x^2} - 2)} \tag{A.17}$$

Integration with respect to x_2 in Eq. (3.63) acounting for Eq. (A.17)

$$I_2 = \int_{-\infty}^{\infty} I_1 dx_2 = \frac{2\pi^2\sigma_\omega^2\sigma_x^2}{\sqrt{1+p^2\sigma_\omega^2\sigma_x^2}} \tag{A.18}$$

The spectral density of the radiation is

$$S(x) = J(x = x_1 = x_2) = \sqrt{2\pi}\sigma_\omega e^{-\frac{x^2}{\sigma_x^2}} \tag{A.19}$$

The degree of coherence according to Eq. (3.63) is

$$\zeta = \frac{1}{\sqrt{1+2p^2\sigma_\omega^2\sigma_x^2}} \tag{A.20}$$

In this case, it is assumed that the partial coherence of the beam is introduced by the grating.

Taking into consideration a simple grating equation and assuming diffraction into the first oder

$$\lambda\bar{d} = cos(\theta_i) - cos(\theta_d) \tag{A.21}$$

where $\bar{d}$ is the grating's grooves density, θ_i and θ_d are incident and diffracted angles accordingly. Differentiation of Eq. (A.21) gives

$$\frac{d\theta_d}{d\lambda} = \frac{\bar{d}}{\theta_d} \tag{A.22}$$

Taking into account Eq. (A.9) one can find the PFT from the grating parameters [181]

$$p = \frac{dk_x}{d\omega} = -\frac{kd\theta_d}{d\omega} = \frac{\lambda}{c}\frac{d\theta_d}{d\lambda} = \frac{\lambda\bar{d}}{c\theta_d} \tag{A.23}$$

Degree of coherence may be calculated according to Eq. (A.20) as

$$\zeta = \frac{1}{\sqrt{1+\frac{2\lambda^2\bar{d}^2\sigma_\omega^2\sigma_x^2}{c^2\theta_d^2}}} \tag{A.24}$$

It is assumed that the degree of coherence will not change with the propagation, unless additional optics is introduced. It is assumed that a VLS grating may be substituted by a plane grating with the same groove density $\bar{d}$ followed by the 'virtual' lens with the focal distance f, determid by the VLS grating paramters. In this case additional focusing factor may play a significant role. A transmission function of the 'virtual' lens should be introduced as

$$T_f(x) = e^{\frac{-ikx^2}{2f}}, \tag{A.25}$$

and the propagator for the focal distance f in the paraxial approximation as

$$P_f(x) = \sqrt{\frac{-ik}{2\pi f}} e^{\frac{ik(x-x')^2}{2f}}. \tag{A.26}$$

Then for the amplitude at the focal plane of the VLS, taking into account Eqs. (A.10), (A.14), (A.25),(A.26) one gets the following expression

$$E_f(x') = \sqrt{\frac{-ik}{2\pi f}} e^{\frac{ik(x')^2}{2f}} \int_{-\infty}^{\infty} e^{\frac{-x^2}{2\sigma_x^2}} e^{-ip\Delta\omega x} e^{-\frac{i2\pi x x'}{\lambda f}} dx \tag{A.27}$$

Integration in the Eq. (A.27) gives

$$\begin{aligned} E_f(x') &= \frac{\sqrt{2\pi}\sigma_x}{\sqrt{if\lambda}} e^{\frac{i\omega x'^2}{2cf} - \frac{\sigma_x^2(fp\lambda\Delta\omega + 2\pi x')^2}{2\lambda^2 f^2}} \\ &= \frac{\sqrt{\sigma_x}}{\sqrt{i}\sqrt{\sigma_f}} e^{\frac{i\omega x'^2}{2cf} - \frac{1}{2\sigma_f^2}(\frac{fp\Delta\lambda\omega}{2\pi} + x')^2} \end{aligned} \tag{A.28}$$

where $\sigma_f = f\lambda/2\pi\sigma_x$ represents the focused beam for a single frequency. The same result can be obtained taking into account Fourier properties of the lens. In this case the field in the focal position is FT from the input field (Eq. (A.14))

$$f(k_x) \approx e^{\frac{-\sigma_x^2 k_x^2}{2}}, \tag{A.29}$$

and the PFT is taken into account according to Eq. (A.11), by the variable substitution. The correlation function is

$$\begin{aligned} J(x_1, x_2) &= \int_{-\infty}^{\infty} E_f^*(x_1) E_f(x_2) |f(\Delta\omega)|^2 d\Delta\omega \\ = \frac{\sigma_x}{\sigma_f} \int_{-\infty}^{\infty} & e^{-\frac{1}{2\sigma_f^2}(\frac{fp\lambda\Delta\omega}{2\pi} + x_1)^2} e^{-\frac{1}{2\sigma_f^2}(\frac{fp\lambda\Delta\omega}{2\pi} + x_2)^2} e^{\frac{i\omega(x_2 - x_1)^2}{2cf}} e^{\frac{-\Delta\omega^2}{2\sigma_\omega^2}} d\Delta\omega \\ &= \frac{\sqrt{2\pi}\sigma_x\sigma_\omega}{\sigma_f\sqrt{1 + 2p^2\sigma_x^2\sigma_\omega^2}} e^{-\frac{1}{4\sigma_f^2}\left[(x_1 - x_2)^2 + \frac{(x_1 + x_2)^2}{1 + 2p^2\sigma_x^2\sigma_\omega^2}\right]} \end{aligned} \tag{A.30}$$

Integration with respect to x_1 and x_2 in (3.63)

$$\iint_{-\infty}^{\infty} J(x_1, x_2) dx_1 dx_2 = \frac{2\pi^2\sigma_\omega^2\sigma_x^2}{\sqrt{1 + 2p^2\sigma_\omega^2\sigma_x^2}} \tag{A.31}$$

Integration of the the spectral density of the radiation gives

$$\begin{aligned} \int_{-\infty}^{\infty} S(x) dx &= \int_{-\infty}^{\infty} J(x = x_1 = x_2) dx \\ = \int_{-\infty}^{\infty} \frac{\sqrt{2\pi}\sigma_x\sigma_\omega}{\sigma_f\sqrt{1 + 2p^2\sigma_x^2\sigma_\omega^2}} & e^{-\frac{1}{\sigma_f^2}\frac{x^2}{1 + 2p^2\sigma_x^2\sigma_\omega^2}} dx = \sqrt{2}\pi\sigma_x\sigma_\omega \end{aligned} \tag{A.32}$$

The degree of coherence according to Eq. (3.63) is

$$\zeta = \frac{1}{\sqrt{1 + 2p^2\sigma_\omega^2\sigma_x^2}} \tag{A.33}$$

or the same value through the focusing parameters σ_f and f

$$\zeta = \frac{\sigma_f}{\sqrt{\sigma_f^2 + \frac{f^2\lambda^2 p^2 \sigma_\omega^2}{4\pi^2}}} \tag{A.34}$$

A.6.5 Conclusion

From results of the simulations it is seen that due to the dispersive properties of the grating, the spatial coherence properties of the photon beam after the grating are entangled with its spectral properties and exhibit a certain dependency. The spatio-frequency coupling is caused by the spatial redistribution of different wavelength by the grating. Photon beams with different wavelengths still overlap at the exit slit position. The degree of overlap is determined by the reflection order, size of the individual photon beams of each wavelength and the intrinsic grating properties such as spacing. In the decoupled state, as it is the case upstream of the grating before despersion occurs, the degree of spatial coherence is unaffected. Hence, it is assumed that the spatio-frequency coupling is the root cause of the spatial coherence degradation. Caution is advised when the photon bandwidth becomes so large that the quasi-monochromatic approximation no longer applies and the temporal coherence properties affect the spatial coherence properties. It was found that the degree of spatial coherence after the exit slit is mainly determined by the bandpass and thus the angular dispersion of the grating if a large photon beam (large energy bandwidth) is incident on the exit slit, which is the case at the beamline. Thus, due to this dependence, the transmitted beam is to a large extent independent of the spatial coherence of the incident beam. Nevertheless, the simulated data show that the VLS plane grating monochromator can lead to a non-negligible spatial coherence degradation. This effect of coherence degradation of the beam in the dispersive direction was experimentally observed utilizing first [87, 95, 190] and second order correlation theory [97]. Further simulations with varying photon energies and grating parameters can be performed to find out to what extent this effect can be mitigated to ensure an optimal coherent flux even for highly-coherent radiation sources.

Appendix B

Theoretical analysis of the HBT interferometry at XFELs

In this chapter, theoretical derivations are given to analyze the propagation of x-ray pulses through the VLS monochromator and then further to the pixelated detector, where spatial HBT measurements are typically performed. The detector's position is usually considered so that there will be sufficient resolution to resolve individual spatial modes of the incoming x-ray pulses. The interplay between the monochromator resolution and the size of the exit slits of the monochromator is especially considered. The relationship between the beam statistics determined in HBT interferometry and the statistical properties of the x-ray beam incoming to the VLS monochromator is demonstrated. Results for the Gaussian Schell model pulses describing the statistical properties of the XFELs are provided. The following section starts with the elemental analysis of x-ray propagation through the VLS monochromator.

B.1 Propagation of the X-ray beams through the VLS grating

The incoming field is considered in the form

$$E'_{in}(\mathbf{r},t) = E_{in}(\mathbf{r},t)e^{i\mathbf{k_0}\mathbf{r}-i\omega_0 t}, \tag{B.1}$$

where $\mathbf{k_0} = k_0\mathbf{s_0}$, $k_0 = \omega_0/c$, $\mathbf{s_0}$ is the direction of the incoming momentum vector, ω_0 is the carrier frequency, and c is the speed of light. In Eq. (B.1) it is assumed that incoming field $E_{in}(\mathbf{r},t)$ is slow varying function of its arguments. By performing the Fourier transform for the incoming amplitude $E_{in}(\mathbf{r},t)$ it is possible to change to spatial-frequency domain:

$$E_{in}(\mathbf{r},t) = \frac{1}{2\pi}\int_{-\infty}^{\infty} E_{in}(\mathbf{r},\omega)e^{-i\omega t}d\omega. \tag{B.2}$$

Substituting Eq. (B.2) in Eq. (B.1) shows the total frequnecy $\omega_t = \omega_0+\omega$ and the region of convergence in the frequency domain ($\omega \ll \omega_0$) of the integral in Eq. (B.2).

Each amplitude $E_{in}(\mathbf{r},\omega)$ for the further analysis is propagated separately through the beamline, and the final amplitude $E_f(\mathbf{r},\omega)$ in spatial-frequency and in spatial-time will be deter-

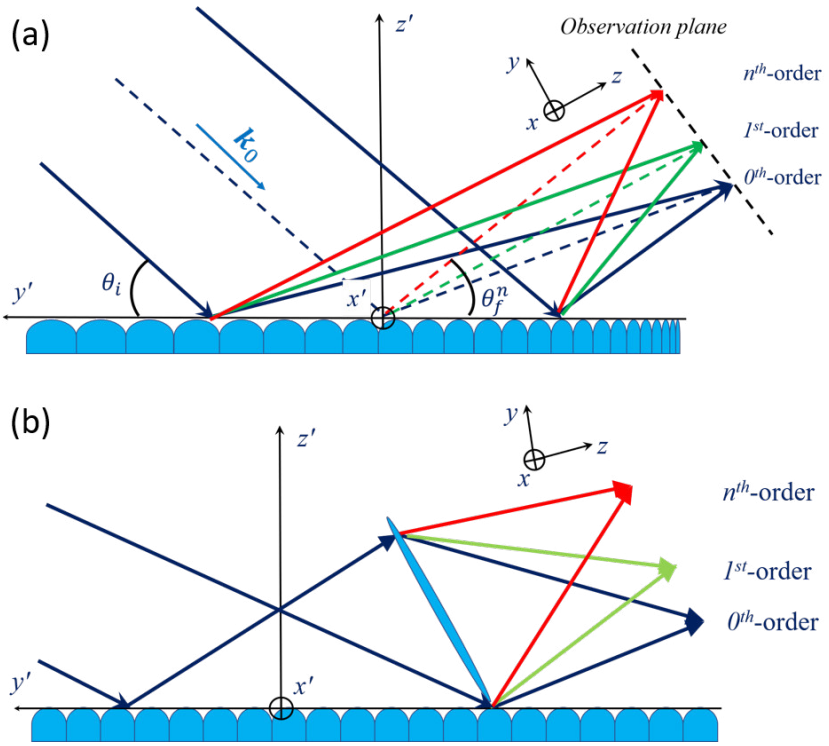

Figure B.1: (a) Scattering from the VLS grating is shown. Different spectral components of the incoming beam are focused at the focal distance f forming the zeroth, first, and n^{th} orders of grating reflections. The coordinate systems for the grating and for the scattered beams are also shown. (b) Scattering from the VLS grating is substituted by the scattering on a grating with the constant period d_0 followed by a virtual lens with the focusing distance f.

mined. The latter obtained by the Fourier transform:

$$E_f(\mathbf{r},t) = \frac{1}{2\pi}\int_{-\infty}^{\infty} E_f(\mathbf{r},\omega)e^{-i\omega t}d\omega. \tag{B.3}$$

The intensity obtained from the amplitude as

$$I_f(\mathbf{r},t) = |E_f(\mathbf{r},t)|^2 = \frac{1}{(2\pi)^2}\iint_{-\infty}^{\infty} E_f^*(\mathbf{r},\omega)E_f^*(\mathbf{r},\omega')e^{-i(\omega-\omega')t}d\omega d\omega'. \tag{B.4}$$

where integration over the times gives $\int\int_{-\infty}^{\infty} exp[i(\omega-\omega')t]dt = 2\pi\delta(\omega-\omega')$. So that the final integrated intensity at the position $\mathbf{r}$ [195]

$$I_f(\mathbf{r}) = \int_{-\infty}^{\infty}|E_f(\mathbf{r},t)|^2dt = \frac{1}{(2\pi)}\int_{-\infty}^{\infty}|E_f(\mathbf{r},\omega)|^2d\omega. \tag{B.5}$$

Expression (B.5) shows the conservation of the beam energy in time and frequency domains. The scattering of the incoming fields is considered if the form of Eqs. (B.1) and (B.2) on a VLS grating in reflection geometry as shown in Fig. B.1(a). Each apmlitude $E_{in}(\mathbf{r},\omega)$ will be propagated independently through the grating. The VLS grating is usually characterized by changing the groove spacing according to

$$d(y) = d_0 + d_1 y + d_2 y^2 + ..., \tag{B.6}$$

where d_0 is the spacing at the pole of the grating located at the coordinate $y = 0$ and d_1 abd d_2 are the parameters for the variation of the line spacing with the coordinate y. If the expansion (B.6) only the first two terms are kept, such grating will focus the incoming beam at the focal distance

$$f = \left[\frac{\lambda d_1}{d_0^2 sin^2\theta_f}\right]^{-1} \tag{B.7}$$

where θ_f is the exit scattering angle (see Fig. B.1(a)). It is clear that such VLS grating may be substituted by a plane grating with spacing d_0 followed by the 'virtual' lens with the focal distance given by expression (B.7) (see Fig. B.1(b)). In the following this geometry will be considered for the description of scattering on the VLS grating.

The scattered filed $E_{gr}(\mathbf{r}, \omega)$ from such a VLS grating can be written as

$$E_{gr}(\mathbf{r}, \omega) = E_0 \int R_{gr}(\mathbf{r}')T_f(\mathbf{r}')P_f(\mathbf{r} - \mathbf{r}')E_{in}(\mathbf{r}', \omega)e^{i\mathbf{k_0}\mathbf{r}'}d\mathbf{r}' \tag{B.8}$$

where E_0 is the amplitude of the filed, containing nonessential preintegral factors. In the following, where it is not specifically indicated, the integration is performed from minus to plus infinity. In Eq. (B.8) $R_{gr}(\mathbf{r}')$ is the reflection function of the grating and $T_f(\mathbf{r}')$ is the transmission function of the 'virtual' lens given by the following equation

$$T_f(\mathbf{r}) = exp(-i\frac{k}{2f}\mathbf{r}^2), \tag{B.9}$$

and

$$P_f(\mathbf{r} - \mathbf{r}') = (\frac{-ik_0}{2\pi f})exp\left[i\frac{k}{2f}(\mathbf{r} - \mathbf{r}')^2\right] \tag{B.10}$$

is the propagator, for the focal distance f in the paraxial approximation. Consider the plane grating location in the origin of the coordinate system as shown in Fig. B.1. The groovs are considered along the x' axis. In this geometry $R_{gr}(\mathbf{r}')$=$R_{gr}(y')$. It is assumed that the virtual lens in Eq. (B.9) is focusing only in one y direction (see Fig. B.1(b)), $T_f(\mathbf{r}')$=$T_f(y')$, and the observation plane is located at the focal plane of this lens. In this case

$$T_f(y')P_f(\mathbf{r} - \mathbf{r}')e^{i\mathbf{k_0}\mathbf{r}'} = (\frac{-ik_0}{2\pi f})^{1/2}exp\left[i\frac{k}{2f}y^2 - iq_y y'\right]P_f(x - x') \tag{B.11}$$

where $q_y = ks^y - k_0 s_0^y$, s^y is the y component $s^y = y/f$ of the unit vector $\mathbf{s}$ towards the observation point, and $P_f(x - x')$ is the propagator in the x direction. The x component of the unit vector in Eq. (B.11) is considered $s_0^x = 0$ (see Fig. B.1(a)). Substituting everything listed above in Eq. (B.8), the scattered field is

$$E_{gr}(x, q_y, \omega) = E_0 \iint R_{gr}(y')P_f(x - x')E_{in}(x', y', \omega)e^{-iq_y y'}dx'dy'. \tag{B.12}$$

Integrating over x' in the Eq. (B.12) will give expression for the scattered amplitude

$$E_{gr}(x, q_y, \omega) = E_0 \int R_{gr}(y') E_{in}(x, y', \omega) e^{-iq_y y'} dy', \tag{B.13}$$

where

$$E_{in}(x, y', \omega) = \int P_f(x - x') E_{in}(x', y', \omega) dx'. \tag{B.14}$$

The function of the finite size grating is introduced as

$$R_{gr}(y') = \sum_{n=-N/2}^{N/2} r_{gr}(y' - y_n) = R_N(y') \sum_{n=-\infty}^{\infty} r_{gr}(y' - y_n) = R_N(y') \sum_{h_n=-\infty}^{\infty} r_{gr}(h_n) e^{ih_n y'}, \tag{B.15}$$

where N is the number of grating periods, $r_{gr}(y)$ is the reflection function of one period, and $y_n = d_0 n$, and $n = 0, \pm 1, \pm 2....$ In Eq. (B.15) $R_N(y)$ is a finte window of the size of the grating, which can be introduced as

$$R_N(y') = rect(\frac{y'}{D_N}), \tag{B.16}$$

where $D_N = d_0 N$ and $rect(y)$ is the rectangular function defined as

$$rect(y) = \begin{cases} 1, & \text{if } |y| \leq 1/2 \\ 0, & \text{if } |y| > 1/2 \end{cases}. \tag{B.17}$$

In Eq. (B.15) the decomposition of the finite periodic function over reciprocal space was used with $h_n = (2\pi/d_0)n$, and the Fourier transform of the reflection function of one grating period was introduced as

$$r_{gr}(h_n) = \frac{1}{d} \int_{-d/2}^{d/2} r_{gr}(y) e^{-ih_n y} dy. \tag{B.18}$$

Substituting Eq. (B.15) in Eq. (B.13) and changing order of summation and integration will give

$$E_{gr}(x, q_y, \omega) = E_0 \sum_{h_n=-\infty}^{\infty} r_{gr}(h_n) \int R_N(y') E_{in}(x, y', \omega) e^{-i(q_y - h_n)\cdot y'} dy' \tag{B.19}$$

Assuming that the incoming amplitude is constant over the grating in the vertical direction $E_{in}(x, y', \omega) \cong E_{in}(x, \omega)$ from the Eq. (B.19)

$$E_{gr}(x, \omega) = E_0 \sum_{h_n=-\infty}^{\infty} r_{gr}(h_n) E_{in}(x, \omega) \int R_N(y') e^{-i(q_y - h_n)\cdot y'} dy' \tag{B.20}$$

and integrating

$$\int R_N(y') e^{-i(q_y - h_n)\cdot y'} dy' = \left[(q_y - h_n)\frac{D_N}{2}\right]^{-1} sin\left[(q_y - h_n)\frac{D_N}{2}\right] = sinc[\alpha_n], \tag{B.21}$$

where

$$\alpha_n = (q_y - h_n)D_N/2 \tag{B.22}$$

the amplitude of the filed scattered from the grating is finnaly obtained.

$$E_{gr}(x,\omega) = E_0 \sum_{h_n=-\infty}^{\infty} r_{gr}(h_n) sinc[\alpha_n] E_{in}(x,\omega) \tag{B.23}$$

The scattered amplitude for one of the grating order n is

$$E_{gr}(x,\omega) = E_0 r_{gr}(h_n) sinc[\alpha_n] E_{in}(x,\omega). \tag{B.24}$$

The argument α_n of the *sinc* function can be presented as

$$\alpha_n = (q_y - h_n)D_N/2 = (ks^y - k_0 s_0^y - h_n)D_N/2 = (kcos\theta_f - k_0 cos\theta_i - h_n)D_N/2. \tag{B.25}$$

The maximum of the *sinc* function is at $\alpha_n = 0$ that gives for the central frequency ω_0 the grating equation [196]

$$k_0(cos\theta_f^n - cos\theta_i) = h_n, \tag{B.26}$$

where θ_i and θ_f^n are the incidence and scattered angles from the VLS grating as shown in Fig. B.1(a). Taking into account that $k = (\omega_0 + \omega)/c$ and $\theta_f = \theta_f^n + \theta$, where $\omega \ll \omega_0$ and $\theta \ll \theta_f^n$, the paramter α_n from Eq. (B.25) is obtained, neglecting small terms of the second order

$$\alpha_n = cos\theta_f^n \left[\left(\frac{\omega}{\omega_0} \right) - \theta tan\theta_f^n \right] \frac{k_0 D_N}{2} \tag{B.27}$$

Condition $\alpha_n = 0$ in Eq. (B.25) should also be valid for the other frequencies and corresponding angles. so that

$$kcos\theta_f - k_0 cos\theta_i = h_n. \tag{B.28}$$

Performing similar expansion as before, $k = (\omega_0 + \omega')/c$ and $\theta_f = \theta_f^n + \theta$, where the frequency ω' in the observation plane is introduced, one obtains

$$\left(\frac{\omega'}{\omega_0} \right) = \theta tan\theta_f^n \tag{B.29}$$

Substituting this Eq. (B.29) in Eq. (B.27), the paramter α_n is obtained

$$\alpha_n = cos\theta_f^n \left(\frac{\omega - \omega'}{\omega_0} \right) \frac{k_0 D_N}{2}. \tag{B.30}$$

To determine an expression for the intensity in the observation plane, the scattered amplitude value in Eq. (B.24) is substituted to Eq. (B.5) so that

$$I_{gr}(x,\omega') = |E_0|^2 |r_{gr}(h_n)|^2 \int R(\omega' - \omega) |E_{in}(x,\omega)|^2 d\omega, \tag{B.31}$$

where the function $R(\omega' - \omega)$ is introduced as

$$R(\omega' - \omega) = sinc^2(\alpha_n) \tag{B.32}$$

It will be shown that this function is, in fact, a resolution function of the monochromator unit. Indeed, if one considers that the incoming field is monochromatic, with a fixed frequency ω_0, the incoming field can be written as $E_{in}(x, \omega) \rightarrow (2\pi)\delta(\omega - \omega_0)E_{in}(x)$. this expression in Eq. (B.31) gives

$$I_{gr}(x, \omega') = |E_0|^2 |r_{gr}(h_n)|^2 R(\omega' - \omega_0)|E_{in}(x)|^2, \tag{B.33}$$

that shows that the function $R(\omega' - \omega_0)$ givesthe broaening of the monochromatic frequency ω_0 and may be treated as the resolution function. The full width at half maximum (FWHM) of the resolution function $R(\omega' - \omega)$ defines, typically, the resolution of the VLS grating. The resolution function of the monochromator is often considered to be a Gaussian function,

$$R(\omega) = exp\left(- \frac{\omega^2}{2\sigma_r^2} \right) \tag{B.34}$$

where σ_r is the root mean square (rms) value of the resolution function with FWHM equal to $2\sqrt{2ln2}\sigma_r \simeq 2.355\sigma_r$.

In a typical experiment at an XFEL in order to obtain spectral characteristics of the pulse the measured two-dimensional intensity distribution $I_{gr}(x, \omega)$ is integrated over the x axis thus providing the one-dimensional spectrum $I_{gr}(\omega)$. Performing such integration in Eq. (B.31) and also taking into account Eq. (B.14) the spectrum is obtained

$$I_{gr}(\omega) = \int I_{gr}(x, \omega)dx = |E_0|^2 |r_{gr}(h_n)|^2 \iint R(\omega - \omega')|E_{in}(x', \omega')|^2 d\omega' dx', \tag{B.35}$$

In this derivation, the following property of the propagator was considered:

$$\int P_f^*(x - x')P_f(x - x'')dx = \delta(x' - x'') \tag{B.36}$$

Equation (B.35) provides an expression for the measurements of the single pulse spectrum at the XFEL experiment by the VLS grating spectrometer expressed through the incoming beam intensity $|E_{in}(x', \omega')|^2$.

In the next section, will be determined which kind of information may be obtained by performing HBT analysis in the spectral domain and relate it to the statistical properties of the beam incoming to the monochromator unit.

B.2 Second-order correlations in the frequency domain

The second-order correlation functions in the frequency domain defined as

$$g^{(2)}(\omega_1, \omega_2) = \frac{< I_{gr}(\omega_1) I_{gr}(\omega_2) >}{< I_{gr}(\omega_1) >< I_{gr}(\omega_2) >} \tag{B.37}$$

where intensities $I_{gr}(\omega)$ are defined in Eq. (B.35). Substituting these intensities in Eq. (B.37) gives

$$g^{(2)}(\omega_1,\omega_2) = \frac{\int R(\omega_1-\omega')R(\omega_2-\omega'') < |E_{in}(x',\omega')|^2|E_{in}(x'',\omega'')|^2 > dx'dx''d\omega'd\omega'')}{\int R(\omega_1-\omega') < |E_{in}(x',\omega')|^2 > d\omega'dx' \int R(\omega_2-\omega') < |E_{in}(x',\omega')|^2 > d\omega'dx'}. \tag{B.38}$$

Assuming Gaussian statistics for the incoming field the average correlation can be written in the following form

$$\begin{aligned} &< |E_{in}(x',\omega')|^2|E_{in}(x'',\omega'')|^2 >= \\ &=< |E_{in}(x',\omega')|^2 >< |E_{in}(x'',\omega'')|^2 > +| < E^*_{in}(x',\omega')E^*_{in}(x'',\omega'') > |^2 = \\ &= S_{in}(x',\omega')S_{in}(x'',\omega'') + |W_{in}(x',x'',\omega',\omega'')|^2, \end{aligned} \tag{B.39}$$

where the spectral density introduced as

$$S_{in}(x,\omega) =< |E_{in}(x,\omega)|^2 >, \tag{B.40}$$

and cross-spectral density as

$$W_{in}(x',x'',\omega',\omega'') =< E^*_{in}(x',\omega')E_{in}(x'',\omega'') > \tag{B.41}$$

Substituting Eq. (B.38) in Eq. (B.39) the following expression for the $g^{(2)}(\omega_1,\omega_2)$ is obtained

$$g^{(2)}(\omega_1,\omega_2) = 1 + \frac{\int R(\omega_1-\omega')R(\omega_2-\omega'')|W_{in}(x',x'',\omega',\omega'')|^2dx'dx''d\omega'd\omega''}{\int R(\omega_1-\omega')S_{in}(x',\omega')d\omega'dx' \int R(\omega_2-\omega')S_{in}(x',\omega')d\omega'dx'} \tag{B.42}$$

The cross-spectral purity of the incoming x-ray beam implies

$$W_{in}(x',x'',\omega',\omega'') = W_{in}(\omega',\omega'')W_{in}(x',x'') \tag{B.43}$$

and

$$S_{in}(x',\omega') = S_{in}(\omega')S_{in}(x') \tag{B.44}$$

Substituting these expressions in Eq. (B.42), the final general expression for the $g^{(2)}(\omega_1,\omega_2)$ function is obtained

$$g^{(2)}(\omega_1,\omega_2) = 1 + \zeta g_{in}(\omega_1,\omega_2), \tag{B.45}$$

where

$$\zeta = \frac{\int\int |W_{in}(x',x'')|^2dx'dx''}{[\int S_{in}(x)dx]^2} \tag{B.46}$$

and

$$g_{in}(\omega_1,\omega_2) = \frac{\iint R(\omega_1-\omega')R(\omega_2-\omega'')|W_{in}(\omega',\omega'')|^2 d\omega' d\omega''}{\int R(\omega_1-\omega')S_{in}(\omega')d\omega' \int R(\omega_2-\omega')S_{in}(\omega')d\omega'}. \tag{B.47}$$

By that, the second-order correlation function $g^{(2)}(\omega_1,\omega_2)$ measured in the frequency domain was expressed through the statistical properties of the x-ray radiation incoming to the monochromator unit. It is immediately seen that the $g^{(2)}(\omega_1,\omega_2)$ function defined in Eq. (B.45) is determined by the degree of spatial coherence ζ of the incoming x-ray beam. We have to recall here that the spectral density in spatial $W_{in}(x_1,x_2)$ and frequency $W_{in}(\omega_1,\omega_2)$ domains is defined through its first-order correlation functions as

$$\begin{aligned} W_{in}(x_1,x_2) &= \sqrt{S_{in}(x_1)}\sqrt{S_{in}(x_2)}g^{(1)}_{in}(x_1,x_2), \\ W_{in}(\omega_1,\omega_2) &= \sqrt{S_{in}(\omega_1)}\sqrt{S_{in}(\omega_2)}g^{(1)}_{in}(\omega_1,\omega_2), \end{aligned} \tag{B.48}$$

where the first-order correlation functions $g^{(1)}_{in}(x_1,x_2)$ and $g^{(1)}_{in}(\omega_1,\omega_2)$ are defined as

$$\begin{aligned} g^{(1)}_{in}(x_1,x_2) &= \frac{< E^*_{in}(x_1)E_{in}(x_2) >}{\sqrt{< |E_{in}(x_1)|^2 >}\sqrt{< |E_{in}(x_2)|^2 >}}, \\ g^{(1)}_{in}(\omega_1,\omega_2) &= \frac{< E^*_{in}(\omega_1)E_{in}(\omega_2) >}{\sqrt{< |E_{in}(\omega_1)|^2 >}\sqrt{< |E_{in}(\omega_2)|^2 >}}. \end{aligned} \tag{B.49}$$

The expression for the correlation function $g^{(1)}_{in}(\omega_1,\omega_2)$ in Eq. (B.47) can be further analyzed. It should be noted that resolution of the monochromator is typically much narrower than the bandwidth of the incoming radiation. Assuming perfect monochromator resolution or substituting resolution function by a delta function $R(\omega_1-\omega') \to \delta(\omega_1-\omega')$, a simplified expression of Eq. (B.47) is obtained

$$g_{in}(\omega_1,\omega_2) = \frac{|W_{in}(\omega_1,\omega_2)|^2}{S_{in}(\omega_1)S_{in}(\omega_2)} = |g^{(1)}_{in}(\omega_1,\omega_2)|^2 \tag{B.50}$$

and the for the Eq. (B.45)

$$g^{(2)}(\omega_1,\omega_2) = 1+\zeta|g^{(1)}_{in}(\omega_1,\omega_2)|^2. \tag{B.51}$$

By this expression the $g^{(2)}$ function in the spectral domain is expressed through the square modulus of the first-order correlation function of the incoming beam. This expression is valid only if one can assume an ideal resolution of the monochromator. It is interesting to note also, that for a chaotic source the second-order correlation function in the spectral domain at maximum is $g^{(2)}_{max} = 1+\zeta$. It is seen that the $g^{(2)}$-function is directly related to the degree of spatial coherence of the incoming beam (see Eq. (B.45)) as $g^{(2)}_{max} \leq 2$, and will be equal to 2 only

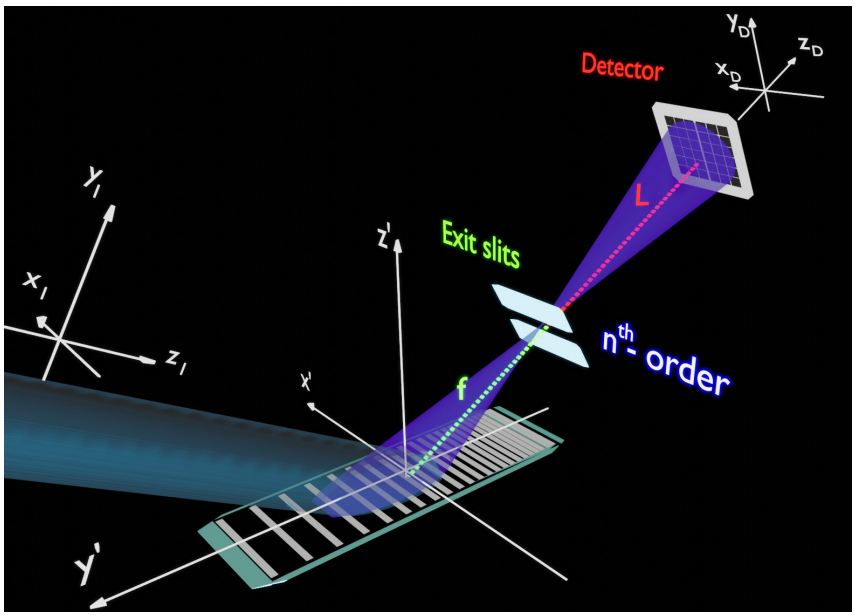

Figure B.2: Schematic layout of the HBT experiment performed at the XFEL facility. The incoming beam is scattered on the VLS grating. The exit slits are positioned at the focal plane of the VLS grating at the grating order n. The second-order spatial correlation measurements are performed by the pixelated detector positioned far from the monochromator unit to resolve spatial modes of the incoming x-ray pulses. The coordinate systems for the incoming beam, the grating, and detector are shown.

for the fully coherent beam in the spectral domain. It will be shown in the following how these results will be modified when the final resolution of the VLS monochromator will be taken into account. In the next section, will be determined which kind of information may be obtained by performing the HBT interferometry in the spatial domain and how its related to the statistical properties of the beam incoming to the VLS monochromator.

B.3 Second-order correlations in the spatial domain

The HBT experiments in the spatial domain at the soft x-ray beamlines at the XFEL facilities are performed on a pixelated detector positioned far from the focal plane of the beamline. Such arrangement provides sufficient resolution to separate spatial modes of the individual XFEL pulses of the incoming x-ray beam at the detector position.

A two-dimensional (2D) detector is introduced with the coordinates x_D, y_D at which single pulse intensities $I_D(x^D, y^D)$ from the XFEL are measured for further correlation analysis (see Fig. B.2). As soon as the intensities are measured, they are connected with the amplitudes of the incoming field in the spatial-frequency domain as (see Eq. (B.5))

$$I_D(x^D, y^D) = \frac{1}{2\pi} \int_{-\infty}^{\infty} |E_D(x^D, y^D, \omega)|^2 d\omega \tag{B.52}$$

Each of these intensities is typically integrated in the vertical (dispersion) direction to provide

a one-dimensional (1D) distribution of the intensity,

$$I_D(x^D) = \frac{1}{2\pi}\iint_{-\infty}^{\infty} |E_D(x^D, y^D, \omega)|^2 d\omega dy^D. \tag{B.53}$$

The basic idea of HBT interferometry is the correlation of intensities at different spatial positions, or, in other words, measurements of the second-order correlation functions. In such measurements, the normalized second-order correlation function can be defined as

$$g^{(2)}(x_1^D, x_2^D) = \frac{< I_D(x_1^D) I_D(x_2^D) >}{< I_D(x_1^D) >< I_D(x_2^D) >}, \tag{B.54}$$

where averaging, denoted by brackets $< ... >$, is performed over a large ensemble of different realizations of the wave field. In the HBT experiment for the nonstationary source, such as XFELs, averaging may be performed over different pulses, with the assumption that all pulses are realizations of the same statistical process.

Now, the intensities $I_D(x_1^D)$ will be expressed, as given in Eq. (B.53) through the amplitudes of the wave field incoming to the monochromator unit and then will be correlated according to Eq. (B.54). The x-ray field amplitudes are the result of propagation over the free space from the exit slits of the monochromator equipped by the VLS grating. Such slits are located in the focal plane of the VLS grating and the field amplitudes $E_D(x^D, y^D, \omega)$ may be presented as

$$E_D(x^D, y^D, \omega) = \iint P_L(x^D - x') P_L(y^D - y') E_{sl}(x', y', \omega) dx' dy', \tag{B.55}$$

where PL $P_L(x^D - x')$ is the propagator (see Eq. (B.10)), the distance L is defined in Fig. B.2 as the distance from the exit slits of the monochromator to the detector plane, $E_{sl}(x', y', \omega)$ is the amplitude of the field passing through the exit slits, and x', y' are the coordinates in the slits plane.

The amplitude of the field after the exit slits $E_{sl}(\mathbf{r}, \omega)$ may be obtained by multiplying the amplitude of the field scattered from the VLS grating to a fixed order $E_{gr}(x, \omega)$ (see Eq. (24)) by the transmission function of the slits, $T_{sl}(\omega)$,

$$\begin{aligned} E_{sl}(x', y', \omega) &= T_{sl}(\omega) E_{gr}(x, \omega) \\ &= E_0 r_{gr}(h_n) T_{sl}(\omega) sinc[\alpha_n] \int P_f(x' - x_1) E_{in}(x_1, \omega) dx_1, \end{aligned} \tag{B.56}$$

where an expression (B.14) was taken into account for the incoming amplitude $E_{in}(x, \omega)$. In Eq. (B.56), the transmission function of the slits $T_{sl}(\omega)$ is defined as a finite window in the spectral domain of the size of the spectral bandpass D_ω^{sl} as

$$T_{sl}(\omega) = rect\left[\frac{\omega}{D_\omega^{sl}}\right], \tag{B.57}$$

where $rect(x)$ is the rectangular function defined in Eq. (B.17). Substituting Eqs. (B.55) and

(B.56) in Eq. (B.53) we obtain for the intensity on the detector,

$$I_D(x^D) = |E_0|^2 |r_{gr}(h_n)|^2 \iiint_{-\infty}^{\infty} P^*_{f+L}(x^D - x_1) P_{f+L}(x^D - x_2) \times \hat{T}_{sl}(\omega) E^*_{in}(x_1, \omega) E_{in}(x_2, \omega) dx_1 dx_2 d\omega, \tag{B.58}$$

where a function $\hat{T}_{sl}(\omega)$ was introduced as

$$\hat{T}_{sl}(\omega) = \int T^2_{sl}(\omega') R(\omega - \omega') d\omega'. \tag{B.59}$$

In deriving Eq. (B.58) the following properties of the propagator was used

$$\int P_{L_2}(x' - x) P_{L_1}(x' - x'') dx = P_{L_1+L_2}(x' - x'') \tag{B.60}$$

as well as Eq. (B.36). According to Eq. (B.59), the square of the exit slit transmission function $T^2_{sl}(\omega')$ defined in Eq. (B.59) is convoluted with the resolution function $R(\omega)$ given in Eq. (B.34). For the function $T^2_{sl}(\omega)$ in Eq. (B.59) the following relationship is valid, $T^2_{sl}(\omega) = T_{sl}(\omega)$, due to its definition in Eq. (B.57).

Expression in Eq. (B.58) for the intensity $I_D(x^D)$ is substituted in Eq. (B.54) for the $g^{(2)}$ function and it is assumed that the incoming x-ray radiation obeys Gaussian statistics. In this case

$$\begin{aligned} &< E^*_{in}(x_1, \omega_1) E_{in}(x_2, \omega_1) E^*_{in}(x_3, \omega_2) E_{in}(x_4, \omega_2) >= \\ &=< E^*_{in}(x_1, \omega_1) E_{in}(x_2, \omega_1) >< E^*_{in}(x_3, \omega_2) E_{in}(x_4, \omega_2) > + \\ &+ < E^*_{in}(x_1, \omega_1) E_{in}(x_4, \omega_2) >< E^*_{in}(x_3, \omega_2) E_{in}(x_2, \omega_1) > . \end{aligned} \tag{B.61}$$

Further the spectral density function and cross-spectral density function in the spatial-frequency domain are introduced as given in Eqs. (B.40) and (B.40) and, cross-spectral purity of the incoming x-ray radiation is assmued as in Eqs. (B.43) and (B.44). After straightforward deriaviation one can, obtain for the $g^{(2)}$ function,

$$g^{(2)}(x^D_1, x^D_2) = 1 + \zeta(D_\omega) |g_{in} x^D_1, x^D_2|^2. \tag{B.62}$$

In this expression, the contrast function $\zeta(D_\omega)$, which depends on the radiation bandwidth D_ω is defined as

$$\zeta(D_\omega) = \frac{\iint \hat{T}_{sl}(\omega_1) \hat{T}_{sl}(\omega_2) |W_{in}(\omega_1, \omega_2)|^2 d\omega_1 d\omega_2}{[\int \hat{T}_{sl}(\omega) S_{in}(\omega) d\omega]^2} \tag{B.63}$$

and a correlation function $g_{in}(x^D_1, x^D_2)$ is determined by

$$g_{in}(x^D_1, x^D_2) = \frac{\iint P^*_{f+L}(x^D_1 - x_1) P_{f+L}(x^D_2 - x_2) W_{in}(x_1, x_2) dx_1 dx_2}{\sqrt{S_D(x^D_1)} \sqrt{S_D(x^D_2)}}, \tag{B.64}$$

where

$$S_D(x_i^D) = \int\int P^*_{f+L}(x_i^D - x_1) P_{f+L}(x_i^D - x_2) W_{in}(x_1, x_2) dx_1 dx_2, \tag{B.65}$$

and $i = 1, 2$.

By that, the second-order correlation function measured at the far detector (Eq. (B.62)) was expressed through the statistical properties of x-ray radiation incoming to the VLS monochromator. It will be shown in the following that by changing the exit slits opening D_ω the contrast function $\zeta(D_\omega)$ also changes according to Eq. (B.63). This, finally, allows to determine the pulse duration of the incoming x-ray pulses. In the next section, the incoming x-ray pulses will be represented by the Gaussian Schell model.

B.4 Gaussian Schell model X-ray pulses

After receiving these general results in both the frequency and spatial domains a special type of incoming pulsed beams in the form of the Gaussian Schell model (GSM) pulses will be considered. In this case, the cross-spectral density in the spatial-frequency domain can be written as

$$W_{in}(x_1, x_2; \omega_1, \omega_2) = W_0 W(x_1, x_2) W(\omega_1, \omega_2), \tag{B.66}$$

where the spatial dependence is defined by the function

$$W(x_1, x_2) = exp\left[-\frac{x_1^2 + x_2^2}{4\sigma_I^2} - \frac{(x_2 - x_1)^2}{2\xi^2} \right]. \tag{B.67}$$

where σ_I is the rms size and ξ is the spatial coherence of the incoming beam. The frequency dependence is defined by

$$W(\omega_1, \omega_2) = exp\left[-\frac{\omega_1^2 + \omega_2^2}{4\Omega^2} - \frac{(\omega_2 - \omega_1)^2}{2\Omega_c^2} \right], \tag{B.68}$$

where Ω is the rms spectral width of radiation, Ω_c is the spectral coherence, and it is assumed that the frequency is counted from the corresponding grating order. The parameters Ω and Ω_c can also be expressed through the rms values of the pulse duration σ_T and coherence time τ_c of the pulse in front of the monochromator unit,

$$\Omega^2 = \frac{1}{\tau_c^2} + \frac{1}{4\sigma_T^2}, \quad \Omega_c = \frac{\tau_c}{\sigma_T}\Omega. \tag{B.69}$$

For the self-amplified spontaneous emission (SASE) pulses at XFELs for most of the cases the coherence time τ_c in front of the monochromator unit is much shorter than the pulse duration $\sigma_T (\tau_c \ll \sigma_T)$. Taking this into account Eq. (B.69) can be simplified

$$\Omega \approx \frac{1}{\tau_c}, \quad \Omega_c \approx \frac{1}{\sigma_T} \tag{B.70}$$

In this limit, the spectral density defined as

$$S_{in}(\omega) = S_0 exp\left[-\frac{\tau_c^2 \omega^2}{2} \right], \tag{B.71}$$

and the first-order correlation function defined as

$$g^{(1)}(\omega_2 - \omega_1) = exp\left[-\frac{\sigma_T^2 (\omega_2 - \omega_1)^2}{2} \right]. \tag{B.72}$$

Here, it should be noted that if one can neglect the monochromator resolution then Eq. (B.51) will be valid. With a combination of Eq. (B.72) this allows to determine the average pulse duration through analysis of the $g^{(2)}$ function as a function of $\Delta\omega$ in the spectral domain. In the next section, it will be shown which results may be obtained if the finite energy resolution of the monochromator unit will be taken into account. The spectral and spatial domains will be considered separately in the following.

B.5 Spectral domain in the frame of GSM

The integration in Eqs. (B.46) and (B.47) can be performed assuming that the incoming beam obeys the Gaussian Schell model. Substituting in these equations expressions (B.66)–(B.68) for the incoming cross-spectral density function the degree of coherence is obtained

$$\zeta = \left[1 + 4\left(\frac{\sigma_I}{\xi} \right)^2 \right]^{-1/2}, \tag{B.73}$$

and the correlation function

$$g_{in}(\omega_2 - \omega_1) = \frac{\alpha exp\left[-\frac{1}{\alpha\beta} \frac{(\omega_2 - \omega_1)^2}{\Omega_c^2} \right]}{(\alpha\beta)^{1/2}}, \tag{B.74}$$

where

$$\alpha = 1 + \left(\frac{\sigma_r}{\Omega} \right)^2, \quad \beta = 1 + \left(\frac{\sigma_r}{\Omega} \right)^2 \left[1 + 4\left(\frac{\Omega}{\Omega_c} \right)^2 \right]. \tag{B.75}$$

In the limit of Eq. (B.70) one has

$$g_{in}(\omega_2 - \omega_1) = \frac{\alpha exp\left[-\frac{\sigma_T^2}{\alpha\beta} (\omega_2 - \omega_1)^2 \right]}{(\alpha\beta)^{1/2}}, \tag{B.76}$$

where

$$\alpha = 1 + \left(\sigma_r \tau_c \right)^2, \quad \beta = 1 + \left(\sigma_r \tau_c \right)^2 \left[1 + 4\left(\frac{\sigma_T}{\tau_c} \right)^2 \right]. \tag{B.77}$$

First, it is immediately seen that if the monochromator has a perfect resolution $\sigma_r = 0$, then both α and β are equal to 1 and $g_{in}(\omega_2 - \omega_1) = |g_{in}^{(1)}(\omega_2 - \omega_1)|^2$, where $g_{in}^{(1)}(\omega_2 - \omega_1)$ is defined

by Eq. (B.72). It should be noted that this result coincides with previous result of Eqs. (B.52) and (B.52). It is also should be noted that for typical SASE beams the product $\sigma_r\tau_c \ll 1$. In this case, the coefficients in Eq. (B.77) are $\alpha \approx 1$ and $\beta \approx 1 + 4(\sigma_r\sigma_T)^2$. Substituting this in Eq. (B.76) the following expression is obtained

$$g_{in}(\omega_2 - \omega_1) = \frac{exp\left[-\frac{\sigma_T^2}{1+4\sigma_r^2\sigma_T^2}(\omega_2 - \omega_1)^2\right]}{(1 + 4\sigma_r^2\sigma_T^2)^{1/2}} \tag{B.78}$$

It is seen from this expression that when the finite resolution of the monochromator σ_r is taken into account, the function $g_{in}(\omega_2 - \omega_1)$ does not reach unity even at $\omega_1 = \omega_2$. Its maximum value at the same frequency values is equal to

$$g_{in}(0) = \frac{1}{(1 + 4\sigma_r^2\sigma_T^2)^{1/2}} \tag{B.79}$$

Substituting this value of $g_{in}(\omega_2 - \omega_1)$ in the expression for the $g^{(2)}$ function (B.45), and assuming that the resolution of the VLS monochromator is known, one may determine the pulse duration σ_T as

$$\sigma_T = \frac{1}{2\sigma_r}\left[\frac{\zeta^2}{(g_{in}^{(2)}(\omega,\omega) - 1)^2} - 1\right]^{-1/2}. \tag{B.80}$$

Therefore, HBT analysis in the spectral domain with the assumption that XFEL pulses obey the GSM provides the way to determine the pulse duration.

B.6 Spatial domain in the frame of HBT

B.6.1 Contrast function

In this subsection focus will be on the evaluation of the contrast function $\zeta(D_\omega)$ in Eq. (B.63) and show how an average pulse duration of XFEL pulses may be determined by evaluating this contrast function. Expressing the cross-spectral density in the frequency domain through its first-order correlation function (see Eq. (B.48)) gives for the contrast function in Eq. (B.63)

$$\zeta(D_\omega) = \frac{\iint \hat{T}_{sl}(\omega_1)\hat{T}_{sl}(\omega_2)S_{in}(\omega_1)S_{in}(\omega_2)|g_{in}^{(1)}(\omega_1,\omega_2)|^2 d\omega_1 d\omega_2}{[\int \hat{T}_{sl}(\omega)S_{in}(\omega)d\omega]^2}. \tag{B.81}$$

It is assumed that the spectral first-order correlation function is uniform or of the Schell type. This means that it depends only on the difference of frequencies as $g_{in}^{(1)}(\omega_1,\omega_2) = g_{in}^{(1)}(\omega_2 - \omega_1)$. In this case, after changing the variables, one has, for the nominator of the contrast function

$\zeta(D_\omega)$ in Eq. (B.81),

$$\begin{aligned}&\iint_{-\infty}^{\infty} \hat{T}_{sl}(\omega_1)\hat{T}_{sl}(\omega_2)S_{in}(\omega_1)S_{in}(\omega_2)|g_{in}^{(1)}(\omega_2-\omega_1)|^2 d\omega_1 d\omega_2 \\ &= \int_{-\infty}^{\infty} F(\omega)g_{in}^{(1)}(\omega)|^2 d\omega\end{aligned} \tag{B.82}$$

where $F(\omega)$ is the autocorrelation function,

$$F(\omega) = \int_{-\infty}^{\infty} \hat{\hat{T}}_{sl}(\omega')\hat{\hat{T}}_{sl}(\omega'+\omega)d\omega' \tag{B.83}$$

and

$$\hat{\hat{T}}_{sl}(\omega) = S_{in}(\omega)\hat{T}_{sl}(\omega) \tag{B.84}$$

the contrast function $\zeta(D_\omega)$, after substituting these results in Eq. (B.81) is deined as

$$\zeta(D_\omega) = \frac{\int_{-\infty}^{\infty} F(\omega)|g_{in}^{(1)}(\omega)|^2 d\omega}{\left[\int_{-\infty}^{\infty} \hat{\hat{T}}_{sl}(\omega)d\omega\right]^2}, \tag{B.85}$$

This is quite a general expression assuming only uniformity of the spectral first-order correlation function. The next approximation can be made by the assumption that the bandwidth of x-ray radiation incoming to the monochromator unit is much wider than the transmitted one by the exit slits $D_\omega^{sl} \ll \Omega$. In this case, it can be also assumed that $S_{in}(\omega)$ is constant in the integration region in Eq. (B.83), and $\hat{\hat{T}}_{sl}(\omega)$ can be substituted by $\hat{T}_{sl}(\omega)$ in this equation.

By substituting Eq. (B.72) in Eq. (B.85) and varying the bandwidth of x-ray radiation by opening and closing the exit slits, a typical dependence of the contrast function can be obtained. Fitting this curve to the experimentally determined values of the contrast will give us the rms value of the pulse duration σ_T and hence the average pulse duration $T = 2.355\sigma_T$.

Two limits for the evaluation of the contrast function $\zeta(D_\omega)$ will be considered in the following. In the first limit, the opening of the slits will be much larger than the resolution function width $D_\omega^{sl} \gg \sigma_{res}$ and in the second limit, the opposite will be assumed, $D_\omega^{sl} \ll \sigma_{res}$. In the first limit, the function $\hat{T}_{sl}(\omega)$ in Eq. (B.59) may be, with a good approximation, substituted by the rectangular function $\hat{T}_{sl}(\omega) \cong T_{sl}^2(\omega)$ =$T_{sl}(\omega)$=$rect[\omega/D_\omega^{sl}]$. In this case the autocorrelation function $F(\omega)$ in Eq. (B.83) is represented as,

$$F(\omega) = \int_{\infty}^{\infty} T_{sl}(\omega')T_{sl}(\omega'+\omega)d\omega' = \begin{cases} 1 - \left|\frac{\omega}{D_\omega^{sl}}\right|, \omega \le D_\omega^{sl}, \\ 0, \omega > D_\omega^{sl} \end{cases} \tag{B.86}$$

Substituting Eq. (B.86), as well as the first-order correlation function from Eq. (B.72), in expression (B.85) the contrast function $\zeta(D_\omega)$ is found as

$$\zeta(D_\omega) = \frac{\int_{-D_\omega^{sl}}^{D_\omega^{sl}} [1 - \frac{\omega}{D_\omega^{sl}}] e^{-\sigma_T^2\omega^2} d\omega}{[D_\omega^{sl}]^2} \tag{B.87}$$

Performing the integration, the contrast function $\zeta(D_\omega)$ in this limit (see, for example, [197]) is obtained

$$\zeta(D_\omega) = \frac{\sqrt{\pi}}{D_\omega^{sl}\sigma_T} erf(D_\omega^{sl}\sigma_T) + \frac{1}{(D_\omega^{sl}\sigma_T)^2}[e^{-(D_\omega^{sl}\sigma_T)^2} - 1] \tag{B.88}$$

where $erf(x)$ is an error function.

According to the definition of the coherence time for rectangular slits $\tau_c = 2\pi/D_\omega^{sl}$, in the limit $\tau_c \ll 1$ for the contrast function $\zeta(D_\omega) \sim [1/(2\sqrt{\pi})](\tau_c/\sigma_T) = \sim [1/(2\sqrt{\pi})](1/M_t)$, where M_t is the number of temporal modes.

In the other limit, $D_\omega^{sl} \ll \sigma_r$, according to Eq. (B.59), the function $\hat{T}_{sl}(\omega)$ can be represented by the resolution function $R(\omega)$. Substituting an expression (B.34) for the resolution function $R(\omega)$ into Eqs. (B.83) and (B.83), one can show that the contrast function $\zeta(D_\omega)$ in this limit has the following form:

$$\zeta(D_\omega) = \frac{1}{\sqrt{1 + 2(\sigma_r\sigma_T)^2}} \tag{B.89}$$

In this case of a Gaussian spectrum, coherence time is well approximated by $\tau_c = \sqrt{\pi}/\sigma_r$ and substituting it in expression (B.89) gives

$$\zeta(D_\omega) = \frac{1}{\sqrt{1 + 2\pi(\sigma_T/\tau_c)^2}} \tag{B.90}$$

In the limit of $\tau_c/\sigma_T \gg 1$ the contrast function is given by $\zeta(D_\omega) \cong 1 - \pi(\sigma_T/\tau_c)^2$. Expressions (B.89) and (B.90) indicate that in the case of a limited resolution of the monochromator the contrast function is always below 1. If the resolution of the monochromator is known, in the conditions $D_\omega^{sl} \ll \sigma_r$, an estimate of the pulse duration can be given from Eq. (B.89) as

$$\sigma_T = \frac{1}{\sigma_r}\sqrt{\frac{1 - \zeta^2(D_\omega)}{2\zeta^2(D_\omega)}}. \tag{B.91}$$

This equation provides an alternative (to spectral domain) way to determine the pulse duration of XFEL pulses in the conditions of the GSM.

B.6.2 Spatial correlations

In this subsection the spatial part of the second-order correlation function given in Eq. (B.64) will be expressed with an assumption that the incoming field is of the Gaussian Schell model type. It is assumed that measurements are performed in the far field and the propagators in Eqs. (B.64) and (B.65) may be expressed by simple exponential functions:

$$P_{f+L}(x^D - x) \propto e^{-iq^D x}, \quad q^D = k\frac{x^D}{(f+L)} \tag{B.92}$$

Substitution of these relations for the propagator in Eqs. (B.64) and (B.65) gives, for the correlation function,

$$g_{in}(q_1^D, q_2^D) = \frac{\iint exp[iq_1^D x_1 - iq_2^D x_2] W_{in}(x_1, x_2) dx_1 dx_2}{[S_D(q_1^D)]^{1/2} [S_D(q_2^D)]^{1/2}}, \tag{B.93}$$

and for $S_D(q_i^D)$

$$S_D(q_i^D) = \int exp[iq_1^D x_1 - iq_2^D x_2] W_{in}(x_1, x_2) dx_1 dx_2. \tag{B.94}$$

The correlation function $g_{in}(q_1^D, q_2^D)$ is found by integrating Eqs. (B.93) and (B.94) with the cross-spectral density function given in Eqs. (B.66) and (B.67)

$$\begin{aligned} &\iint exp[iq_1^D x_1 - iq_2^D x_2] W_{in}(x_1, x_2) dx_1 dx_2 = \\ &= exp(-[a(x_1^2 + x_2^2) - 2bx_1 x_2]) exp(iq_1^D x_1 - iq_2^D x_2) dx_1 dx_2 \\ &= \frac{\pi}{(a^2 - b^2)^{1/2}} exp\left\{ -[\alpha((q_1^D)^2 + (q_2^D)^2) - 2\beta q_1^D q_2^D] \right\} \end{aligned} \tag{B.95}$$

where

$$\alpha = \frac{a}{4(a^2 - b^2)}, \quad \beta = \frac{b}{4(a^2 - b^2)}. \tag{B.96}$$

This result is obtained by the use of the known integral

$$\int e^{-\alpha t^2} e^{iqt} dt = \sqrt{\frac{\pi}{\alpha}} e^{-q^2/4\alpha}. \tag{B.97}$$

In the denominator similar integration of Eq. (B.94) gives

$$S_D(q_i^D) = \int exp[iq_1^D x_1 - iq_2^D x_2] W_{in}(x_1, x_2) dx_1 dx_2 = \frac{\pi}{(a^2 - b^2)^{1/2}} e^{-2(\alpha - \beta) q_i^D}. \tag{B.98}$$

Substituting the results of integration in Eqs. (B.95) and (B.98) in Eq. (B.93) gives.

$$g_{in}(q_1^D, q_2^D) = e^{-\beta(q_2^D - q_1^D)^2}. \tag{B.99}$$

where parameter β is equal to

$$\beta = \frac{2\sigma_I^4}{\xi^2 + 4\sigma_I^2} \tag{B.100}$$

Finnaly, the second-order correlation function in Eq. (B.62) in the far field and for the GSM pulses for the incoming x-ray radiation is given by the following expression,

$$g^{(2)}(x_1^D, x_2^D) = 1 + \zeta(D_\omega) e^{-2\beta(q_2^D - q_1^D)^2} \tag{B.101}$$

where the contrast function D_ω is defined by the expression (B.85).

Appendix C

Modeling of the HBT experiment

C.1 Simulations related to the EuXFEL

C.1.1 Modeling of the FEL statistical properties

To investigate the statistical properties of the SASE3 undulator at the EuXFEL and the behavior of the intensity correlation $g^{(2)}$-functions, additional simulations were performed. Simulations of the stochastic XFEL-type radiation in the time-frequency domain were performed as proposed in the work [171]. In these simulations, first, the spectral amplitude as

$$E_{in}(\omega) = \sqrt{S_{in}(\omega)}e^{i\phi_r}$$

To investigate the statistical properties of the SASE3 undulator at the EuXFEL and the behavior of the intensity correlation $g^{(2)}$-functions, additional simulations were performed. Simulations of the stochastic XFEL-type radiation in the time-frequency domain were performed as proposed in the work [171]. In these simulations, first, the spectral amplitude as Q is defined, where S_{in} is the defined spectral density, and ϕ_r is a random phase. Next, this amplitude is Fourier transformed to the time domain, and a new envelope function in the time domain with a certain pulse duration is applied. After that, to this amplitude back Fourie transform is applied, and final spectral distribution is obtained. We note here that a single pulse is fully coherent as soon as the Fourier transform connects frequency and time domains, but due to initial random phases, the ensemble of these pulses obeys a Gaussian statistic. For initial simulations, the average spectrum was considered to be Gaussian and centered at the frequency ω_0, corresponding to the resonant energy of E_0 = 1.2 keV. The spectral width was considered to be ΔE^{FWHM} = 5 eV, and an average pulse duration was also considered to be Gaussian with the duration T^{FWHM} = 10 fs. To simulate the stochastic XFEL radiation $5 \cdot 10^3$ pulses were generated by this method.

C.1.2 Spectral simulations

To study the effect of the monochromator resolution on the results of the second-order correlation analysis, the following simulations were performed. The spectral density $S_{in}(\omega)$ gen-

erated for each pulse, was convolved with the monochromator resolution function $R(\omega)$ given in Eq. (7.20) as

$$S(\omega) = \int S_{in}(\omega')R(\omega - \omega')d\omega' \tag{C.1}$$

For the resolution function $R(\omega)$ the FWHM value of 0.2 eV was used, to match the spike width in simulations. The same features were observed in our experiment. Further, the spectral values defined by Eq. (C.1) were correlated according to Eq. (7.16) in order to determine second-order correlation function $g^{(2)}(\omega_1, \omega_2)$ in frequency domain.

The other important effect, which may influence the outcome of the HBT analysis, is the frequency chirp. The situation when the average electron energy at the head of the electron bunch differs significantly from that on the tail of the bunch is known as energy chirp. The resulting radiation pulse, in this case, is also frequency chirped. Such frequency chirp in the simulations was set by introducing a linear correction to the resonant frequency as $\omega(t) = \omega_0 + \alpha t$, where $\alpha = d\omega/dt$ is the linear chirp coefficient. This frequency chirp was applied to the amplitude function in the time domain on the last step prior to the final inverse Fourier transform to the frequency domain. For the chirped pulses, a linear chirp coefficient value of α=0.62 fs^{-2} was considered. For the chirped pulses in the simulations, two situations without and with monochromators resolution function $R(\omega)$ were considered. It also should be noted that for chirped pulses, the spectral width becomes larger, however, the pulse duration does not change.

Results of the spectral analysis for the cases described above are presented in Fig. C.1. First, the significant broadening of the spectrum for the chirped pulses was observed. If initial spectrum had the bandwidth of 5 eV, then for chirped pulses it was obtained about twice larger bandwidth of 9.5 eV (see Fig. C.1 (a,d,g,j) and Table C.1). The same effect was observed for the spike width, which is especially well seen in the analysis of the autocorrelation function (see Fig. C.1(b,e,h,k)). The broadening of the spectral width of the spikes was also observed when the finite monochromator resolution was considered (see Fig. S10). Their FWHM has changed from 0.19 eV to 0.28 eV for non-chirped pulses and from 0.36 eV to 0.42 eV for the chirped pulses (see Table C.1).

The histogram analysis (see Fig. C.1(c,f,i,l)) shows that the number of modes does not depend on the resolution function or chirp effects and stays about the same for all simulations considered here. The number of modes determined by Eq. (8.2) in our simulations was M=28±1 (see Table C.1).

Next, the $g^{(2)}(\omega_1, \omega_2)$ –function was evaluated by applying Eq. (7.16) to the simulated pulses for all cases considered here (see Fig. C.2(a, c, e, g)). First, one can clearly see that the spectral $g^{(2)}(\omega_1, \omega_2)$–function behaves as the one originating from a single chaotic source (see [131]). One can also observe some small modulations of intensity around the value of unity in all cases attributed to the limited statistics ($5 \cdot 10^3$ pulses) in our simulations. The contrast value is about unity for the simulation of the pulses without and with the chirp (see Fig. C.2(a,b) and Fig. C.2(e,f)). However, it reduces when the finite monochromator resolution is considered

Table C.1: Results of simulations with the spectrum bandwidth ΔE= 5 eV and pulse duration 10 fs as input parameters. Here, $5{\cdot}10^3$ pulses were generated for the analysis. The spectral bandwidth as well as the bandwidth of spikes was determined from the autocorrelation function. The number of modes M was determined from the intensity distribution analysis. The contrast ζ_2 value was determined from the maximum of the spectral and spatial g(2)-functions. An averaged pulse duration T (FWHM) was determined from the spectral and spatial analysis. Result are presented for the flowing cases: Initial simulation (IS), simulation of the monochromator resolution (R = 0.2 eV), simulation of the chirped pulses (CP) and chirped pulses with the same resolution

Parameters	IS	R = 0.2 eV	CP	CP (R = 0.2 eV)
Spectral band-width (FWHM), eV	5.0	5.0	9.5	9.5
Spectral band-width of spikes (FWHM), eV	0.19	0.28	0.36	0.42
Numer of modes M	28	28	28	28
Contrast from spectral analysis ζ_{in}	0.97	0.67	1	0.87
Pulse duration T from HBT spectral analysis (FWHM), fsζ_{in}	10.0	10.0	5.1	5.1
Contrast from spatial analysis ζ_{in}	0.98	0.67	0.99	0.87
Pulse duration T from HBT spatial analysis (FWHM), fs	10.0	10.0	5.2	5.2

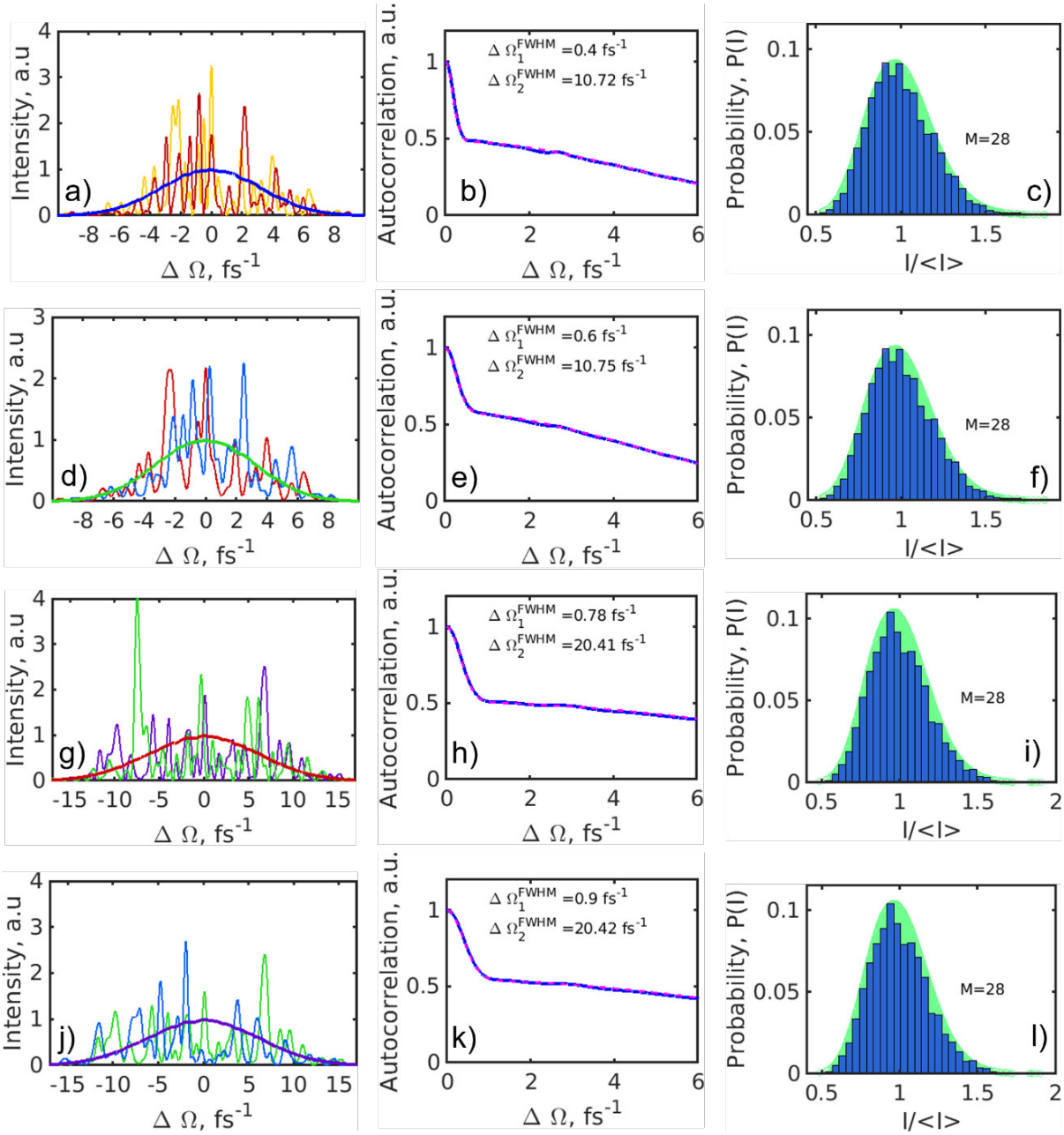

Figure C.1: Spectral analysis simulations. (a, d, g, j) Typical single shot simulated spectra and an averaged spectrum. (b, e, h, k) Autocorrelation function of individual spectral lines averaged over $5 \cdot 10^3$ pulses (blue solid line) and the fit with the two Gaussian functions (magenta dashed line). The FWHM values of the Gaussian fits are also given. (c, f, i, l) Histograms of the spectral pulse intensity distribution (blue). The green background corresponds to the gamma probability distribution function with the given number of modes M. Here (a-c) corresponds to the initially simulated spectra neglecting resolution of the monochromator, (d-f) same spectra as in (a-c) with the monochromator resolution of 0.2 eV, (g-i) same spectra as in (a-c) with the linear frequency chirp of 0.62 $1/fs^2$ and neglecting resolution of the monochromator, (j-l) same spectra as in (g-i) with the monochromator resolution of 0.2 eV.

for both cases (see Fig. C.2(c,d) and Fig. C.2(g,h)). To determine an average pulse duration $T^{FWHM} = 2.355 \cdot \sigma_T$, the $g^{(2)}(\omega_1, \omega_2)$–function along the white dashed line was analyzed. For the cases without the monochromator resolution, these profiles were fitted by the Gaussian function

$$g^{(2)}(\Delta\omega) - 1 = exp(-\sigma_T^2 \Delta\omega^2) \tag{C.2}$$

where it was assumed full spatial coherence of the incoming beam (see Eqs. (7.15, 7.17, 7.22). For the cases with the monochromator resolution Eqs. (7.17, 7.21) were used, assuming full spatial coherence of the incoming beam. The results of the fit for the pulse duration are summarized in Table C.1. As it is seen from this Table, it was possible to get a correct pulse duration of about 10 fs for unchirped pulses, however, the fit gives twice shorter pulse durations, of about 5 fs, for the chirped pulses. This is related to the broadening of the spectrum twice from its nominal initial value. From this, one can conclude that our HBT spectral analysis in the case of chirped pulses provides only the lower boundary for a possible pulse duration. The actual pulse duration, in this case, may be only longer. Unfortunately, it is difficult to determine the actual pulse duration if the type of the chirp (linear quadratic, etc.) and its value are not known.

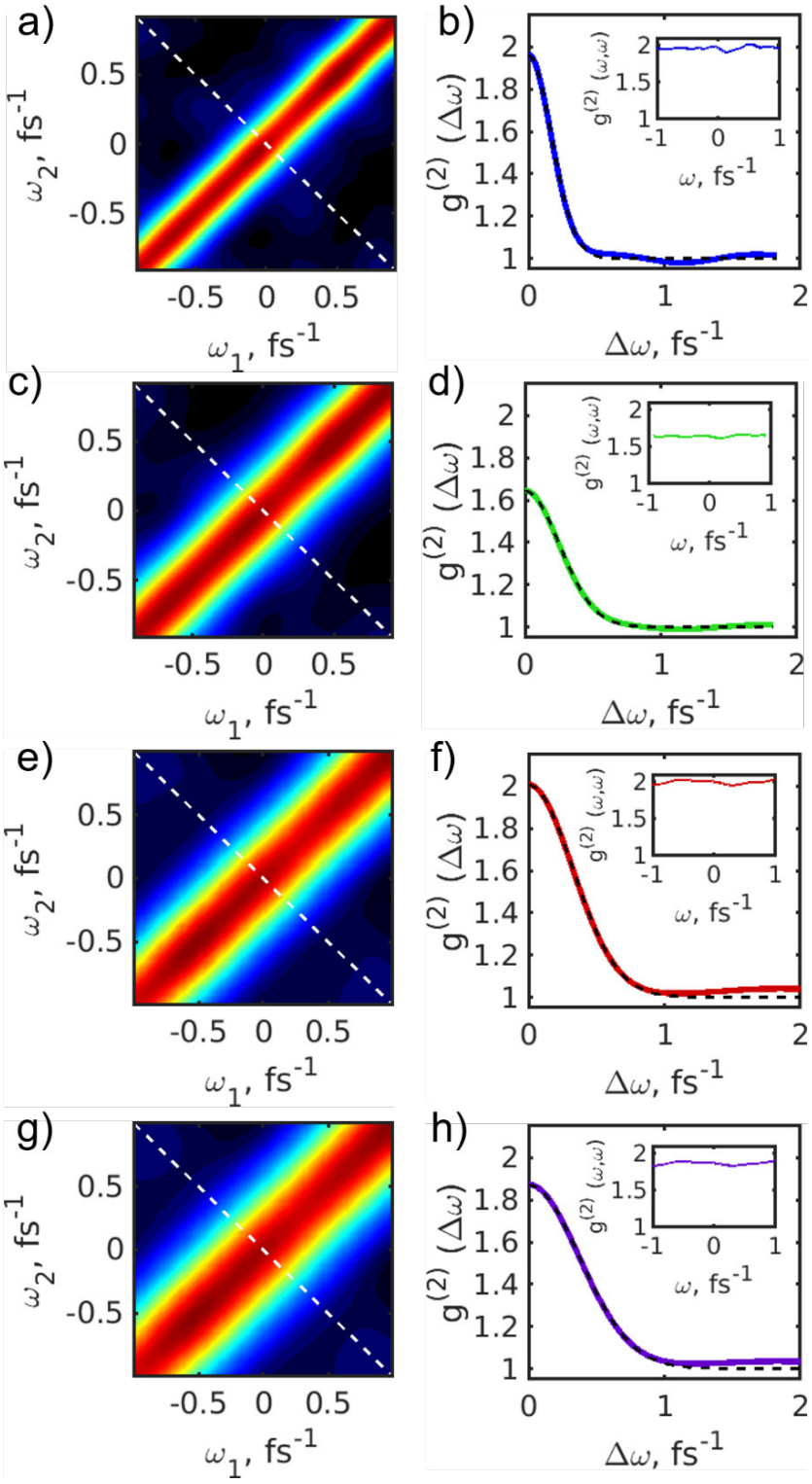

Figure C.2: (a, c, e, g) Intensity correlation functions of simulated spectra $g^{(2)}(\omega_1, \omega_2)$. (b, d, f, h) Cut along the anti-diagonal lines shown by white dashed lines in (a, c, e,g) and its fit (black dashed line). In the inset the profiles along the diagonal of the $g^{(2)}(\omega, \omega)$ function in (a, c, e, g) are shown. Here (a, b) corresponds to the initially simulated spectra neglecting resolution of the monochromator, (c, d) same spectra as in (a,b) with the monochromator resolution of 0.2 eV, (e,f) same spectra as in (a,b) with the linear frequency chirp of 0.62 fs-2 and neglecting resolution of the monochromator, (g, h) same spectra as in (e,f) with the monochromator resolution of 0.2 eV.

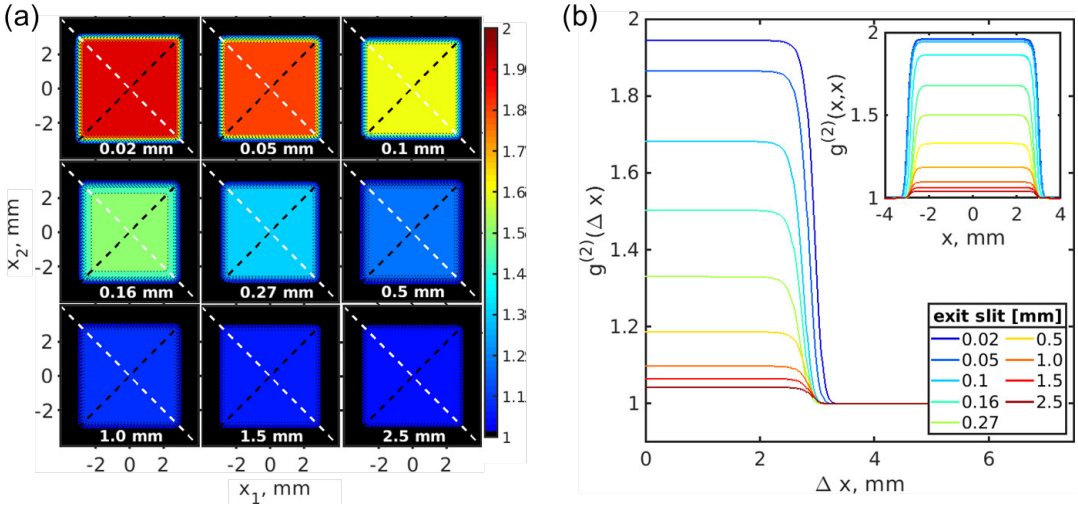

Figure C.3: (a) Intensity correlation functions $g^{(2)}(x_1, x_2)$ simulated in the linear regime of the undulator settings, for different openings of the exit slit of the monochromator. (b) Profiles of the $g^{(2)}(\Delta x)$-function taken along the white dashed anti-diagonal lines shown in panel (a) as a function of the slit opening. In the inset the corresponding autocorrelation functions $g^{(2)}(x, x)$ taken along the black dashed diagonal lines in panel (a) are shown.

C.1.3 Spatial simulations

For the spatial analysis, the focus was made on analyzing the contrast function $\zeta_{in}(D_\omega)$ given in Eq. (7.25), assuming again that in the spatial domain, the pulses are fully coherent. For evaluation of the contrast function $\zeta_{in}(D_\omega)$ the following values of the slit opening were considered: 20 μm, 50 μm, 100 μm, 160 μm, 270 μm, 500 μm, 1 mm, 1.5 mm, and 2.5 mm. The result of the intensity-intensity correlation analysis for the simulation in the original case, with 100 % monochromator resolution, is shown in Fig. C.3. In these simulations, fully coherent beams were considered in the spatial domain, which may be seen from the correlation function in Fig. C.3. The contrast, as the function of the bandwidth, taken as the maximum value of the $g^{(2)}(\Delta x)$-function, obtained from the antidiagonal cuts of the $g^{(2)}(x_1, x_2)$-function. This contrast function shows similar behavior, which was also observed in the experiment.

In the case of the finite monochromator resolution $R(\omega)$ the function $\tilde{T}_{sl}(\omega)$ was determined from Eq. (7.26) and in the case when the monochromator resolution was neglected this function was substituted by the rectangular function $T_{sl}(\omega)$ given in Eq. (7.27). For the resolution function $R(\omega)$ the same FWHM value of 0.2 eV was considered. The cross-spectral density function $W_{in}(\omega_1, \omega_2)$ was generated according to its definition as correlation function of amplitudes in spectral domain: $W_{in}(\omega_1, \omega_2) = < E_{in} * (\omega_1) E_{in}(\omega_2) >$ and the brackets $< \ldots >$ define an ensemble average. The spectral amplitudes for each pulse were the same as generated before for the spectral analysis: the initial ones and the ones with the linear chirp.

As a result of these simulations, the values of the contrast function $\zeta_{in}(D_\omega)$ as a function of coherence time were determined for the same cases as discussed before (see Fig. C.4). To determine an average pulse duration for each case, these contrast values were fitted by Eq. (7.31). In this expression, the autocorrelation function was used $F(\omega)$ defined by Eqs. (7.32,

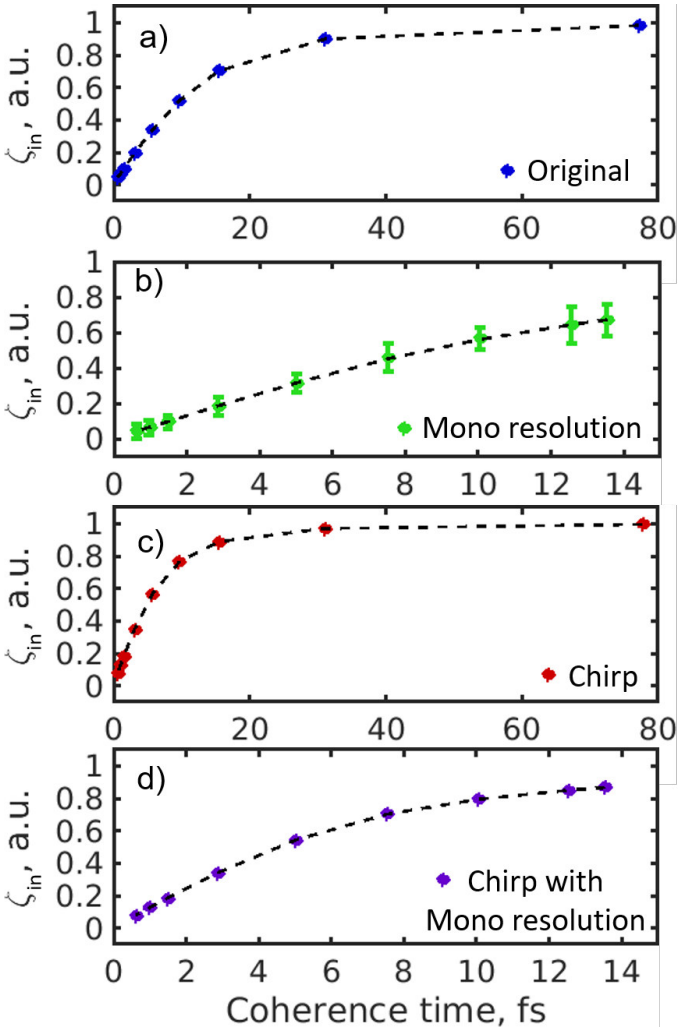

Figure C.4: Contrast values $\zeta_{in}(D_\omega)$ evaluated according to Eq. (7.31) as a function of the coherence time. (a) Simulated intensity patterns neglecting resolution of the monochromator, (b) same intensity patterns as in (a) with the monochrometer resolution of 0.2 eV, (c) same intensity patterns as in (a) with the linear frequency chirp of 0.62 fs^{-2}, (d) same intensity patterns as in (c) with the monochromator resolution of 0.2 eV. Note the reduced value of the contrast function and different range for the coherence time in (b) and (d) due to the finite monochromator resolution.

7.33) as well as the first-order correlation function $g_{in}^{(1)}(\omega)$ defined in Eq. (7.15). As a result of this fit, the pulse duration values were obtained and listed in Table C.1. Similar to spectral analysis, the correct values of pulse durations of about 10 fs were obtained for unchirped pulses and twice shorter pulse durations of about 5 fs for the chirped pulses. This analysis also tells that the spatial analysis will provide only the lower boundary for the pulse duration in the case of chirped pulses.

C.2 Simulations and analysis related to the PAL-XFEL

C.2.1 Modeling of the FEL SASE source

In order to investigate statistical properties of the undulator source at the PAL-XFEL and the behavior of the intensity correlation $g^{(2)}$-functions, additional simulations were done, combining several effects, similar to those, described in section C.1.1. To simulate the stochastic XFEL radiation in the time-frequency domain $5 \cdot 10^3$ pulses were generated by this method for each particular simulation case: initial simulation, resonant energy jitter, pulse duration distribution, and multiple beams. For initial simulations, the average spectrum was considered to be Gaussian and centered at the frequency ω_0, corresponding to the resonant energy of E_0 = 10 keV. The spectral width was considered to be ΔE^{FWHM} = 10 eV, and average pulse duration was also considered to be Gaussian with the duration T^{FWHM} = 5 fs. Results of the simulation for the initial case are shown in Fig. C.5. Typical single shot simulated spectra and an averaged spectrum, as well as autocorrelation function of individual spectral lines, are shown in Fig. C.5(a,b). The ACF analysis showed the size (FWHM) of the average spectrum is 10 eV, and the single spectral spike size (FWHM) is 0.4 eV. Analyzing variation of the integrated spectral intensity distribution, it was concluded that the number of modes, present in the simulated SASE spectrum is around M=28. After building the intensity correlation function of simulated spectra $g^{(2)}(\omega_1, \omega_2)$ (see Fig. C.5(c)), its cut along the anti-diagonal line (function $g^{(2)(\Delta\omega)}$, shown by white dashed lines in Fig. C.5(c)), was fitted according to Eq. (7.15). The fit provided the correct average pulse duration of 5 fs. Following simulations in sections C.2.2, C.2.3, C.2.4 will be compared with these initial ones.

C.2.2 Energy jitter effect

Since the FEL itself is a complicated machine, many instabilities may arise during the electron bunch acceleration and radiation amplification process. One of the results of such instability can manifest itself in the resonant energy jittering effect. In order to study the energy jitter effect on the intensity correlation functions through the simulation, the resonant energy of 10 keV, which was used in the initial simulation, allowed to have variation within 5 eV (rms) photon energy according to Gaussian distribution. Results of the simulation are shown in Fig. C.6. Two typical spectral intensity distributions and the average spectrum are shown in Fig. C.6(a). It is already seen from this figure that some of the spectra have shifted resonant energy within 5 eV distribution, although the average spectrum did not change dramatically. The ACF analysis showed almost the same width (FWHM) of the average spectrum, which is around 10 eV, and the single spectral spike width (FWHM) $\sim$ 0.4eV. The histogram of the spectral pulse intensity distribution and the resonant energy distribution is shown in Fig. C.6(c) and (d) correspondingly. It is seen from the histogram that the number of longitudinal modes stayed the same M=28. Up to this moment, there were no dramatic changes in the considered functions. Significant changes are appearing, and the studied effect manifests itself in the correlation functions. The intensity correlation function of simulated spectra $g^{(2)}(\omega_1, \omega_2)$ in this case, as the result

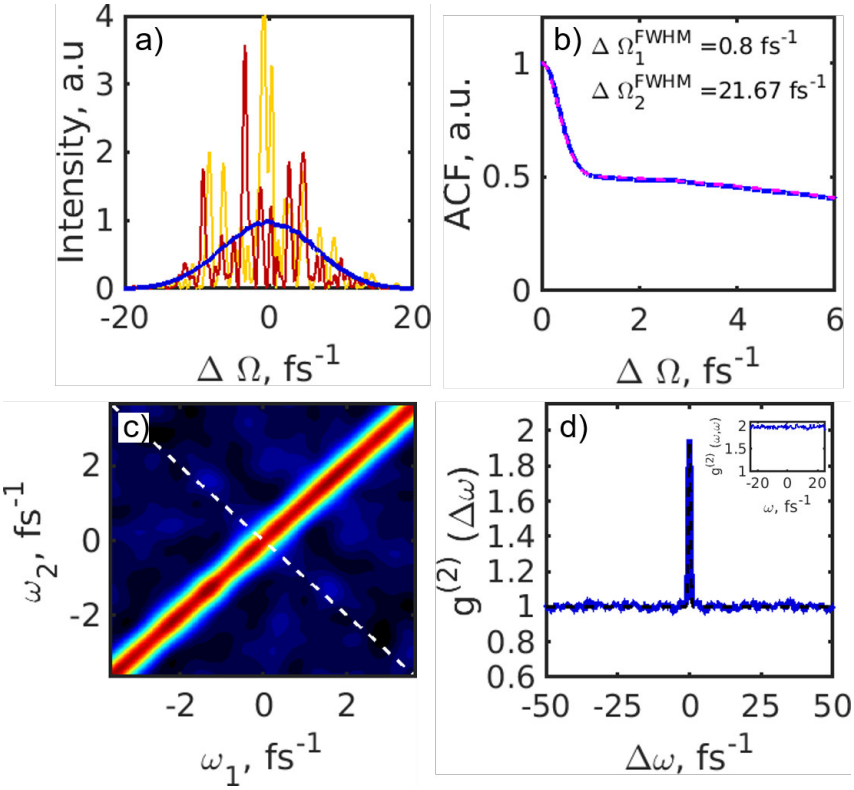

Figure C.5: Spectral analysis simulations. (a) Typical single shot simulated spectra and an averaged spectrum. (b) Autocorrelation function of individual spectral lines averaged over $5 \cdot 10^3$ pulses (blue solid line) and the fit with the two Gaussian functions (magenta dashed line). The FWHM values of the Gaussian fits are also given. (c) Intensity correlation function of simulated spectra $g^{(2)}(\omega_1, \omega_2)$. (d) Cut along the anti-diagonal line shown by white dashed lines in (c) and its fit (black dashed line) with the Eq. (7.15) . In the inset the profile along the diagonal of the $g^{(2)}(\omega, \omega)$ function in (c) are shown.

of the energy jittering effect, shaped in the form of two maxima and two minima, each positioned on the same line but in mutually perpendicular directions (see Fig. C.6(e)). The effect is also clearly seen on the cut (Fig. C.6(f)) along the anti-diagonal line ($g^{(2)(\Delta\omega)}$-function, and the diagonal line (insent in Fig. C.6(f)). Since the $g^{(2)}$ intensity correlation function was distorted, the fit of $g^{(2)(\Delta\omega)}$-function provides with slightly lower pulse duration T_{FWHM}=4.7 fs. Besides this distortion, no other effects of SASE beam parameters under consideration were found. Such laydowns and maxima were also observed in the correlation function obtained in the experiment at PAL-XFEL, indicating at possible energy jittering effects.

C.2.3 Pulse duration distribution

As mentioned earlier instabilities, arising during the acceleration or radiation amplification process, such as an energy jitter, complicate the process of determining the pulse duration. But it is very often that these effects, in turn, do not come alone. Along with the energy jitter, another effect that may deform the correlation functions and make it difficult to determine beam paramters is the pulse duration jittering. The latter means that there is a variation of the pulse duration, which may change from shot to shot. In order to study this effect, the rms value for the Gaussian time filter on the modeling stage allowed to have variation within 1 fs from shot to shot according to Gaussian distribution. Results of this simulation are shown in Fig. C.7. Although, the width of the average spectrum and spectral spike did not change significantly (see Fig. C.7(a,b)), the number of modes, determined from the variation analysis of the integrated spectral intensity distribution, reduced almost twice to M=17 (see Fig. C.7(c)). The pulse variation distribution used in the simulation is shown in Fig. C.7(d). As in the previous case with the energy jitter, the intensity correlation function of simulated spectra $g^{(2)}(\omega_1, \omega_2)$ shaped in the form of two maxima and two minima (see Fig. C.7(e)). Another interesting observation is that the cut of this function along the anti-diagonal line ($g^{(2)(\Delta\omega)}$-function) shows an additional faintly discernible bump around $\Delta\omega$=0. Such bump was also observed in the correlation function obtained in the experiment at PAL-XFEL. Since that, the $g^{(2)(\Delta\omega)}$-function was fitted with two Gaussians (green and black dashed lines in Fig. C.7(f)), providing with slightly higher pulse duration of T_{FWHM}=5.3 fs. The presence of such a bump in correlation functions obtained from experimental data may indicate on possible pulse variation effect.

C.2.4 Multiple sources

The last studied effect, which may arise from the mentioned instabilities and influence the outcome of the HBT interferometry method and the performance of the XFEL, is the effect of multiple beam sources. This effect in the frame of spatial analysis was studied in the work [131] and will not be touched here. In the frame of spectral analysis, it can be simulated by introducing two resonant energies with fixed bandwidth. In order to study effect of multiple sources on the intensity correlation in the spectral domain, half of the simulated shots were generated at resonant energy of 9999 eV and the other half at 10001 eV. Results of the simulation are shown in Fig. C.8. It is seen the Fig. C.8(a) that such procedure of splitting the resonant energy into

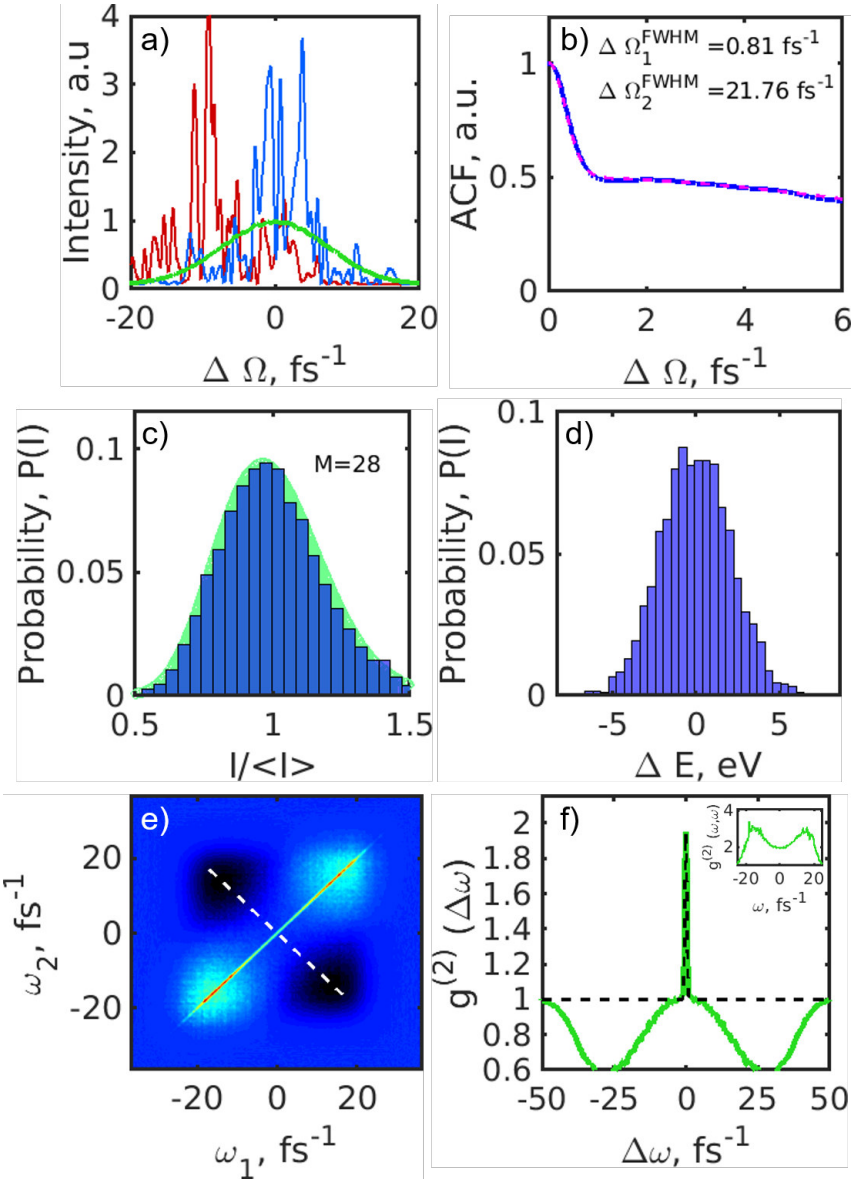

Figure C.6: Spectral analysis simulations with the energy jitter of 5 eV. (a) Typical single shot simulated spectra and an averaged spectrum. (b) Autocorrelation function of individual spectral lines averaged over $5 \cdot 10^3$ pulses (blue solid line) and the fit with the two Gaussian functions (magenta dashed line). The FWHM values of the Gaussian fits are also given. (c) Histogram of the spectral pulse intensity distribution (blue). The green background corresponds to the gamma probability distribution function with the given number of modes M. (d) Histogram of the resonant energy distribution. (e) Intensity correlation function of simulated spectra $g^{(2)}(\omega_1, \omega_2)$. (f) Cut along the anti-diagonal line shown by white dashed lines in (c) and its fit (black dashed line) with the Eq. (7.15) . In the inset the profile along the diagonal of the $g^{(2)}(\omega, \omega)$ function in (e) are shown.

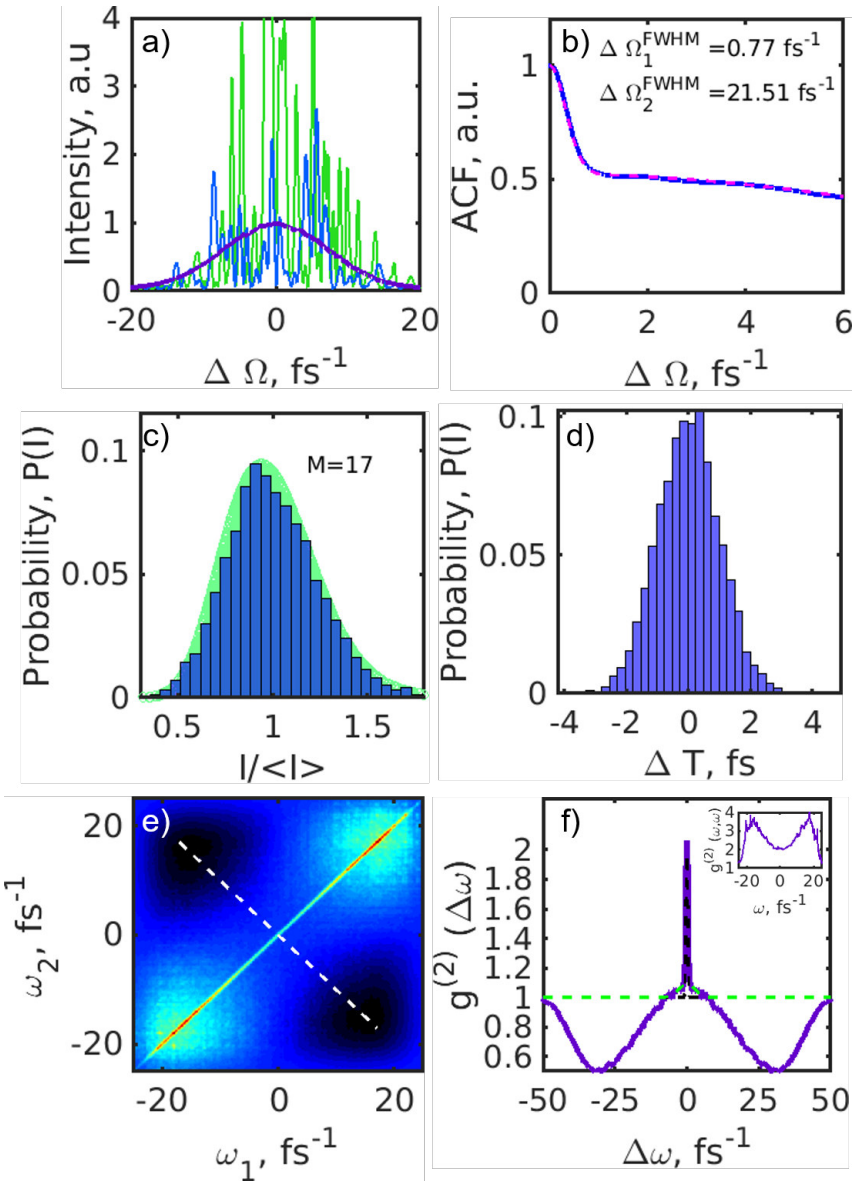

Figure C.7: Spectral analysis simulations with the pulse duration distribution of 1 fs (rms). (a) Typical single shot simulated spectra and an averaged spectrum. (b) Autocorrelation function of individual spectral lines averaged over $5 \cdot 10^3$ pulses (blue solid line) and the fit with the two Gaussian functions (magenta dashed line). The FWHM values of the Gaussian fits are also given. (c) Histogram of the spectral pulse intensity distribution (blue). The green background corresponds to the gamma probability distribution function with the given number of modes M. (d) Histogram of the energy distribution. (e) Intensity correlation function of simulated spectra $g^{(2)}(\omega_1, \omega_2)$. (f) Cut along the anti-diagonal line shown by white dashed lines in (c) and its fit (black dashed line) with the Eq. (7.15) . In the inset the profile along the diagonal of the $g^{(2)}(\omega, \omega)$ function in (e) are shown.

two did not change dramatically the width of the average spectrum or the spike width, which is also confirmed by ACF analysis (see Fig. C.8(b)). The number of modes, determined from the histogram analysis (see Fig. C.8(c)), stayed the same M=28. The only observable artifacts are present in the correlation function in the form of two maxima and minima (see Fig.C.8(e)). The distortion of the $g^{(2)}(\omega,\omega)$, in this case, is less pronounced and can be examined along the diagonal of this function (see Fig. C.8(f) and inset). Although in the present case inhomogeneities are less pronounced, still the fit of $g^{(2)}(\Delta\omega)$-function gives slightly reduced values of the pulse duration T_{FWHM}=4.7 fs.

As a result of these simulations, we determined possible effects, which may influence the correlation functions obtained from the experimental data. It is hard to determine whether one of the listed effects is presented individually or a combination of the effects modifies the spectral intensity correlation function. The presence of these effects can be confirmed indirectly using additional detectors and complementary absorption methods. One way or another, it is still possible in the range of error to determine the average pulse duration of the SASE FEL beam by utilizing the HBT interferometry method.

C.3 HBT interferometry analysis for 120 pC and 200 pC bunch charge

In this section, additional results from the HBT interferometry analysis at PAL-XFEL are presented for the studied SASE and SS operational regimes in the case of 120 pC and 200 pC electron bunch charge. Results concern the Pearson correlation analysis are shown in Fig. C.9 and Fig. C.10, and discussed in Section 9.1. The spectral correlation analysis is presented in Fig. C.11, the analysis and methods discussed in Section 9.2. The results of the HBT interferometry analysis in the spatial domain, for bunch charges of 120 pC and 200 pC, are presented in Fig. C.12, Fig. C.13, and Fig. C.14, Fig. C.15. The results of spatial analysis and methods were discussed in Section 9.3.

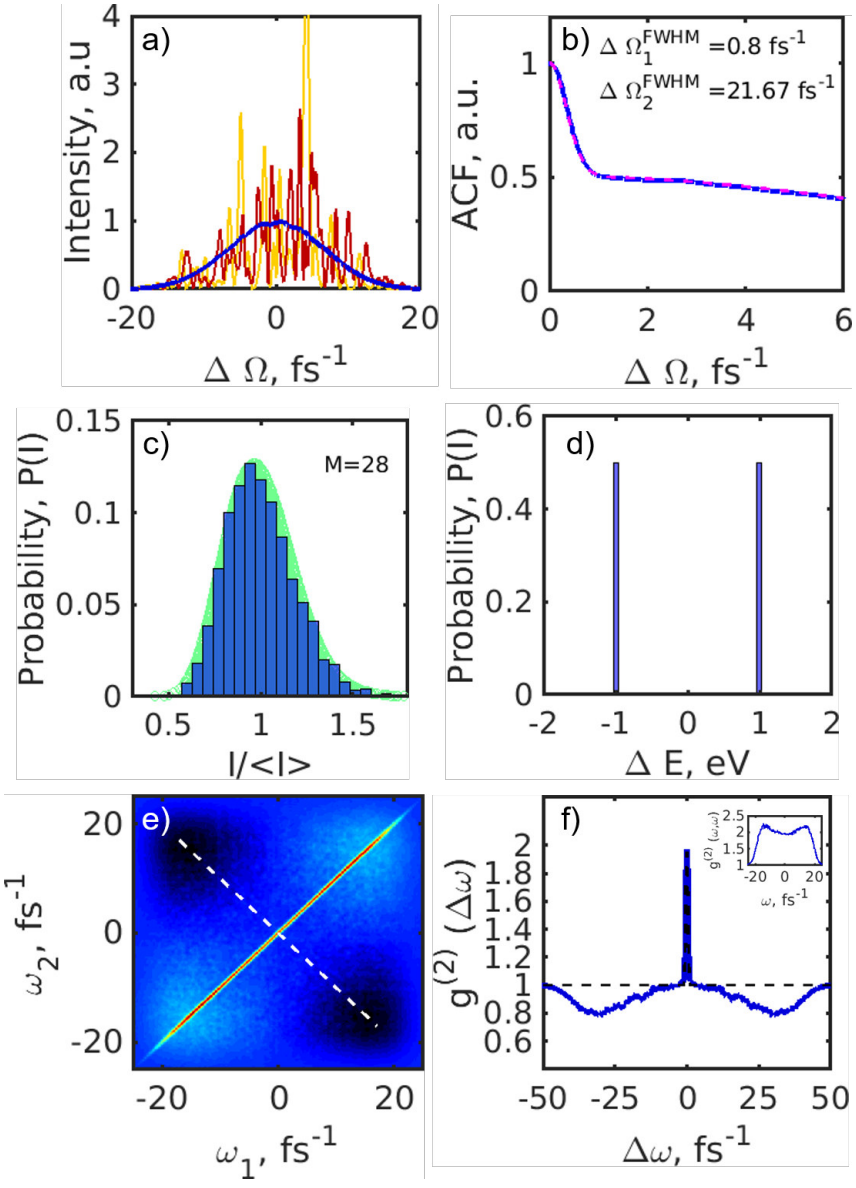

Figure C.8: Spectral analysis simulations of the two beams, with the difference between resonant energies of 2eV. (a) Typical single shot simulated spectra and an averaged spectrum. (b) Autocorrelation function of individual spectral lines averaged over $5 \cdot 10^3$ pulses (blue solid line) and the fit with the two Gaussian functions (magenta dashed line). The FWHM values of the Gaussian fits are also given. (c) Histogram of the spectral pulse intensity distribution (blue). The green background corresponds to the gamma probability distribution function with the given number of modes M. (d) Histogram of the resonant energy distribution. (e) Intensity correlation function of simulated spectra $g^{(2)}(\omega_1, \omega_2)$. (f) Cut along the anti-diagonal lines shown by white dashed lines in (c) and its fit (black dashed line) with the Eq. (7.15) . In the inset the profile along the diagonal of the $g^{(2)}(\omega, \omega)$ function in (e) are shown.

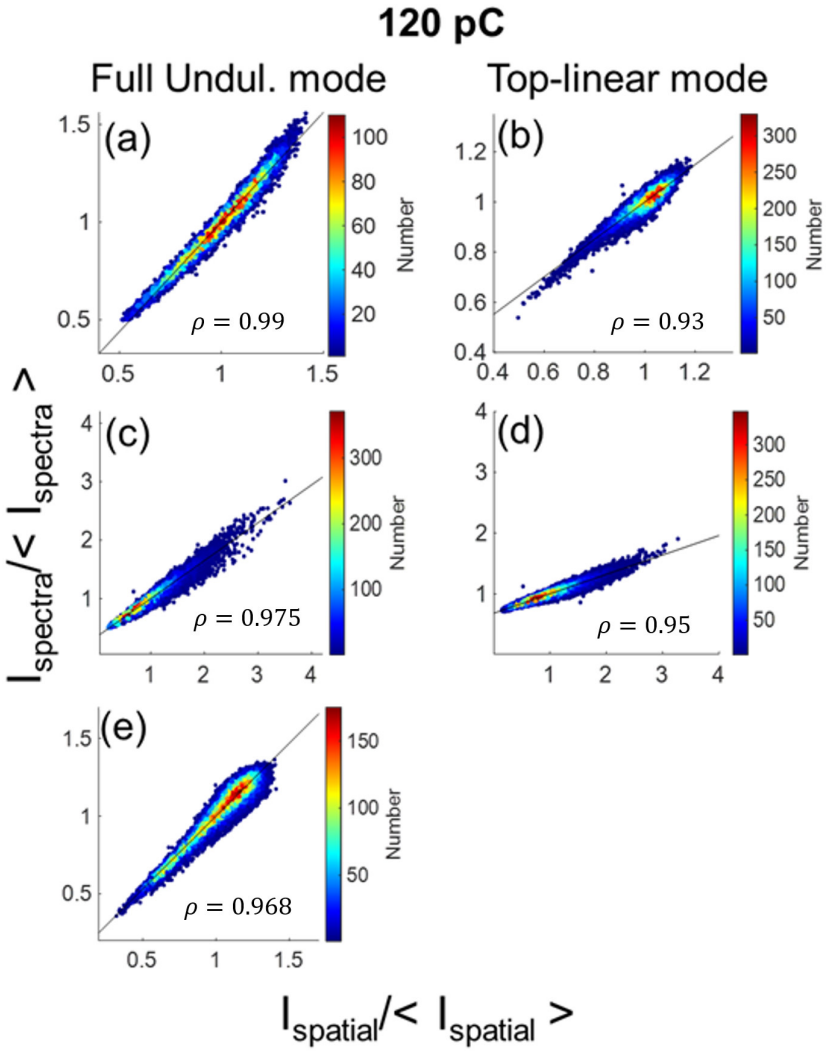

Figure C.9: Pearson correlation of the measured spatial and spectral data in the case of SASE PINK (a,b), MONO (c,d) and SS (e) in linear and saturation regimes of operation. The Pearson correlation coefficient p varies in the range from 0.92 to 0.98, depending on the operating regime in the case of 120 pC charge.

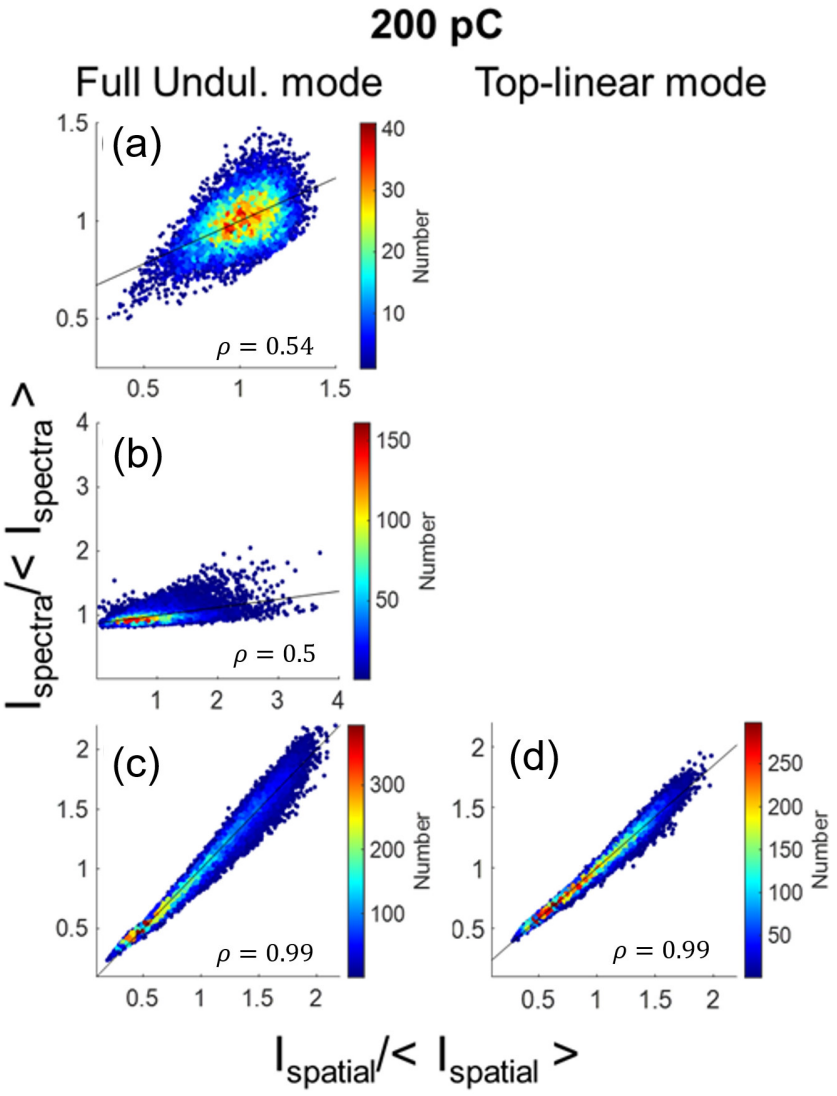

Figure C.10: Pearson correlation of the measured spatial and spectral data in the case of SASE PINK (a), MONO (b) and SS (c) and SS with linear tapering (d). The Pearson correlation coefficient p varies in the range from 0.5 to 1, depending on the operating regime in the case of 200 pC charge.

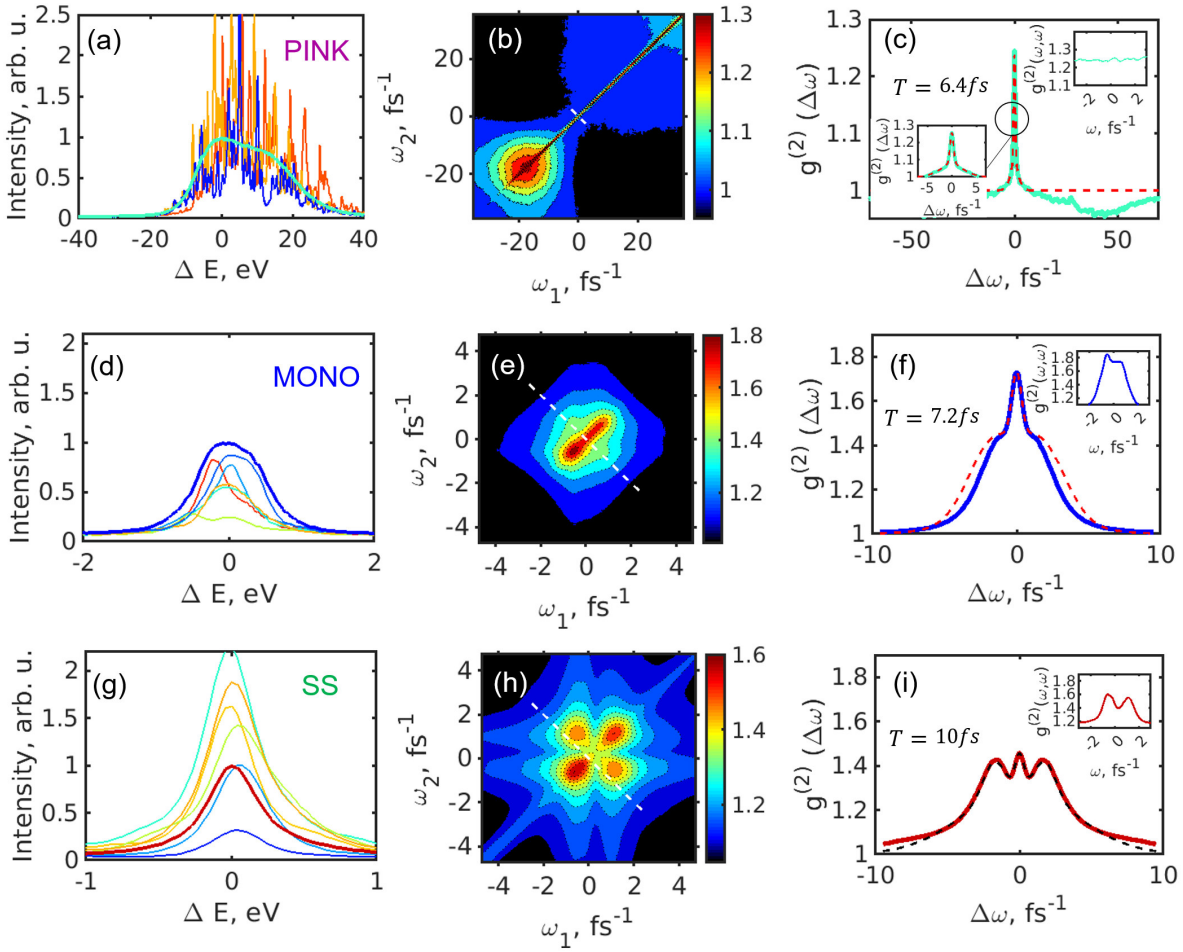

Figure C.11: (a,d,g) Spectral distributions of random shots and average spectrum , for the following regimes of operation: SASE PINK (a,b,c), MONO (d,e,f), and SS (g,h,i) at 200 pC bunch charge. (b, e, h) Intensity correlation functions of spectra $g^{(2)}(\omega_1, \omega_2)$. (c, f, i) Cut along the anti-diagonal lines shown by the white dashed lines in (b, e, h) and its fit with the profile given in Eqs. (7.17, 7.21) (dashed line), taking into account additional background. In the inset the profiles along the diagonal of the $g^{(2)}(\omega, \omega)$ function are shown.

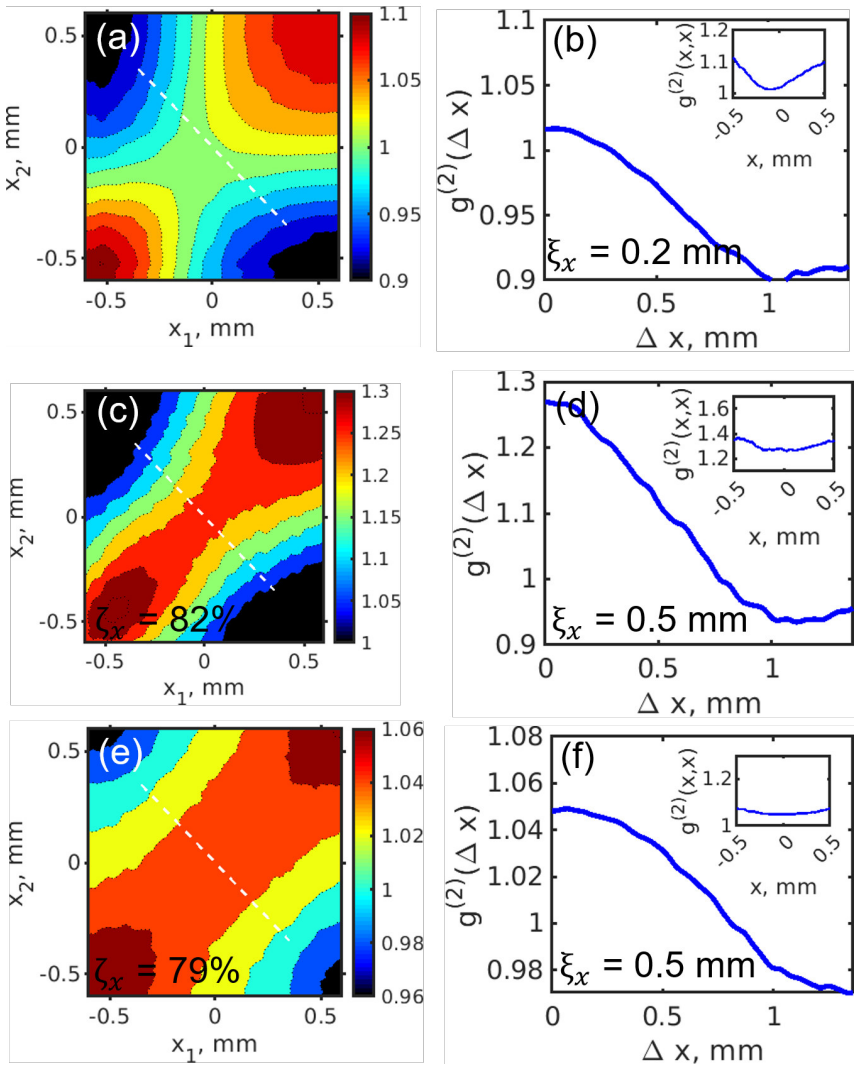

Figure C.12: Intensity correlation functions $g^{(2)}(x_1, x_2)$ (a,c,e) measured by the Hamamatsu detector in the horizontal direction. Profiles of the $g^{(2)}(\Delta x)$ (b,d,j)- function was taken along the white dashed anti-diagonal lines shown in panels (a,c,e). In the inset the corresponding autocorrelation functions $g^{(2)}(x, x)$ taken along the diagonal lines of $g^{(2)}(x_1, x_2)$-function are shown. Here results for the SASE PINK operating regime shown in (a,b), SASE MONO in (c,d) and SS regime in (e,f) shown for the case of 120 pC bunch charge.

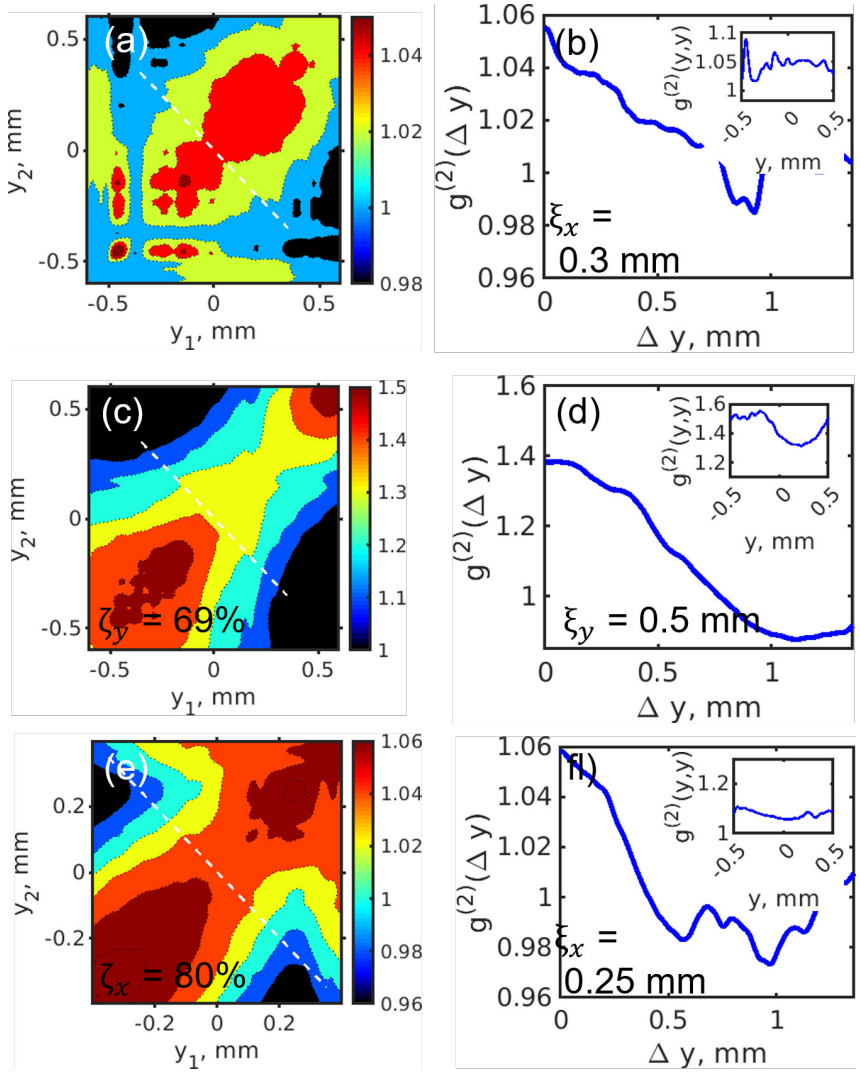

Figure C.13: Intensity correlation functions $g^{(2)}(x_y, y_2)$ (a,c,e) measured by the Hamamatsu detector in the vertical direction. Profiles of the $g^{(2)}(\Delta y)$ (b,d,j)- function was taken along the white dashed anti-diagonal lines shown in panels (a,c,e). In the inset the corresponding autocorrelation functions $g^{(2)}(y,y)$ taken along the diagonal lines of $g^{(2)}(y_1, y_2)$-function are shown. Here results for the SASE PINK operating regime shown in (a,b), SASE MONO in (c,d) and SS regime in (e,f) shown for the case of 120 pC bunch charge.

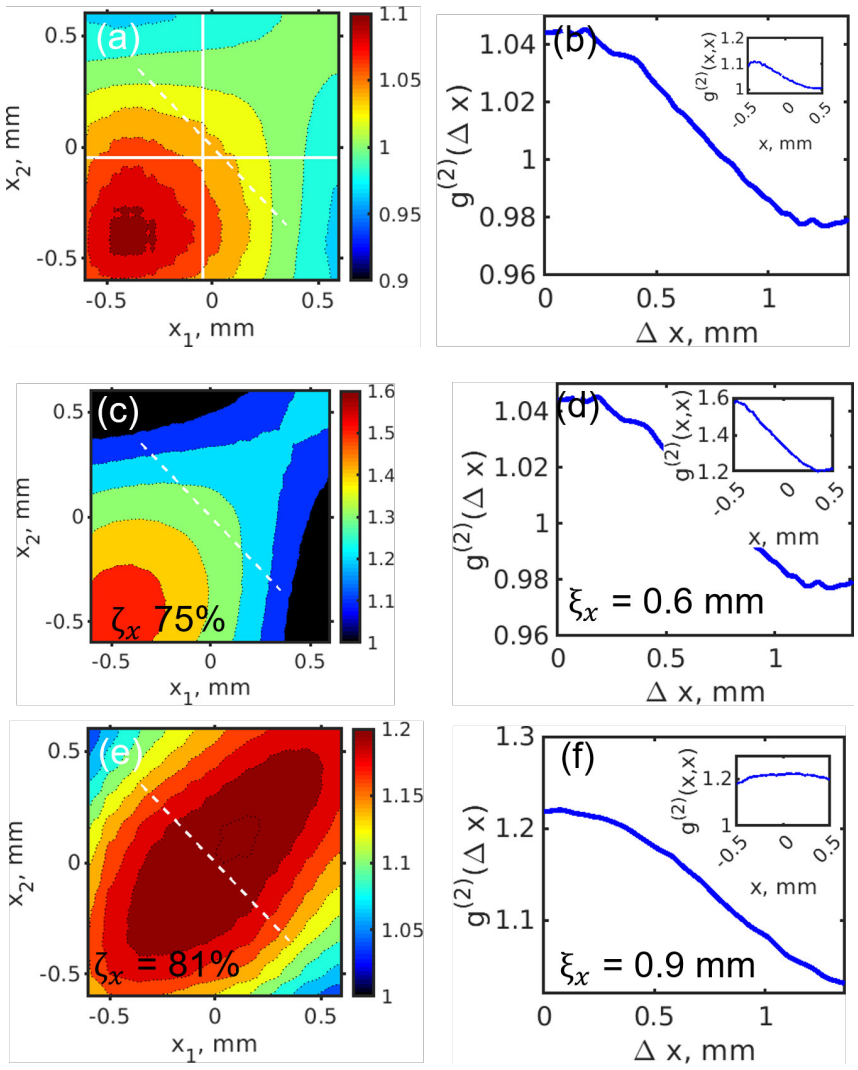

Figure C.14: Intensity correlation functions $g^{(2)}(x_1, x_2)$ (a,c,e) measured by the Hamamatsu detector in the horizontal direction. Profiles of the $g^{(2)}(\Delta x)$ (b,d,j)- function was taken along the white dashed anti-diagonal lines shown in panels (a,c,e). In the inset the corresponding autocorrelation functions $g^{(2)}(x, x)$ taken along the diagonal lines of $g^{(2)}(x_1, x_2)$-function are shown. Here results for the SASE PINK operating regime shown in (a,b), SASE MONO in (c,d) and SS regime in (e,f) shown for the case of 200 pC bunch charge.

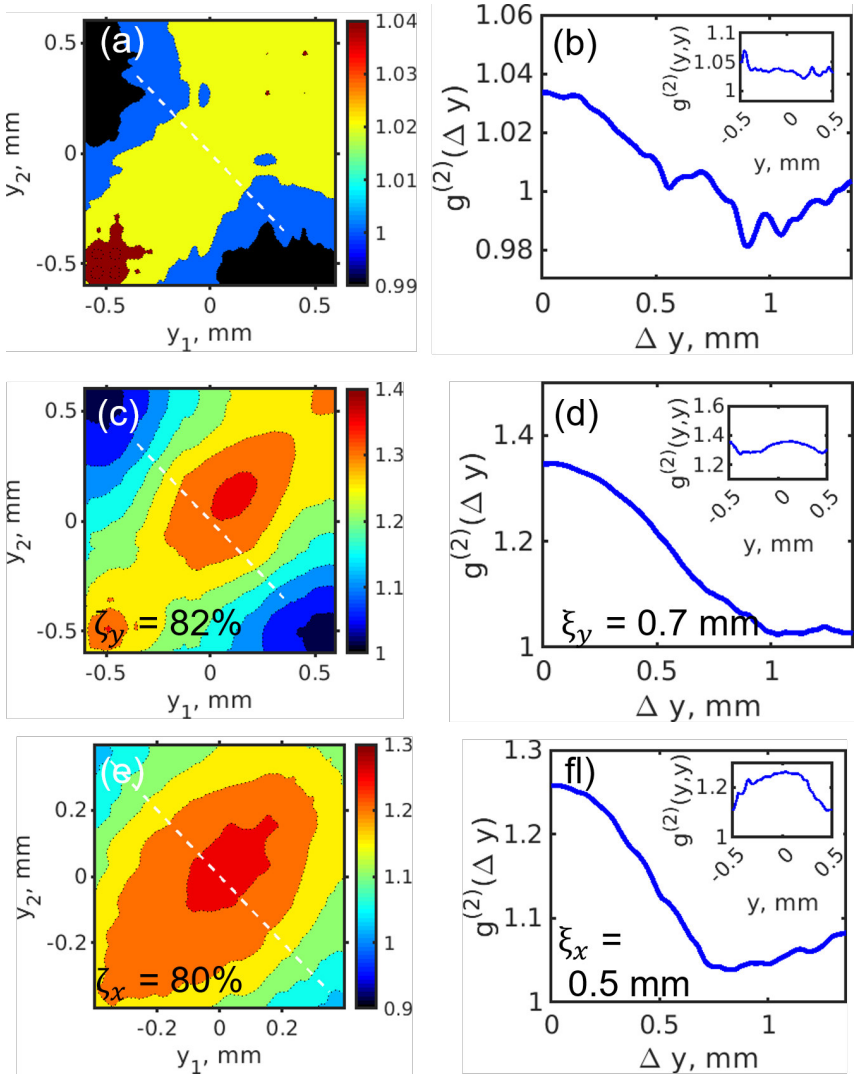

Figure C.15: Intensity correlation functions $g^{(2)}(y_1, y_2)$ (a,c,e) measured by the Hamamatsu detector in the vertical direction. Profiles of the $g^{(2)}(\Delta y)$ (b,d,j)- function was taken along the white dashed anti-diagonal lines shown in panels (a,c,e). In the inset the corresponding autocorrelation functions $g^{(2)}(y, y)$ taken along the diagonal lines of $g^{(2)}(y_1, y_2)$-function are shown. Here results for the SASE PINK operating regime shown in (a,b), SASE MONO in (c,d) and SS regime in (e,f) shown for the case of 200 pC bunch charge.